



AN ELECTROGONIOMETER TO MEASURE SPINAL CURVATURE

PHILIP C. SMIT

**This thesis is submitted in partial fulfillment of the requirements for the Degree
of PhD in Biomedical Engineering.**

Sept 2014

DECLARATION

This thesis is the result of the author's original research. It has been composed by the author and has not been previously submitted for examination which has led to the award of a degree.

The copyright of this thesis belongs to the author under the terms of the United Kingdom Copyright Acts as qualified by University of Strathclyde Regulation 3.50. Due acknowledgement must always be made of the use of any material contained in, or derived from, this thesis.

Signed:

Date:

TABLE OF CONTENTS

ACKNOWLEDGEMENTS		v
DEDICATION		vi
ABSTRACT		vii
LIST OF SYMBOLS		x
LIST OF TABLES		xiv
LIST OF FIGURES		xv
LIST OF ABBREVIATIONS		xxi
CHAPTER 1	INTRODUCTION	1
	1.1 Motivation	2
	1.2 Research Aim	3
	1.3 Thesis Layout	5
CHAPTER 2	LITERATURE REVIEW	8
	2.1 Anatomy of the Spine	8
	2.1.1 Elements and Structure	10
	2.1.2 Supporting Tissue	11
	2.1.3 Range-of-Motion	12
	2.2 Motion Capture Devices and Systems	14
	2.2.1 <i>In Vivo</i> Methods	15
	2.2.2 <i>In Vitro</i> Methods	16
	2.2.2.1 Video Motion Capture Systems	16
	2.2.2.2 Electromagnetic Motion Capture Systems	22
	2.2.2.3 Inertial Sensors	22
	2.2.2.4 Goniometers and Torsiometers	25
	2.2.2.5 Other Devices	29
	2.3 Discussion	31
CHAPTER 3	REQUIREMENTS	34
	3.1 Requirements	34
	3.1.1 Physical Dimensions	35
	3.1.2 Range-of-Motion	36
	3.1.2.1 Translation	36
	3.1.2.2 Rotation	36
	3.1.3 Other Device Characteristics	36
	3.2 A Distributed versus Central Design	37
	3.3 Conclusion	39

CHAPTER 4	MECHANICAL DESIGN	40
	4.1 The Goniometer-Node	40
	4.1.1 Spherical- Prismatic Joint	41
	4.1.2 Universal-Cylindrical Joint	42
	4.1.3 Universal-Revolute-Prismatic Joint	43
	4.1.4 Discussion of Designs	43
	4.2 Kinematic Analysis of the Universal-Cylindrical Joint	44
	4.3 The Electrogoniometer as a Serial Kinematic Chain	45
	4.4 Conclusion	48
CHAPTER 5	KINEMATIC SENSING	49
	5.1 An Overview of Sensor Technologies	49
	5.1.1 Hall-Effect Sensors	50
	5.1.2 Flex Sensors	50
	5.1.3 Inertial Sensors	51
	5.1.4 Optical Sensors	53
	5.1.5 Discussion	53
	5.1.6 Related Work	55
	5.2 Pose Estimation through Optical Sensing	56
	5.2.1 Theoretical Analysis of a Single Emitter-Detector Pair	56
	5.2.2 Multi Emitter-Detector Pairs and its Application to sense the Pose of the Universal-Cylindrical Joint	59
	5.2.3 Cylindrical Joint Emitter-Detector Pair Analysis	60
	5.2.3.1 Lower Section Analysis	60
	5.2.3.2 Upper Section Analysis	62
	5.2.3.3 Summary of Analysis	62
	5.2.4 Universal Joint Emitter-Detector Pair Analysis	64
	5.2.4.1 Analysis	64
	5.2.4.2 Summary of Analysis	65
	5.3 Theoretical Results	67
	5.4 Model Validity and Curve-Fitting	69
	5.5 Non-Parametric Model	71
	5.6 Conclusion	73
CHAPTER 6	DESIGN REALISATION	75
	6.1 Development History Overview	75
	6.2 The Goniometer-Node	78
	6.2.1 Electronic Implementation	78
	6.2.2 Mechanical Assembly	80
	6.3 Master-Controller and Slave Chaining	82
	6.4 The Assembled Device	84
	6.5 Remote Processing	85
	6.6 Conclusion	87
CHAPTER 7	CALIBRATION AND TEST INSTRUMENT	88
	7.1 Design and Implementation	88
	7.2 Calibration Procedure	92
	7.3 Conclusion	94

CHAPTER 8	MEASUREMENT AND COMPARISON METHOD	96
	8.1 Motion Capture Setup	96
	8.2 Determining the Mechanical (true) Chain with Qualisys	98
	8.2.1 Notations	99
	8.2.2 Transforming the <i>V</i> -chain to the <i>U</i> -chain	101
	8.2.2.1 Finding the Center-of-Rotation	101
	8.2.2.2 Finding the Minimum Link Length	104
	8.2.2.3 Kinematics of the <i>U</i> -chain	105
	8.2.2.4 Neutral-pose Calibration	106
	8.2.3 Transforming the <i>U</i> -chain to the U_1 -chain	107
	8.3 Estimating the Mechanical Chain with the Electrogoniometer	108
	8.3.1 Determining the Electrogoniometer Chain	108
	8.3.2 Determining the Neutral-pose Compensated Chain	108
	8.4 Comparing Reference Frames	110
	8.4.1 Comparison of Translations	109
	8.4.2 Comparison of Rotations	109
	8.4.1.1 Comparison of Cardan Angles	111
	8.4.1.2 SO(3) Rotation Metrics	112
	8.5 Method Summary	113
	8.6 Conclusion	114
CHAPTER 9	RESULTS	116
	9.1 Theoretical Model	116
	9.2 Goniometer-Node Accuracy and Precision	118
	9.3 Measurement Setup and Qualisys Evaluation	120
	9.3.1 Measurement Setup	120
	9.3.2 Data Acquisition and Analysis	121
	9.3.3 Qualisys Evaluation	123
	9.4 Calibration	124
	9.4.1 Joint Center-of-Rotation, Minimum Link Length and Pose Calibration	125
	9.4.2 Neutral-Pose Calibration	125
	9.5 Electrogoniometer Evaluation	125
	9.5.1 Local Accuracy and Precision	126
	9.5.2 Global Accuracy and Precision	127
	9.6 Conclusion	129
CHAPTER 10	DISCUSSION AND CONCLUDING REMARKS	131
	10.1 Discussion of Calibration and Test Instrument Results	132
	10.2 The Qualisys System as a Benchmark	135
	10.2.1 Translation Errors	135
	10.2.2 Rotation Errors	135
	10.3 Discussion of the Electrogoniometer Results	136
	10.3.1 Static versus Dynamic Measurements	137
	10.3.2 Errors introduced by the CaT Instrument	137
	10.3.3 Errors introduced by the Measurement Method	139

10.3.4 Propagation of Local Errors through a Kinematic Chain	140
10.4 Concluding Remarks	141
10.4.1 Engineering Issues	141
10.4.2 Global versus Local Measuring Devices	141
10.4.3 Research Aims	142
10.4.4 Specifications	143
10.4.5 Applications	144
10.4.6 Future Work	145
10.4.7 Final Remarks	147
APPENDIX	
APPENDIX A	148
A.1 Rotation Matrix of a Goniometer-Node	148
A.2 CaT Instrument: $(\alpha, \beta) \mapsto (\phi, \theta)$ Transformation	148
A.3 Solution to the SCoRE Problem	150
APPENDIX B	153
B.1 Detector Datasheet	153
B.2 Emitter Datasheet	156
B.3 Goniometer-Node Schematics	159
B.4 Master-Controller Schematics	161
REFERENCES	165

Acknowledgements

I would like to thank my supervisors, Dr Philip Riches and Professor Bernard Conway for supporting me through this process. Despite being very busy, I could always count on Dr Riches' support and advice. He gave me the freedom to explore new ideas and was never judgmental about mistakes I have made. I also would like to thank Mr Danny Rafferty from Glasgow Caledonian University and Dr Craig Childs from Strathclyde University who help with the video motion capture and offer valuable advice. Gratitude is also due to Dr Ben Stansfield from Glasgow Caledonian University who helped support my application for this PhD. And finally, and extra special thank you to my wife, Rolinda, who proofread this thesis.

Dedication

Embarking on a PhD is a lonely journey, yet it could not have been done without the support from the people closest to me. I would like to thank my lovely wife, Rolinda, and my two boys Adam and Daniel for their love and support. When I was in the "wilderness", they had to content without a husband and dad. I have lost my Mom during this journey. I wish she could see the final results of my work. I know she approves. This research is also dedicated to my Grandfather whose constant curiosity kept me inspired. He was and still is a great influence on my life.

In loving memory of my Mother and my Grandfather ...



SUSANNA LUCEA NORTJE (1950 - 2012)



CHRISTIAAN COENRAAD JOUBERT (1924-2014)

Abstract

Biomechanical motion capture is the process of recording the movements of people or animals. As an analysis tool it offers valuable insight into human motion and is useful to monitor treatment during rehabilitation. The spine in particular receives a significant amount of attention by biomechanical researchers, as spinal health is directly related to the quality-of-life of an individual. Spinal motion capture improves the understanding of the function and vulnerabilities of the spine as a mechanical structure and the analysis of spinal kinematics, in conjunction with spinal loading, offers a method for analysing therapeutic interventions.

Numerous motion capture systems and devices are currently available, each with its own strengths and weaknesses. The systems or devices selected by researchers are usually determined by study objectives. For example, a video motion capture system would clearly not be appropriate in a study designed to monitor lower back movements of factory workers. Instead, unobtrusive accelerometry based devices would be more suitable to measure kinematics in a free-living environment. Accelerometry has its drawbacks however. It is limited to only global pitch and roll measurements and requires a subject to make relatively slow movements (i.e. the acceleration component of movement measured by the accelerometer must be significantly smaller than one g). In general, trade-offs exist between accuracy, obtrusiveness, ease-of-use, cost, mobility (degrees-of-freedom) and clinical versus free-living measurements.

This thesis proposes an electrogoniometer, which meets many of the above mentioned criteria. The electrogoniometer aims to be accurate yet unobtrusive, low cost (perhaps less than £5 000, compared to the £100 000 price tag of high-end marker-based video motion capture system) and measures high mobility movement (typically the rotation components of a spinal motion segment) and do so within a free-living setting.

The electrogoniometer is composed of discrete goniometers, referred to as goniometer-nodes. The goniometer-nodes are chained serially together to construct a multi degree-of-freedom electrogoniometer. The goniometer-nodes consist of mechanical structures embedded with optical sensors, each capable of measuring four degrees-of-freedom (three rotations and one translation). The mechanical structure's articulation is determined by

processing the optical sensor data using the principles of triangulation and trilateration. The articulation is measured relative to a local reference frame (i.e. relative to the proximal-end of the node). Since local reference frame measurements are involved, accuracy and precision are important. Poor accuracy and precision will result in measurement errors propagating through the chain. The rotation accuracy is estimated to be better than 2° per axis (which is much less than the typical 5° accuracy of commercial goniometers) and a displacement (translation) accuracy of less than 0.2 mm. Precision is estimated better than 0.5° degrees per axis and 0.1 mm.

The device is particularly suitable to measure spinal movement. It is attached to the back of a subject, similar to commercial electrogoniometers. It monitors the spinal kinematics on a continuous basis and transmits the data to a computer via a wireless adaptor. The kinematic data is then available for further analysis.

This thesis initially investigates the mechanical and sensor design of the goniometer-nodes. A mechanical composite structure consisting of an universal (two rotations) and cylindrical (one rotation and translation) joint was utilised. Optical emitter-detector pairs were embedded within the structure, and a mathematical model was derived to predict the response of the detectors based upon the kinematic input. A custom instrument was developed to calibrate the nodes. Five nodes were assembled and calibrated, and then chained together to produce the electrogoniometer.

The second part of the thesis evaluates the device. Reflective triads were attached to the base of each node within the chain. The device was then manipulated manually and compared against a video motion capture system for accuracy and precision. Analysis of the results showed a local reference frame accuracy and precision of $1.9 \pm 1.0^\circ$ per axis for rotation and 3.5 ± 1.8 mm for translation. The video captured measurements were also compared to the calibration results and proved to be worse than predicted. The cause was traced to the calibration instrument and the measurement method.

Although the accuracy and precision specification were not met, it was concluded that the proof-of-concept electrogoniometer demonstrated here has merit as a low-cost motion capture device. The optical measurement method from which the electrogoniometer kinematics are determined, shows promise as a novel kinematic sensing method. It was concluded that with further refinement and improvements of the custom-build calibration

instrument, the accuracy and precision requirements can be met. Nonetheless, the concepts and principles have been shown to be valid, and with additional resources, this electrogoniometer can be a viable biomechanical research device.

List of Symbols

Symbol	Description
$\mathbf{0}_{1 \times 3}$	Zero 1 x 3 row vector
$\mathbf{0}_{3 \times 1}$	Zero 3 x 1 column vector
α	Calibration instrument axis
α_0	Design parameter; angle between detectors in cylindrical joint.
β	Calibration instrument axis
β_{ji}	Angle between emitter j and detector i in the $x - z$ plane of the cylindrical joint.
β'	Misalignment angle about z axis (degrees).
δ	Kinematic input variable; goniometer-node translation in z axis (mm).
${}_{i+1}^i \delta_0^{(U)}$	Minimum link length between joint i and $i+1$ (mm).
${}_{i+1}^i \delta_1^{(U)}$	Distance between joint i and $i+1$ (mm).
ε	Angle error (degrees).
n_θ	Noise component associated with rotation θ .
n_ϕ	Noise component associated with rotation ϕ .
n_ψ	Noise component associated with rotation ψ .
θ	Kinematic input variable; goniometer-node rotation about z axis.
${}^0_i \Theta$	Global random variable (node i relative to node 0).
${}^{i-1}_i \Theta$	Local random variable (node i relative to node $i - 1$).
μ	Sample mean.
${}^0_i \mu$	Mean sample value of node i relative to node 0 .
σ	Sample standard deviation.
${}^{i-1}_i \sigma^2$	Sample variance of node i relative to node $i - 1$.
${}^0_i \sigma^2$	Sample variance of node i relative to node 0 .
Φ_1	Rotation distance metric used by Grankow (2001) (degrees)
Φ_2	Rotation distance metric used Huynh (2009) (degrees).
Φ_3	Rotation distance metric using the Manhattan distance of the Cardan angles (degrees).
ϕ	Kinematic input variable; goniometer-node rotation about x axis (degrees).
φ_e	Emitter radiation flux (W).
χ_d	Angle of light incident relative to detector axis (degrees).
$\chi_{d_{ji}}$	Angle of light incident relative to detector i axis and emitted from emitter j (degrees).
χ_e	Angle of light radiating relative to an emitter axis and towards a detector (degrees)
$\chi_{e_{ji}}$	Angle of light radiating relative to emitter j axis and towards detector i (degrees).
ψ	Kinematic input variable; goniometer-node rotation about y axis (degrees).
\mathbf{d}	Vector distance in direction of goniometer-node y axis (mm).

d	Euclidean length in goniometer-node (mm).
d'	Translation distance of upper section of the cylindrical joint (mm).
${}^0_i\mathbf{d}^{(G_V)}$	Global distance from node O to node i of chain (mm).
${}^{i+1}_i\mathbf{d}^{(T)}$	Local vector distance from node i to $i + 1$ of chain T .
${}^{i+1}_i d^{(T)}$	Local Euclidean distance from node i to $i + 1$ of chain T .
${}^{i+1}_i\mathbf{d}^{(T_1)}$	Local vector distance from node i to $i + 1$ of chain T_1 .
${}^i_i\mathbf{d}^{(V_U)}$	Local vector distance from node i of chain V to node i of chain U .
${}^{i+1}_i\mathbf{d}^{(U_1)}$	Local vector distance from node i to $i + 1$ of chain U_1 .
${}^{i+1}_i d^{(U_1 T_1)}$	Local Euclidean distance from node i to $i + 1$ of chain $U_1 T_1$.
d_{max}	Internal height of cylindrical joint (mm).
E	Emitter irradiance (W/m^2).
E_d	Irradiance received by the detector (W/m^2).
f_d	Detector directivity pattern (function).
f_e	Emitter directivity pattern (function).
G	Global reference frame.
g	Gain parameter.
${}^0_i\mathbf{G}_U$	Global transformation matrix of node i in chain U relative to G .
${}^0_i\mathbf{G}_V$	Global transformation matrix of node i in chain V relative to G .
h_δ	Transfer function relating the detector voltages (independent variables) to the kinematic variable δ .
h_θ	Transfer function relating the detector voltages (independent variables) to the kinematic variable θ .
h_ϕ	Transfer function relating the detector voltages (independent variables) to the kinematic variable ϕ .
h_ψ	Transfer function relating the detector voltages (independent variables) to the kinematic variable ψ .
$\mathbf{I}_{3 \times 3}$	3 x 3 identity matrix.
I_e	Emitter radiant intensity (W).
$I_{e_{iso}}$	Maximum emitter radiant intensity (W).
k	Detector constant.
k_R	Detector constant including detector circuit resistance.
l_0	Universal and cylindrical joint dimension parameter (mm).
l_1	Universal and cylindrical joint dimension parameter (mm).
l_2	Universal joint dimension parameter (mm).
l_3	Universal joint dimension parameter (mm).
l_ε	Vertical distance between emitters in cylindrical joint (mm).
\mathbf{n}_{ji}	Unit vector in y axis.
$\mathbf{Q}_{x,\phi}$	Global basic rotation matrix of ϕ degrees about the x axis.
$\mathbf{Q}_{y,\beta_{ji}}$	Global basic rotation matrix of β_{ji} degrees about the y axis.
$\mathbf{Q}_{z,\theta}$	Global basic rotation matrix of θ degrees about the z axis.

$R_{\gamma\mu}$	Universal joint rotation matrix.
R_{ζ}	Sequence of basic location rotations ($R_{\zeta} = R_{y,\psi}R_{z,\theta}R_{x,\phi}$).
$R_{x,\phi}$	Basic local rotation about x axis.
$R_{x,\psi}$	Basic local rotation about y axis.
$R_{z,\theta}$	Basic local rotation about z axis.
r	Universal joint rotation radius (mm).
R_d	Series resistor in detector circuit (ohm).
${}^0R^{(G_V)}$	Transformation matrix of joint i in chain V relative to the global reference frame G .
${}^{i+1}R^{(T)}$	Rotation matrix of reference frame $i + 1$ relative to i in chain T .
${}^{i+1}R^{(T_0)}$	Rotation matrix of reference frame $i + 1$ relative to i in chain T_0 .
${}^{i+1}R^{(U)}$	Rotation matrix of reference frame $i + 1$ relative to i in chain U .
${}^{i+1}R^{(U_0)}$	Rotation matrix of reference frame $i + 1$ relative to i in chain U_0 .
${}^{i+1}R^{(U_1)}$	Rotation matrix of reference frame $i + 1$ relative to i in chain U_1 .
$R^{U_1}(\psi, \theta, \phi)$	Rotation matrix of reference frame $i + 1$ relative to i in chain U_1 .
$R_{x,\phi}$	Basic location rotation matrix about the x axis.
$R_{x,\phi}^{U_1}(\phi)$	Basic rotation matrix of reference of a joint in the U_1 chain about the x axis.
$R_{y,\psi}$	Basic location rotation matrix about the y axis.
$R_{y,\psi}^{U_1}(\psi)$	Basic rotation matrix of reference of a joint in the U_1 chain about the y axis.
$R_{z,\theta}$	Basic location rotation matrix about the z axis.
$R_{z,\theta}^{U_1}(\theta)$	Basic rotation matrix of reference of a joint in the U_1 chain about the z axis.
${}^{i+1}R^{(U_1T_1)}$	Distance rotation matrix of reference frame $i + 1$ relative to i between chain U_1 and T_1 .
${}^{i+1}R^{(V)}$	Rotation matrix of reference frame $i + 1$ relative to i in chain V .
s	Euclidean distance between detector and emitter (mm)
S_{ji}	Euclidean distance between emitter j and detector i (mm).
\widehat{S}_{ji}	Normalised vector distance between emitter j and detector i (mm).
S_{ji}	Sensitivity of detector i relative to emitter j .
T_{ζ}	R_{ζ} expressed as a homogeneous transformation matrix.
T	Kinematic chain T .
T	The matrix product of the homogenous rotation and translation matrices.
${}^{i-1}T$	Local transformation of joint i relative to joint $i - 1$ of kinematic chain T .
0T	Global transformation of node i relative to joint 0 of kinematic chain T .
0T_1	Global transformation of node i relative to joint 0 of kinematic chain T_1 .
T_d	The translation component expressed as a homogeneous transformation matrix.
T_{ji}	Kinematic transformation from emitter j to detector i .
U	Kinematic chain U .
${}^{i+1}U$	Local transformation of joint i relative to joint $i - 1$ of kinematic chain U .
U_1	Kinematic chain U_1 .

${}^{i+1}U_1$	Reference frame of joint $i + 1$ relative to joint i of kinematic chain U_1 .
V	Kinematic chain V .
v_a	Difference voltage of detector pair 0-1 embedded within the universal joint (V).
v_b	Difference voltage of detector pair 2-3 embedded within the universal joint (V).
v_{dji}	Detector i voltage when irradiated by emitter j (V).
iV_U	Inter-chain transformation of joint i in chain V relative to joint i in chain U .
Δx	Misalignment error (mm).

List of Tables

Table 2.1	A heat map comparison of different devices and systems used by biomechanists.
Table 3.1	Summary of the electrogoniometer and goniometer-node requirements.
Table 4.1	Design criteria applied to the proposed mechanical designs.
Table 5.1	Comparison of different sensing technologies and methods to determine orientation and position.
Table 5.2	Summary of the system of equations describing the kinematic variables d and ψ as measured by the multiple emitter-detector pairs scheme in figures 5.3 and 5.4.
Table 5.3	Summary of the system of equations describing the kinematic variables ϕ and θ as measured by the multiple emitter-detector pairs scheme in figure 5.5.
Table 8.1	Summary of the measurement method.
Table 9.1	Accuracy (μ) and precision (σ) errors of the four kinematic variables as measured by the calibration and test instrument.
Table 9.2	Qualisys static and dynamic precision as measured by the V -chain.
Table 9.3	Qualisys static and dynamic precision as measured by the U -chain.
Table 9.4	The CoR fit errors and MLL as calculated from the Qualisys motion capture data.
Table 9.5	Local accuracy and precision errors as calculated from the distance error metric (equation 8.25).
Table 9.6	Local accuracy and precision errors as calculated from the rotation error metric (equation 8.32).
Table 9.8	Global errors as calculated from the distance error metric.
Table 9.9	Global accuracy and precision errors as calculated from the rotation error metric.
Table 10.1	Summary of the actual and original specifications of the electrogoniometer and goniometer-nodes (original specifications are in brackets; green: actual specification is better than original specification; red : actual specification is worse than original specification).
Table B.1	Goniometer-node bill of materials.
Table B.2	Master-controller bill of materials.

List of Figures

- Figure 1.1 Eadweard Muybridge illustrated through a series of photographs that a galloping horse has all four hooves off the ground (slide three) at some point during a trot (Muybridge, 1882).
- Figure 1.2 An example of marker-based video motion capture (Herda et al., 2001).
- Figure 1.3 Artist rendering of the proposed device. The purpose of the device is to measure complex spinal movement.
- Figure 2.1 The spinal column and the four different regions: the cervical, thoracic, lumbar and sacral spines.
- Figure 2.2 Elements of the spine.
- Figure 2.3 Muscles of the back.
- Figure 2.4 Range of motion of a normal spine (White and Panjabi, 1990).
- Figure 2.5 The Schober and Ott Test to determine spinal mobility.
- Figure 2.6 X-ray system developed by Pearcy (1985) to measure 3D inter-vertebral articulation.
- Figure 2.7 Test robot developed by Windolf et al. (2008) to test the accuracy and precision of the Vicon 460 system.
- Figure 2.8 Rotation and translation accuracy and standard deviation (error bars) versus camera distance of the Optotrak 3020 system (Maletsky et al., 2007).
- Figure 2.9 Biomechanical model as acquire from the Stanford Markerless Motion Capture Project a) Human shape identification and reconstruction; b) Model fitting against a database of shapes; c) Shape integration with musculoskeletal system; d) Real-time skeletal markerless kinematics. (<https://ccrma.stanford.edu/~stefanoc/Markerless/Markerless.html>)
- Figure 2.10 The inertial sensor system proposed by Wong and Wong (2009). The system consists of three inertial modules.
- Figure 2.11 Commercial a) uni-axial mechanical goniometer (www.noraxon.com); b) bi-axial fibre-optic electrogoniometer (Szulc et al., 2011).
- Figure 2.12 a) Lumbar spine device developed by Williams et al., b) ShapeTape is at the core of the device.
- Figure 2.13 The Lumbar Motion Monitor: a tri-axial goniometer developed at Ohio State University. (<http://www.nexgenergo.com/ergonomics/lumbarmm.html#Sec2>)
- Figure 2.14 The CA6000 Spine Motion Analyzer (Mieritz et al., 2013)
- Figure 2.15 Spine monitor device developed by Consmüller et al. (2012). The device use strain sensors and accelerometers.
- Figure 2.16 Determining the range of motion of a spine using the SpinalMouse (Kellis et al., 2008).
- Figure 3.1 Conceptual design of a) the goniometer-node; b) the electrogoniometer.
- Figure 4.1 Three different geometries for a four DOF goniometer-node a) Spherical-

- prismatic joint; b) Universal-cylindrical joint; c) Universal-revolute-prismatic joint.
- Figure 4.2 Rotation sequence for the goniometer-node: a) No rotated (proximal and distal axis are aligned) b) First rotation is about the x axis ($R_{x,\phi}$) c) Second rotation is about the z axis ($R_{z,\theta}$); d) Third rotation is about the y axis ($R_{y,\psi}$); e) Rotation applied to universal-cylindrical joint structure.
- Figure 4.3 The electrogoniometer as a serial chain of the goniometer-nodes with attached reference frames.
- Figure 5.1 The position and orientation system using optical emitters and detects developed by Heo et al. (2011).
- Figure 5.2 a) Typical receiver and transmitter spatial directivity patterns of a detector and emitter (Vishay Semiconductors, 2008); b) Infrared emitter and detector circuit.
- Figure 5.3 Kinematic variables and parameters of the lower section of the cylindrical joint.
- Figure 5.4 Kinematic variables and parameters of the upper section of the cylindrical joint.
- Figure 5.5 Kinematic variables and parameters of the universal joint.
- Figure 5.6 Transfer function of the six detectors in the cylindrical joint. The system parameters are: $l_0 = 4mm$, $l_1 = 4.6mm$, $f_e(\chi_e) = \cos\chi_e$, $f_d(\chi_d) = \cos\chi_d$. Transfer function of the four universal joint detectors with system parameters $l_0 = 1mm$, $l_1 = 5.5mm$, $l_2 = 4.5mm$, $l_3 = 3.15mm$, $f_e(\chi_e) = \cos\chi_e$, $f_d(\chi_d) = \cos\chi_d$. a) $v_{d_{00}}$; b) $v_{d_{01}}$; c) $v_{d_{02}}$; d) $v_{d_{10}}$, $v_{d_{11}}$ and $v_{d_{12}}$.
- Figure 5.7 Transfer functions of the cylindrical joint. The system parameters are: $l_0 = 1mm$, $l_1 = 5.5mm$, $l_2 = 4.5mm$, $l_3 = -3.15mm$, $f_e(\chi_e) = \cos\chi_e$, $f_d(\chi_d) = \cos\chi_d$. a) $v_{d_{00}}$ and $v_{d_{11}}$; b) $v_{d_{22}}$ and $v_{d_{33}}$; c) $v_a = v_{d_{00}} - v_{d_{11}}$; d) $v_b = v_{d_{22}} - v_{d_{33}}$.
- Figure 5.7 Issues affecting the accuracy of the model: a) Optical and mechanical axis of emitters and detectors are not aligned; b) Multipath reflections will cause unpredictable detector signals; c) Location of optical components may differ from model parameters.
- Figure 6.1 Evolution of the goniometer-node design: a) Experimental setup to test the concepts and principles of kinematic measurements through optical sensing; Goniometer-nodes based upon b) spherical-prismatic; c) universal-cylindrical and d) universal-revolute-prismatic joint designs.
- Figure 6.2 The electronic components of a goniometer-node (the full schematic is in appendix B.3).
- Figure 6.3 Flow diagram illustrating the processes involved to acquire raw detector data and transmit it to the master-controller.
- Figure 6.4 Description of the packet carrying data payload.
- Figure 6.5 Realisation of the goniometer-node: a) Mechanical and electronic

- components; b) Design; b) Implementation.
- Figure 6.6 Electronic chaining of the master-slaves setup.
- Figure 6.7 Flow diagram illustrating the control the master-controller exercise over the slave-nodes.
- Figure 6.8 The electrogoniometer without a silicone skin.
- Figure 6.9 a) The electrogoniometer in relation to the spinal column; b) The electrogoniometer attached to the back.
- Figure 6.10 Flow diagram of the different processes running on the PC.
- Figure 6.11 The 3D rendering of the electrogoniometer data in a virtual environment.
- Figure 7.1 a) CAD design showing the primary components of the calibration and test instrument; b) Implementation of the design with supporting electronic hardware.
- Figure 7.2 Open loop stepper-motor control setup.
- Figure 7.3 Graphical user interface of the application to calibration goniometer-nodes.
- Figure 7.4 An alignment rod is used to initially align the ϕ axis of the goniometer-node with the β -axis of the calibration instrument.
- Figure 8.1 a) Qualisys motion capture setup. The global reference frame (G) as defined by the Qualisys system is shown in red; b) Electrogoniometer with reflective triads.
- Figure 8.2 Symbolic representation of the Qualisys mechanical and electrogoniometer kinematic chains.
- Figure 8.3 Reference frame representation of the kinematic chains. Black transformations are known through direct measurements and red transformations has to be determined algorithmically. The objective is to determine chain U_i which can serve as benchmark to compare electrogoniometer measurements against.
- Figure 8.4 Notations used to describe matrices in terms of the joints and chains they are related to.
- Figure 8.5 Determining the CoR of joint i using the SCoRE method.
- Figure 8.6 The link length in relation to the goniometer-nodes. The link length is decomposed into two components: the minimum link length (MLL) and measured displacement.
- Figure 8.7 Neutral poses obtained from a non-curved pose. Red is the neutral pose axes and blue the actual measured axes.
- Figure 8.9 The neutral-pose compensated (T_i) chain which is derived from the T -chain. The T_i chain is later compared against the U_i -chain to determine the accuracy of the electrogoniometer.
- Figure 8.10 a) Difference in position of reference frames ${}_{i+1}^iU_1$ and ${}_{i+1}^iT_1$; b) Difference in rotation frames ${}_{i+1}^iU_1$ and ${}_{i+1}^iT_1$ (note, the chain rotations super- and subscripts are omitted in the text to reduce clutter).
- Figure 9.1 Comparison of the transfer functions of detectors 0, 1 and 2 as

- determined by the a) mathematical model; b) calibration and test instrument.
- Figure 9.2 Transfer functions of detectors 0, 1 as determined by the a) theoretical model and; b) CaT instrument. Transfer functions of detectors 2, 4 as determined by the c) theoretical model and; d) CaT instrument.
- Figure 9.3 Qualisys motion capture setup. The global reference frame (G) as defined by the Qualisys system is shown in red.
- Figure 9.4 The triad with attached reference frame.
- Figure 9.5 a) The graphical user interface of the data analysis application; b) 3D rendering of the captured data by the same application. The Qualisys chain is slightly transparent and the electrogoniometer chain is solid in appearance.
- Figure 9.6 Static and dynamic testing of the Qualisys system. The device is attached to an acrylic sheet so ensure no inter node movement during testing.
- Figure 9.8 a) Local errors as calculated from the distance error metric (equation 8.25); b) Local errors as calculated from the rotation error metric (equation 8.32).
- Figure 9.9 a) Global distance error calculated from the distance metric; b) Global errors as calculated from the rotation error metric.
- Figure 10.1 Sensitivity versus the precision of the ψ axis (lighter shades of grey represent good sensitivity): a) Sensitivity of detector 0; b) Sensitivity of detector 1; c) Sensitivity of detector 2; d) Average sensitivity of the three detectors.
- Figure 10.2 Different sensitivities of the transfer function detector 0 where $d = 1$ mm.
- Figure 10.3 Upper bound estimation of the rotation error about a single angle based upon the accuracy error reported by Windolf using a 9.5 mm marker.
- Figure 10.4 a) The CoR of the CaT instrument; b) Misalignment of the CaT instrument's CoR and the universal joint's CoR will cause the joint to be subjected to an angle of β' instead of β degrees; c) The angular error due to the misalignment where $r = 4.6$ mm and with a misalignment of $\Delta x = 250$ μm .
- Figure 10.5 Statistical nature of the local and global accuracy and precision errors for the example stated in the text. The example assumes the local accuracy errors are unbiased. a) Local reference frame errors; b) Global reference frame errors.
- Figure 10.6 The 32-bit Kinetis KL03 microcontroller by Freescale measure only 1.6 x 2 mm.
- Figure A.1 Conversion between the CaT instrument and goniometer-node reference frames.
- Figure B.1 Goniometer-node schematics.
- Figure B.2 Goniometer-node layout.

Figure B.3 Master-controller schematics.

Figure B.4 Master-controller layout.

List of Abbreviations

Abbreviation

CoR	Centre-of-rotation
DOF	Degrees-of-freedom
MLL	Minimum link length
SCoRE	Symmetrical centre-of-rotation estimation

1.0 Introduction

Motion capture is the recording of the movement of an object. Within the biomedical discipline the "object" is usually a person or animal (referred to as the subject). Eadweard Muybridge (1830-1904) is considered to be the father of motion capture through the medium of photography (Hendricks, 1975). Born near London, he immigrated to the United States age twenty five. Books have been written not only about his professional but also controversial personal life (Braun, 2012) and his work to capture man and animal locomotion is considered to be a fusion of art and science.

Muybridge was commissioned by Leland Stanford, the former governor of California and founder of Stanford University, to take a sequence of photos of a trotting horse (figure 1.1). At the time there was a debate whether a trotting horse had all four hooves off the ground at some point during the trot. As a horse-owner, Stanford wanted to prove this is indeed the case. A sequence of snapshot allowed Muybridge to observe what was previously very difficult to see with the human eye. Though elementary in today's context, Muybridge's groundbreaking motion capture work has all the hallmarks of modern scientific method. The result of this experiment is the now famous "The Horse in Motion" (Muybridge, 1882), which supports Stanford's claim as clearly shown in slide three of figure 1.1.

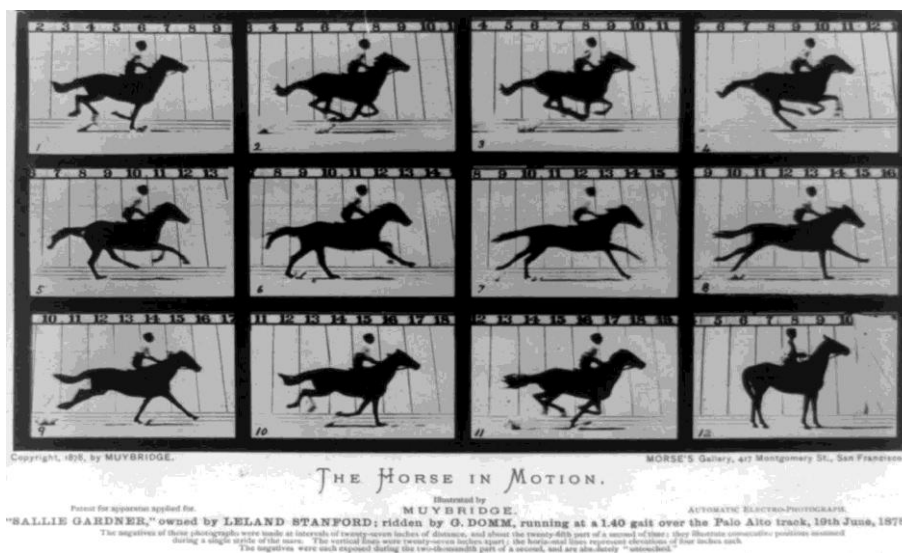


Figure 1.1: Eadweard Muybridge illustrated through a series of photographs that a galloping horse has all four hooves off the ground (slide three) at some point during a trot (Muybridge, 1882).

Although Muybridge's experiment was sufficient to proof Stanford's hypothesis, it may not be adequate to answer other suppositions. Most modern biomechanical problems cannot be accessed through direct visual examination of video evidence alone. In most cases one or more post-processor are required to translate the video observations into something more useful. A typical output of a post-processor for a video based system is the kinematics of the subject under observation. As shown in figure 1.2, locations are identified by markers on the subject of which the kinematics is then determined.

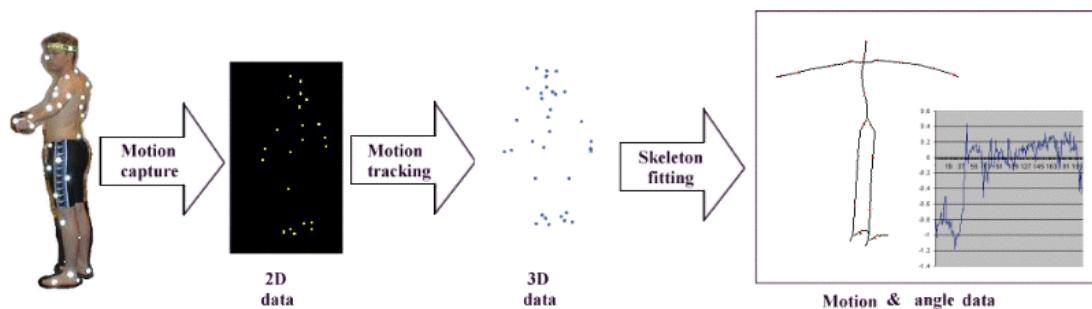


Figure 1.2: An example of marker-based video motion capture (Herda et al., 2001).

The modern bio-mechanist has access to a range of tools, instrumentation and devices, ranging from a simple mechanical goniometer to advanced video capture systems. It is however the opinion of the author that the limitations of current tools offers a clear justification to develop a device that can accurately measure biomechanical movement in a free-living environment. The literature review (chapter two) suggests the typical rotation accuracy of "free-living" devices are 5° and that of laboratory based video capture systems a fraction of a degree. The proposed device must therefore be comparable to a video-capture system in terms of accuracy, yet be unobtrusive enough to function in a free-living environment for extended periods of time.

1.1 Motivation

Video systems offer detailed observations. Marker-based systems offered by for example Vicon (Oxford, United Kingdom) are considered to be the gold standard in motion capture (Barker, 2006). Video systems are however by no means the only motion capture systems available, as no single system can claim a "one size fit all" solution. Consider for example a

research study to continuously assess lumbar posture in the workplace (Burdorf and van Riel, 1996). The method requires the workers to be monitored over an extensive period of time within their work environment. A marker-based video system will clearly be impractical. Firstly, the workers will be subjected to a clinical environment which will affect their normal activity. Secondly, extensive monitoring will be extremely difficult and labour intensive. It has long been known that the outcome of a study can be affected by the clinical environment. Bias can be introduced by a researcher actively accessing the study (sometime referred to as experimenter's bias) (Rosenthal, 1966) and white-coat syndrome (a phenomenon where a participant's behaviour is affected by the mere presence of the clinician) (Owens et al., 1999).

Devices exist that are more suitable to monitor activity in a free-living environment. Examples are optical electrogoniometers and inertial motion sensors (which typically consists of three axis accelerometers and gyroscopes). Current optical electrogoniometers typically measure two degrees-of-freedom and has been extensively used to monitor activity in a free-living environment (e.g. Duc et al., 2013; de Niet et al., 2007). The accuracy of optical electrogoniometers is in the order of 5° (Jonsson et al., 2007). Inertial sensors have had success in a similar environment (Yang and Hsu, 2010) and have a typical accuracy of 5° (Wong and Wong, 2008).

These devices are however limited in their capabilities. Commercial electrogoniometers are limited in their ability to measure mobility. For example, the SG-150 manufactured by Biometrics Ltd (Gwent, UK) can measure angles in only two planes. Extensive research has also been conducted using inertial motion sensors in spinal research (e.g. Wong and Wong, 2008; Theobald et al., 2012). Both these devices are unobtrusive but offer limited accuracy due to their inherited measurement characteristics.

1.2 Research Aim

The aim of this research study is to develop a non-invasive device that can accurately and precisely measure spinal movement down to the inter-vertebrae articulation. The device

must be unobtrusive and suitable to monitor spinal kinematics in a non-clinical environment.

A device is envisioned that is attached to the skin along the spinal column. It is functionally similar to an electrogoniometer but with a much higher degree of mobility allowing complex spinal movement to be measured. Figure 1.3 shows an artist rendering of how such a device will be attached to a subject. The device presented here is however less detailed as the one illustrated in the figure. Since it is a proof-of-concept, it only contains five discrete goniometers (also referred to as goniometer-nodes). The device is therefore only suitable to measure a section of the spine (for example the lumbar spine).

From a mechanical point of view, the device can almost be compared to a section of rubber cord. It can bend, stretch and twist (within limits) allowing it to mimic complex spinal kinematics and do so while having a minimal impact on the movement of the subject. Sensors, internal to the device, measure the shape of the device and transmits the related data to a personal computer, where it is processed and analysed.

Although the emphasis in this work is on spinal kinematics, the device could have many other potential applications. It could be used within the biomechanical research domain to monitor any joint (e.g. the hip), although the minimum bend radius of the prototype device may be a limiting factor for certain joints. The bend radius of the device is specified in chapter three to be 90 mm which may not be sufficient to measure for example a joint like the elbow when fully flexed. Other applications out with biomechanics include physical rehabilitation, the entertainment industry (in particular gaming and live performance capture) and sport performance analysis (a sub-category of biomechanics).



Figure 1.3: Artist rendering of the proposed device. The purpose of the device is to measure complex spinal movement.

An important aspect of the research is the evaluation of the device against a known standard. Marker-based video motion capture systems have been used as a comparative measure for many similar devices (e.g. Sato et al., 2009; Schulze et al., 2012) and is therefore considered a suitable benchmark.

1.3 Thesis Layout

The thesis starts with an overview of the spine. The measurement of spine kinematics is suggested as a potential application of the proposed device. Subsequently, similar biomedical devices are reviewed in the literature and their functional characteristics identified. The review helps to define the requirements of the proposed device in the next chapter.

Chapter three argues a case for a device consisting of discrete four degree-of-freedom goniometers, and linked into a serial chain to construct the electrogoniometer. A basic requirement is formulated which serves as a guideline for the development of the device.

The design, presented in chapters four and five, is divided into a mechanical and sensor (electronic) design. It is argued that the mechanical and sensor design cannot be considered in isolation. A trade-off is identified between the mechanical complexity and algorithmic complexity contained within the sensor design. A mechanical design providing a good trade-off between structural and algorithmic complexity is proposed. The kinematics of the chained discrete mechanical structure is discussed next.

The chapter on sensor design first reviews technologies suitable to sense kinematics. A decision is made to use optical sensors based on the pros and cons of the different sensing technologies. Importantly, the optical sensing method relies on local reference frame measurements. A parametric model to sense the movement of the discrete goniometers is then developed from first principles. The accuracy of the model is questioned due to practical aspects that is difficult to incorporate in the model. A non-parametric approach, in the form of a polynomial fit, is subsequently opted for.

The manufacturing and assembly of the device is discussed in chapter six. An short overview of the engineering issues is given. A discussion on the implementation of the software and construction of the hardware follows.

Chapter seven discusses a custom instrument specifically designed to calibrate the discrete goniometers. The instrument systematically manipulates the mechanical axes of the goniometers while measuring the response of the optical sensors. Polynomial functions, mapping the sensor data to the kinematic axes, are then fitted to the calibration data.

Chapter eight proposes a measurement method that compare the electrogoniometer to a marker-based video motion capture (which acts as the benchmark). Triads are attached to each of the goniometers in the serial chain comprising the electrogoniometer. A measurement method is subsequently devised that compares the kinematic chains of the electrogoniometer to the video motion capture systems. Metrics are defined to compare the serial chains in terms of translation and rotation differences.

The results are presented in chapter nine. Firstly, the non-parametric (polynomial fit) and parametric model transfer functions of the discrete goniometers are compared. The video motion capture system is then assessed as a benchmark. It confirms the video system has sufficient accuracy and precision to act as benchmark (i.e. the accuracy and precision of the video system is much better than the accuracy and precision required from the electrogoniometer). The chapter concludes with the electrogoniometer results as determined from the measurement method discussed in the previous chapter. It is shown that the device exhibits good global reference frame accuracy (6° per axis for rotation and 16.1 mm for translation over a four node chain). It is however poorer than the 0.14° and $135 \mu\text{m}$ accuracy for the video motion capture system. The electrogoniometer accuracy may however be sufficient as it very much depends on the application and what is acceptable to the researcher.

The final chapter discusses the results and offer concluding remarks about the project claims and outcomes. The discussion focuses in particular on the reasons behind the accuracy and precision errors. The causes are mainly traced to the measurement method and custom calibration instrument. It is argued that the electrogoniometer will measure to a similar degree of accuracy and precision as the benchmark system if these problems are solved. The outcome will then be an unobtrusive device, costing a fraction of marker-based video motion capture systems, yet with comparable performance, and with applications in a free-living environment.

2.0 Literature Review

The electrogoniometer proposed here specifically addresses the issue of measuring the kinematics of the highly mobile spinal structure. The spine is the most complex component of the human musculoskeletal system (OzKaya and Nordin, 1999). From a mechanical system point of view, its complexity is directly related to its probability of failure (reliability). It is therefore not surprising that spinal conditions are very common occurrences. According to Balagué et al. (2012), non-specific low back pain alone has a lifetime prevalence of up to 84%, chronic low back pain affects approximately 23% of the population and 12% suffers from debilitating low back pain. Proper/optimal function of the spine it therefore paramount to ensure a good quality of life.

This literature review is divided into two sections. The chapter starts with a short overview of the anatomy of the spine. Of particular interest is the anatomy structure and how it may affect the design of an in vitro device used to measure its movement. The understanding of the spine's anatomy is useful to help define the requirements of the proposed device in chapter three.

The section part of the chapter literature review considers current motion captures devices and systems, especially those used to measure spinal kinematics. The emphasis here is not on the technology behind the systems, but rather on the applications in biomechanical research. The chapter concludes with a short comparative discussion of the devices and systems, which helps establish the rationale of the proposed device discussed in the chapters hereafter.

2.1 Anatomy of the Spine

The spine is a highly complex structure consisting of the vertebral column, spinal cord and surrounding muscle and ligament tissue. As a mechanical structure, its primary function is to support the trunk (i.e. to provide stability), allow trunk mobility, separate the thorax from the pelvis and acts as muscle attachment points (Adams et al., 2007). It consists of

thirty three vertebrae, with pliable inter-vertebral discs sandwiched in between. The spine is divided into four primary regions as illustrated in figure 2.1: the cervical (7 vertebrae), thoracic (12 vertebrae), lumbar (5 vertebrae) and the pelvic (consisting of 9 vertebrae and sometimes divided into the sacral and coccygeal) vertebrae. The pelvic segment is functionally fused and can therefore not be mechanically manipulated.

The first letter of the vertebral region's name and a number is the accepted convention to name individual vertebrae. For example, starting from the top, the first vertebra (located in the cervical region) will be C1 and the second from the top lumbar vertebra will be L2. Inter-vertebral discs are categorised by their adjacent (superior and inferior) vertebrae. For example T3-4 identifies the disc between vertebrae three and four of the thoracic region.

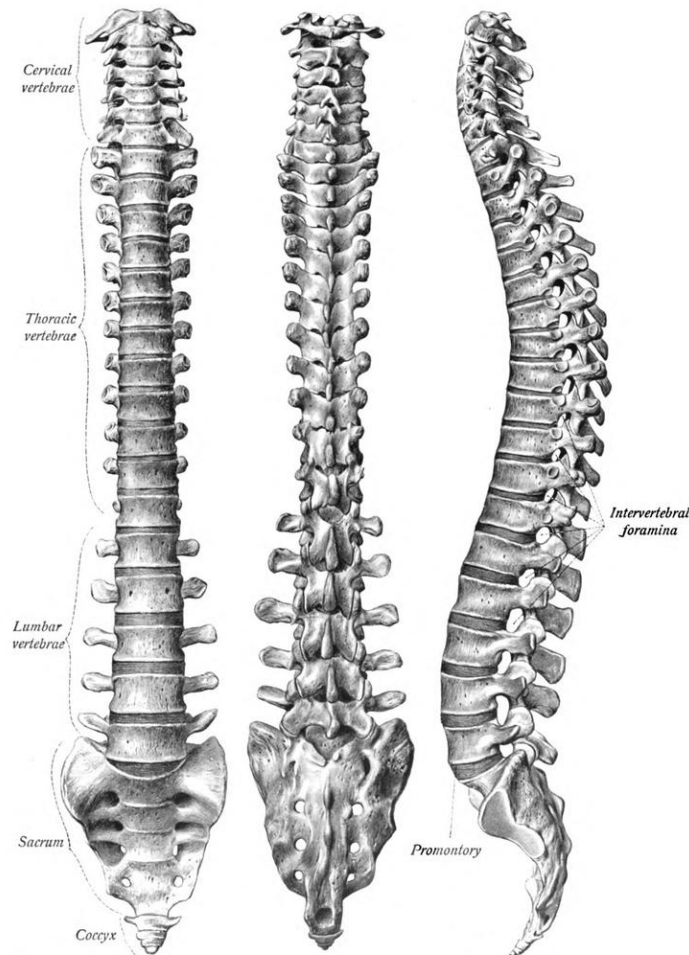


Figure 2.1: The spinal column and the four different regions: the cervical, thoracic, lumbar and sacral spines (this image has no copyright restrictions).

2.1.1 Elements and Structure

The cervical or neck spine is flexible to allow for head movement. C2 (also called the axis) has a little peg (called the odontion peg) which joins with C1 (the atlas) to allow mostly rotation in the sagittal plane. The cervical spine is connected to the thoracic spine which is more rigid in nature. The rigidity ensures that the ribcage, which extends from the thoracic spine, provides a firm structure capable of protecting the vital organs like the heart and lungs in the upper trunk. The thoracic spine is connected to the lumbar spine, which similar to the cervical spine, is fairly mobile. As it supports the entire upper trunk, it is more susceptible to injury. The pelvic spine is the lower most region of the spine. The vertebrae are fused together and forms a rigid structure.

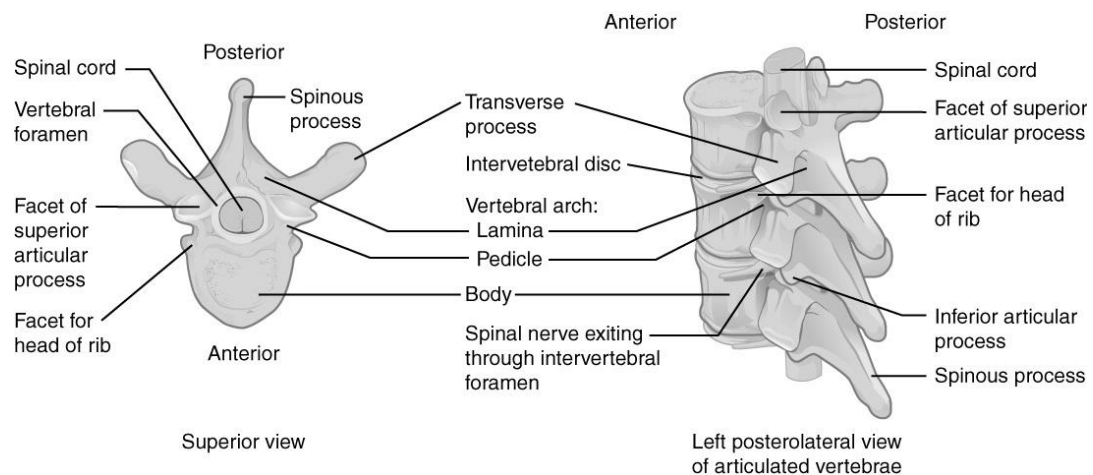


Figure 2.2: Elements of the spine (OpenStax College - Anatomy & Physiology, Connexions Web site. <http://cnx.org/content/col11496/1.6/>, Jun 19, 2013).

The spine is a non-linear structure consisting of four curvatures. The cervical and lumbar regions are concave anteriorly and the thoracic and pelvic regions are concave posteriorly. The shape of the rigid thoracic and pelvis spinal regions is formed before birth whereas the flexible lumbar and cervical regions' contours only settle during adolescence. The spine's familiar "S" shape allows it to manage much larger loads than what it could if it was straight. This feature also allows the spine to absorb shocks during gait (Adams et al., 2007).

A typical lumbar vertebra is divided into a vertebral body and vertebral arch (figure 2.2). The anterior located vertebral body and posterior vertebral arch enclose the vertebral foramen – an opening in the axial direction through which the medulla spinalis (spinal cord)

runs. The vertebral arch is populated by pedicles and laminae. They support seven processes: four superior articular, two transverse and one spinous.

The vertebrae are stacked upon one another to create a pillar-like structure. When linked in such a manner two roundish openings are visible between adjacent vertebrae. These openings, known as the vertebral foramina, are below the transverse process and above the facet (zygapophysical) joint of two adjacent vertebrae. Nerves from the spinal cord exit the spinal column through these apertures and connect to the rest of the body to enable motor control and sensory function. It is essentially the communication system through which the brain communicates with the rest of the body.

The inter-vertebral discs joining the vertebral bodies are important within the spinal structure. The discs serve a number of functions: they act as load bearing shock absorbers (especially in the case of axial forces); provide mobility to the spine (i.e. allowing it to bend and twist) and thirdly separate the vertebrae so that the nerve roots can branch off the spinal cord (Adams et al., 2007). The vertebral foramina and inter-vertebral disc are in close proximity, meaning that discs conditions like a hernia can irritate or pinch the spinal nerves resulting in pain, loss of sensation or even paralysis. The inter-vertebral disc is not the only structure joining vertebrae. The inter-vertebral disc forms a tripod structure with the two anterior located facet joints. When collectively viewed as a joint, it allows for rotation and translation movements between vertebrae (a topic discussed in more depth in section 3.2.2). The inter-vertebral discs bear about 80 to 90% of the load although the amount does depend on trunk posture and the health of the spine (Pollintine et al., 2004).

2.1.2 Supporting Tissue

Other important functional components of spine are the muscles, ligaments and tendons. These anatomical structures stabilize and support the spine. Without these structures the spinal column will not be able to remain upright or have spinal mobility. Healthy ligaments and muscles ensure proper posture and that other anatomical structures like the inter-vertebral discs and vertebrae are not over loaded.

Ligaments are cordlike fibrous structures that interconnect bones. They consist of tough durable material that is slightly elastic, and joins adjacent vertebrae to one another as illustrated in figure 2.3. Ligaments can be compared to stiff rubbery bands and therefore

allows some flexibility. The function depends on the length and thickness of ligaments. The primary functions of the ligaments are to secure the shape of the spinal column and allow spinal mobility within the normal range of motion.

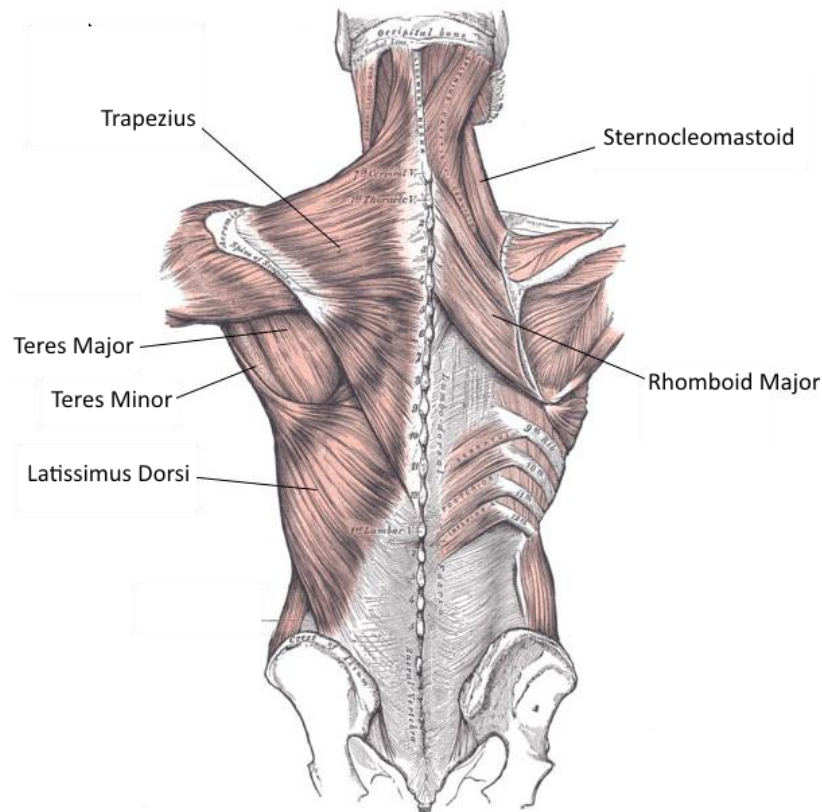


Figure 2.3: Muscles of the back (this image has no copyright restrictions).

As with ligaments, muscles are cordlike interconnecting structures (figure 2.3). Muscles are more elastic than ligaments and unlike passive ligaments, play an active role in spinal movement. By contracting and relaxing muscles are shortened and lengthened thereby manipulating the spinal structure kinematically. Muscles are not attached directly to the bone but to tendons which in turn are joined to the bone.

2.1.3 Range-of-Motion

Since the proposed device measures spinal kinematics, the range of motion of the spine is an important issue and will dictate the requirements and subsequent design in later chapters. Inter-vertebral motion generally has six degrees-of-freedom, each with a different

degree of stiffness (Wu et al., 2002). There is however no fixed joint axis so rotation can only be represented by a moving (instantaneous) center of rotation (Wu et al., 2002).

According to White and Panjabi (1990) the maximum inter-vertebral flexion-extension is in the order of 25°, approximately 12° for lateral flexion, and about 40° rotation in the axial. The individual rotations are summarised in figure 2.4. Note, the 40° axial rotation is largely due to the rotation between the atlas and the scull. The remaining angular rotation is in the same order as lateral bending.

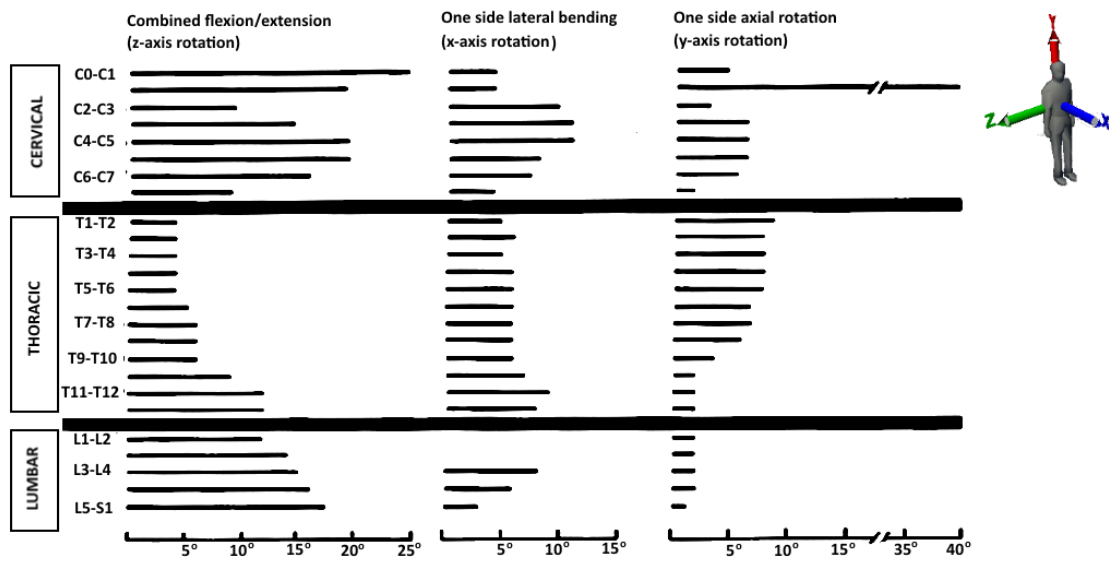


Figure 2.4: Range of motion of a normal spine (White and Panjabi, 1990).

Flexing the spine increases the path length along the skin surface between the top and bottom of the spine. The Schober Test considers a lumbar spine to be healthy if a subject can extend the path length by about 50% (Malanga and Nadler, 2006). The test is conducted by identifying S1 and then marking 10 cm above the S1 when the subject is in the upright position (see figure 2.5). The path length is then measured again when the subject bends forward to flex his spine.

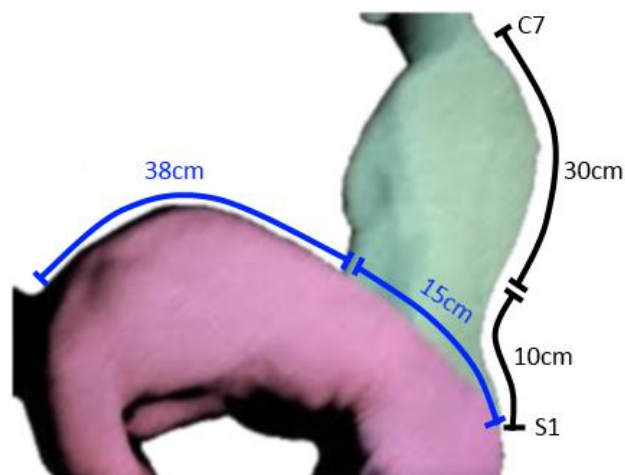


Figure 2.5: The Schober and Ott Test to determine spinal mobility.

The mobility of the remainder of the spine is assessed by Ott's Test (Schulte and Schumacher, 2006). It is similar to the Schober Test but the landmarks are C7 and then 30 cm below C7 as illustrated in figure 2.5. A healthy spine is expected to increase by about 25% when flexed.

The above increase in path length is mainly due to the flexing of the spine. The motion segments can however also experience relative translations. To illustrate, when the spine is loaded, the soft inter-vertebral disc will naturally compress and thus reduce the distances between the vertebrae. A lateral shear motion can also occur. According to Stokes et al. (2002), a shear-force of 100N is enough to cause a lateral shear of more than 1 mm in a pig motion segment when no pre-loading is applied. Pioneering research by Pearcy (1985), has shown a relative vertebral translation of 1 to 2 mm during lateral bending of the lumbar spine.

2.2 Motion Capture Devices and Systems

The anatomy, complexity and degrees-of-freedom of the spine clearly pose significant challenges for the biomechanical motion assessment. Motion capture systems can be categorised as *in vivo* or *in vitro*. *In vivo* methods aspire to measure the true kinematics of the spine and this is mostly accomplished through medical imaging techniques. *In vitro* methods on the other hand use video capture systems or devices that are externally

attached to the spine of a subject. A major concern with *in vitro* techniques are that the devices or systems do not measure true spinal kinematics, but skin movement instead.

2.2.1 *In Vivo* Methods

In vivo methods use radiographic techniques (e.g. fluoroscopy, X-rays and MRI) to measure spinal movement at the inter-vertebral level. Measurements are considered to be accurate since, unlike *in vitro* methods, inter-vertebral movement is measured directly. These methods however also have limitations in what they can and cannot measure.

Pearcy (1985) developed a stereo radiography system to measure lumbar spinal motion. His system featured two orthogonally orientated X-ray systems (figure 2.6). From the two X-ray images he identified nine anatomical landmarks from which he could determine the 3D inter-vertebral articulation of the lumbar spine. He validated his calculations against a set of steel spheres attached to known locations on a test model. The steel spheres' positions were four times more accurately identifiable than that of the landmarks (0.1 mm and 0.4 mm respectively), mainly due to its known circular shape and high contrast. Based upon his calculations, Pearcy concluded he could determine the accuracy of a vertebra to a root means square (RMS) error of less than 2 mm for location and 1.5° for rotation.

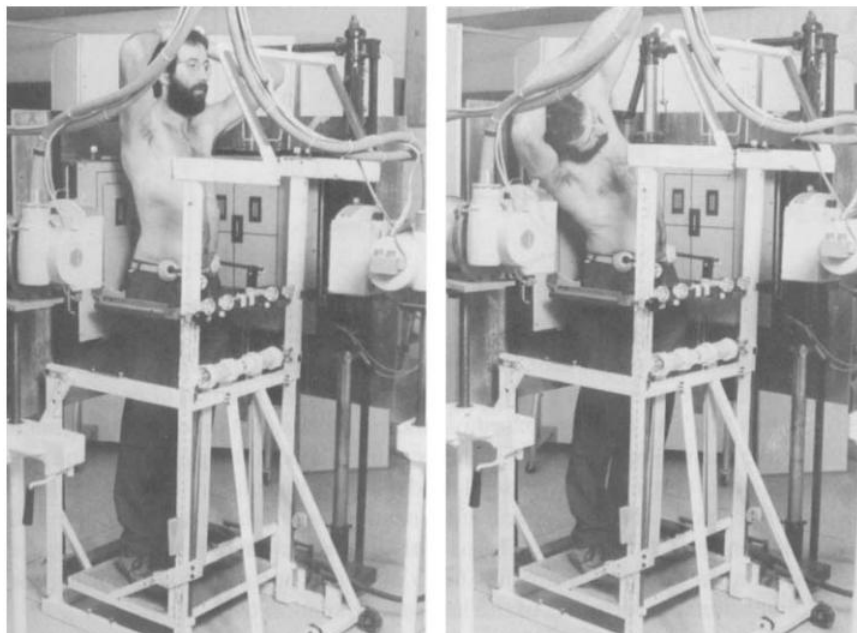


Figure 2.6: X-ray system developed by Pearcy (1985) to measure 3D inter-vertebral articulation.

More recent work by Li et al. (2009) created a 3D model of the spines of subjects scanned by an MRI scanner. The lumbar spine was then imaged through dual fluoroscopes while the subjects performed flexion-extension, lateral bending, and axial twisting. The MRI model was then matched to the fluoroscopy sequence of images using appropriate software to obtain the six degree-of-freedom kinematics of the individual vertebrae. The authors claim a mean accuracy of 0.4 mm for translation and a repeatability of less than 0.3 mm and 0.7° for translation and rotation respectively.

In vivo techniques have very specific applications, but also distinct drawbacks. One major disadvantage of *in vivo* techniques is the inability to measure activities of daily living. Many of these imaging techniques requires a subject to be static within a confined space while being scanned. Even though a sequence of snapshots is possible (for example through video fluoroscopy), the working volume is limited and restricts natural movement. Furthermore, repeat imaging of subjects using X-rays are undesirable due to the potential harmful nature of radiation on living tissues. Additionally, the equipment is also very expensive and require specialist training to operate, making studies of large subject groups difficult.

2.2.2 In Vitro Methods

In vitro devices and systems include video motion capture (both marker-based and markerless), goniometers, inertial sensors and various proprietary systems specifically developed to measure spinal kinematics. As *in vivo* methods, each system/device has strengths and weaknesses.

2.2.2.1 Video Motion Capture Systems

Video motion capture systems are broadly divided into two categories: marker-based systems and markerless systems. The former is considered to be the *de facto* standard for biomedical motion capture (Cheng et al., 2010; Kugler et al., 2012; Yang et al., 2014).

Marker Based Systems

Passive marker-based systems (for example the Vicon Nexus, Oxford Metrics Limited, Oxford, United Kingdom) consist of a series of infrared (IR) sensitive cameras, arranged around a test volume. IR light sources, adjacent to the camera apertures, irradiates retro reflective markers attached to a subject or object. The cameras, spectrally matched to the IR source, record the resulting images and use software to process and determine the 3D

location of the markers within the test volume. In addition to location, the orientation of a marker set (consisting of at least three rigidly connected markers) can also be determined.

Since the device developed here is validated against a video motion capture system, knowledge of a video system's reliability is an essential piece of information in order to make quantitative and qualitative comparisons. Windolf et al. (2008) investigated a marker-based video capture system for both accuracy and precision. They designed a systematic experiment to determine the performance of a Vicon 460 video capture system. The setup consisted of four cameras surrounding a small $180 \times 180 \times 150 \text{ mm}^3$ test volume. A measurement robot moving on three orthogonal axes (as shown figure 2.7) was designed. L-shape with four reflective markers was attached to the robot. The position of the robot could be controlled to an accuracy of $15 \text{ }\mu\text{m}$, thus ensuring the experiment could be repeated. The study determined the accuracy and precision for four different setup parameters: camera arrangement; testing volume; markers size and lens filters.

A conclusion drawn from the study is that performance was location and calibration dependent. When the markers moved outside the calibration volume, the accuracy dropped significantly to $210 \pm 60 \text{ }\mu\text{m}$ (mean \pm standard deviation). However, precision is not affected as it is not a calibration concern. Furthermore, accuracy improves as the marker size increased (approximately $65 \text{ }\mu\text{m}$ and $85 \text{ }\mu\text{m}$ for marker sizes of 25 mm and 9.5 mm respectively). Interestingly enough, no significant correlation between the accuracies and average calibration residuals were witnessed. Windolf et al. have however not tested system performance for marker roundness, lighting conditions or the reflective ability of the markers, and all their results must therefore be interpreted within the scope of their study. Critically, they also did not determine the rotation accuracy and performance.

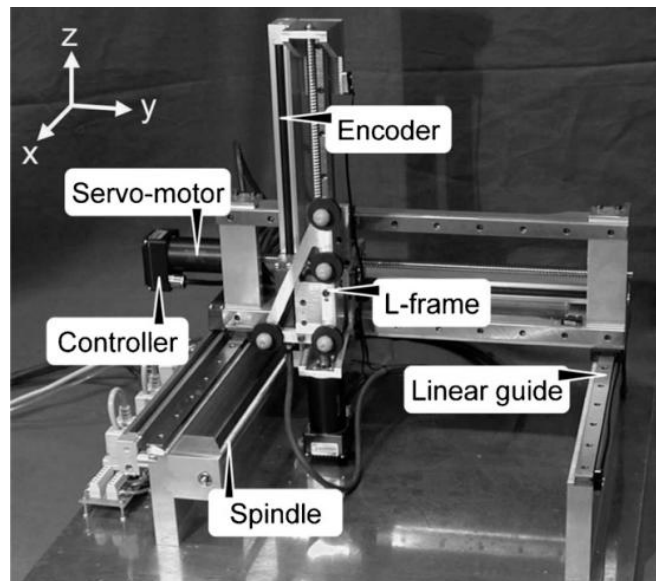


Figure 2.7: Test robot developed by Windolf et al. (2008) to test the accuracy and precision of the Vicon 460 system.

Windolf's study also excluded any biomechanical component. Most research studies require skeletal motion (typically gait or posture) to be measured. Unlike Windolf's study, markers are not attached to rigid structures but to soft tissue (skin) and are therefore prone to additional movement. Peters et al. (2009) investigated the placement of marker locations on the tibial segment and determined the areas least affected by skin movement were the bony landmarks which were not impeded by muscle and fatty tissue. Other sources of errors can be attributed to the difference in how examiners use the equipment (e.g. the placement of the markers) and thus producing different results (also referred to as examiner errors). Secondly, the behaviour of the subject being tested may change after a long tiresome motion capture session and he or she may thus become less cooperative (Smith, 2011).

The Vicon system is an example of a passive system. Other marker-based systems popular amongst the biomechanical research community use active markers (e.g. Optotrak, Northern Digital, Inc., Waterloo, Ontario, Canada). These systems do not rely on reflected light. Instead, actively emitting markers (usually LEDs) are attached to a subject. Wires connect the markers since they require a power supply (making the system slightly more obtrusive). Typical accuracy claimed by Maletsky et al. (2007) for a Optotrak 3020 system (Northern Digital Inc., Waterloo, Ontario) was found to be 0.05° and 0.03 mm for

orientation and location respectively. However, this was under static conditions and increased as the camera distance is increased (figure 2.8).

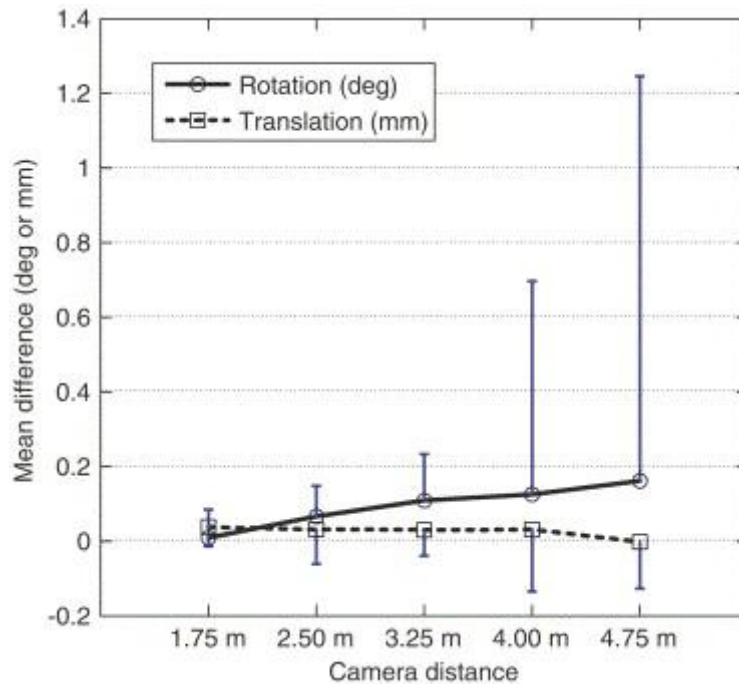


Figure 2.8: Rotation and translation accuracy and standard deviation (error bars) versus camera distance of the Optotrak 3020 system (Maletsky et al., 2007).

Markerless Systems

Markerless systems have made significant strides over the last decade with more commercial systems emerging on the market (for example Organic Motion, New York, USA). It has already found widespread acceptance in the entertainment community, but the accuracy and precision required for biomechanical research are still debatable.

Unlike marker-based systems, markerless systems do not require markers or any other wearable equipment but instead infer human motion through computer vision algorithms. This is a very complex task, requiring the software to identify and recognize (one or more) human shapes, and then to model the skeletal structure using machine learning algorithms. As with marker-based systems, raw video is delivered by multiple cameras enabling extraction of three-dimensional information.

The Stanford Markerless Motion Capture Project (Ganapathi et al., 2010; Corazza et al., 2007) is a good example of a current research markerless system. The Stanford group's

expressed aim is to capture human motion for applications in biomechanics. As illustrated in figure 2.9a, the first task is to identify and recognise the human shape from the acquired video streams. The shape is then reconstructed in a 3D environment. An appropriate model obtained from a database of models is attached to the shape (figure 2.9b) and the optimal joints locations are then determined through machine learning algorithms (figure 2.9c). The result is a markerless motion capture system that can determine kinematic data at rates of up to 200 Hz (figure 2.9d).

One immediate concern biomechanical researchers may have with such a system is the methods used to obtain the skeletal information and subsequent kinematics. The identification and reconstruction of the human shape will inevitably introduce errors which may be unacceptable for some research studies. Secondly, the skeletal kinematics itself is obtained through a model fitting process which will further reduce the accuracy of the output.

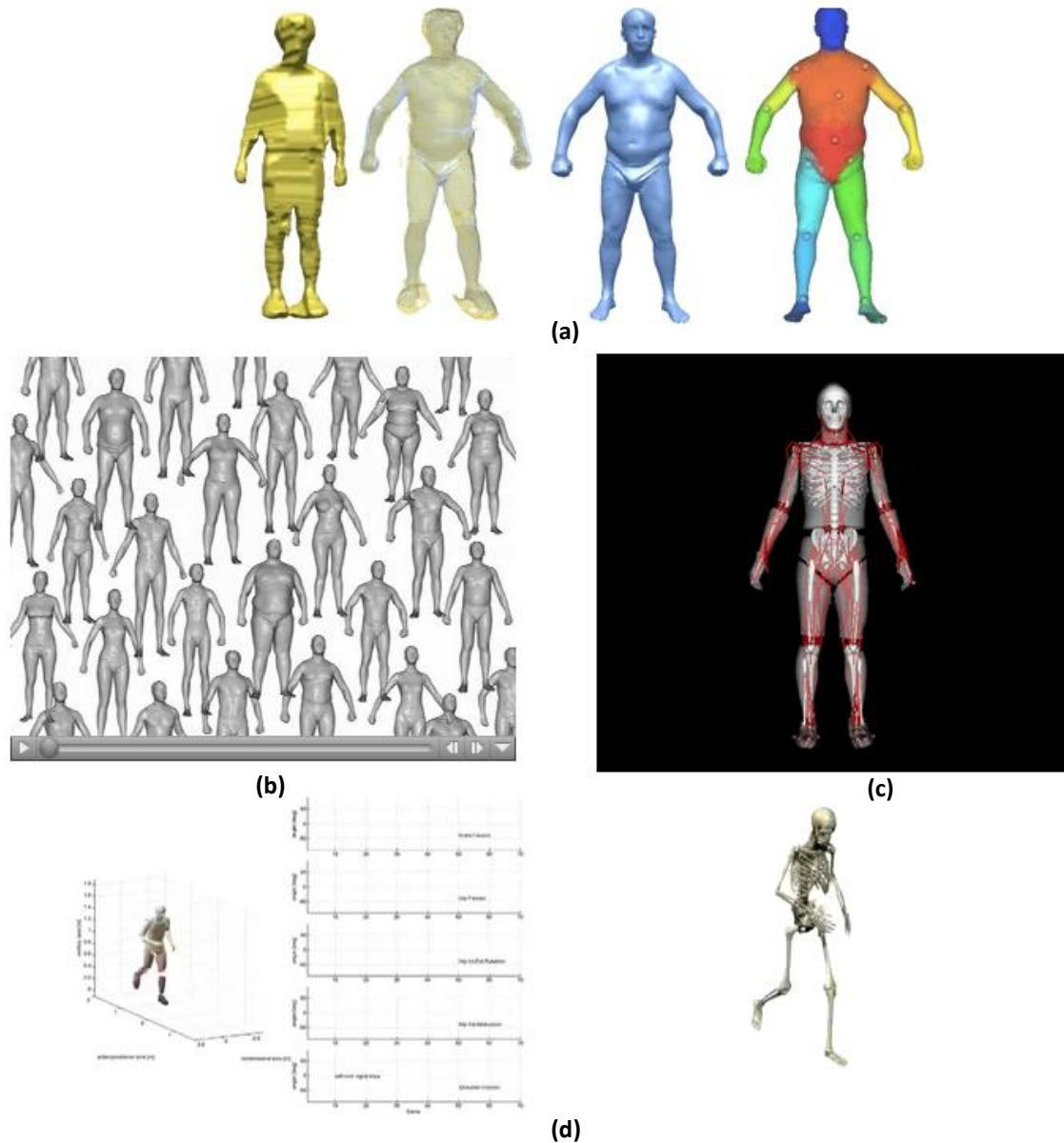


Figure 2.9: Biomechanical model as acquire from the Stanford Markerless Motion Capture Project
a) Human shape identification and reconstruction; b) Model fitting against a database of shapes;
c) Shape integration with musculoskeletal system; d) Real-time skeletal markerless kinematics.
 (<https://ccrma.stanford.edu/~stefanoc/Markerless/Markerless.html>)

Despite these drawbacks, markerless motion capture is already making an impact on the biomechanical research community. Since markers are not required, markerless motion capture is more suitable for the non-laboratory environment. The lighting and background affects system performance but advances in computer vision are addressing these issues. Leu et al. (2011) for example, has shown how such a system can be applied in a natural environment. Gait patterns in healthy subjects and subjects with irregular gait patterns

were monitored. It was discovered that gait parameters compared well with that found in literature. Other applications include gait recognition (Krzyszowski et al., 2012; Świtonski et al., 2012), risk of falls assessment through body sway measurements (Wang et al., 2010) and the estimation of shoulder, elbow and wrist joint centers of swimmers performing a front crawl (Ceseracciu et al., 2011).

2.2.2.2 Electromagnetic Motion Capture Systems

Another noteworthy motion capture system is based upon electromagnetic sensing. Fastrak (Polhemus Inc., Colchester VT., USA) is an example of such a system. Transmitter coils are used to generate 3D alternating magnetic fields. The artificial magnetic fields are then measured by receiver units which can establish the orientation and position (i.e. six degrees-of-freedom) of the receivers relative to the transmitters. Due to the alternating nature of the magnetic field, the system is not affected by the earth's much weaker (and constant) magnetic field. However, as with any magnetic system, it is affected by ferrous metals in its immediate vicinity. The test space is also much smaller than that of video capture systems. The manufacturer claims a static position accuracy of 0.76 mm and 0.15° for rotation.

2.2.2.3 Inertial Sensors

Thanks to advances in *micro-electromechanical systems* (MEMS), inertial sensors have had a significant impact on the biomechanics and healthcare sector over the last decade. The primary advantage of inertial sensors is their application in studies involving the monitoring of subjects in free living environments for extended periods of time. These devices are unobtrusive, robust and low cost, thus making them ideal for applications outside the laboratory environment. Modern inertial motion sensors usually consist of three-axis accelerometers and/or gyroscopes and/or magnetometers.

Nevins et al. (2002) developed a system consisting of six tri-axial accelerometers. They suggested that such a system could be used to monitor the posture of patients recovering from back surgery. Wong and Wong (2008) proposed a system consisting of three tri-axial accelerometers. Their aim was to monitor postural changes during sitting, and claim their system can measure postural changes in the sagittal and coronal planes with an error of less than 5°.

Accelerometer only based systems are limited in their postural measurement capabilities (more about this in chapter five). Performance can however be improved by adding tri-axial gyroscopes. Duc et al. (2013) used two inertial sensors (consisting of tri-axial accelerometers and gyroscopes) attached to the sternums and foreheads of subjects, to compare post-operative cervical spine patients with healthy control subjects. The addition of gyroscopes meant that the lateral bending, axial rotation and flexion–extension could be monitored. Wong and Wong (2009) improved on their previous accelerometer-only system, also adding the gyroscopes and validating their system against a Vicon video system (figure 2.10). They reported RMS differences between their system and the validation system of less or equal than 4.5° for trunk postural estimation (a slight improvement over their previous system).

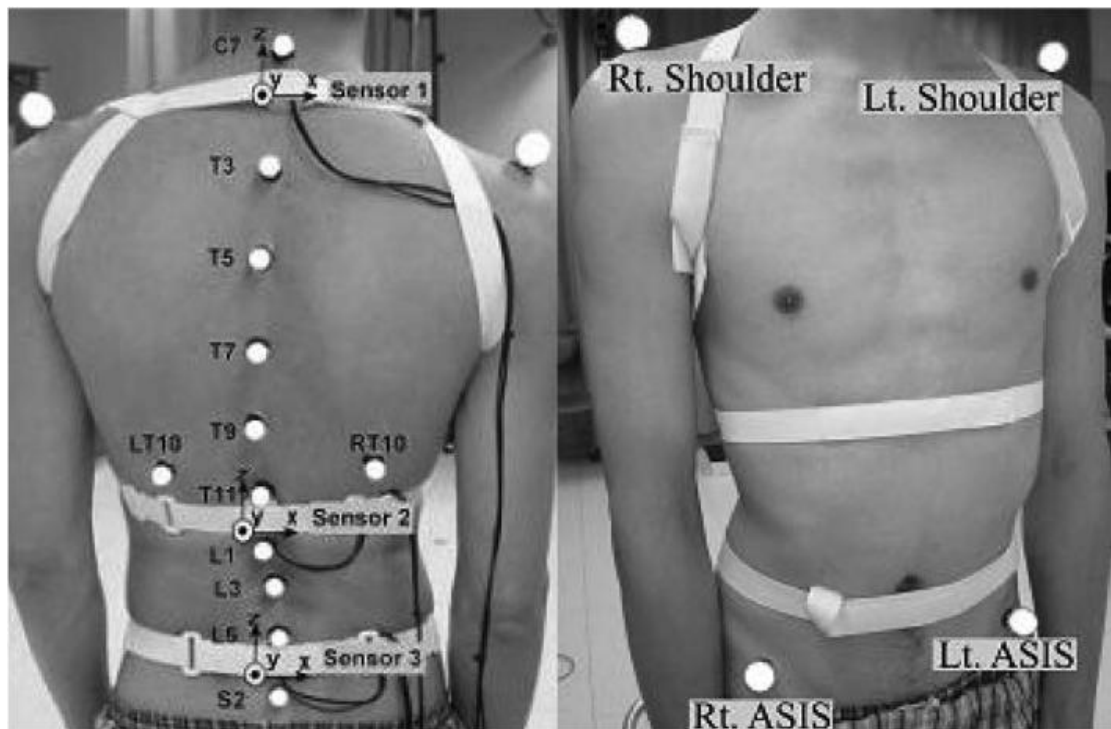


Figure 2.10: The inertial sensor system proposed by Wong and Wong (2009). The system consists of three inertial modules.

Lee and Park (2011) specifically investigated spinal motion during staircase walking, an activity that is difficult to measure in an laboratory environment. Their system integrated tri-axial magnetometers with the inertial sensors, thus offering true orientation sensing.

Similar systems have been developed by Zhang et al. (2011) to assess back pain and rehabilitation, and by Szeto et al. (2013) to measure the activities of community nurses.

The inconspicuous nature of inertial-magnetic sensors also make them ideal for applications in the entertainment industry. Commercial systems have been developed by, amongst other, XSens (Xsens Technologies, Netherlands) and Motion Workshop (Motion Workshop, Seattle, USA) and typically capture full body motion. The author of this thesis has also developed a system that can capture upper body motion and animate a character within a virtual environment from a first and third person point-of-view (Smit et al., 2009).

Many of the inertial-magnetic sensor based spinal monitors remain in the research domain. MVN BioMech (Xsens Technologies, Netherlands) is a commercial system with applications in biomechanical research. XSens claims the system have "optimal magnetic immunity" and can therefore operate in most environments (Xsens 3D motion tracking, 2013). However, De Vries et al. (2009) have evaluated XSens inertia-magnetic sensors and concluded that these sensors are susceptible to magnetic interference.

Most of the "non-commercial" spinal monitors consist of two or three inertial-magnetic nodes and therefore only offer limited approximation of the curvature of the spine. These monitors can however easily be scaled up however by adding more nodes, and thus producing a more accurate representation of the spine. According to the literature discussed above, the current systems have a typical accuracy of 5°. The effectiveness of the data fusion algorithms which calculate the kinematic data is also dependent on the type of activities performed by the person using the device. These algorithms usually rely on zero velocity periods during which the gyroscope drifting can be reset (Youssef et al., 2012). In the case of gait analysis, gait can be determine fairly accurately with inertial-magnetic sensors when embedded a shoe, since the drift can be reset during the gait stance phase (Bebek et al., 2010). However in the case of for example continuous gymnastic activity, a period reset may not be possible, thus causing drifting errors to accumulate.

In contrast, the electrogoniometer proposed here will not have the problems associated with inertial-magnetic sensors as discussed above. The optical measurement method discussed in chapter five will not be affected by the environment and does not depend on the activities it measures, thus offering a clear advantage over inertial-magnetic sensors.

2.2.2.4 Goniometers and Torsiometers

One and Two Degree-of-Freedom Devices

At present most commercial goniometers are limited to measure one or two axes of rotation. The simplest single axis mechanical goniometer is a protractor type device, that consists of two rotating arms and requires a clinician to read the measurement from the device. More sophisticated versions have a sensor (usually a potentiometer) that measures the angle, and logs or transmits the data for further processing (figure 2.11a). These mechanical devices can interfere with a person's movement because they have a fixed center of rotation (although some models include a plunger to increase the freedom of movement) and are therefore not particularly popular with researchers.

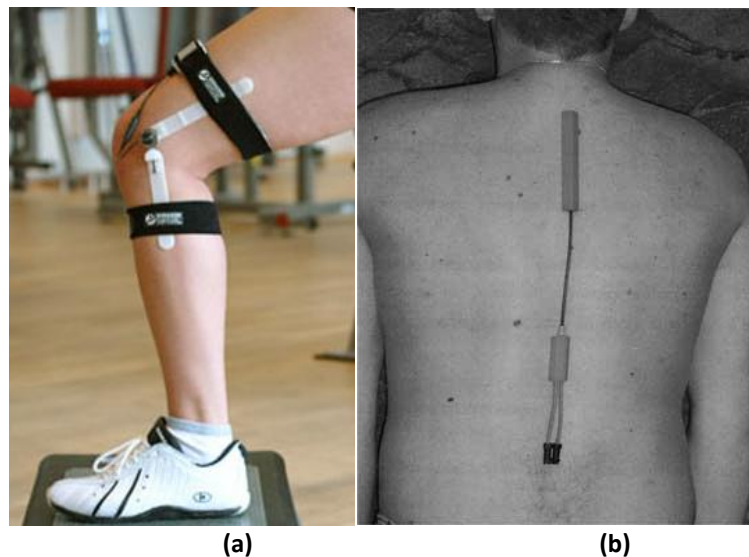


Figure 2.11: Commercial a) uni-axial mechanical goniometer (www.noraxon.com); b) bi-axial fibre-optic electrogoniometer (Szulc et al., 2011).

Electrogoniometers using fibre-optic technology are less conspicuous and, with some models, capable of measuring two axis (flexion/extension and lateral flexion) of rotation. These devices do not have a fixed center of rotation. Instead, two hard segments are connected via a flexible optical fibre as shown in figure 2.11b. These devices work on the principle of light being introduced into the fibre, is attenuated when the fibre is bent, thus giving an indication of the relative angular displacement (Donno et al. 2008). Fibre optic devices using other light intensity modulation techniques are discussed later on.

Rowe et al. (2001) validated such a device (model M180, manufactured by Biometrics Ltd, Gwent, UK) against a Vicon motion capture system. They measured knee joint kinematics in five healthy subjects and concluded that the device offered accurate, precise and repeatable measurements for angles less than 40°. Jonsson et al. (2007) reported accuracy better than 5° when measuring thumb movement (model SG-110, Biometrics Ltd) although the manufacturer claims less than 2°.

Due to its unobtrusive nature, electrogoniometers have a relevance similar to inertial sensor in spinal kinematic research, especially concerning activities of daily living. Bible et al. (2010) for example used an electrogoniometer and torsionmeter to determine the lumbar range of motion (ROM) of subjects performing fifteen activities of daily living.

Higher Degree-of-Freedom Devices

The goniometers discussed so far have a limited capabilities to measure complex shapes and curves. To measure more complex curves requires devices with higher degrees of freedom. A number of new devices are emerging from academic research. Williams et al. (2010) used a multi degree-of-freedom fibre-optic device to measure lumbar spinal curvature (illustrated in figure 2.12). The technology itself is however not new and have been used before by, amongst other, Morin and Reid (2002) to measure joint angles. The device presented by Williams et al. has been adapted from a commercially available device called ShapeTape (Measurand Inc., New Brunswick, Canada).

ShapeTape approximate a curve through a number of discrete serially chained fibre-optic sensors. Each discrete fibre-optic sensor has an internal spatial arrangement that can sense twisting and bending (i.e. two degrees-of-freedom). In order to prevent movement in other directions, the sensors are laminated to a thin metal ribbon (ensuring that only twisting and bending can occur) (figure 2.12b). The method and principles of sensing curves is discussed in detail by Danisch et al. (1999).

Since the device cannot be stretched, Williams et al. added a sliding mechanism enabling the device to move freely when the subject flexes/extends his/her spine. A major disadvantage of the device is that it cannot sense lateral movement and is limited to sagittal and axial measurements. The study conducted by Williams et al. however only

measured sagittal motion as the subject bent and lifted a crate. When compared to the Vicon system, they found the device produced an RMS error of less than 2.5°.

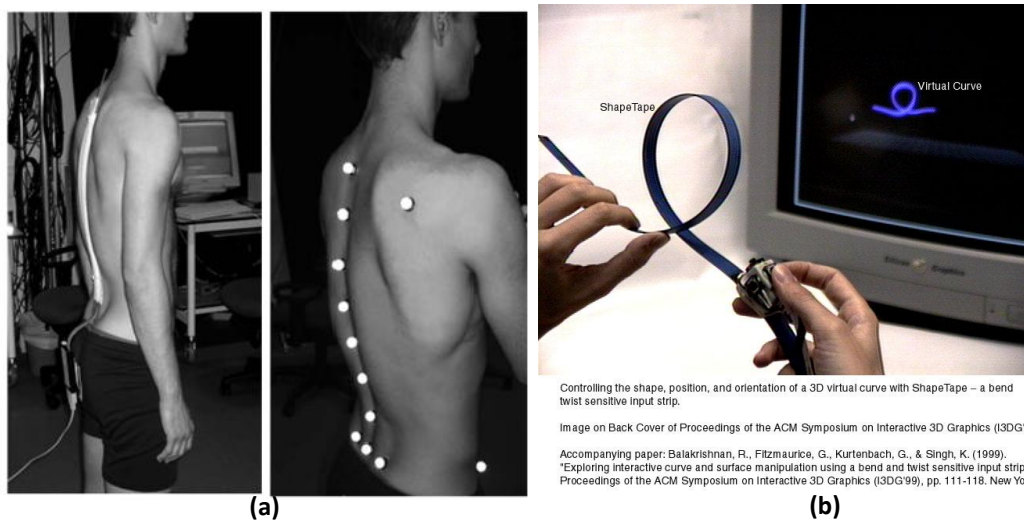


Figure 2.12: a) Lumbar spine device developed by Williams et al., b) ShapeTape is at the core of the device.

Industrial Lumbar Motion Monitor (figure 2.13) is a tri-axial electrogoniometer developed in the early nineties at Ohio State University. According to its patent, four wires are used to control separate potentiometers, connecting the upper and lower part of the exoskeleton device through a series of T-shape elements (Davis et al., 1991). The potentiometer voltages are processed to determine sagittal, lateral, axial movement. A less bulkier version, the Industrial Lumbar Motion Monitor™, has since been developed and works on a similar principle.



Figure 2.13: The Lumbar Motion Monitor: a tri-axial goniometer developed at Ohio State University. (<http://www.nexgenergo.com/ergonomics/lumbarmm.html#Sec2>)

Marras et al. (1992), validated the device for accuracy and precision (it should be noted Marras is one of the inventors). They constructed a special test bench with a three-dimensional reference frame to test the device. They concluded that for different range of movements their system on average had an accuracy of 1.71° in the frontal plane, 0.96° in the sagittal plane and 0.5° in the transverse plane.

The device has been used in a number of research studies, most notably to determine trunk motion of workers in an industrial environment (Allread and Marras, 2000); spinal loading of workers during lifting (Ferguson et al., 2002) and a comparison of spinal motion of elite golfers (Lindsay and Horton, 2002).

The CA6000 Spine Motion Analyzer (OSI, Union City, CA, USA), as illustrated in figure 2.14, consists of a mechanical linkage system. A total of six potentiometers are attached to the link joints from which the six degrees of freedom motion between an upper and lower harness section could be determined. A feature of this device is the linkage system which can also be connected between the upper trunk and head to measure the related movement. Applications are however limited to laboratory and clinical environments due to the conspicuous nature of the device.

The device has been validated by Schuit et al. (1997) and Dopf et al. (1994). It has since been used to assess spinal motion. For example, a recent study by Mieritz et al. (2013) used the device to measure the flexion and extension characteristics of the lumbar spine in 220 individuals with chronic lower back pain. Based upon the measurements, they extracted five kinematics parameters (range of motion, mean flexion velocity, maximum flexion and extension velocity, phase-plot area and the jerk index). They concluded that the data may be sufficiently reliable for group statistical analysis but not to identify problems at an individual level.

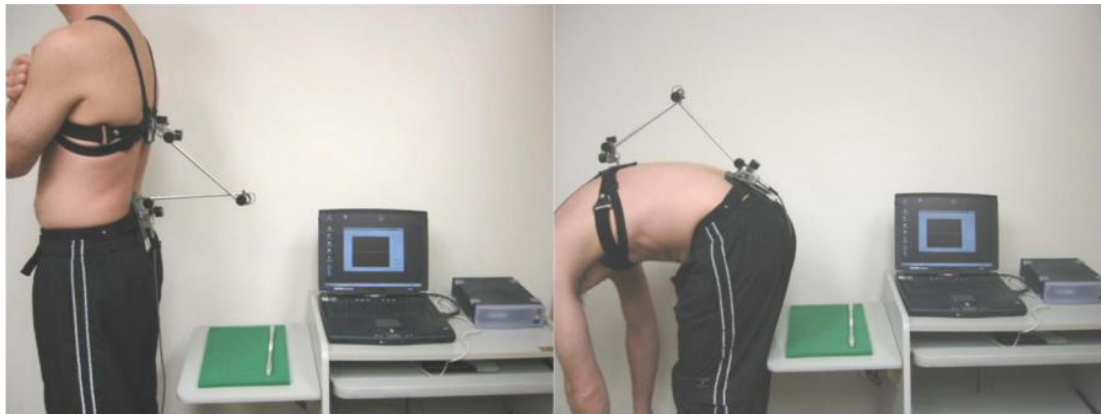


Figure 2.14: The CA6000 Spine Motion Analyzer (Mieritz et al., 2013).

2.2.2.5 Other Devices

Another interesting wearable device is the Epionics SPINE. It is discussed in detail by Consmüller et al. (2012). It is a fairly recent development of the company (Epionics Medical GmbH, Germany) founded in 2008. The device consists of two strips with embedded strain sensors as shown in figure 2.15. The base of each strip contains tri-axial accelerometers to provide a sense of direction. The device can therefore not be considered a true goniometer but rather a hybrid system.

As is the case with the modified ShapeTape device presented by Williams et al., the strips cannot stretch but slide within a hollow tube so not to restrict trunk movement. Unlike ShapeTape however, the individual strips cannot measure twisting (axial) movements. The device measures the difference movement between the strips instead to derive twisting. Pure lateral bending can also not be measured from the strip deformation but is instead determined by the accelerometers. The device is therefore not quite suitable for accurate postural measurements, but has applications as a diagnostic and rehabilitation tool. Consmüller (2013) for example used the device to recognise flexion/extension, lateral bending and axial rotation.

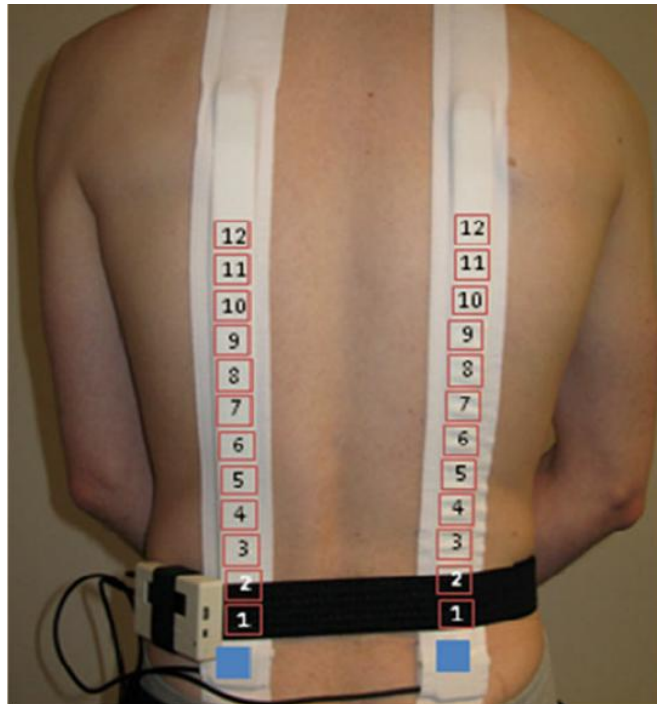


Figure 2.15: Spine monitor device developed by Consmüller et al. (2012). The device use strain sensors and accelerometers.

Finally, the SpinalMouse (Aditus System Inc, Loguna Niguel, California, USA) is a handheld device used to assess spinal posture, mobility and range of motion (figure 2.16). A subject is asked to assume a static spinal posture while the device is moved by hand starting at a base marker along the spinal column. Angle and distance measurements are determine from two wheels which track the spinous processes as the device is moved along the spine. Based upon these measurements, the relative positions of the vertebral bodies can be determined to reveal the contour of the spine. The device can only capture static spinal posture and thus has limited applications in a free-living environment and less relevance to this study.

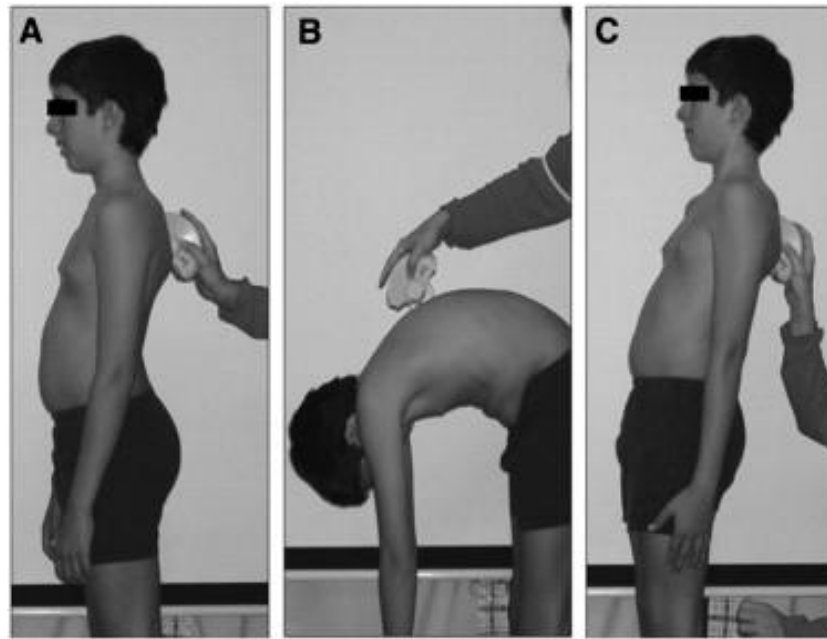


Figure 2.16: Determining the range of motion of a spine using the SpinalMouse (Kellis et al., 2008).

2.3 Discussion

The devices and systems discussed in sections 2.2 have each their own strengths and weaknesses, and as stated before, there is no single system available that will meet all the requirements of a biomechanical researcher. Consequently researchers sometimes have to adapt their research methods simply because the appropriate tools are not available to meet their research requirements. A case can therefore be made to develop a more versatile device.

Based upon the literature review, the characteristics of the devices and systems are summarised in table 2.1. Also included (bottom of table) is the proposed electrogoniometer discussed hereafter. Although not yet commercialised, the attributes are assigned to the electrogoniometer according to the requirements specified in chapter three. Characteristics that may be important to biomechanists, especially when related to kinematic research are: suitability for use in a laboratory/clinical as well in a natural environment; the ability to measure inter-vertebra articulations; cost and finally the obtrusiveness of the device or system.

	Cost	Obtrusive	Accuracy	Sample rate	Measures inter-vertebrae articulation	Measure activities of daily living
Radio graphic (in vivo) (Pearcy, 1985)	Unknown, but very expensive.	Yes	Translation: 2 mm Rotation: 1.5°	Not applicable	Yes	No, the equipment limits movement to a small working volume.
Marker -based video mocap (Vicon 460)	£100 000	Yes, due to reflective markers worn on the body.	Translation: 135 µm rotation: 0.14° (setup dependent)	200 Hz	Yes	No, the subject is confined to a laboratory environment.
Markerless video mocap (Stanford Markerless Motion Capture Project)	Unknown (system not commercialised).	No	Rotation: 1-2° (setup dependent)	200 Hz	Yes	Yes, but the subject must be within the view of the cameras.
Electroagnetic mocap (Fastrak)	£4 000	No, if sensors are wireless, it can be worn under clothing.	Translation: 0.76mm rotation: 0.14°	<120 Hz	Yes	No, the system has a small working volume (approximately 1 m).
Inertial sensors (Wong and Wong, 2009)	Unknown (system not commercialised).	No, sensors can be worn under clothing.	Rotation: 5°	Unknown	Yes	Yes
Optic fibre (2 DOF) (model SG-110)	Approximately £300.	No, the device can be worn under clothing.	Rotation: 5°	Up to 20 kHz	No	Yes
ShapeTape (Williams et al., 2010)	Unknown. ShapeHand, a data clove based on the same technology cost \$11 000.	No, the device can be worn under clothing.	Rotation: 2.5°	Unknown	Yes	Yes
Epionics SPINE	Unknown	No, the device can be worn under clothing.	Not applicable	Unknown	No	Yes
CA 6000 SPA	Unknown	Yes	Unknown	Not applicable	No	No
Proposed device	£5 000 (estimate).	No, the device can be worn under clothing.	Translation: 0.2mm Rotation: 2°	30 Hz	Yes	Yes

Table 2.1: Summary of the key characteristics of different motion capture devices and systems.

One of the key features of the proposed electrogoniometer is that it can measure inter-vertebral articulation, a characteristic that not many other free-living devices have. ShapeTape can measure inter-vertebral movement but this is limited to rotations in the sagittal and axial plane. Inertial-magnetic sensors by Wong and Wong can theoretically also measure inter-vertebra movement but rotation accuracy is limited to 5°. The required sample rate is dependent on what the researcher wants to monitor or measure. Typical sample rates are 30 Hz for normal daily living activities, up to 200 Hz for sport related activities. Cost is correlated with the accuracy and measurement capabilities (for example to measure inter-vertebra movement) of the device or system. The more expensive devices or systems are also mostly laboratory based and therefore excludes daily living measurements.

To summarise, the electrogoniometer proposed here aims to be affordable, measure spinal movement accurately and unobtrusively at the inter-vertebral level, and does so in a free-living environment. In essence the device is a combination of all the desirable characteristics of the different systems and devices discussed here.

3.0 Requirements

The aim of this thesis is to develop a biomedical device that can best be described as an electrogoniometer. The device will differ from other similar devices to the extent it can measure the mobility of the spine. To do so, the electrogoniometer will be constructed from a chain of *simpler electrogoniometers*. (To avoid confusion, the term "simpler electrogoniometer" will be referred to as a goniometer-node (or simply a node) and the chained device in its entirety as an electrogoniometer.) Each goniometer-node (figure 3.1a) will be capable of measuring four degrees-of-freedom (DOF). Goniometer-nodes are the building blocks of the electrogoniometer. Mechanically the four degrees of freedom will be realised with a spherical and prismatic joint as illustrated in figure 3.1b. Contained within each node will be sensors that measure the related kinematics (figure 3.1c). From a mechanical view point, the electrogoniometer is a serial open chain. If it consists of n nodes and each node had four DOF, then its mobility is $4n$ DOF (McCarthy and Soh, 2010).

This chapter starts by stating the requirements of the device. The requirements are based upon the range-of-motion of the spine's motion-segments. Other requirements include accuracy and precision, sample rate, resolution and the physical dimensions of the device. Next the issue is investigated whether to use a distributed or centralised electronic design. A centralised design is pursued here since it is more practical to implement from an electronics point of view.

3.1 Requirements

The development of any new device necessitates the formulation of requirements. As it is only a prototype, it is not compulsory to develop a device covering the entire spinal column. Instead, a prototype consisting of five goniometer-nodes will be sufficient to demonstrate the concepts and principles. A five-node device can for example be used to measure the lumbar spine.

The prototype will not be over-engineered (e.g. being able to stretch up to 70% of the device's length whereas a flexed lumbar spine only increases the path length about 50%). The five spinal regions differ significantly in terms of physical appearance and kinematic characteristics. This prototype will assume an "average spine" and may therefore not be suitable to measure range of motion of all spinal regions (the range of motion of the different spinal sections has been discussed in chapter two).

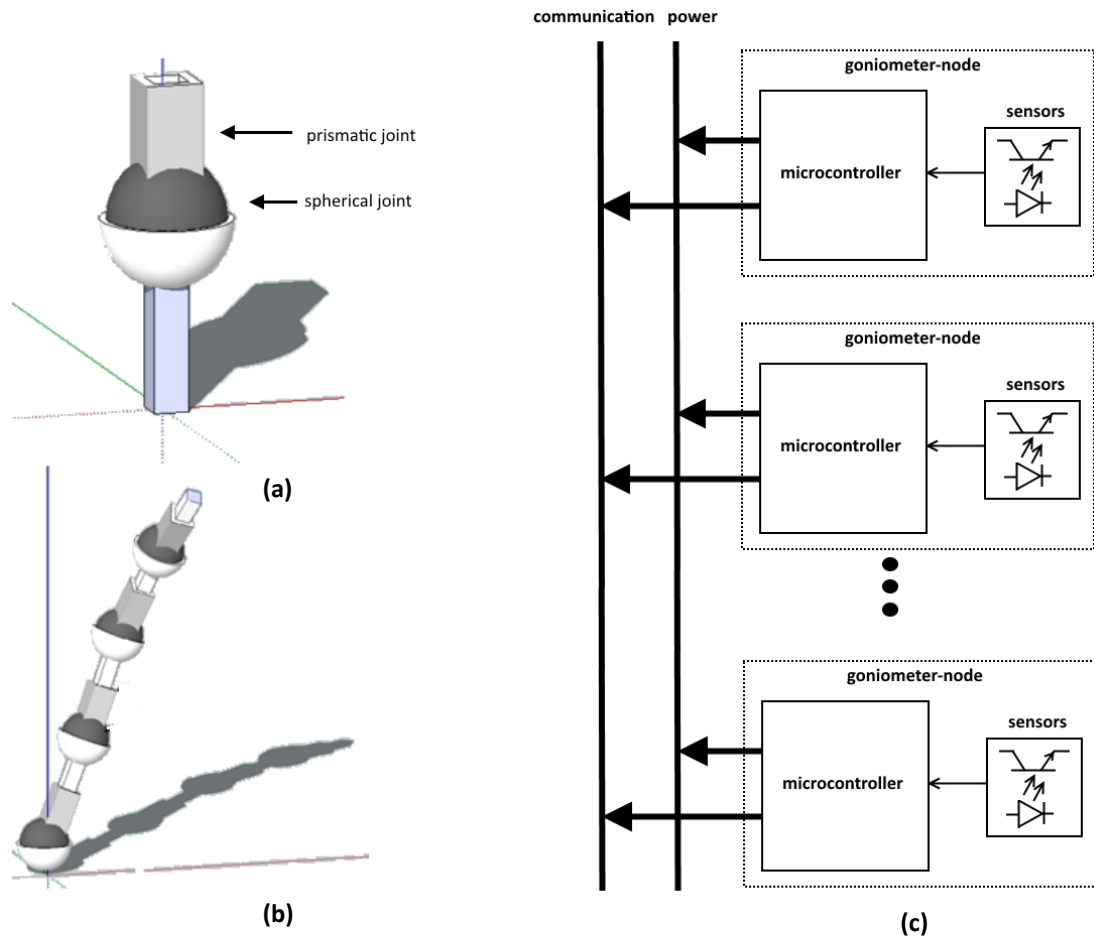


Figure 3.1: Conceptual design of a) the goniometer-node; b) the electrogoniometer as a serial chain of goniometer-nodes; c) sensors and electronic chaining of the goniometer-nodes.

3.1.1 Physical Dimensions

The dimensions of the intended electrogoniometer are derived from the spinal column parameters. The T1-S1 segment of the spine is taken as a functional region an *in vitro* device can be attached to. The typical length of the T1-S1 segment for an adult male is about 45 cm (Akbarnia et al., 2010), and consists of 17 vertebrae. The average vertebrae

and disc height is therefore 27 mm. Based upon these dimensions, a goniometer-node must therefore be approximately 27 mm in length to measure inter-vertebra movement.

The choice of the diameter is a trade-off between construction complexity and obtrusiveness when worn. The thinner the device, the more effort it will require to construct, however it will be less obtrusive to wear. A diameter of 15 mm is perhaps an acceptable compromise for a prototype device.

3.1.2 Range-of-Motion

3.1.2.1 Translation

The device will be attached to the skin along the spinal processes. Any movement measured by the device (either rotation and/or translation) will therefore be dictated by the movement of the spinal processes and skin. When flexing the spine, vertebrae wedge open posteriorly. As a result, a relative translation of the spinal processes occur due to the rotation of the vertebral bodies.

The path length of a flexed lumbar spine increases roughly with 50% and the remainder of the spine by about 25% (figure 2.5). On average the spinal path length increases with about 33%. A goniometer-node must therefore extend its own length by about a third (or 9 mm). Shear translations are relative small and for all practical purposes ignored here. A goniometer-node will therefore measure only a single degree of translational freedom.

3.1.2.2 Rotation

A motion segment has three degrees of rotational freedom. The per axis rotation is typically less than $\pm 20^\circ$ (i.e. a total deviation of 40°) (White and Panjabi, 1990). For that reason, a goniometer-node is expected to measure at least $\pm 20^\circ$ of rotational in three axes.

3.1.3 Other Device Characteristics

Initially the device developed here will consist of five interlinked goniometer-nodes, each with a mobility of four DOF. The device therefore has a total mobility of twenty DOF. Bluetooth communication is integrated to make the device portable.

Accuracy is an important measurement characteristic, especially considering that a goniometer-node measures relative to a reference frame local to the node. Any

measurement errors will therefore propagate through the chain and affect the accuracy as measured relative to the global reference frame of the device. Commercial optical electrogoniometers have a typical accuracy of 5° (section 2.2.2.4). Since measurements are made relative to a local reference frame, a goniometer-node accuracy of 2° is suggested here. This device is unique in the sense that it can measure translation as well (a property not normally associated with goniometers). A translation accuracy of 0.2 mm (or 2.2% of its extendable length) is suggested (as a comparison, HoneyWell's series SS490 Hall-effect linear position sensors offer an accuracy of $\pm 3\%$). The precision is taken to be a fraction of accuracy and values of 0.5° for rotation and 0.1 mm for translation is suggested. Since the electrogoniometer is an experimental device, an effort was made in chapter ten to determine whether or not the accuracy and precision requirements have been met.

Other requirements include the resolution and sample rate. The resolution must be greater than the desired accuracy and is therefore elected to be a tenth of the accuracy. The sample rate is taken to be 30 Hz which is less than typical commercial systems but sufficient for a prototype.

The requirements established here are by no means exhaustive. Other important characteristics are hysteresis, linearity, bandwidth etc. However, these properties have been deemed out with the scope of the current project. The basic requirements as discussed above are summarised in table 3.1.

3.2 A Distributed versus Central Design

An important issue that became clear early on in the project was whether to pursue a distributed or central electronic hardware paradigm. The decision has far reaching consequences on the requirements and subsequent design. The mechanical chain shown in figure 3.1 already suggests that the mechanical aspect of the device consists of independent "sub-structures" (i.e. the goniometer-nodes). A distributed electronics approach will therefore be a natural continuation of the design paradigm.

	Property	Value
Electrogoniometer	Diameter	15 mm
	Number of goniometer-nodes	5
	Mobility	20 DOF
	Bend radius	90 mm
	Stretching in long axis (%)	33%
	Communication method	Wireless (Bluetooth)
Goniometer-node	Mobility	4 DOF
	Rotation range (each axis)	-20° to 20°
	Rotation accuracy	2°
	Rotation precision	0.5°
	Displacement range	0 to 9 mm
	Displacement accuracy	0.2 mm
	Displacement precision	0.1 mm
	Displacement range	27to 36 mm
	Resolution	0.2° for rotation, 20 μm for translation
	Sample rate	30 Hz

Table 3.1: Summary of the electrogoniometer and goniometer-node specification.

Furthermore, there are a number of arguments against a central design. Processors are limited in the number of sensor signals (analogue in particular) they can measure through the available hardware interfaces. For example Freescale's MCF51AC 32-bit microcontrollers offer up to 24 analog-to-digital converters. However, a five node electrogoniometer generates 50 analog signals (10 signals per node as discussed in chapter five). It will also simply be impractical for up to fifty wires to run through the electrogoniometer since it will be problematic to bend, twist and stretch the device. And finally, it will make the device difficult to scale (i.e. added nodes to the electrogoniometer).

A mostly distributed system is therefore opted for. However, the notion of central processing is not totally abandoned. It is suggested that goniometer-nodes, each with its own low-end processor, measure the sensors locally and then transmit the results to a central processor via a network connection. The number of wires interconnecting the nodes are consequently drastically reduced, and the digital data makes the system almost immune to noise. Another major benefit a distributed system will offer, is its ability to be scaled easily.

In effect what is suggested here is a master-slave configuration: the slave processors will sample the sensors and transmit the data to a master controller for further processing.

3.3 Conclusion

This research project is approached from an engineering point of view. Specifications are a prerequisite for the design phase. The requirements define the mechanical and sensing characteristics of the device. The physical requirements are mostly derived from the literature review. An argument is made to develop a device consisting of discrete kinematic sensing nodes. Each node measures four DOF. Baseline characteristics like accuracy, precision, resolution, mobility and form factor have been defined. Accuracy and precision are of particular importance, since the primary aim of this research is to develop a device that has performance similar to a benchmark commercial motion analysis system.

4.0 Mechanical Design

The mechanical design investigates the goniometer-node design and interlinking of several such structures to attain a high degree-of-freedom device. A few different goniometer-node designs are compared and contrasted. As is the case with many engineering applications, several of the design decisions are based upon tradeoffs. It is argued that the goniometer-node's mechanical complexity is inversely related to the complexity of the mathematical algorithm required to determine the pose (articulation) from the internal sensors measurements. The mechanical and sensing design can therefore not be completely separated but have to be considered jointly.

The proposed mechanical design is composed of an universal and cylindrical joint. The design is considered to be of average mechanical complexity and requires moderately complex algorithms to determine the pose (rotation and translation). Collectively the two joints implements three Cardan rotations followed by a translation, which can be expressed as a single homogeneous transformation. When linked with other nodes, the pose of any node relative to another node in the serial chain, is described by the familiar forward kinematics equation (Siciliano and Khatib, 2008).

4.1 The Goniometer-Node

The conceptual design, shown in figure 3.1, consists of a spherical (ball-and-socket) and prismatic joint. This is not necessarily the most practical design. The mechanical design also has to consider the electronic sensing and accompanying signal processing algorithms. It was discussed in chapter three that the embedded sensors measure local pose and then transmit the data to a master controller for further processing. This decision imposes two important requirements on the mechanical design. Firstly the mechanical structure must have enough space to house the sensors and supporting electronics. Yet, the form factor must be compact enough to meet the dimension requirements specified in the previous

chapter. Secondly, given the available budget and resources, the mechanical design must not be too complex to manufacture.

It turns out (as will be demonstrated) that the mechanical complexity is inversely related to the algorithmic (signal processing) complexity, i.e. a simple mechanical design requires complex algorithms and vice-versa. Three mechanical structures with equivalent kinematic design (i.e. three degrees of rotation and one degree of translation) are presented in figure 4.1. The mechanical designs impose three local rotations: first about the x -axis, followed by rotation about the transformed z -axis (z') and then about the double transformed y -axis (y'') and is commonly referred to as Cardan or Tait–Bryan angles (Zatsiorsky, 1998).

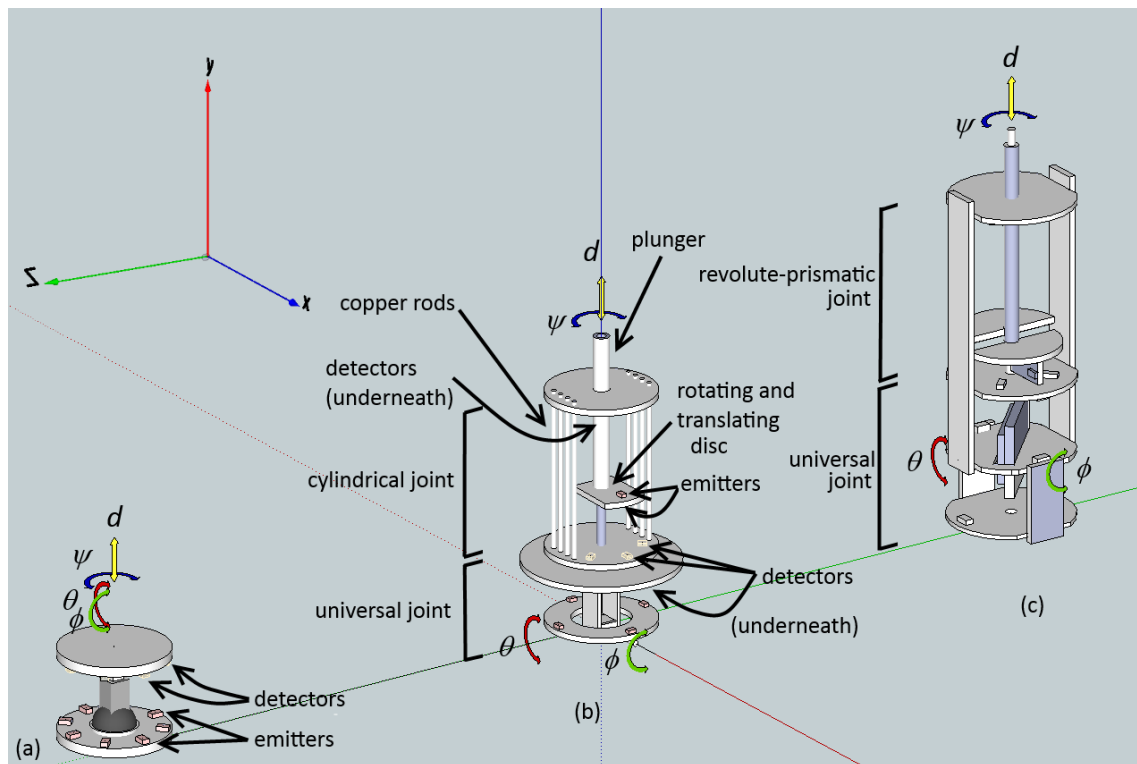


Figure 4.1: Three different geometries for a four DOF goniometer-node a) Spherical-prismatic joint; b) Universal-cylindrical joint; c) Universal-revolute-prismatic joint.

4.1.1 Spherical- Prismatic Joint

Figure 4.1a is based upon the original spherical-prismatic joint shown in figure 3.a. The structure is mostly constructed of printed circuit boards (PCBs) and metal components to realise the mechanical movement. Embedded in the structure are optical emitters and detectors, responsible for sensing the node articulation. For discussion purposes, eight

optical emitters and detectors are embedded in the bottom and top PCBs respectively. The emitters are switched on sequentially. During each on period all eight detectors are sampled. The detector signals (measured in volts) provide an indication of the distance between the detectors and the emitter currently on. Thus, a set consisting of sixty four (= 8 x 8) raw signal measurements are recorded and have to be processed to determine the node articulation.

This particular configuration has a simple mechanical design, a small form-factor when compared to the universal-revolute-prismatic joint, but produces a large amount of data (sixty four individual signals). The size of the signal set is directly related to the amount of algorithmic processing required to determine the node articulation. As will be discussed later, the universal-revolute-prismatic joint produces only eight signals. The spherical-prismatic joint can therefore expect to process at least eight times the amount of data of the universal-revolute-prismatic joint.

4.1.2 Universal-Cylindrical Joint

The second design (figure 4.1b) separates the three rotations and one translation axes into two distinct joints. The bottom section consists of a universal joint (two axes of rotation) and the top section of a cylindrical joint (one axis of rotation and one axis of translation).

The reduced mobility of the bottom section (when compared to the four DOF of the previous design) requires only four emitter-detector pairs to measure the two axes of rotation. Further, the emitters do not need to be switched on sequentially. Instead the emitters are switched on, the detectors sampled and then switched off again (to reduce power expenditure).

The cylindrical joint consists of two emitters and six detectors. Copper rods connect the upper and lower PCBs of the cylindrical joint. The rods ensure mechanical rigidity and at the same time act as electrical connections between the two PCBs. Two opposite facing emitters are embedded on a disc. The disc can be rotated and translated through a plunger as shown in figure 4.1b. Two opposing sets of three detectors (thus six detectors in total) are located at the bottom and top of the joint. As with the universal joint, the emitters are switched on periodically and the detectors sampled. It will be shown in chapter ten that the number of detectors are critical to the sensitivity of the design.

The design senses the four kinematic axes with ten detector and six emitters (compared to the sixty-four signals of the spherical-prismatic joint). It is about twice the length of the spherical-prismatic joint but mechanically more complex to manufacture.

4.1.3 Universal-Revolute-Prismatic Joint

The third design (figure 4.1c) has separate joints for all the mechanical axes. The bottom section is again a universal joint but the two axis rotations are now measured separately. The upper section consists of a revolute and prismatic joint and each axis movement measured separately. A total of eight emitters and eight detectors are used in the design, producing a set of eight signals.

The dimensions (height in particular) are the largest of the three designs (almost three times the spherical-prismatic joint). Size is an important issue since the goniometer-node length is restricted to approximately 27 mm (as was discussed in chapter three). Mechanically universal-revolute-prismatic joint it is also the most difficult to construct because all the joints are separate. However, from a algorithmic point of view it offers the simplest solutions since each axis is measured independently.

4.1.4 Discussion of Designs

From an engineering viewpoint there is a trade-off between the mechanical complexity on the one hand and the algorithmic complexity on the other. None of the three options offer a perfect solution. The spherical-prismatic design is appealing but the computational requirements are an unknown factor (not only in terms of the algorithmic requirements but, also the amount of data that has to be communicated between the node and PC).

The universal-revolute-prismatic design is complex mechanically with a larger form-factor although algorithmically speaking, much simpler. The design would also require precision manufacturing which is problematic on a limited budget.

Based upon these arguments, the intermediate design is selected for further consideration. The universal-cylindrical joint design is of medium mechanical complexity, has a fairly compact form-factor and has a small signal set (and therefore tolerable algorithmic complexity). Table 4.1 is summary of the designs and the related issues.

Mechanical Geometry	Form factor	Mechanical complexity	Algorithm complexity
Spherical- Prismatic	Poor	Low	High
Universal-Cylindrical	Medium	Medium	Medium
Universal-Revolute-Prismatic	Good	High	Low

Table 4.1: Design criteria applied to the proposed mechanical designs.

4.2 Kinematic Analysis of the Universal-Cylindrical Joint

The proposed mechanical design is now analysed in more detail. Three Cardan angles (ϕ , θ and ψ) are assigned to the axes of rotation as shown in figure 4.2a. The variable d is assigned to the translation component and is aligned with the ψ axis. A right-handed reference frame is attached to the base (proximal end) of the goniometer-node. A floating reference frame is assigned to the distal-end of the structure. The distal reference frame can therefore rotate (in three axes) and translate (in one axis) relative to the proximal reference frame.

The mechanical design imposes a sequence of three Cardan rotations. Starting at the proximal-end, the first rotation is ϕ degrees about the x axis (figure 4.2b); the second rotation is θ degrees about the z axis (figure 4.2c) and the final rotation of ψ degrees is about the y axis (figure 4.2d). The overall rotation, R_ζ , of the distal-end relative to the proximal-end can then be expressed by the following 3x3 rotation matrix:

$$R_\zeta = R_{y,\psi} R_{z,\theta} R_{x,\phi} \quad \text{equ 4.1}$$

where $R_{x,\phi}$, $R_{z,\theta}$ and $R_{y,\psi}$ are the *basic local rotation matrices* (the result of multiplying the matrices are shown in appendix A.1). (Note, the basis vectors constituting the rotation matrices are row vectors.) The rotation can also be expressed as a rotation component within a homogenous transformation matrix:

$$T_\zeta = \begin{bmatrix} R_\zeta & \mathbf{0}_{3 \times 1} \\ \mathbf{0}_{1 \times 3} & 1 \end{bmatrix} \quad \text{equ 4.2}$$

where the subscripts 1x3 indicates a row vector with three entries and 3x1 a column vector with three entries.

Next, the translation kinematic variable, d , is introduced. The distal-end, when not rotated, (i.e. R_ζ is a 3x3 identity matrix $I_{3 \times 3}$) is collinear with the y axis and is expressed by the following 3x1 column vector:

$$\mathbf{d} = I_{3 \times 3} \begin{bmatrix} 0 \\ d \\ 0 \end{bmatrix} \quad \text{equ 4.3}$$

(Note, vectors are written in bold and scalar values in non-bold.) The homogenous transformation matrix is then:

$$\mathbf{T}_d = \begin{bmatrix} I_{3 \times 3} & \mathbf{d} \\ \mathbf{0}_{1 \times 3} & 1 \end{bmatrix} \quad \text{equ 4.4}$$

The overall transformation, relating the rotation and translation of the distal-end relative to the proximal-end can then be expressed as a product of the above two homogenous transformation matrices, i.e.:

$$\begin{aligned} \mathbf{T} &= \mathbf{T}_\zeta \mathbf{T}_d \\ &= \begin{bmatrix} \mathbf{R}_\zeta & \mathbf{0}_{3 \times 1} \\ \mathbf{0}_{1 \times 3} & 1 \end{bmatrix} \begin{bmatrix} I_{3 \times 3} & \mathbf{d} \\ \mathbf{0}_{1 \times 3} & 1 \end{bmatrix} \\ &= \begin{bmatrix} \mathbf{R}_\zeta & \mathbf{R}_\zeta \mathbf{d} \\ \mathbf{0}_{1 \times 3} & 1 \end{bmatrix} \quad \text{equ 4.5} \end{aligned}$$

4.3 The Electrogoniometer as a Serial Kinematic Chain

From a mechanical perspective the electrogoniometer is a serial kinematic chain. The nodes making up the chain are attached to one another, so that the distal-end of a particular node is (rigidly) aligned with the proximal-end of the adjacent (succeeding) node. The base of the electrogoniometer (i.e. the proximal end of the first node) serves as the global reference frame of the device (although this selection is arbitrary).

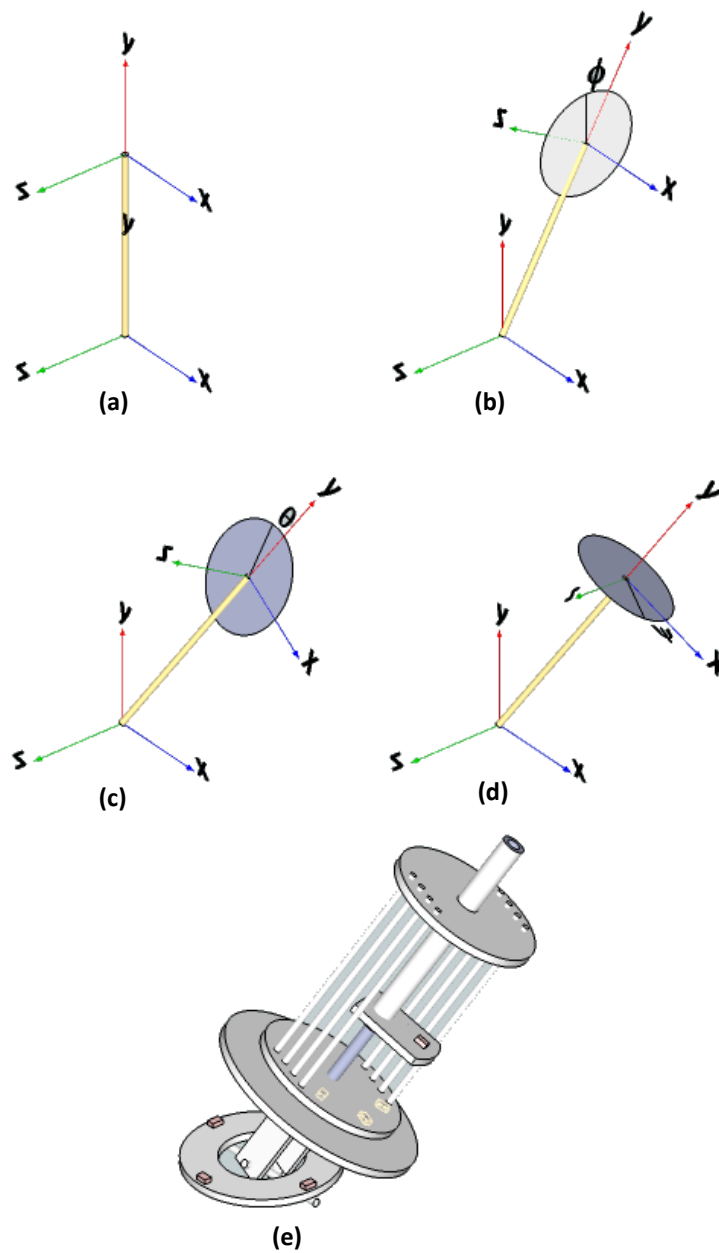


Figure 4.2: Rotation sequence for the goniometer-node: a) No rotation (proximal and distal axis are aligned); b) First rotation is about the x axis ($R_{x,\phi}$); c) Second rotation is about the z axis ($R_{z,\theta}$); d) Third rotation is about the y axis ($R_{y,\psi}$); e) Rotation applied to universal-cylindrical joint structure.

Some additional notation is necessary to describe the kinematics of the chain. Assume the chain consists of n goniometer-nodes. Mechanically, this means n links and n joints as illustrated in figure 4.3. Thus, the proximal-end of node i is labeled joint $i - 1$, and terminates with joint i via link i at the distal-end. The proximal and distal-end reference

frames of any two joining nodes are therefore static relative to each other and considered to be the same frame. Furthermore, the pose of joint i relative to joint $i - 1$ is the local transformation matrix ${}^{i-1}T_i$ as expressed by equation 4.5.

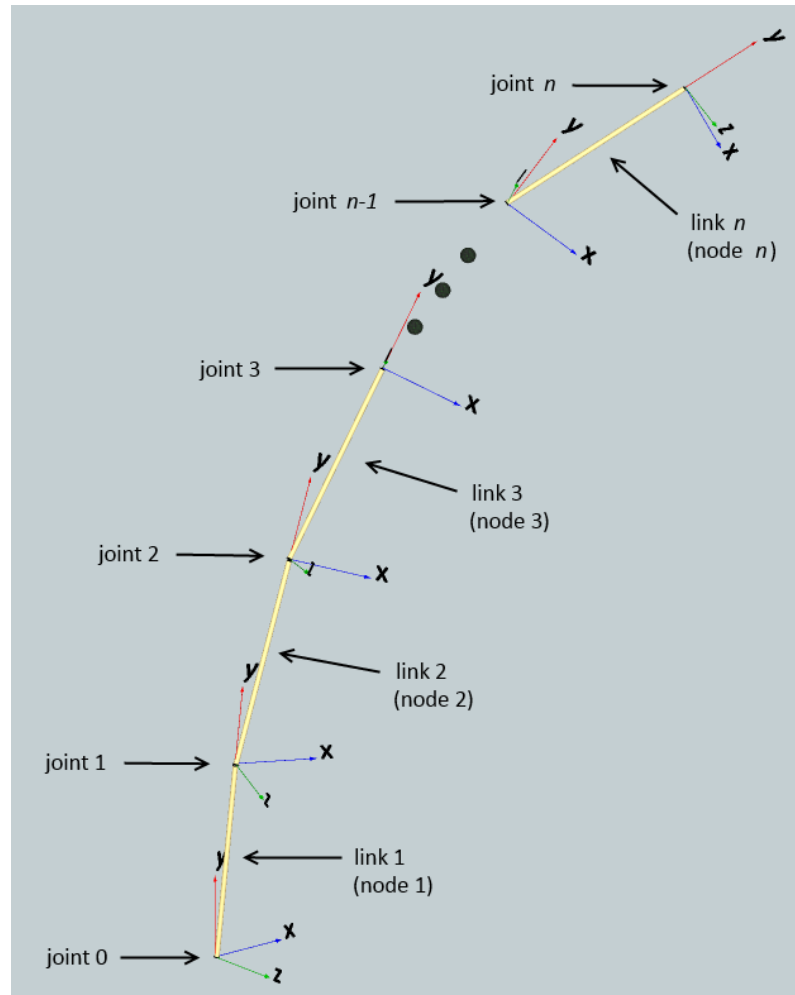


Figure 4.3: The electrogoniometer as a serial chain of the goniometer-nodes with attached reference frames.

If all local transformations are known, the global transformation can also be determined. The global transformation describes the pose of joint i relative to the global reference frame. It is determined by applying a sequence of transformations (better known as the forward kinematics procedure):

$${}^0T_i = \prod_{j=1}^i {}^{j-1}T_j \quad i = 1, \dots, n \quad \text{equ 4.6}$$

The kinematics of the electrogoniometer is graphically illustrated in figure 4.3.

4.4 Conclusion

The requirements established in the previous chapter set the guidelines according to which the device is designed. Firstly the mechanical design is considered although it cannot be considered in complete isolation from the sensing (electronic) design. The design was very much a trial-and-error process. Three different mechanical goniometer-node designs were considered. The three design were built (discussed in chapter six) but it was quickly realised that there is a trade-off between the complexity of the mechanical design and the algorithms required to extract the kinematic information. As the most complex mechanical design, the universal-revolute-prismatic joint was almost immediately discarded. It would have been difficult to manufacture with limited resources. Instead, the universal-cylindrical joint was selected since its structure is fairly simply to manufacture and only produces ten signals (compared to the sixty-four of the spherical-prismatic joint) to be processed. Fewer signals implies less computational effort.

The mechanical structure of the universal-cylindrical joint is composed of a cylindrical and universal joint to produce three rotation and a single translation axis. The kinematics are expressed through a sequence of local rotations followed by a single translation. The kinematics of the goniometer-nodes when chained together, are then described by the forward kinematics equation.

5.0 Kinematic Sensing

This chapter examines the electronic hardware and mathematical models and algorithms required to determine the goniometer-node kinematics. The local transformation (${}^{i-1}_i\mathbf{T}$) is as yet unknown and must somehow be determined through sensors embedded in the goniometer-nodes. It is a difficult task since most sensors do not measure angles and translation directly. Mathematical models are therefore required to process the raw sensor data and to convert it into kinematic information.

The chapter starts with an overview of sensors that may be suitable for measuring the node kinematics. An optical configuration consisting of various emitter-detector pairs are subsequently proposed as a viable sensing solution. A mathematical model, predicting the detector response when the emitter-detector pair is subjected to kinematic input, is developed. The equation describing the model cannot solve a multiple degree-of-freedom movement problem since it is underdetermined. A multiple emitter-detector configuration is introduced to solve this problem. The solution is applied separately to the universal and cylindrical joints. The theoretical transfer functions of both joints are then determined. Practical issues that impact on the implementation are then considered. It is argued that instead of solving the system of equations describing the detector transfer functions, a polynomial fit is used to solve the inverse curve-fit problem. The chapter concludes with a discussion on practicalities that affect the accuracy of the mathematical models.

5.1 An Overview of Sensor Technologies

A number of different sensors are available to measure kinematics. In some cases the sensors are multipurpose with kinematic sensing as only one of many applications. As stated earlier, space is at a premium, and the sensor size (form-factor) is therefore an important consideration when selecting a sensor. Other issues that must be considered are the complexity of the signal processing required to extract kinematic information from the raw signals; environmental robustness (i.e. not being affected by the environment);

bandwidth (frequency response of the sensor); power consumption; microcontroller interfacing (i.e. analogue or digital); cost and whether the sensors sense relative to a global or local reference frame.

The last attribute requires more explanation. Some sensors measure relative to a local reference frame. For example, a resistive flex (bend) sensor measures the angle between the ends. Other sensors measure relative to an external (global) source. A good example is an accelerometer measuring tilt. Here, the earth's gravitational field acts as a global reference frame. These type of sensors are sometimes referred to as being sourceless, since they are not stimulated by artificial means (Bachmann et al., 2001). Sensors that may be appropriate to sense kinematics are now discussed.

5.1.1 Hall-Effect Sensors

A hall-effect sensor produces a voltage proportional to the flux density of the magnetic field it senses. A magnet is usually used as a (constant) magnetic source, although alternating fields can also be sensed. The magnetic flux density decreases as the distance between the sensor and the magnetic source increases, thus making it suitable for position sensing.

Melexis Microelectronic Systems, (Ieper, Belgium) developed an interesting 3D sensing hall-effect sensor. The sensor (part number MLX90333) is marketed as a 3D joystick position sensor. The manufacturer does not state the accuracy of the sensor. The sensor has a small form factor (6 x 4 x 1.7 mm) and a digital interface, thus eliminating the need for external components.

However, a magnetic sensor has two major disadvantages. Firstly, the artificial magnetic field is affected by the environment. Any ferromagnetic material in the vicinity will disturb the field, causing inaccurate measurements. Secondly, each goniometer-node will require its own magnet. When the electrogoniometer is bent and twisted, crosstalk interference can be expected between the nodes. Magnetic shielding offers a possible solution to the interference problem but its effectiveness is difficult to predict.

5.1.2 Flex Sensors

The resistance of a flex sensor decreases (normally in a non-linear manner) as it is bent. Flex sensors based upon a capacitive principle are also available. Flex sensors may be

applied to measure a single axis of rotation. Flexpoint Sensors Systems (Utah, USA) manufactures a range of flex sensors. Their sensors have been used in data gloves and are therefore suitable to measure relatively large bend angles (Gentner and Classen, 2009).

Additional external components are required to convert the sensor resistance to a voltage. The non-linear response of the sensors will also adversely affect the goniometer-node, although analogue conditioning circuitry and processing can solve the problem to an extent. A final issue concerning flex sensors is the constant bending of the sensor may cause it to fail due to fatigue.

5.1.3 Inertial Sensors

Orientation sensors based upon tri-axial accelerometer, gyroscope and magnetometer have already been discussed in the literature review. An accelerometer measures any acceleration component exerted on it, including gravity. When static (or when moving at a constant velocity), the global roll and pitch of an accelerometer can be determined by using the earth's gravity field as reference (Sun et al., 2010). Unfortunately in most applications, the accelerometer is not static and neither is the velocity constant (i.e. the accelerometer is subjected to Newton second law). The accelerometer will consequently measure the total acceleration, making it difficult to determine its orientation relative to the earth's gravity field. In theory the position of the accelerometer can also be determined by double integrating the acceleration measurements. However, MEMS devices are fairly noisy and double integration will therefore add a significant drift component over time, making it difficult to determine position accurately without repeated position-fixing (Thong et al., 2004).

Accelerometers can only measure at best two degrees of rotational freedom. A second reference vector can be obtained from a tri-axial magnetometer which measures the earth's magnetic field. The direction of the field depends on the global location of the magnetometer. At the poles the angle is perpendicular to the surface and parallel at the magnetic equator. Orientation (roll, pitch and yaw) can then be determined by combining the accelerometer and magnetometer measurements. There are however a few requirements that need to be met: the magnetic and gravity field vectors must not be closely aligned (which will happen when moving closer to the magnetic poles) and the

motion must comply with Newton's first law (i.e. be stationary or move at a constant velocity).

Gyroscopes are another source of kinematic data. MEMS gyroscopes usually measure angular rate, making it theoretically possible to determine orientation by simply integrating the rate measurements. Unfortunately, as with accelerometers, these sensors are noisy and angular readings will drift over time (Woodman, 2007). However, orientation can be determined for short periods but accuracy will decline over time due to the integration of noise and dc offsets.

The orientation of a device consisting of all three sensor types, can be determined by combining the measurements (a process sometimes referred to as data fusion) (Woodman, 2007). The accelerometer and magnetometer measure two references but as discussed above, are only accurate under certain conditions. The gyroscope is useful for angular measurement when the device motion obeys Newton's second law. However due to the noise the gyroscope compensation will become less exact over time due to noise and dc offset integration. A number of sophisticated data fusion algorithms have been developed by Yun and Bachmann (2006), Woodman (2007) and Sun et al. (2010) to effectively combine the data from the three different sensors.

Despite increasing sophistication, orientation sensors have their vulnerabilities. As mentioned, noise affects the performance of gyroscopes and magnetic sensors are affected by ferrous metal and other magnetic disturbances (e.g. alternating magnetic fields e.g. due to power cables). The earth's magnetic field strength is also constantly changing (Unsöld and Baschek, 2001), requiring the magnetometers to be recalibrated on a regular basis. And finally, accelerometers measure any force applied to it.

One major advantage of orientation sensors are that they measure orientation relative to a global reference frame (i.e. relative to the earth's gravity and magnetic field). Thanks to recent advances in MEMS technology, the modules are also becoming increasingly smaller. STMicroelectronics (Geneva, Switzerland), for example, manufactures a tri-axial accelerometer, gyroscope and magnetometer integrated circuit (IC) that measures only 4 x 4 x 1 mm (part number LSM9DS0).

5.1.4 Optical Sensors

The final sensing method investigated here is that of optical sensing. The Vicon system discussed in chapter two is an example of position and rotation sensing through optical means. Another example is the Wii gaming console. The console consists of only a single camera (embedded within a handheld device) and a IR bar placed on top of a television. The bar has IR emitters embedded which is visible to the handheld camera. Based upon the known locations of the IR sources, the orientation of the remote can be determined relative to the IR bar by analysing the camera's image content (Gregory, 2009). Image sensors are becoming smaller and feature better resolution. However, the primary disadvantage of such approach, given the scope of this research project, is the amount of processing required to determine the relative orientation and position.

A simpler approach is to use single (discrete) detectors as the sensing mechanism instead of image sensors. A detector (typically a phototransistor) acts similarly to a pixel in an image sensor. Based on the intensity of light received by the detector, it becomes possible to determine the emitter's location relative to the detector. However such an approach will require multiple emitters and one or more detectors to solve the position and orientation problem. The operating principles are based on the inverse square law and varying directivity of the emitters and detectors. Devices based upon these principles have been reported by Welch et al. (1999) and more recent notably work by Heo et al. (2011).

From a hardware and signal analysis perspective, this approach offers a simpler solution to the position and orientation problem when compared to imaging sensors. It has a compact form-factor and consists of a few low-cost detectors and emitters and a microcontroller to capture the data. Neither camera lenses, nor computational intensive and power hungry image processing are required.

5.1.5 Discussion

The benefits and drawbacks of the different sensing methods and technologies are summarised in table 5.1. Based upon the comparison, the inertial sensors and emitter-detector sensors offer the most benefits. The fact that inertial sensors measure relative to a global reference frame is a major advantage, however such devices are vulnerable to environmental interference and have questionable performance under dynamic conditions

Sensing Technology	Pros	Cons
Hall-Effect Sensors	<ul style="list-style-type: none"> • Small form-factor (MLX90333: 6 x 5 x 1.6 mm) • Low cost (MLX90333: £4.50) 	<ul style="list-style-type: none"> • Require magnetic source • Environmental interference • Cross-talk interference • Cannot sense position • Unexplored technology • Measures relative to a local reference frame
Flex Sensors	<ul style="list-style-type: none"> • Low cost (FS-L-0095-103-ST: £10.80) • Computational simple to determine position and rotation 	<ul style="list-style-type: none"> • Can sense only one DOF of rotation • Difficult to sense position • Fatigue due to constant bending • Measures relative to a local reference frame • Poor accuracy, precision and hysteresis (Tactilus Flex Sensor : $1\pm 3^\circ$ and 7% hysteresis)
Inertial Sensors	<ul style="list-style-type: none"> • Measures relative to a global reference frame • Small form factor (LSM9DS0: 4 x 4 x 1 mm) • Well established technology with known performance characteristics (2° to 5° accuracy) • Low cost (LSM9DS0: £6.70) 	<ul style="list-style-type: none"> • Affected by ferrous metals and power lines. • Has to be repeatedly recalibrated • Cannot measure position over prolonged periods.
Optical Sensor: Imaging	<ul style="list-style-type: none"> • Can measure 6 DOF • Low cost (OV07675-A23A: £2.00) • Small form factor (OV07675-A23A: 3 x 3 mm) 	<ul style="list-style-type: none"> • Complex design • Unknown accuracy • Computational intensive image processing required • High power consumption (OV07675-A23A: 100 mW) • Measures relative to a local reference frame • Low sample rate (OV07675-A23A: 30 Hz)
Optical Sensor: Emitter and detectors	<ul style="list-style-type: none"> • Low cost (TEMT7100X01: £0.30; VSMB1940X01: £0.30) • Small form-factor (2 x 1.25 x 0.85 mm) • Simple hardware design • Simpler signal analysis than image sensor • Uses known principles • Can measure 6 DOF 	<ul style="list-style-type: none"> • Unknown accuracy • Measures relative to a local reference frame

Table 5.1: Comparison of different sensing technologies and methods to determine orientation and position.

(De Vries et al., 2009). Position can also not be adequately measured by these devices over prolonged periods. Emitter-detector sensors on the other hand can sense six degrees-of-freedom but measure relative to a local reference frame and has unknown accuracy and precision.

Based upon the arguments, the emitter-detector sensing method is selected. This method of spatial sensing has not yet extensively been used to solve position and orientation problems and will therefore introduce challenges. However, if an electrogoniometer can be developed using this sensing method, it will make a valuable contribution to goniometry with many other possible applications.

5.1.6 Related Work

The closest recent research and development based upon similar sensing principles are by Heo et al. (2011). They developed a system consisting of IR emitters housed in a handheld device. The emitters irradiate four IR detectors located on corners of a monitor as illustrated in figure 5.1. The position and orientation of the handheld device are determined relative to the detectors. The method exploits the spatial directivity of the emitters and detectors and the notion that light intensity decreases according to the inverse square law as the distance between the emitters and detectors increases.

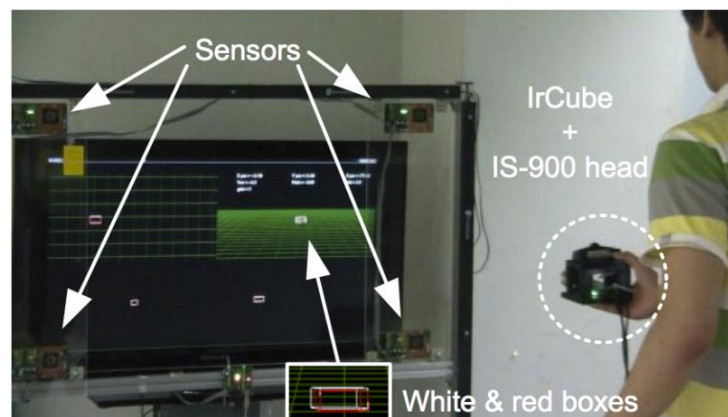


Figure 5.1: The position and orientation system using optical emitters and detectors developed by Heo et al. (2011).

They found their system to have a static and dynamic position error of better than 2.75 cm and 3.41 cm respectively. The distance between the emitters and detectors was about 2 m, which translates to 1.38% and 1.71% static and dynamic errors respectively. They reported

maximum orientation errors of 1.73° under static conditions and 2.9° under dynamic conditions.

The device presented by Heo et al. can be considered a *meter* application of the concepts, considering the dimensions (work space) of their system. The device presented here is a millimeter application, since the goniometer-nodes have a diameter of 15 mm and are roughly 27 mm long. Scaling down presents a few challenges, especially considering the tolerances required to manufacture the proposed device. Other than that, the principles remain the same.

5.2 Pose Estimation through Optical Sensing

A model is now formulated from first principles to determine the orientation and position of a goniometer-node's distal-end relative to its proximal-end through optical sensing. Firstly a basic model describing a single emitter-detector pair is developed. Such an arrangement is however not sufficient to determine the pose of the node. A more complex design consisting of numerous emitter-detector pairs is then examined and is shown to be capable of solving the pose estimation problem.

5.2.1 Theoretical Analysis of a Single Emitter-Detector Pair

Consider the setup in figure 5.2b. It consists of an IR emitter (part number: TEMT7100X01) illuminating an IR detector (part number: VSMB1940X01). The primary reasons for selecting these components are they are cheap (about £0.30 each) and available in small packages (2x1.25x0.85mm). It is assumed that the detector has six degrees-of-freedom relative to the emitter. An idealised point emitter and detector (i.e. the photosensitive areas are much smaller than the distance between the emitter and detector) are assumed and with no ambient noise sources. The emitter radiates a constant radiation flux of φ_e watt at a distance s from the detector. The detector, as part of a functioning electronic circuit, senses a fraction of the radiation and produces a current as a result of the radiation. Consequently, a voltage appears across the resistor as predicted by Ohm's Law. The current is a product of the received power density, sensitivity, spectral response, and receiver and transmitter's spatial directivity patterns (manufacturer datasheets are included in appendix B). The

amount of current (and therefore voltage) is assumed to be approximately linearly related to the received irradiance (the relationship is stated in the datasheets of the phototransistor).

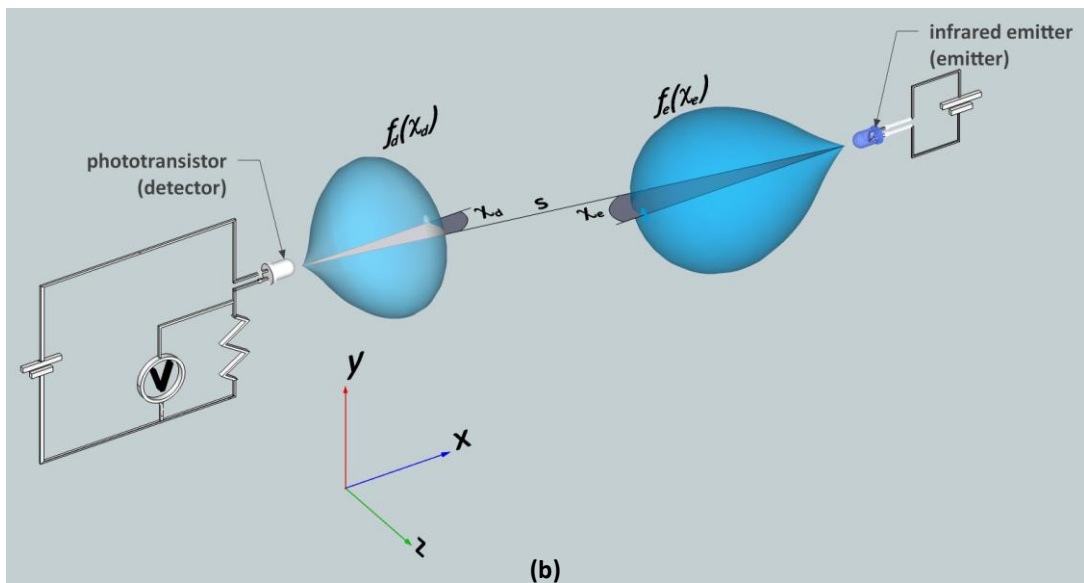
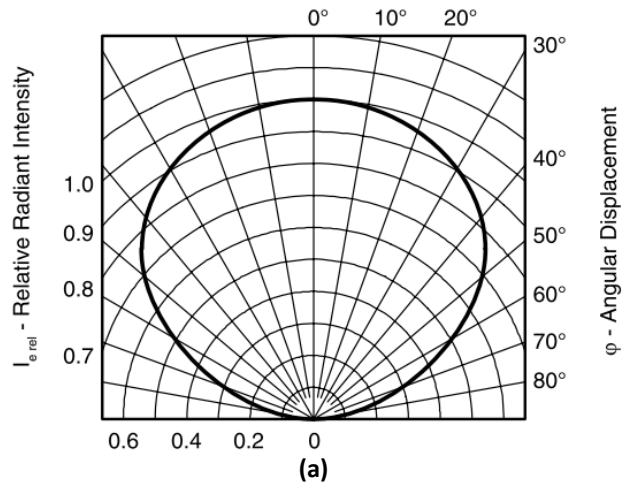


Figure 5.2: a) Typical receiver and transmitter spatial directivity patterns of a detector and emitter (Vishay Semiconductors, 2008); b) Infrared emitter and detector circuit.

The relationship between the radiant intensity of the emitter and the voltage measured across the resistor in the detector circuit is now derived. Under the assumption of an isotropic emitter with constant radiant intensity I_e , the irradiance, E , at a distance s from the emitter is:

$$E(s) = \frac{I_e}{s^2} \tag{equ 5.1}$$

The equation is commonly referred to as the inverse square law for a point source (Langer and Zucker, 1997). In practice, the emitter radiates in an anisotropic manner and the radiant intensity is therefore dependent on χ_e (the angle between the emitter's optical axis and the point in space where the irradiance is measured). Thus:

$$I_e(\chi_e) = I_{e_{iso}} f_e(\chi_e) \quad \text{equ 5.2}$$

The angular dependency, $f_e(\chi_e)$, is usually specified in the technical datasheets (typically as a dimensionless normalised radiant intensity – see figure 5.2a). $I_{e_{iso}}$ is a constant (since the emitter radiates at a constant radiation flux) and indicates the maximum radiant intensity in the case of an isotropic radiator.

As with the emitter, the detector directivity pattern properties are anisotropic in nature. The received irradiance is thus a function, $f_d(\chi_d)$, of its angle relative to the detector's optical axis (some manufactures specify this as a normalised sensitivity). The actual irradiance available to excite the detector is therefore:

$$E_d(\chi_d, s) = E(s) f_d(\chi_d) \quad \text{equ 5.3}$$

Note, the functions $f_e(\chi_e)$ and $f_d(\chi_d)$ account for the emitter/detector lens characteristics and the fact the effective area “viewed” by the emitter/detector relative to each other varies according to Lambert's cosine law.

The detector current, according to the datasheets, is linearly related to the irradiance received by the detector. Thus by applying Ohm's law, the irradiance can be related to the voltage measured across the resistor, R_d , in the detector circuit:

$$v_d = k R_d E_d(\chi_d, s) \quad \text{equ 5.4}$$

where k is a constant which relates the current to the irradiance.

Finally, equation 5.2 is substituted into 5.1 and then into 5.3. The result is then substituted into 5.4 to reveal the voltage across the detector resistor as a function of the directivity patterns and distance between the emitter and detector:

$$v_d = g(\chi_e, \chi_d, s)$$

$$= k_R \frac{f_e(\chi_e) f_d(\chi_d)}{s^2} \quad \text{equ 5.5}$$

where $k_R = kR_d I_{e_{iso}}$. Equation 5.5 will from now on be referred to as the transmission equation.

It is interesting to note the equation's similarity to Newton's universal law of gravity, the main difference being the point masses in Newton's gravity equation are assumed to be caused by isotropic gravity fields. The equation also agrees with the one presented in Heo et al. (2011) although they did not show how they derived it.

Equation 5.5 explicitly states that the measured voltage, v_d , is a function of the three independent kinematic variables (two angular (χ_e and χ_d) and one distance (s)). Unfortunately the transmission equation is incapable of solving the six degrees of movement problem posed in figure 5.2b. Firstly because χ_e , χ_d and s do not map uniquely to six degrees-of-freedom and secondly because χ_e , χ_d and s cannot be uniquely determined from the measured detector voltage.

The obvious solution is to introduce multiple emitter-detector pairs. Mathematically the kinematic sensing problem is then described as a system of (transmission) equations. The method essentially combines triangulation (location identification through angles (White and Garrot, 1990) and trilateration (location identification through distances, (Manolakis, 1996)).

5.2.2 Multi Emitter-Detector Pairs and its Application to sense the Pose of the Universal-Cylindrical Joint

The analysis that follows will consider multiple emitters-detectors pairs and is specifically applied to the universal-cylindrical joint design discussed in chapter four. Each joint is analysed separately.

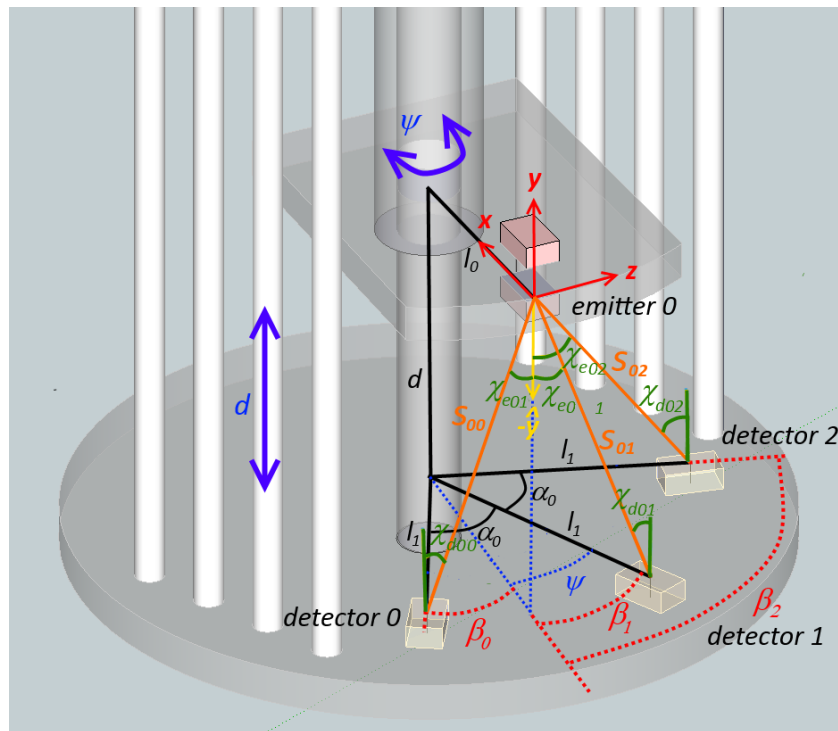


Figure 5.3: Kinematic variables and parameters of the lower section of the cylindrical joint.

5.2.3 Cylindrical Joint Emitter-Detector Pair Analysis

The cylindrical joint has six detectors and two emitters. The lower three detectors are illuminated by a single emitter mounted on a disc mechanically capable of rotating and translating. A complementary emitter-detector arrangement is reproduced at the upper section of the structure.

5.2.3.1 Lower Section Analysis

The lower section of the cylindrical joint is shown in figure 5.3.. The objective is to determine the response (output) of each detector, given the (input) kinematic variables (ψ and d). The problem requires χ_e , χ_d and s to be described in terms of ψ and d . The variables χ_e , χ_d and s are therefore intermediate variables relating the input kinematic variables to the detector response (χ_e , χ_d and s are from now on referred to as the intermediate kinematic variables).

The intermediate kinematic variables could be determined through trigonometry but the geometric algebra approach used in chapter four (section 4.2) is used instead to determine the chain kinematics (arguably a more eloquent approach). The distance, s_{ji} , is determined

from the sequence of transformations, T_{ji} , starting at emitter j and ending at detector i , i.e.:

$$\begin{aligned} T_{ji} &= \begin{bmatrix} I & l_0 \\ \mathbf{0}_{1 \times 3} & 1 \end{bmatrix} \begin{bmatrix} I & d \\ \mathbf{0}_{1 \times 3} & 1 \end{bmatrix} \begin{bmatrix} Q_{y,\beta_{ji}} & \mathbf{0}_{3 \times 1} \\ \mathbf{0}_{1 \times 3} & 1 \end{bmatrix} \begin{bmatrix} I & l_1 \\ \mathbf{0}_{1 \times 3} & 1 \end{bmatrix} \\ &= \begin{bmatrix} Q_{\beta_{ji}} & l_0 + d + Q_{y,\beta_{ji}} l_1 \\ \mathbf{0}_{1 \times 3} & 1 \end{bmatrix} \quad \text{where } i \in \{0,1,2\}, j \in \{0\} \quad \text{equ 5.6} \end{aligned}$$

The translation component is then the vector from the emitter to the detectors, i.e.:

$$s_{ji} = l_0 + d + Q_{y,\beta_{ji}} l_1 \quad \text{where } i \in \{0,1,2\}, j \in \{0\} \quad \text{equ 5.7}$$

and where l_0 , l_1 , d and $Q_{y,\beta_{ji}}$ are:

$$l_0 = \begin{bmatrix} l_0 \\ 0 \\ 0 \end{bmatrix}; \quad l_1 = \begin{bmatrix} -l_1 \\ 0 \\ 0 \end{bmatrix}; \quad d = \begin{bmatrix} 0 \\ d \\ 0 \end{bmatrix}; \quad \text{and } Q_{y,\beta_{ji}} = \begin{bmatrix} \cos\beta_{ji} & 0 & \sin\beta_{ji} \\ 0 & 1 & 0 \\ -\sin\beta_{ji} & 0 & \cos\beta_{ji} \end{bmatrix} \quad \text{equ 5.8}$$

l_0 and l_1 are dimension parameters and d is the unknown kinematic variable to be determined. $Q_{y,\beta_{ji}}$ is the *basic global rotation matrix* about the y axis.

The Euclidean distance between the emitter and a detector is then the magnitude of the distance vector, i.e.:

$$s_{ji} = \|s_{ji}\| \quad \text{where } i \in \{0,1,2\}, j \in \{0\} \quad \text{equ 5.10}$$

The kinematic angle, ψ , is related to the measurement angle, β_{ji} , i.e.:

$$\beta_{ji} = \psi + (1 - i)\alpha_0 \quad \text{where } i \in \{0,1,2\}, j \in \{0\} \quad \text{equ 5.11}$$

where α_0 is the angles between detectors as shown in figure 5.3. The final unknowns are the receive and transmit angles ($\chi_{e_{ji}}$ and $\chi_{d_{ji}}$). As evident from figure 5.3, the angles are simply the dot product between the y axis and s_{ji} :

$$\chi_{e_{ji}} = \chi_{d_{ji}} = \cos^{-1}(-\widehat{s_{ji}} \cdot \widehat{y}) \quad \text{where } i \in \{0,1,2\}, j \in \{0\} \quad \text{equ 5.12}$$

where \widehat{s}_{ji} is the normalised distance vector between the emitter and detector i and \widehat{y} is an unit vector in the direction of the y axis.

5.2.3.2 Upper Section Analysis

The analysis of the upper section of the cylindrical joint is very similar to that of the lower section. The main difference is the translation, d' , of the upper section is complementary to the translation, d , of the lower section and thus the following relationship exists:

$$d' = d_{max} - d - l_\epsilon \tag{equ 5.13}$$

where d_{max} is the internal height and l_ϵ is the distance between the two emitters as illustrated in figure 5.4.

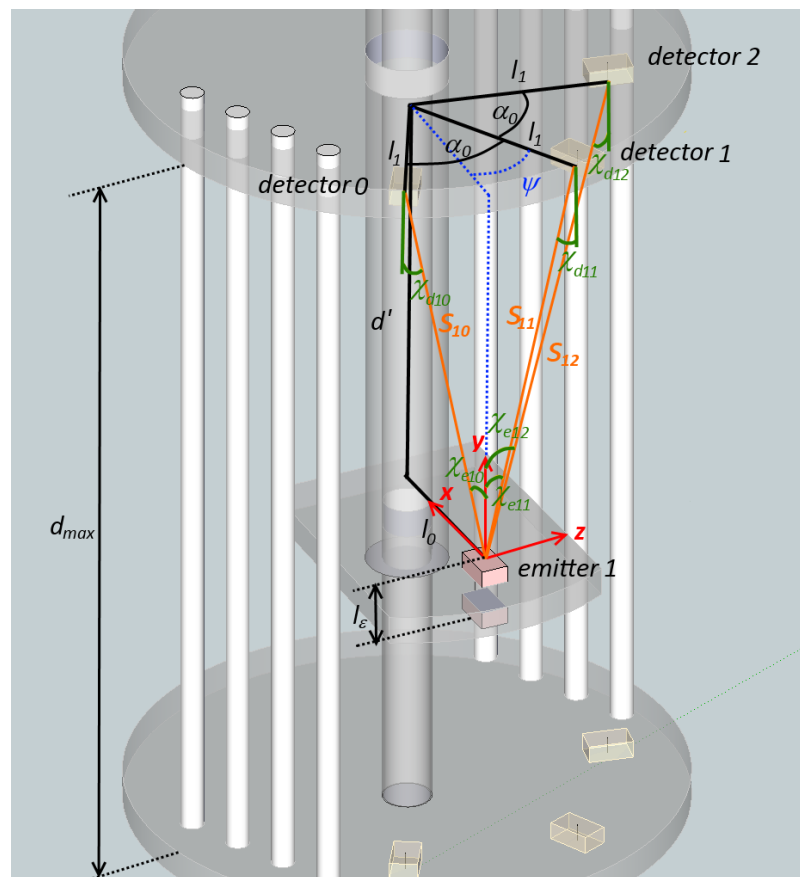


Figure 5.4: Kinematic variables and parameters of the upper section of the cylindrical joint.

5.2.3.3 Summary of Analysis

A framework is now in place to describe the detector voltages as a function of the cylindrical joint's kinematic variables, i.e.:

$$v_{d_{ji}} = g_{ji}(d, \psi) \quad \text{where } (j, i) \in \{(0,0), (0,1), (0,2), (1,0), (1,1), (1,2)\} \quad \text{equ 5.14}$$

and with possible solutions:

$$d = h_d(v_{d_{00}}, v_{d_{01}}, v_{d_{02}}, v_{d_{10}}, v_{d_{11}}, v_{d_{02}}) \quad \text{equ 5.15}$$

and

$$\psi = h_\psi(v_{d_{00}}, v_{d_{01}}, v_{d_{02}}, v_{d_{10}}, v_{d_{11}}, v_{d_{02}}) \quad \text{equ 5.16}$$

The system of equations with intermediate equations are summarised in table 5.2.

$v_{d_{ji}} = g_{ji}(d, \psi) = k_R \frac{f_e(\chi_{eji}) f_d(\chi_{dji})}{s_{ji}^2} \quad \text{where } (j, i) \in \{(0,0), (0,1), (0,2), (1,0), (1,1), (1,2)\}$
with intermediate equations:
<ul style="list-style-type: none"> lower section ($j = 0$): $s_{ji} = l_0 + d + Q_{y, \beta_{ji}} l_1 \quad \text{where } i \in \{0,1,2\}, j \in \{0\}$ $\chi_{e_{0i}} = \chi_{d_{ji}} = \cos^{-1}(-\widehat{s_{0i}} \cdot \widehat{y})$ $\beta_{0i} = \psi + (1 - i)\alpha_0 \quad \text{where } i \in \{0,1,2\}$ upper section ($j = 1$): $s_{ji} = l_0 + d' + Q_{y, \beta_{ji}} l_1 \quad \text{where } i \in \{0,1,2\}, j \in \{1\}$ $\chi_{e_{1i}} = \chi_{d_{ji}} = \cos^{-1}(\widehat{s_{1i}} \cdot \widehat{y})$ $d' = d_{max} - d - l_\varepsilon$ $\beta_{1i} = \psi + (1 - i)\alpha_0 \quad \text{where } i \in \{0,1,2\}$
and where f_e and f_d are specified by the emitter and detector manufacturer (see appendix B).
The general solution to the system of equations is:
$d = h_d(v_{d_{00}}, v_{d_{01}}, v_{d_{02}}, v_{d_{10}}, v_{d_{11}}, v_{d_{02}})$ $\psi = h_\psi(v_{d_{00}}, v_{d_{01}}, v_{d_{02}}, v_{d_{10}}, v_{d_{11}}, v_{d_{02}})$

Table 5.2: Summary of the system of equations describing the kinematic variables d and ψ as measured by the multiple emitter-detector pairs scheme in figures 5.3 and 5.4.

5.2.4 Universal Joint Emitter-Detector Pair Analysis

A similar analysis is now applied to the universal joint. As shown in figure 5.5, four emitter-detector pairs are embedded in a quadrant configuration within the mechanical structure. The PCB housing the detectors firstly rotate about the ϕ axis, followed by a rotation about the θ axis.

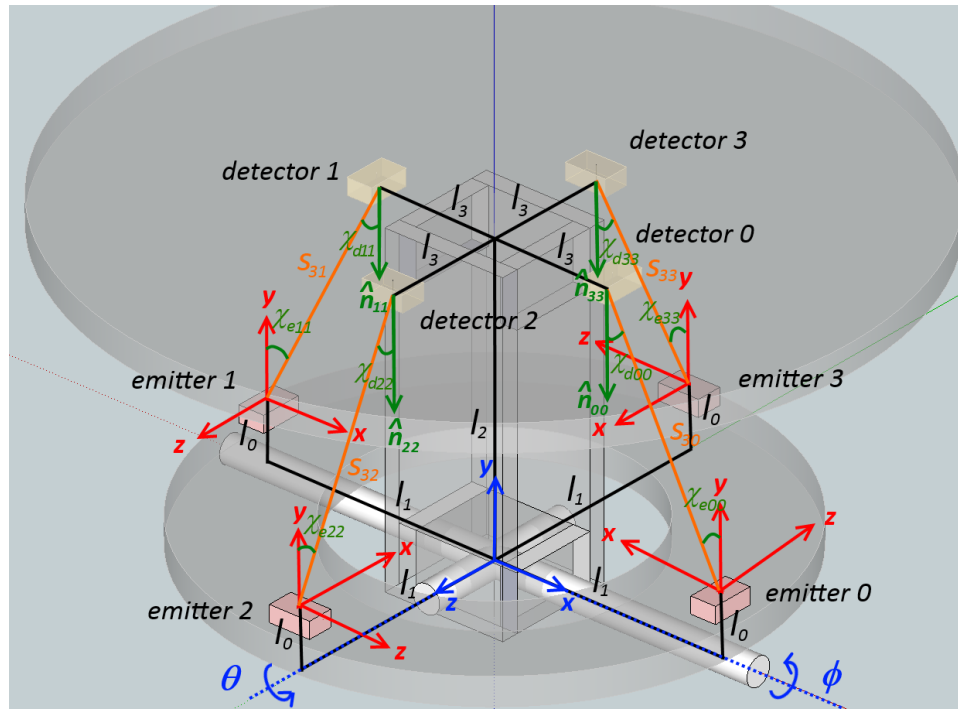


Figure 5.5: Kinematic variables and parameters of the universal joint.

5.2.4.1 Analysis

The analysis of the universal joint is similar to that of the cylindrical joint. The universal joint is described in figure 5.5. A more compact analysis is achieved by orientating the emitter reference frames (shown in red in figure 5.5) relative to the universal joint's frame (shown in blue). The process is started by determining the distance vector from emitter j to detector i :

$$s_{ji} = l_0 + l_1 + R_{\gamma_{ji}}(l_2 + l_3) \quad (j, i) \in \{(0,0), (1,1), (2,2), (3,3)\} \quad \text{equ 5.17}$$

The vectors l_0, l_1, l_2 and l_3 are dimensioned parameters and defined as:

$$\mathbf{l}_0 = \begin{bmatrix} 0 \\ -l_0 \\ 0 \end{bmatrix}; \mathbf{l}_1 = \begin{bmatrix} l_1 \\ 0 \\ 0 \end{bmatrix}; \mathbf{l}_2 = \begin{bmatrix} 0 \\ l_2 \\ 0 \end{bmatrix}; \mathbf{l}_3 = \begin{bmatrix} -l_3 \\ 0 \\ 0 \end{bmatrix}$$

The rotation $\mathbf{R}_{\gamma_{ji}}$ is a sequence of two Euler rotations and depends on the orientation of the emitter reference frame relative to the universal joint's frame: $\mathbf{R}_{\gamma_{00}} = \mathbf{Q}_{x,-\phi} \mathbf{Q}_{z,-\theta}$; $\mathbf{R}_{\gamma_{11}} = \mathbf{Q}_{x,\phi} \mathbf{Q}_{z,\theta}$; $\mathbf{R}_{\gamma_{22}} = \mathbf{Q}_{z,\phi} \mathbf{Q}_{x,\theta}$; $\mathbf{R}_{\gamma_{33}} = \mathbf{Q}_{z,-\phi} \mathbf{Q}_{x,-\theta}$ **equ 5.18**

where \mathbf{Q} is the *basic global rotation matrix* and defined as:

$$\mathbf{Q}_{x,\phi} = \begin{bmatrix} \mathbf{1} & 0 & 0 \\ 0 & \cos\phi & -\sin\phi \\ 0 & \sin\phi & \cos\phi \end{bmatrix} \quad \text{and} \quad \mathbf{Q}_{z,\theta} = \begin{bmatrix} \cos\theta & -\sin\theta & 0 \\ \sin\theta & \cos\theta & 0 \\ 0 & 0 & 1 \end{bmatrix}$$

The Euclidean distance between the emitter and a detector is the magnitude of the distance vector, i.e.:

$$s_{ji} = \|\mathbf{s}_{ji}\| \quad (j, i) \in \{(0,0), (1,1), (2,2), (3,3)\} \quad \text{equ 5.19}$$

Unlike in the case of the cylindrical joint, the angles χ_e and χ_d are not equal. The emitter angle, $\chi_{e_{ji}}$, is the dot product between the emitters optical axis, $\widehat{\mathbf{n}}_{ji}$, and the normalised distance vector, $\widehat{\mathbf{s}}_{ji}$:

$$\begin{aligned} \chi_{e_{ji}} &= \cos^{-1}(\widehat{\mathbf{y}} \cdot \widehat{\mathbf{s}}_{ji}) \\ &= \cos^{-1}\left(\frac{[0,1,0]^T \cdot \mathbf{s}_{ji}}{s_{ji}}\right) \quad (j, i) \in \{(0,0), (1,1), (2,2), (3,3)\} \quad \text{equ 5.20} \end{aligned}$$

The detector angles, $\chi_{d_{ji}}$, are slightly more complicated since the optical angle depends on the rotation matrix $\mathbf{R}_{\gamma_{ji}}$:

$$\begin{aligned} \chi_{d_{ji}} &= \cos^{-1}(\widehat{\mathbf{n}}_{ji} \cdot \widehat{\mathbf{s}}_{ji}) \\ &= \cos^{-1}\left(\frac{\mathbf{R}_{\gamma_{ji}} [0,-1,0]^T \cdot \mathbf{s}_{ji}}{s_{ji}}\right) \quad (j, i) \in \{(0,0), (1,1), (2,2), (3,3)\} \quad \text{equ 5.21} \end{aligned}$$

5.2.4.2 Summary of Analysis

All the equations are now in place to describe the detector responses as a function of the universal joint's kinematic variables ϕ and θ , i.e.:

$$v_{d_{ji}} = g_{ji}(\phi, \theta) \quad \text{where } (j, i) \in \{(0,0), (1,1), (2,2), (3,3)\} \quad \text{equ 5.22}$$

and has possible solutions:

$$\phi = h_{\phi}(v_{d_{00}}, v_{d_{11}}, v_{d_{22}}, v_{d_{33}}) \quad \text{equ 5.23}$$

and

$$\theta = h_{\theta}(v_{d_{00}}, v_{d_{11}}, v_{d_{22}}, v_{d_{33}}) \quad \text{equ 5.24}$$

The system of equations with intermediate equations are summarised in table 5.3.

$v_{d_{ji}} = g_{ji}(\phi, \theta) = k_R \frac{f_e(\chi_{e_{ji}}) f_d(\chi_{d_{ji}})}{s_{ji}^2} \quad \text{where } (j, i) \in \{(0,0), (1,1), (2,2), (3,3)\}$ <p>with intermediate equations:</p> $\mathbf{s}_{ji} = \mathbf{l}_0 + \mathbf{l}_1 + \mathbf{Q}_{\gamma_{ji}}(\mathbf{l}_2 + \mathbf{l}_3) \quad (j, i) \in \{(0,0), (1,1), (2,2), (3,3)\}$ $\mathbf{l}_0 = \begin{bmatrix} 0 \\ -l_0 \\ 0 \end{bmatrix}; \quad \mathbf{l}_1 = \begin{bmatrix} l_1 \\ 0 \\ 0 \end{bmatrix}; \quad \mathbf{l}_2 = \begin{bmatrix} 0 \\ l_2 \\ 0 \end{bmatrix}; \quad \mathbf{l}_3 = \begin{bmatrix} -l_3 \\ 0 \\ 0 \end{bmatrix}$ $\mathbf{R}_{\gamma_{00}} = \mathbf{Q}_{x,-\phi} \mathbf{Q}_{z,-\theta}; \quad \mathbf{R}_{\gamma_{11}} = \mathbf{Q}_{x,\phi} \mathbf{Q}_{z,\theta}; \quad \mathbf{R}_{\gamma_{22}} = \mathbf{Q}_{z,\phi} \mathbf{Q}_{x,\theta}; \quad \mathbf{R}_{\gamma_{33}} = \mathbf{Q}_{z,-\phi} \mathbf{Q}_{x,-\theta}$ $s_{ji} = \ \mathbf{s}_{ji}\ \quad (j, i) \in \{(0,0), (1,1), (2,2), (3,3)\}$ $\chi_{e_{ji}} = \cos^{-1} \left(\frac{[0,1,0]^T \cdot \mathbf{s}_{ji}}{s_{ji}} \right) \quad (j, i) \in \{(0,0), (1,1), (2,2), (3,3)\}$ $\chi_{d_{ji}} = \cos^{-1} \left(\frac{\mathbf{R}_{\gamma_{ji}} [0,-1,0]^T \cdot \mathbf{s}_{ji}}{s_{ji}} \right) \quad (j, i) \in \{(0,0), (1,1), (2,2), (3,3)\}$ <p>The general solution to the system of equations is:</p> $\phi = h_{\phi}(v_{d_{00}}, v_{d_{11}}, v_{d_{22}}, v_{d_{33}})$ $\theta = h_{\theta}(v_{d_{00}}, v_{d_{11}}, v_{d_{22}}, v_{d_{33}})$
--

Table 5.3: Summary of the system of equations describing the kinematic variables ϕ and θ as measured by the multiple emitter-detector pairs scheme in figure 5.5.

5.3 Theoretical Results

The system of equations describing the cylindrical and universal joints are functions only of two independent variables (d and ψ for the cylindrical joint and ϕ and θ for the universal joint). Thus only two equations are required in both cases to solve the problem. The question can be asked why a decision was made to design a goniometer-node that appears to be mathematically over-determined (i.e. there is more equations than unknowns)?

The answer is found by examining the theoretical responses as predicted by the system of (transmission) equations. Figure 5.6a shows the six emitter-detector pairs transfer functions of the cylindrical joint. The non-linear response as predicted by the inverse square law is clearly illustrated in the figure. For a specific pair, the greater the distance between the emitter and detectors, the less sensitive the device becomes to any changes in input. This decline in sensitivity is the primary reason why six instead of two emitter-detector pairs are used.

The universal joint transfer functions of the four emitter-detector pairs are shown in figure 5.7. Figures 5.7a and b show the individual transfer functions of the four emitter-detector pairs. It is clear that an emitter-detector pair and its opposing pair has complementary responses. It therefore makes sense to subtract the complementary response, i.e.:

$$v_a = v_{d_{00}} - v_{d_{11}} \quad \text{equ 5.25}$$

and

$$v_b = v_{d_{22}} - v_{d_{33}} \quad \text{equ 5.26}$$

The results are displayed in figures 5.7c and d respectively.

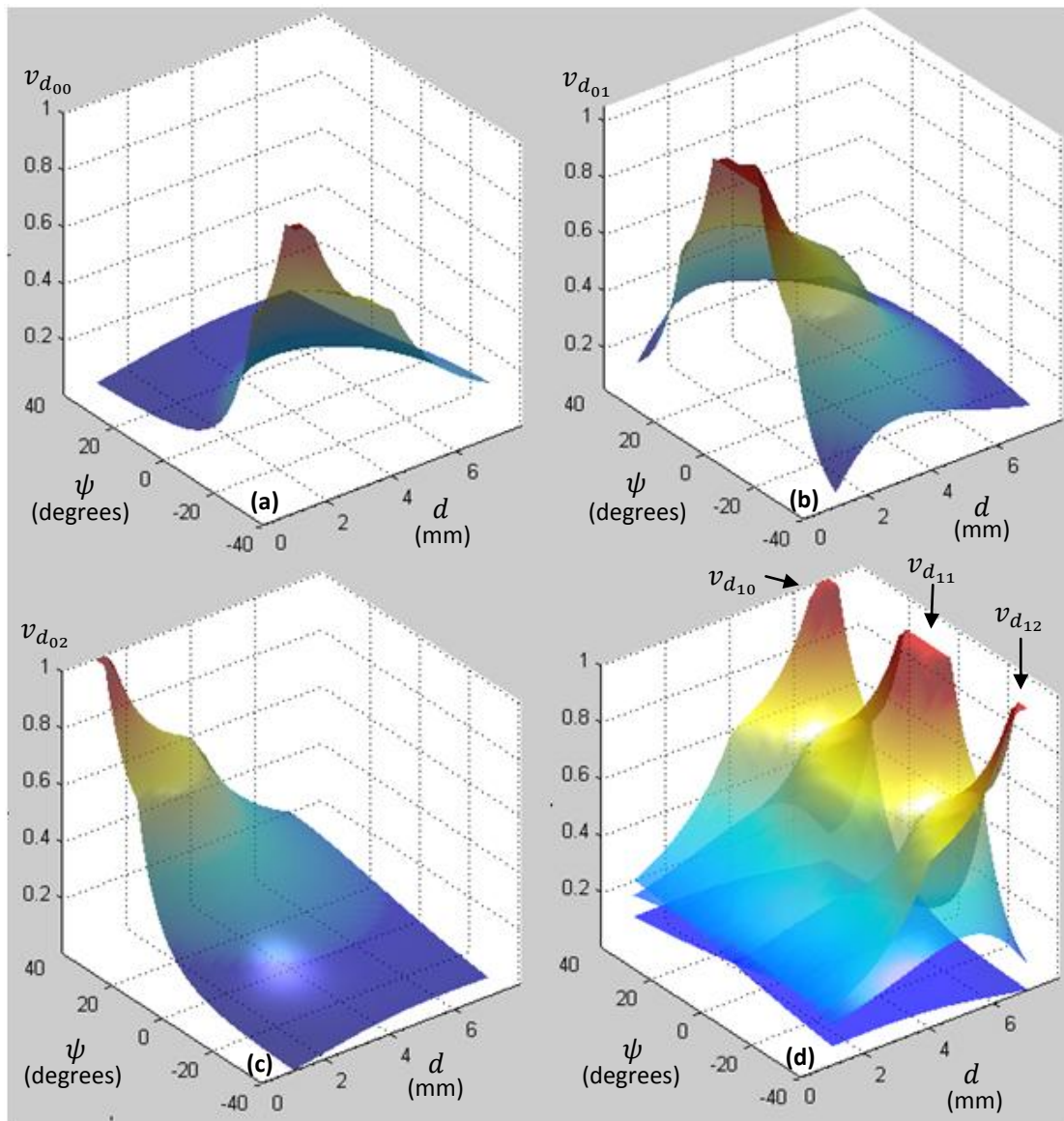


Figure 5.6: Transfer function of the six detectors in the cylindrical joint. The system parameters are: $l_0 = 4\text{mm}$, $l_1 = 4.6\text{mm}$, $f_e(\chi_e) = \cos\chi_e$, $f_d(\chi_d) = \cos\chi_d$. Transfer function of the four universal joint detectors with system parameters $l_0 = 1\text{mm}$, $l_1 = 5.5\text{mm}$, $l_2 = 4.5\text{mm}$, $l_3 = 3.15\text{mm}$, $f_e(\chi_e) = \cos\chi_e$, $f_d(\chi_d) = \cos\chi_d$. a) $v_{d_{00}}$; b) $v_{d_{01}}$; c) $v_{d_{02}}$; d) $v_{d_{10}}$, $v_{d_{11}}$ and $v_{d_{12}}$.

When compared to that of the cylindrical joint, the non-linear nature of the transfer functions is not so evident for the universal joint. The primary reasons are the joint design (i.e. the allowed relative motion of the emitters relative to the detectors) and the joint range which is relatively small compared to that of the cylindrical joint. The responses, v_a

and v_a , have also been largely linearised by subtracting the complementary signals as is evident in figures 5.7c and d.

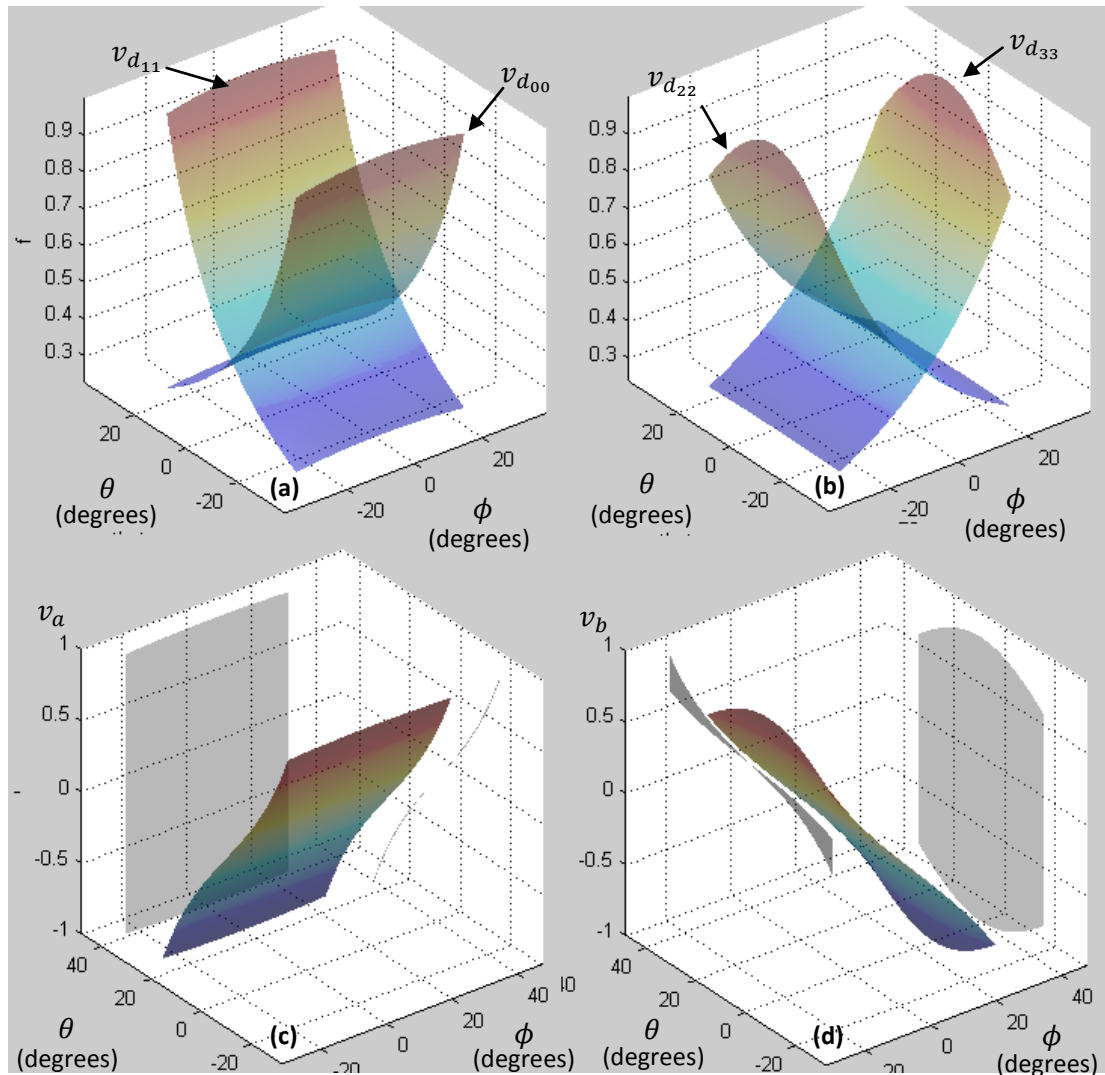


Figure 5.7: Transfer functions of the cylindrical joint. The system parameters are: $l_0 = 1\text{mm}$, $l_1 = 5.5\text{mm}$, $l_2 = 4.5\text{mm}$, $l_3 = -3.15\text{mm}$, $f_e(\chi_e) = \cos\chi_e$, $f_d(\chi_d) = \cos\chi_d$. a) v_{d00} and v_{d11} ; b) v_{d22} and v_{d33} ; c) $v_a = v_{d00} - v_{d11}$; d) $v_b = v_{d22} - v_{d33}$.

5.4 Model Validity and Curve-Fitting

The system of equations defined in tables 5.2 and 5.3 are considered to describe a parametric model. The model has parameters α_0 , l_0 , l_1 , l_2 , l_3 , f_e , f_d and k_R and the

detector transfer functions are determined by applying the inputs (d , ψ , ϕ and θ) to the model.

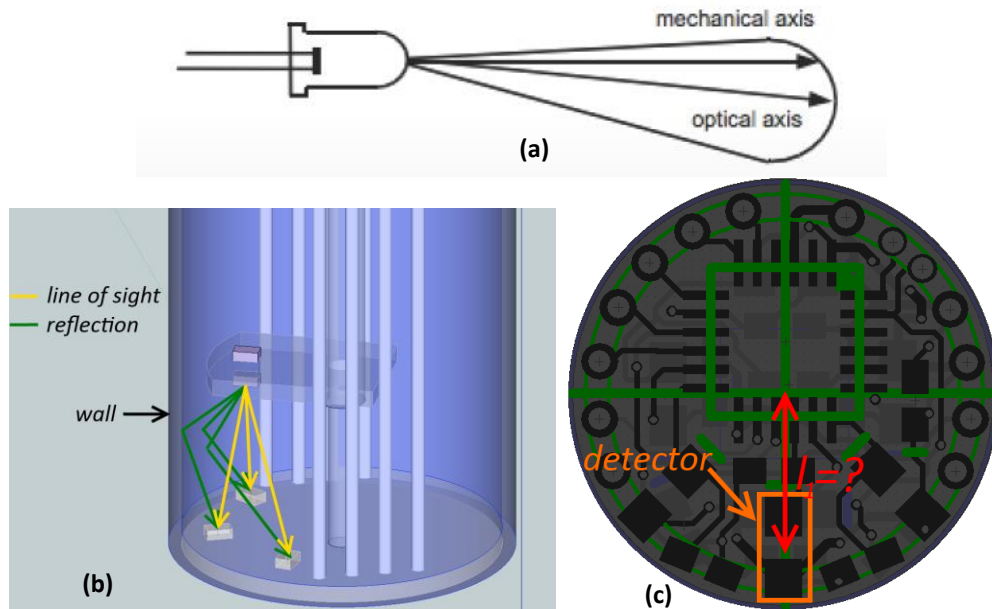


Figure 5.7: Issues affecting the accuracy of the model: a) Optical and mechanical axis of emitters and detectors are not aligned; b) Multipath reflections will cause unpredictable detector signals; c) Location of optical components may differ from model parameters.

There are however a number of issues that may affect the model that have not been factored in. The analysis up to now has assumed ideal emitters and detectors. Yet, practical emitter and detector parameters, especially low cost ones, vary between components. Comprehensive parameter statistics are normally not available but only average values are stated by manufacturers instead (see for example the datasheets included in Appendix B).

One particular concern is that of the mechanical and optical axes not necessarily aligned (illustrated in figure 5.7a) (Konica Minolta, 2014). The alignment varies from component to component and is dependent on manufacturing tolerances. The non-alignment affects f_e and f_d and has a direct consequence on the predictive ability of the model.

Another notable concern is that of multipath propagation. Multipath is the result of the detector receiving signals from the same emitter via more than one path as shown in figure 5.7b. Multipath is however a well understood concept and can be modelled mathematically (Fuchs, 2010).

The final factor affecting the validity of the parametric model is that of the hardware assembly. As the goniometer-node has a small and compact form factor, the accurate placement of the components (as defined by the parameters α_0 , l_0 , l_1 , l_2 and l_3) is crucial. Modern automated assembly systems have a typical tolerance of $100\ \mu\text{m}$ (Khandpur, 2005). Although small, if $l_1 = 4\text{mm}$ (see figure 5.7c), then $100\ \mu\text{m}$ is 2.5% of the length, which will have a significant effect on the accuracy of the device.

Based upon the above arguments, the parametric model as described by the idealised transmission equation may be too simplistic to provide a goniometer-node with a sufficiently accurate performance. The system of equations were however solved by Heo et al. (2011) (discussed earlier) to determine the location and orientation of a handheld device relative to a computer monitor (figure 5.1). As stated earlier, they reported a 1.71% and 2.9° error for location and orientations respectively under dynamic testing conditions. The location error is within the specifications (2.2%) but the rotation error is larger than 2° stated in table 3.1. Since the errors are related to local reference frame measurements, they will propagate through the kinematic chain, resulting in poor global reference frame measurements. Two alternative solutions are consequently explored.

The first option is to augment the model complexity to incorporate phenomena like multipath artifacts and poor axis alignment. A further refinement is to assume the model parameters, as stated by the manufacturers' datasheets are inaccurate. Instead the parameters are derived through calibration. This typically requires a set of known kinematic input data and detector output measurements to be generated and then the model parameters adjusted until the data fit the model within reasonable limits. This procedure is generally referred to as model fitting (Fox, 2012). A more complex model is certainly possible but may still be lacking since not all phenomena affecting the model may be accounted for.

5.5 Non-Parametric Model

The second option is not to assume a specific model but to apply a general model instead (for example a neural network or polynomial fit). Such an approach has the disadvantage

that it requires a huge dataset to determine/train the model coefficients. Typically as the number of parameters increase, the amount of data required increases exponentially (a problem commonly referred to as the "curse of dimensionality" (Bishop, 1995)).

The advantage of a non-parametric model is that there is no need to solve a system of equations. Instead the kinematic variables are determined directly from the detector voltages, or stated differently, the detector voltages are mapped through functions so that for the cylindrical joint:

$$d = h_d(v_{d_{00}}, v_{d_{01}}, v_{d_{02}}, v_{d_{10}}, v_{d_{11}}, v_{d_{02}}) \quad \text{equ 5.27}$$

$$\psi = h_\psi(v_{d_{00}}, v_{d_{01}}, v_{d_{02}}, v_{d_{10}}, v_{d_{11}}, v_{d_{02}}) \quad \text{equ 5.28}$$

Here h_d and h_ψ are the mapping functions as determined by a polynomial fit. A similar mapping is applied to the universal joint. The detector voltages map to the kinematic variables through h_ϕ and h_θ , i.e.:

$$\phi = h_\phi(v_{d_{00}}, v_{d_{11}}, v_{d_{22}}, v_{d_{33}}) \quad \text{equ 5.29}$$

$$\theta = h_\theta(v_{d_{00}}, v_{d_{11}}, v_{d_{22}}, v_{d_{33}}) \quad \text{equ 5.30}$$

The latter (general model) approach has been opted for here because it is easy to implement (despite the amount of data required for the model fit). A polynomial function was selected as the model because the tools are readily available in Matlab. Chapter seven discusses the instrumentation required to produce the dataset for the model fitting procedure and chapter nine the application of the polynomial fit to map the detector signals to the kinematic variables.

The parametric model discussed earlier will thus not be used to establish the kinematic solution. It does however offer valuable insight to determine the transfer functions of the universal and cylindrical joints. In chapter ten the parametric model will be used as an analysis tool to identify the reasons for the poor sensitivity of the cylindrical joint.

5.6 Conclusion

The articulation (four DOF) of the discrete goniometer-nodes is sensed with internal sensors. Different technologies were investigated. A decision was made, based upon a comparative argument, to use optical sensors consisting of emitter-detector pairs - a method that has not extensively been used before to measure kinematics. Unlike other optical measurement methods (like Vicon systems and the Wii controller), this method thus not rely on imaging. The novelty of the electrogoniometer is in the manner in which the sensors have been integrated with the mechanical structure. Although there are many benefits to the optical sensors, one major disadvantage is the fact that measurements are made relative to a local reference frame. By implication, it requires the nodes to be measure kinematics accurately and precisely otherwise the measurement errors will propagate through the kinematic chain.

The sensor scheme consists of optical emitter-detector pairs strategically placed within the mechanical structure to sense the mechanical articulation. An equation was derived to show the spatial relationship between the emitter radiance and detector signal. It was shown that a single emitter-detector pair is not sufficient to sense multiple degrees-of-freedom. It was consequently suggested to use multiple pairs, thus establishing a system of equations to describe the kinematic problem in terms of the detector voltages. The sensing solution was applied separately to the cylindrical and universal joint constituting a goniometer-node, and a mathematical model was developed describing the measured voltages in terms of the kinematic input.

A number of practical issues were identified that may affect the accuracy of the model. The model can therefore not be applied as a parametric solution to determine the kinematics in terms of the measured detector voltages (i.e. by solving the inverse problem). The model can however predict the approximate response and is therefore useful as a development tool (i.e. to predict responses during the design phase prior to constructing the goniometer-nodes). Since the model accuracy was in question, no a priori assumption is made about the model. Instead, a non-parametric approach was opted for. The non-parametric model does not assume a specific model (i.e. requires no knowledge of the model discussed in section 5.2). Instead the range of kinematic variables are sampled and then the detector voltages

mapped to the kinematic variables through a non-parametric model (a polynomial function in this case). The instrument for doing so is discussed in chapter seven.

6.0 Design Realisation

The design realisation discusses the implementation of the electro-mechanical design and the practical issues associated with this task. The goniometer-node is the building blocks of the electrogoniometer. Proper construction of the nodes are therefore crucial to the success of the electrogoniometer since any inaccuracies will affect its performance. A five-node (twenty degrees-of-freedom) device is constructed as a prototype. The mechanical components consist mainly of copper and silver tubing, 3D printed plastic enclosures, PCBs and miniature machine screws and nuts. The PCBs serve a dual function: as mechanical structure and electronic layout.

The conjoint goniometer-nodes are connected mechanically and electronically to a master controller. The entire electrogoniometer is enclosed with a silicone rubber skin. The skin protects the sensitive opto-electronics, yet is stretchable and durable enough not to hamper movement. The master-controller acts as a bridge between the goniometer-nodes and a personal computer (PC). The nodes are queried by the master-controller and the accumulated raw data periodically transmitted to the PC via a wireless adaptor. The PC applies the mathematical models discussed in chapter five, converting the raw data into useful kinematic information which is displayed in a near real-time 3D environment.

Eight different versions of the goniometer-nodes were designed and built. Initially the concepts and principles were tested using Lego structures. All three mechanical designs discussed in chapter four were then constructed and tested. Once the decision was made to select the universal-cylindrical joint design, a few more iterations were required to fix and/or improve the mechanical design.

6.1 Overview of the Development History

The development of the electrogoniometer underwent a few design iterations. First a test-bed was constructed to test the principles of sensing rotation and translation through optical means. Figure 6.1a shows a test device with an emitter-detector pair which can be

manipulated in two axes. The test device is manipulated manually and measurements read from a multimeter.

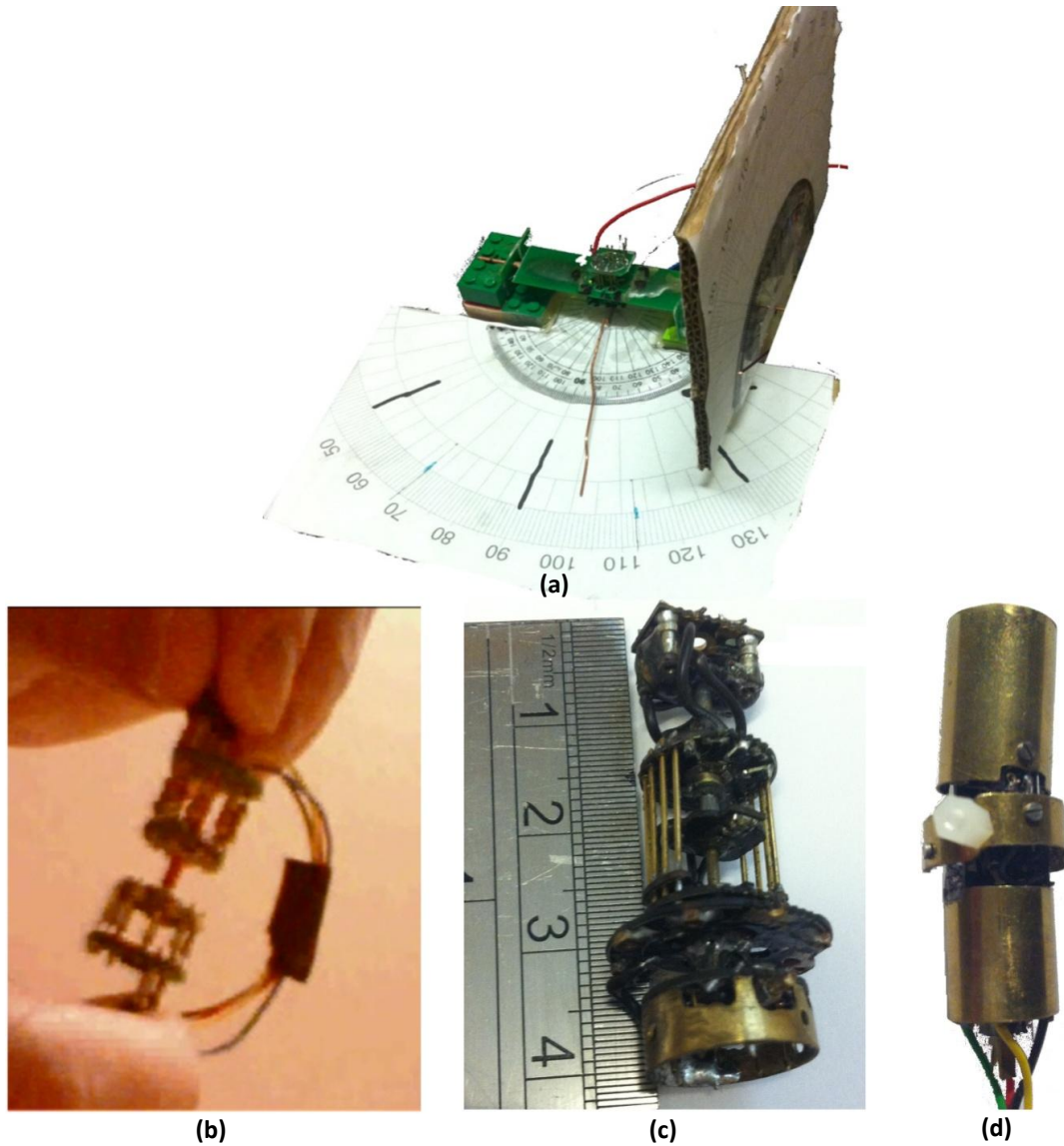


Figure 6.1: Evolution of the goniometer-node design: a) Experimental setup to test the concepts and principles of kinematic measurements through optical sensing; Goniometer-nodes based upon b) spherical-prismatic; c) universal-cylindrical and d) universal-revolute-prismatic joint designs.

The three different goniometer-node designs proposed in chapter four (figure 4.1) were constructed as illustrated in figures 6.1b-d. As discussed in chapter four, the universal-cylindrical joint was the preferred design.

In total eight nodes were designed and built. A single version of the spherical-prismatic and two versions of the universal-revolute-prismatic joint designs were constructed. Once the

universal-cylindrical joint has been identified as the preferential design, another four versions of this design were constructed. Each iteration fixed most manufacturing issues identified during the previous version.

Initially the PCBs were self assembled but to save time, the last version was assembled by the PCB manufacturer. The design, manufacturing and testing of a single version took about three to four weeks and cost around £300 when self assembled and £650 when assembled by the PCB manufacturer.

The biggest manufacturing challenge was the construction of the mechanical parts. A desktop 3D printer greatly help to quickly prototype parts. Unfortunately not all the mechanical part could be manufactured from plastic, and even if they could, the printer's printing tolerances (about 0.1 mm) was not sufficient to allow this. Parts not suitable for printing were manufactured from material typically available from hobby shops and jewelers. Since the parts are small and made by hand, some mechanical errors were inadvertently introduced.

One issue has not yet been satisfactory resolved: the wires running centrally through the electrogoniometer. The wires supply power and communication. Originally eight goniometer-nodes were manufactured but three failed when the wires broke due to metal fatigue during the calibration procedure (discussed in chapter seven). The mating of the nodes were also problematic. It was difficult to rigidly connect the nodes so that they are accurately aligned along the translation axis. The calibration procedure discussed in chapter eight (section 8.3) however helps to remove misalignment errors.

The software was another significant undertaking. Developed in C and C#, it essentially consists of communication and data acquisition protocols. It runs on the embedded hardware and PC, and allows control of the hardware (e.g. setting the sample rate) and data to be acquired through a set of commands.

6.2 The Goniometer-Node

The node implementation is separated into electronic and mechanical assemblies. The electronics is further divided into the hardware and the firmware which runs on an eight-bit microcontroller.

6.2.1 Electronic Implementation

The goniometer-node contains an eight-bit microcontroller (part number: MC9S08SH8CFK, Freescale) which controls and measures a total of six emitters and ten detectors. The primary reasons for selecting this particular microcontroller is its small size (4 x 4 x 1mm), it has twelve analog-to-digital converters and a serial communication interface (SCI) onboard. The microcontroller does not have the processing power to process the data locally, hence the raw data is processed by the PC.

A basic diagram illustrating the setup is shown in figure 6.2. (The schematic and datasheets of the primary components are included in appendix B.) The node does not directly initiate the sampling process. Instead it is under the control of the master-controller.

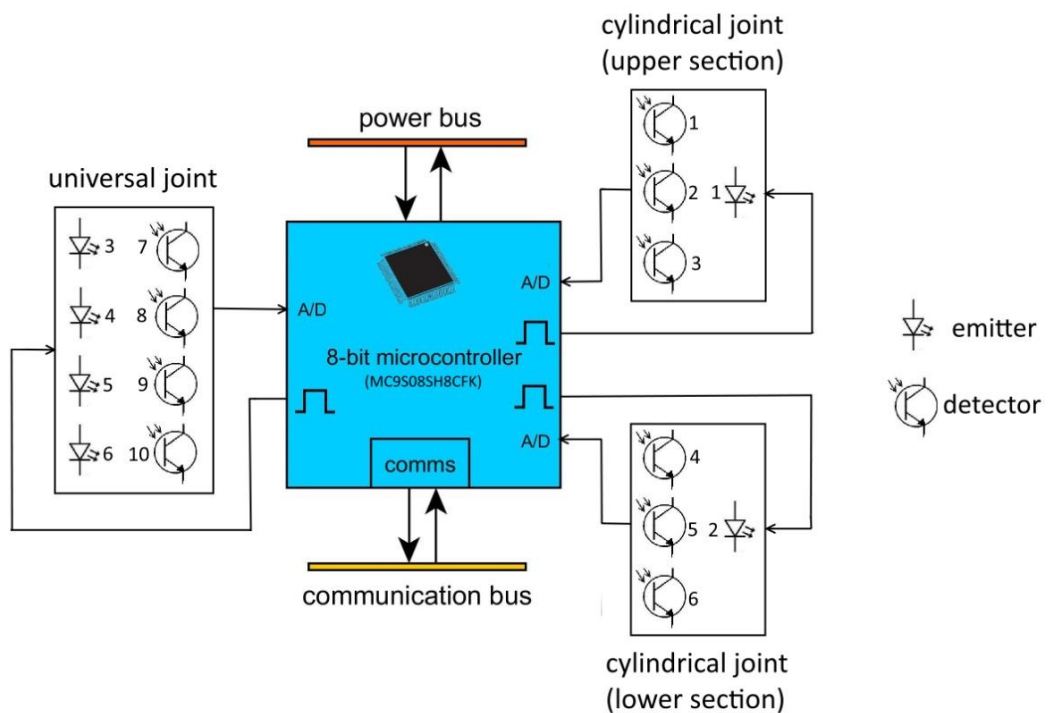


Figure 6.2: The electronic components of a goniometer-node (the full schematic is in appendix B.3).

The slave sampling process is illustrated in figure 6.3. Each slave-node is assigned an unique ID. The master-controller broadcasts an universal command to all the slave nodes, requesting a single ensemble of samples to be taken. Once the command is decoded by the slave nodes, the emitters are switched on and the detectors sampled. The data is then formatted into a packet as shown in figure 6.4. The master-controller then sequentially requests the samples from each node (discussed in more detail section 6.3).

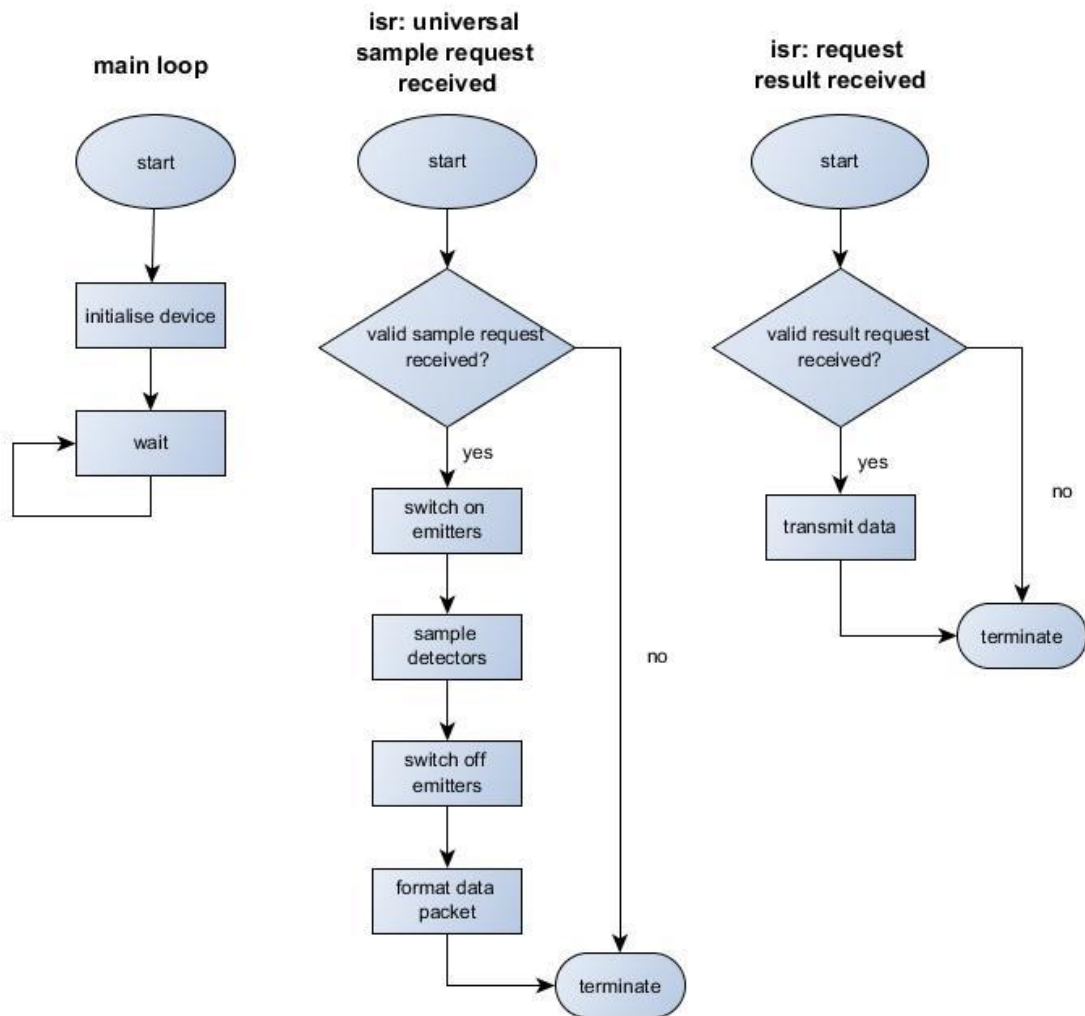


Figure 6.3: Flow diagram illustrating the processes involved to acquire raw detector data and transmit it to the master-controller.

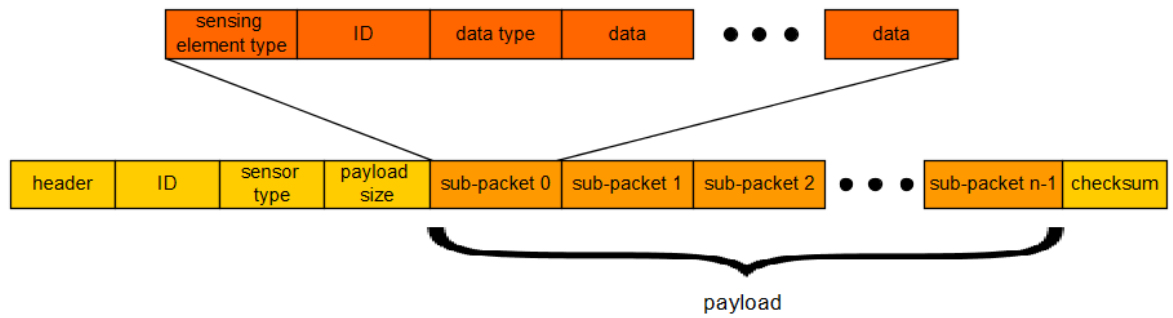


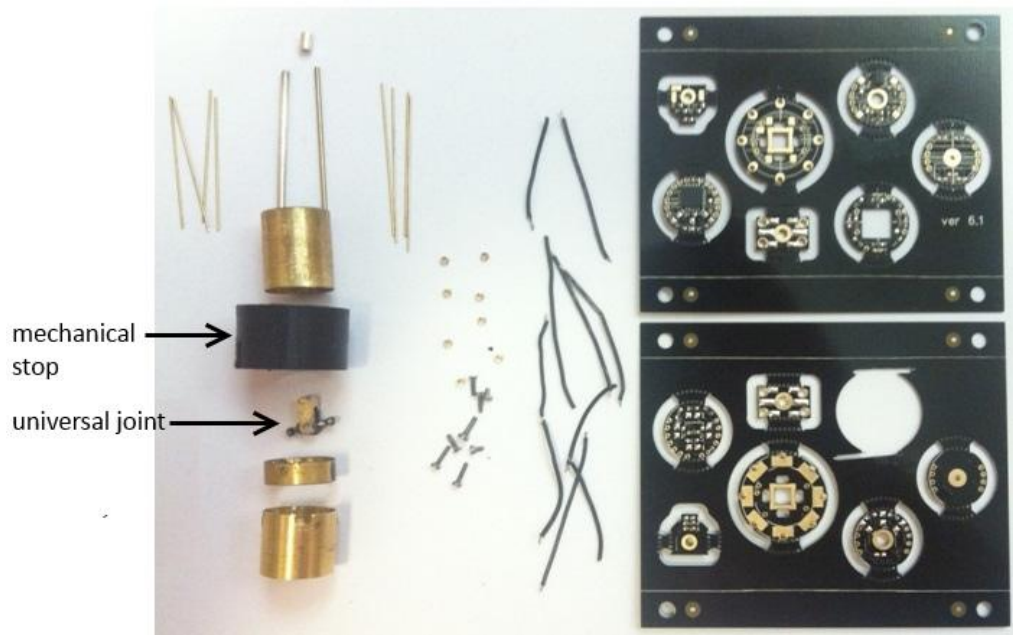
Figure 6.4: Description of the packet carrying data payload.

6.2.2 Mechanical Assembly

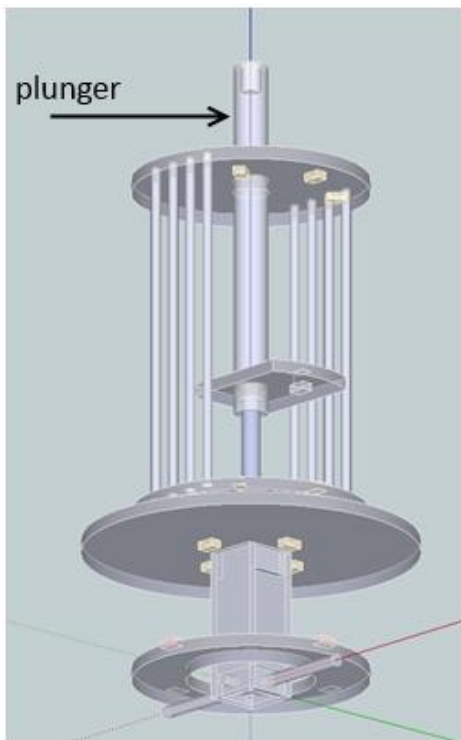
A goniometer-node consists of numerous mechanical components as shown in figure 6.5a. The brass tubing encloses the device and prevents external interference with the optoelectronics (e.g. external light sources). The most complex of the mechanical components is the universal joint which was manufactured by hand (labeled "universal joint" in figure 6.5a).

Wiring interconnects electronic components through moving mechanical parts. The wiring presented a particular challenge. Copper is susceptible to metal fatigue when constantly bent and twisted (Frost et al., 1999). A special 29 gauge 51 strand wire with a very flexible silicone insulation was obtained from NWSL (Hamilton, Montana, USA). Although the wiring was specifically developed for these types of applications, metal fatigue still remains a problem. Wiring containing other metals and alloys were also investigated but proved inadequate.

An assembled goniometer-node is shown in figure 6.5c and its original design in figure 6.5b. The node has a four-pin socket (two for power and two for communications) which mates with the plug of the adjacent node. The socket is rigidly connected to the plunger which allows for rotation and translation.



(a)



(b)



(c)

Figure 6.5: Realisation of the goniometer-node: a) Mechanical and electronic components; b) Design; c) Implementation.

6.3 Master-Controller and Slave Chaining

The custom master-controller is designed and built around a powerful 32-bit microcontroller (MCF51CN128CLH, Freescale). This particular microcontroller is much faster than the 8-bit controllers used for the goniometer-nodes. More importantly, it has enough memory (24 kB RAM) to buffer the received data and then asynchronously transmit it via a separate buffer after it has been formatted into packages. It further controls the slave-nodes and acts as a data gateway between the nodes and PC via a Bluetooth interface. Figure 6.6 shows the physical setup. The nodes, each with an unique ID, are attached via a communication bus to the master-controller.

The master-controller runs two asynchronous tasks as illustrated by the flow diagrams in figure 6.7. The first task is to acquire the raw data from the slave-nodes. It is accomplished by broadcasting a *universal sample request* command over the communication network. All slave nodes receiving the command then sample the detectors and format the sample ensemble into a package. The master-controller then sequentially requests the data from each node via a *request results* command. All communications is thus initiated by the master-controller, preventing any communication clashes on the network.

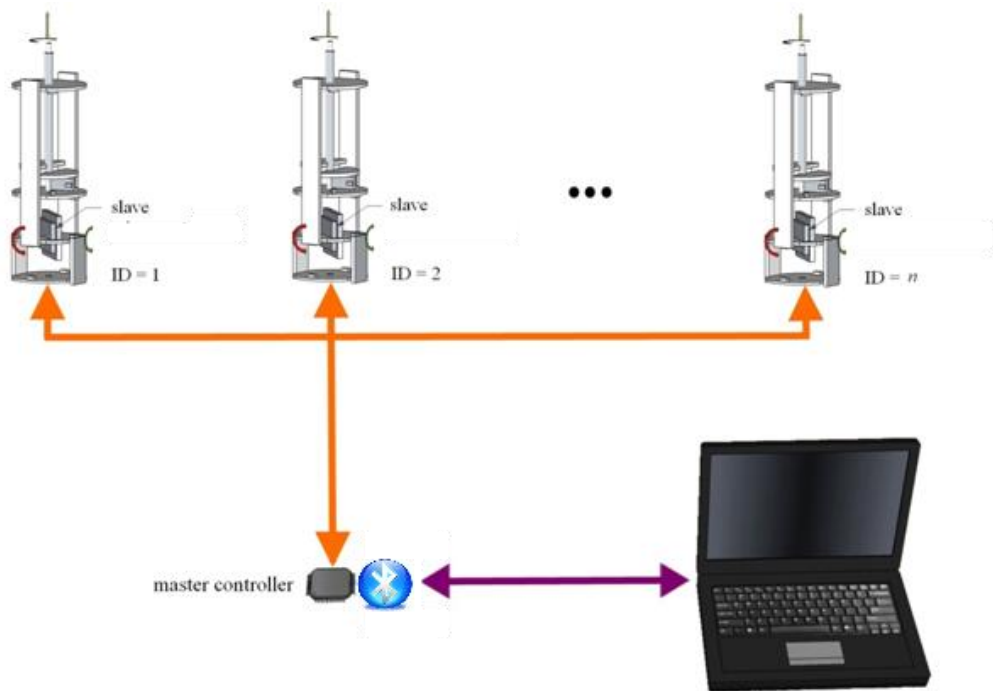


Figure 6.6: Electronic chaining of the master-slaves setup.

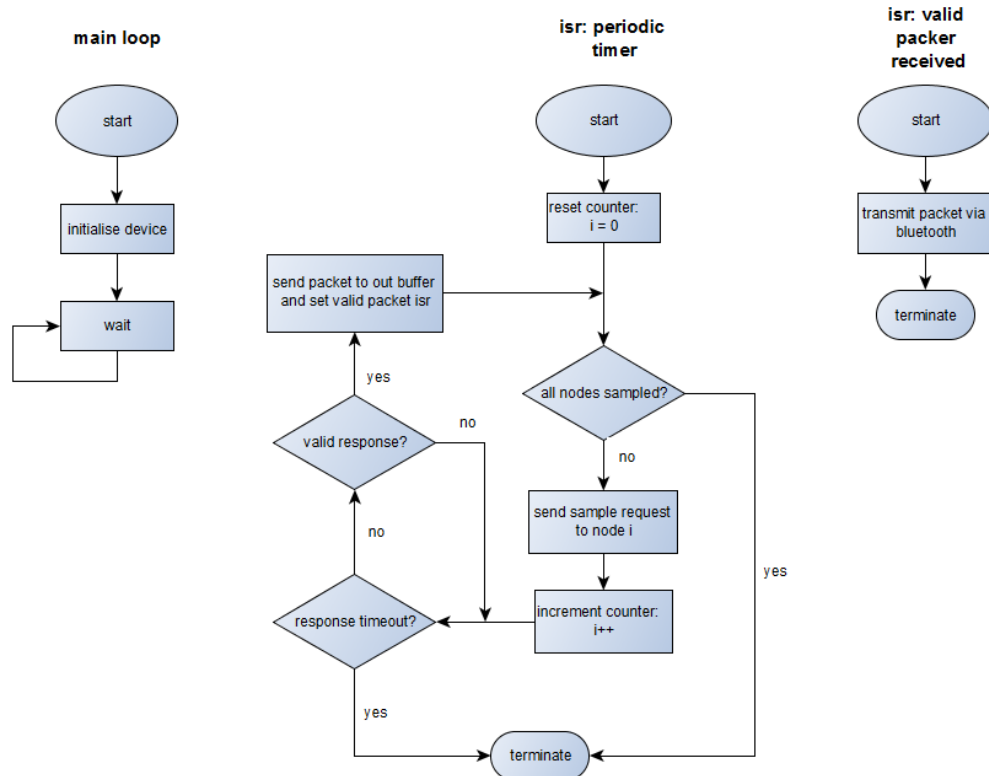


Figure 6.7: Flow diagram illustrating the control the master-controller exercise over the slave-nodes.

When the master-controller receives a data package, a second task is initiated via a interrupt service routine. The second task is responsible for forwarding the packet to the PC via the Bluetooth interface. The sampling process task is repeated until all the nodes has been serviced at which time the task is terminated until the timer expires again.

6.4 The Assembled Device

The electrogoniometer, consisting of five linked goniometer-nodes and a master controller, is shown in figure 6.8. Attached to each node is a threaded post. The post allows a nut to be rigidly connected to the node, which in turn serves as an attachment location for reflective markers. The device, as displayed in figure 6.8, is difficult to attach to a subject. Some of the optics are also exposed to the environment (i.e. susceptible to light or other interference).

To protect the device, it is enclosed with a silicone rubber (Ecoflex® 0030 and made by Smooth-On) as demonstrated in figures 6.9a and 6.9b. The rubber is extremely flexible and will retain its original form even when continuously undergoing stretch cycles. Flanges are attached to the main skin structure to provide enough surface area to attach the device to the back (see figure 6.9b). To ensure proper contact with human skin, a tacky silicone rubber is substrated on the flanges and acts as a "glue" between the silicone skin and human skin. The tacky substance is made from the same silicone rubber but also includes an additive (Slacker®) which "tackifies" the rubber.

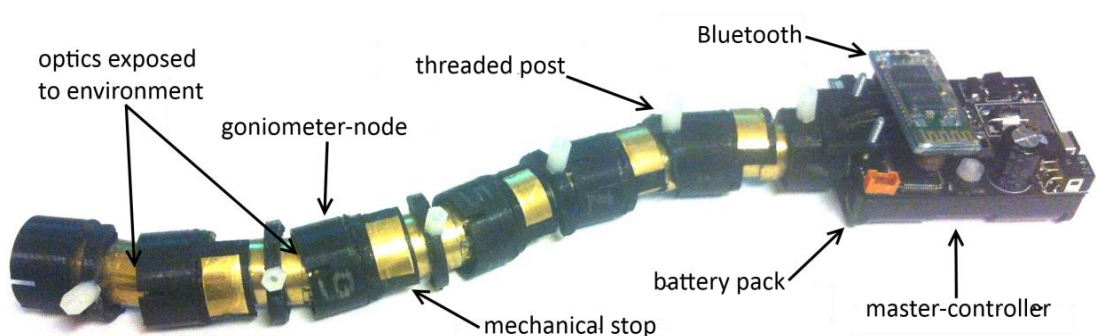


Figure 6.8: The electrogoniometer without a silicone skin.

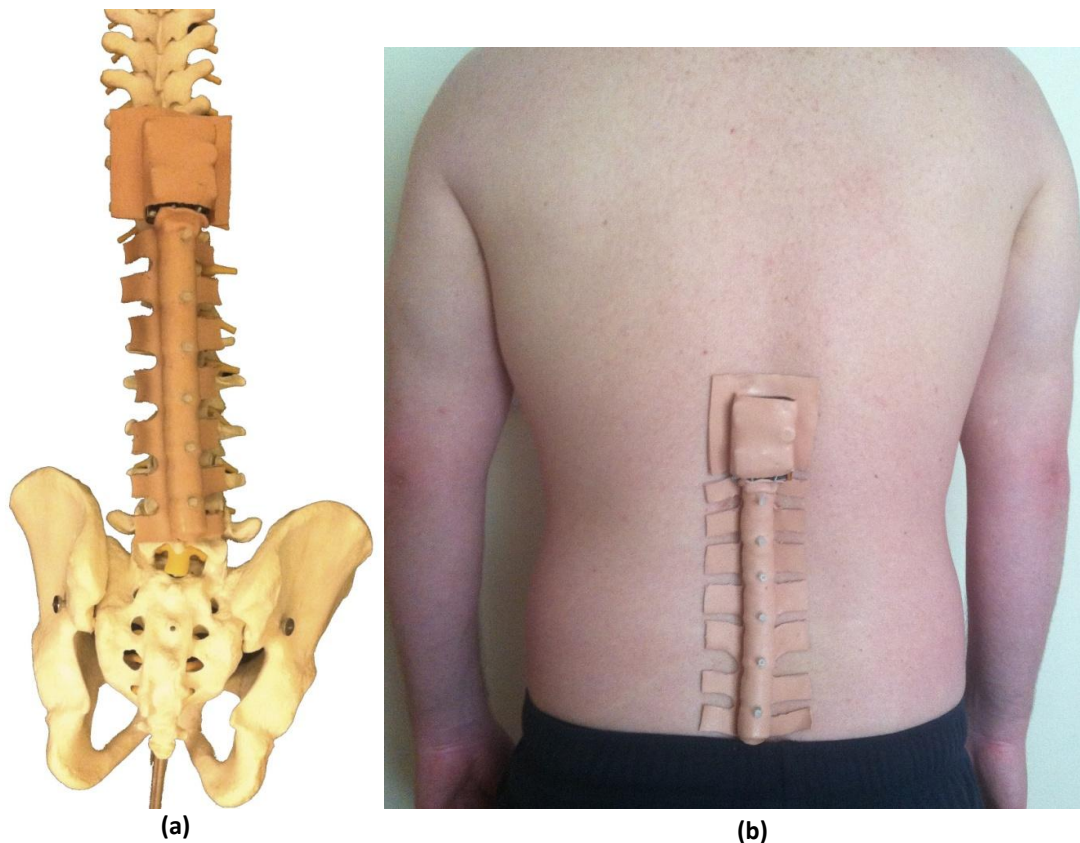


Figure 6.9: a) The electrogoniometer in relation to the spinal column; b) The electrogoniometer attached to the back.

6.5 Remote Processing

The prototype developed here does not process the raw sensor data on the device. The node microcontrollers are not powerful enough to handle the processing requirements. Instead the data is offloaded to a PC which handles the main workload as illustrated in figure 6.10. The PC application, developed in XNA, is divided into three asynchronous processes. The first reads the serial buffer and extracts the packets within the serial stream. The packets are stored in a linked list structure awaiting further processing. The next process reads all the packets in the buffer, decodes them (i.e. extracts the data) and then fits the data to the polynomial functions to obtain the desired kinematic data. The data is again stored in a dynamic list. The final process takes only the most current kinematic results and render the 3D graphics accordingly. Not every sample is therefore rendered in

the 3D environment as this is a computationally intensive process and will drastically slow the refresh rate. A screenshot of the 3D rendering is shown in figure 6.11.

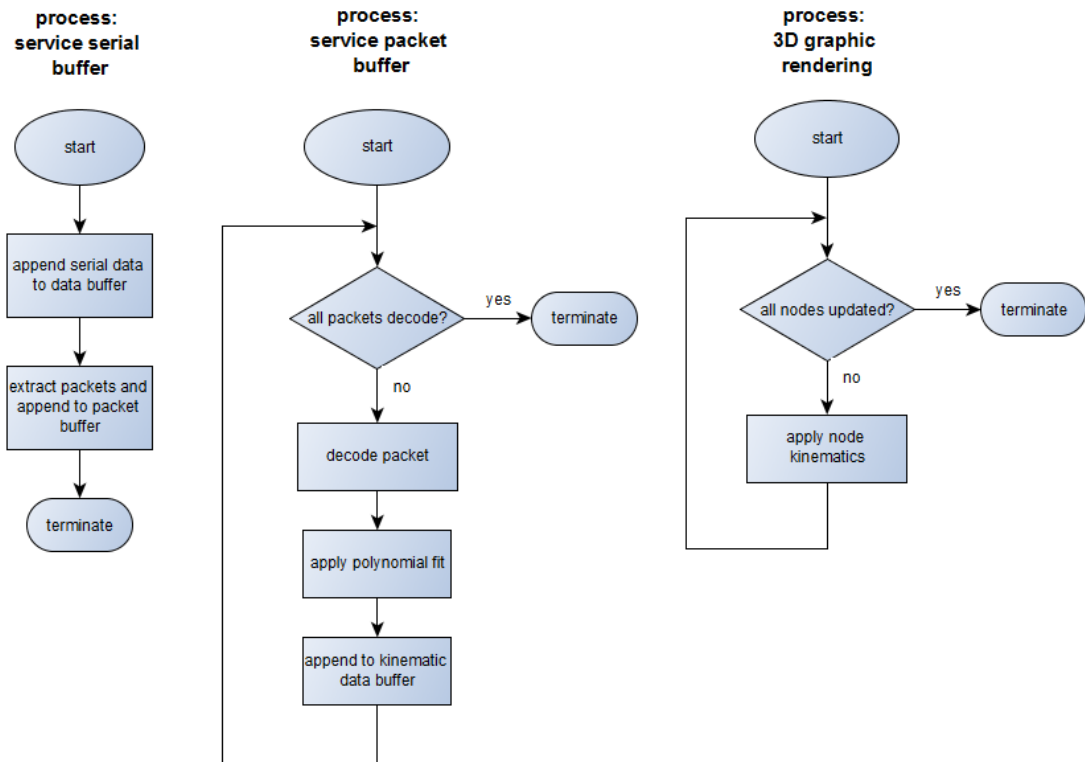


Figure 6.10: Flow diagram of the different processes running on the PC.

If the device is commercialised, processing will most likely be done at the nodes or at the very least the master-controller. In such an event, the processing load will be distributed across an array of processors, thus significantly reducing the PC's processing load. The amount of data transferred between the electrogoniometer and the PC will also be reduced drastically since the kinematics can be represented in a compact format (e.g. as a quaternion plus a single translation component).

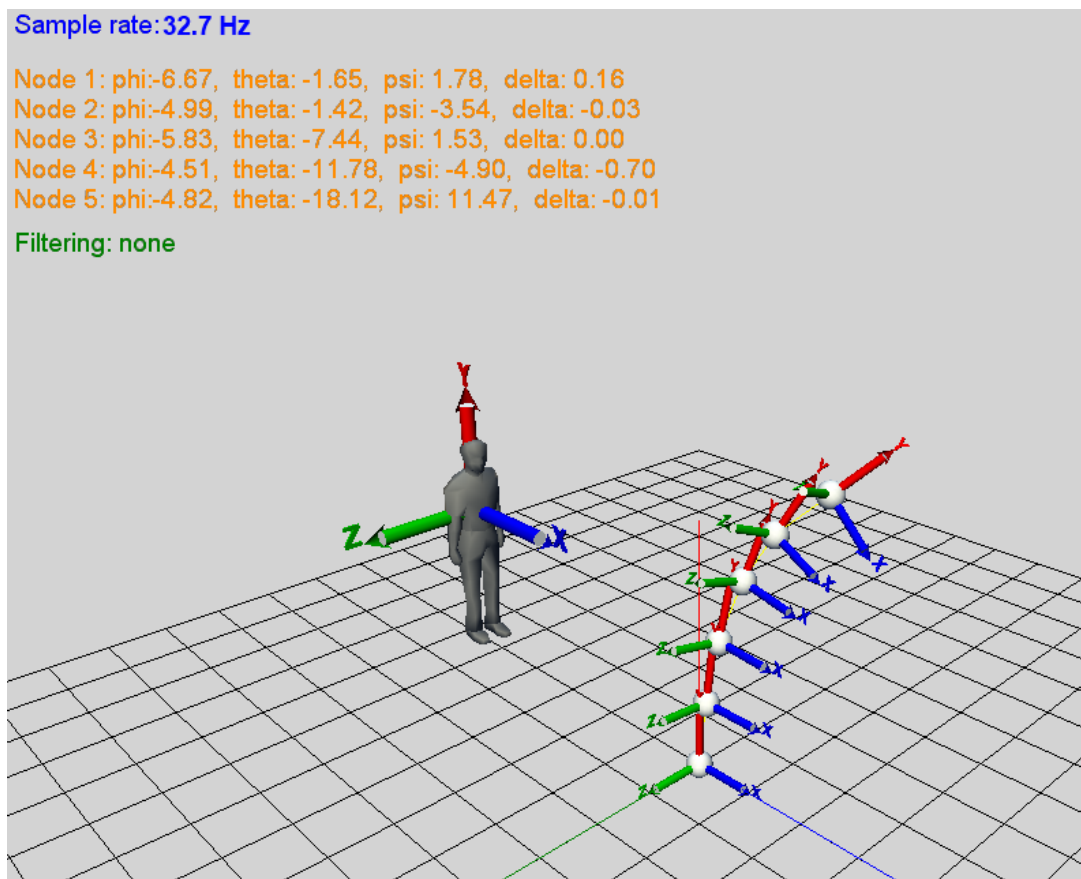


Figure 6.11: The 3D rendering of the electrogoniometer data in a virtual environment.

6.6 Conclusion

A prototype electrogoniometer consisting of five goniometer-nodes was constructed. The nodes were chained mechanically together thus creating a twenty DOF chain. The device was enclosed in a stretchable silicone skin, allowing the device to be manipulated almost like a piece of rubber cord.

The nodes were connected electronically through a local area network. Collectively they were attached to a master-controller, which periodically request samples from the nodes through a custom command and communication protocol. The data is then forwarded wirelessly from the master-controller to a computer, which applies the appropriate algorithms to determine the node kinematics. The kinematics are then rendered in a 3D graphics environment.

7.0 Calibration and Test Instrument

Any measurement instrument requires to be calibrated against a known standard. Calibration presents a challenge for the electrogoniometer (in particular the goniometer-nodes), since the device is custom-made and a calibration instrument therefore does not exist. A calibration instrument was consequently developed to meet the calibration needs. The new instrument itself will also require calibration. This requirement is however met by using, where possible, off-the-shelf components with known performance characteristics.

The instrument discussed here is the second calibration and test (CaT) instrument developed for this research project. The first instrument could measure four degree-of-freedom but was extremely slow. The mechanical components were also not durable enough and started to fail over time. A new instrument was subsequently developed which used more durable components and fast stepper motors. The instrument was also simplified at the expense of measuring one less rotational degree-of-freedom (i.e. the instrument can only measure two rotation axes and one translation). As will be shown later, the mechanical nature of the goniometer-node design lent itself to this simplification as the fourth degree-of-freedom can be determined through a simple mathematical calculation.

7.1 Design and Implementation

The key mechanical components of the CaT instrument are shown in figure 7.1a. The instrument is constructed mainly from acrylic sheet and plywood. A reference frame (shown in figure 7.1a) is attached to the instrument. The instrument and goniometer-node reference frames have to be aligned to ensure an accurate calibration. The instrument has two rotating axes about the y and z axes (with variables α and β assigned respectively) and a translation axis (with variable δ) in the y axis direction.

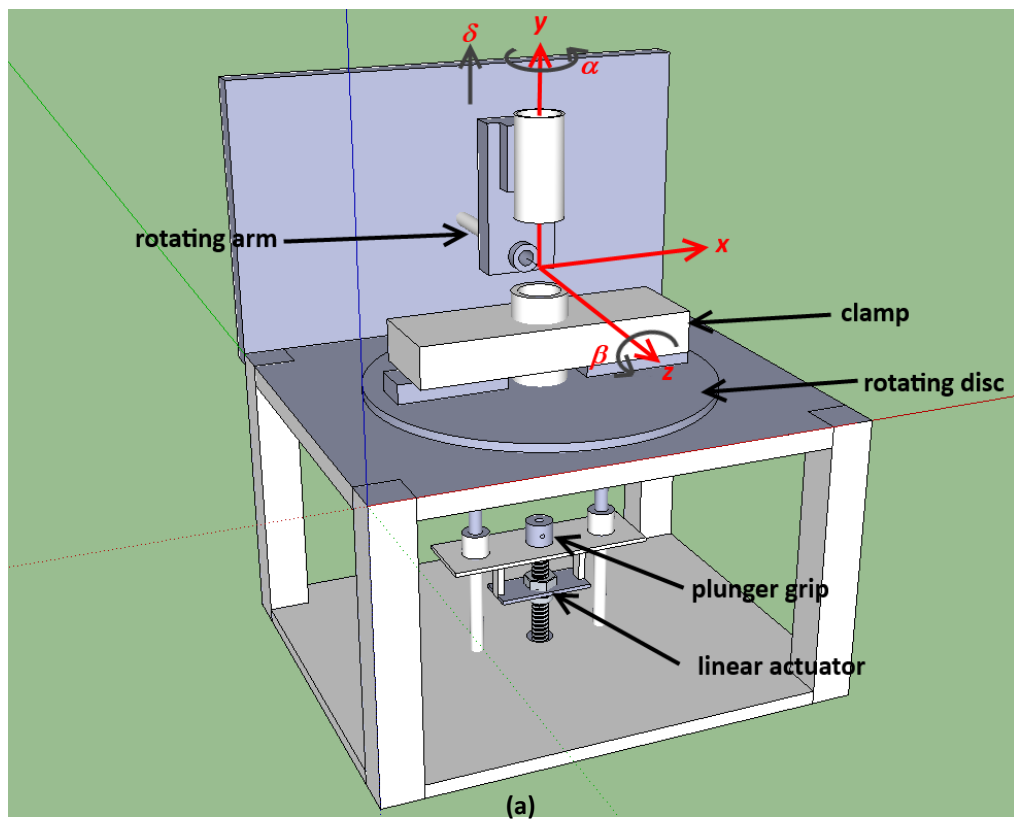
The goniometer-node is clamped into the rotating platform as shown in figure 7.1b. The node's universal joint (with kinematic variables ϕ and θ) is calibrated by controlling the α

and β axes. The relationship between the joint and instrument axes (derived in appendix A.2) is:

$$\phi = \sin^{-1}(-\sin\beta \sin\alpha) \quad \text{equ 7.1}$$

and

$$\theta = \cos^{-1}\left(\frac{\cos\beta}{\cos\phi}\right) \quad \text{equ 7.2}$$



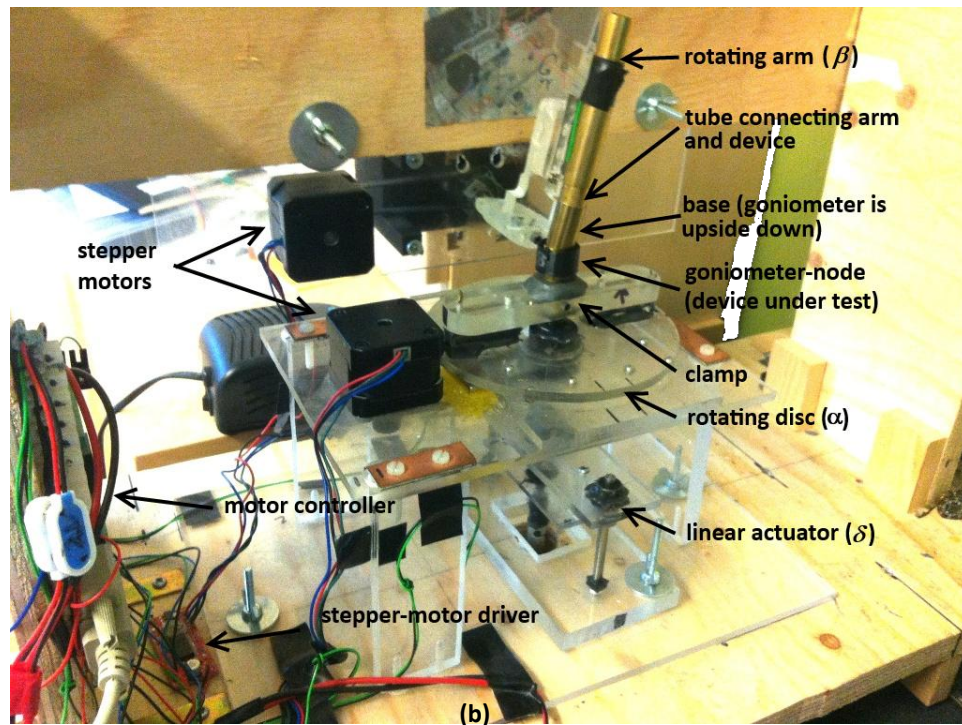


Figure 7.1: a) CAD design showing the primary components of the calibration and test instrument; b) Implementation of the design with supporting electronic hardware.

The cylindrical joint (kinematic variables ψ and d) is calibrated by manipulating the α and δ axes. A direct mapping exists between the variables, i.e.:

$$\psi = \alpha \quad \text{equ 7.3}$$

and

$$d = \delta \quad \text{equ 7.4}$$

The electronic hardware is illustrated in figure 7.2. The three axes are controlled by three stepper-motors (catalogue number: RS 535-0372, RS Components, Glasgow, United Kingdom) and allow rotations and the translation resolutions better than the goniometer-node requirements stated in table 3.1. According to the manufacturer each stepper motor has a 0.9° resolution and a 5% accuracy.

The motors are controlled by a stepper-motor controller (part number: KTA-190), manufactured by Ocean Controls (Victoria, Australia). The stepper-motors are driven by stepper-motor drivers (part number: EasyDriver, distributed by Sparkfun, Colorado, USA). The drivers are set for micro-step control of an eighth of the motor resolution (or 0.1125°).

Timing pulleys further increases the resolution of rotations to 0.0506°/step for the α axis and 0.0675°/step for the β axis. The position of the goniometer-node's plunger is controlled by a linear actuator. The resolution of the actuator is 4.02 $\mu\text{m}/\text{step}$.

A standard serial interface permits communication between a PC and the stepper-motor controller. The stepper-motor controller has a standard set of commands which is issued by the PC and allows for control and status checks of the motors.

	Property	Value	
Mechanical	Mobility	2 rotation, 1 translation	
Control	Motion control	stepper motors	
	Rotation range	α axis	0 to 360°
		β axis	-90 to 90°
	Rotation accuracy	5%/step	
	Rotation resolution	α axis	0.0506°/step
		β axis	0.0675°/step
	Translation range	0 to 15 mm	
	Translation resolution	4.02 $\mu\text{m}/\text{step}$	
	Motor controller	KTA-190 (4 channels)	
	Motor drivers	EasyDriver	
Communication method with PC	RS232		

Table 7.1: Summary of specifications of the calibration and test instrument.

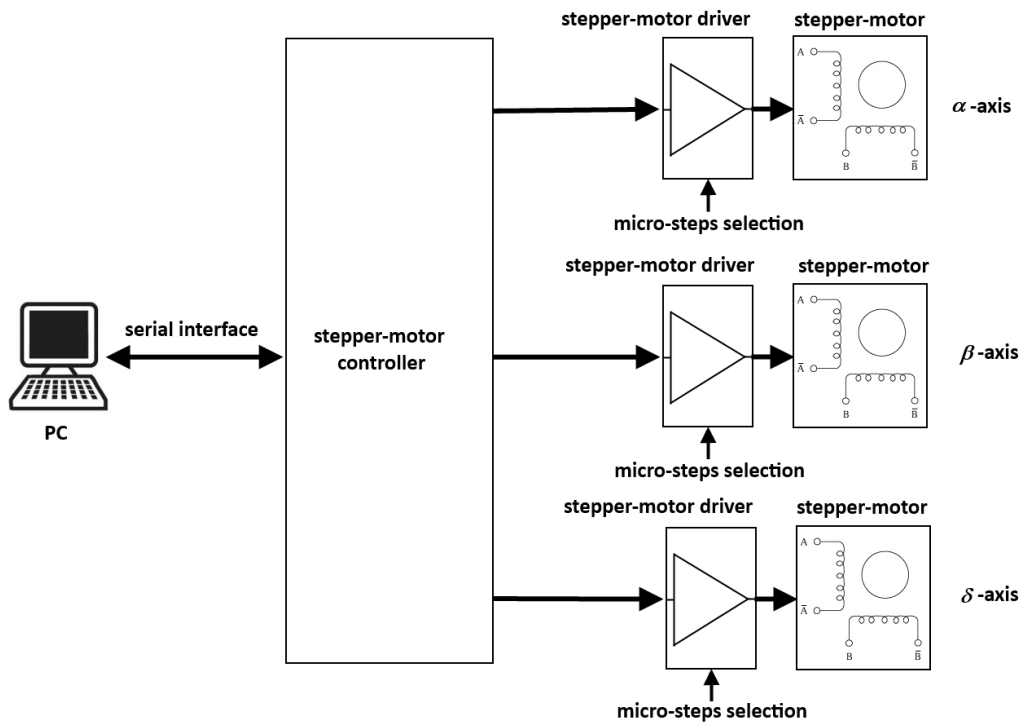


Figure 7.2: Open loop control of the stepper-motors.

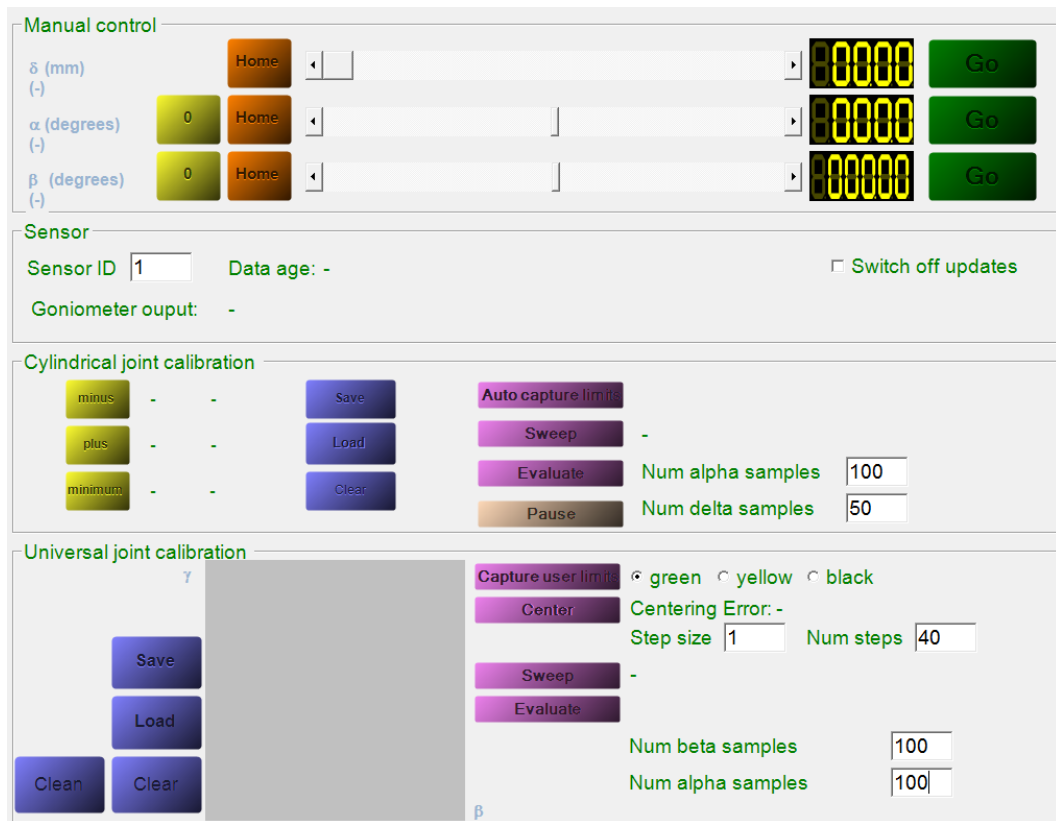


Figure 7.3: Graphical user interface of the calibration application.

7.2 Calibration Procedure

An application (figure 7.3.), written in Visual Studio and using C#, implements the calibration procedure. The application is responsible for controlling the instrument and offers user feedback via status request commands issued to the motor-controller via the serial interface. The procedure for the cylindrical joint calibration is as follow:

- The goniometer-node is inserted and clamped into the rotating platform.
- The plunger of the goniometer-node is then moved to the extremes (by rotating and translating it). The corresponding detector measurements are logged so that the instrument knows the calibration bounds. The plunger is then mechanically fastened with a grip screw.
- The user enters the number of samples to be taken when rotating and translating the axes, followed by clicking the calibrate button.

- By controlling the stepper motors, the application moves the plunger to the starting point.
- The independent variable space (α and δ) will then be systematically sampled based upon the number of sample points entered by the user. Before each sample is taken, the stepper motor is stopped momentarily so that any mechanical oscillations have time to settle. Each sample consisted of the kinematic variables and the associated detector measurements. The data is saved to disc by the user once the procedure is completed.

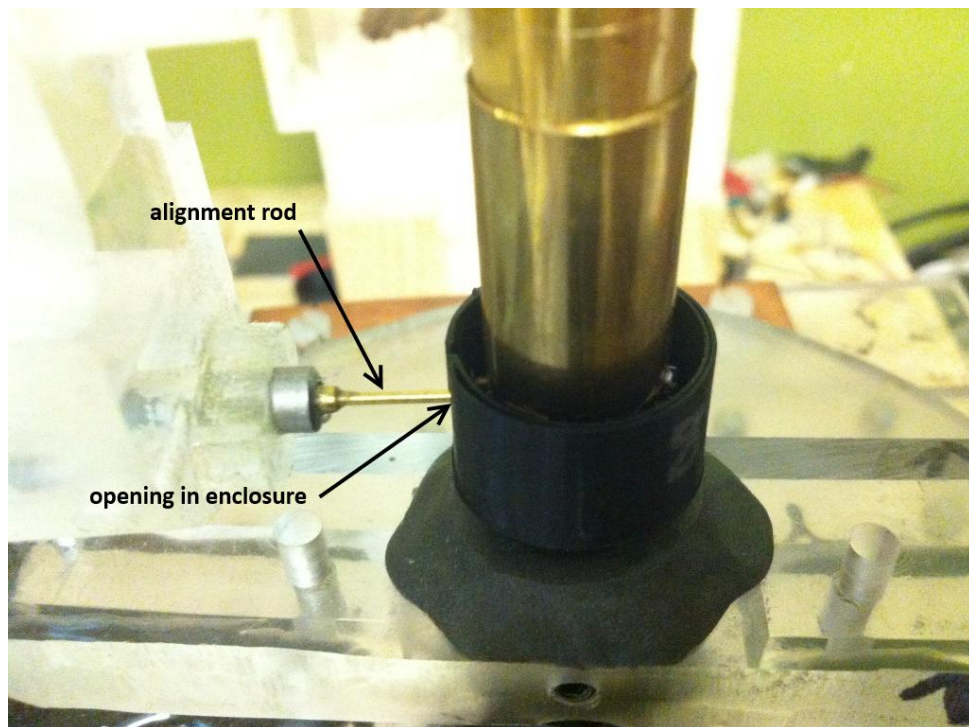


Figure 7.4: An alignment rod is used to initially align the ϕ axis of the goniometer-node with the β -axis of the calibration instrument.

The universal joint follows a very similar procedure:

- If the cylindrical joint was calibrated first, the grip screw attaching the plunger to the instrument is unscrewed. (The bounds of the rotating disc required to calibrate universal and cylindrical joints differs. If the screw is not released the node will be damaged internally.)
- The limits, as measured by the detectors, are then traced out manually by the user by moving the base of the goniometer-node along its boundaries.

- The calibration requires the ϕ -axis to be initially aligned with the β axis of the calibration instrument. This is accomplished by inserting an alignment rod through the (hollow) shaft of the pulley which rotates the arm as illustrated in figure 7.4. A small opening in the enclosure (not visible in the image) ensures the two axes are properly aligned. The rod is removed afterwards.
- A tube is inserted, rigidly connecting the instruments rotating arm to the base of the node (see figure 7.1b).
- The user enters the number of samples to be taken for both rotation axes and click the calibrate button.
- The universal joint is then systematically sampled within the boundaries traced out earlier. After each sample, equations 7.1 and 7.2 are applied to determine ϕ and θ from the current α and β values. As before, the data is logged to disc after the procedure has been completed.

The final process in the calibration procedure is to apply the polynomial fit as discussed in chapter five. The procedure is performed in Matlab. A script file loads the calibration data and applies the polynomial fit. The polynomial coefficients are then saved to disc. Each goniometer-node has its own set of coefficients. The resulting coefficients are available for later use to determine the kinematic variables from the detector measurements. A video clip ([universal_joint_calibration](#) in the *motion capture* folder) is included in the accompanying DVD and illustrates the calibration of the universal joint.

The PC application also implements an evaluation procedure which evaluates the polynomial fit results in terms of accuracy and precision. It consists of the same calibration procedure but the results produced by polynomial fit are compared against the known kinematic variables generated during calibration.

7.3 Conclusion

No standard instrument exists to calibrate goniometer-nodes. An instrument was consequently constructed to meet the calibration and test requirements. An effort was made to use off-the-shelf components with known accuracies and thus remove the need to

calibrate the calibration instrument. The instrument consists of three independent motorised axes (two rotation and one translation). The third rotation axis is determined through a mathematical calculation. The rotation and translation resolutions are approximately $0.05^\circ/\text{step}$ and $4.02 \mu\text{m}/\text{step}$ respectively. Accuracy, as specified by the stepper motor manufacturer, is $5\%/\text{step}$. The mechanical axes are controlled through commands sent serially to the motor controller via a custom PC application.

The instrument is connected to a computer which controls the calibration process by separately manipulating the three stepper motors. The kinematic inputs and accompanying detector data are then saved for later processing. Separate data sets are produced for the cylindrical and universal joints.

The purpose of the instrument is twofold. First a data set is generated and the polynomial functions fitted to the data. The second task is to determine the error of the fit. Another data set is created and then evaluated for accuracy and precision against the polynomial fit (presented in chapter nine).

8.0 Measurement and Comparison Method

A method is presented here that compares the electrogoniometer and marker-based video motion capture kinematics. The video system serves as a benchmark. Video motion capture has extensively been used by the biomechanical research community for well over a decade. It was shown by Windolf et al. (2008) to be both accurate and precise (discussed in section 2.2.2.1).

The chapter first introduces the experimental setup. Two chains of reference frames are defined. The first set of frames are attached to the joint locations of the five goniometer-nodes. The second set of frames consist of reflective triads markers rigidly attached to the nodes. The triad reference frames are external to the device and thus not aligned to the electrogoniometer's reference frames. The *symmetric centre of rotation estimation (SCoRE)* method is applied to translate (reposition) the external reference frames to the internal joint locations (Ehrig et al., 2006). The orientations of the two sets of frames are however not aligned at this point. Alignment is achieved through a neutral-pose calibration technique. The method assumes the device has a predefine shape and each joint frame has a known orientation. The difference between the actual and assumed orientations are then used to calibrate (rotate) the two reference frame chains into alignment.

Once calibrated, the electrogoniometer is compared against the benchmark system in terms of translation and rotation errors. Comparing translation differences are simple enough, but the rotation comparison is a more complex exercise. Rotation metrics are reviewed and a comparison method based upon the average of the three Cardan angles proposed.

8.1 Motion Capture Setup

The motion capture setup, shown in figure 8.1a, consists of a four-camera Qualisys video motion capture system (Qualisys, Gothenburg, Sweden). Six triad sets are attached to the five-node electrogoniometer as shown in figure 8.1b. The base triad serves as a reference

for the measurements. A reference frame is calculated for each triad. The objective is to measure the joint kinematics of each goniometer-node. The triad reference frames are however external to the mechanical chain and are therefore not a true measure of the joint mechanics. To solve this problem, algorithmic solutions are described later to align frames in terms of translations and rotations.

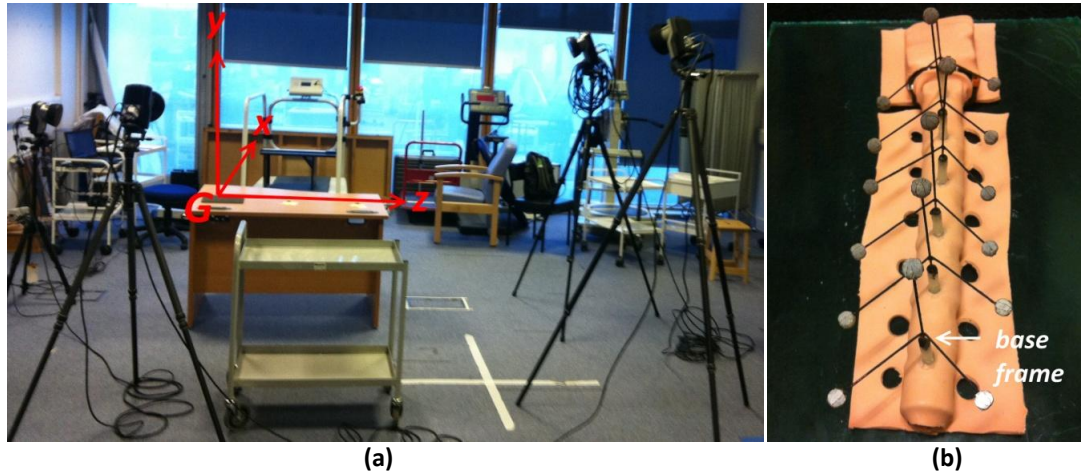


Figure 8.1: a) Qualisys motion capture setup. The global reference frame (G) as defined by the Qualisys system is shown in red; b) Electrogoniometer with reflective triads.

The setup is symbolically expressed as three kinematic chains as illustrated in figure 8.2. The mechanical chain (or *U*-chain) identifies the physical electrogoniometer. Its kinematics are considered to be a "true" representation of the physical world (i.e. it represents a curve/shape in an accurate and precise manner). The mechanical chain is measured by the video system via the triads. A pair of adjacent triads therefore measures the kinematics of a goniometer-node. The video chain (or *V*-chain) is considered a "true" (accurate and precise) measurement of the mechanical chain but with its reference frames not coinciding with that of the mechanical chain.

The electrogoniometer chain (or *T*-chain) is attached to the electrogoniometer (the device under test), and as with the video chain, it is not aligned with the mechanical chain. Misalignment is assumed to be due to the inaccuracy and imprecision of the device. Whereas the *V*-chain is true, the performance accuracy and precision of the electrogoniometer is unknown and has to be determined. However, in order to do so, the two chains must first be aligned.

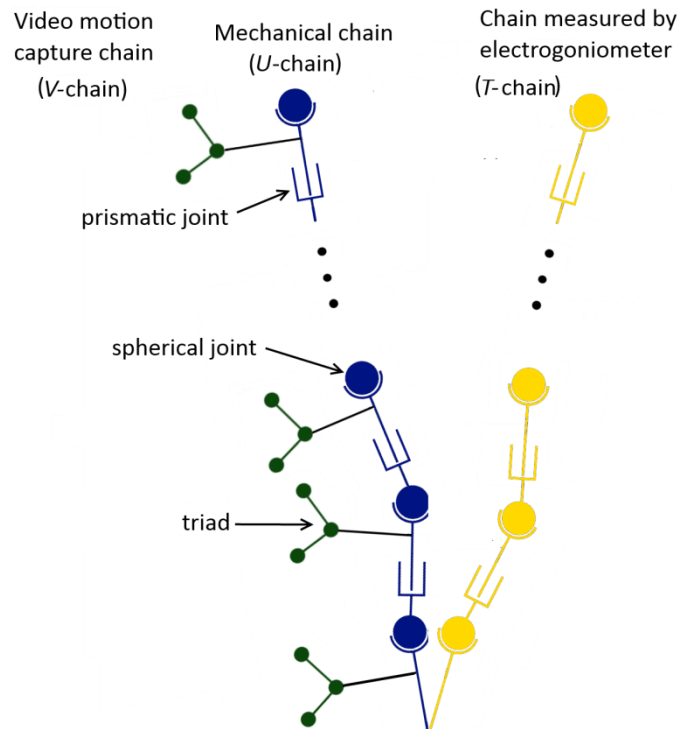


Figure 8.2: Symbolic representation of the video motion capture, mechanical and electrogoniometer kinematic chains.

8.2 Determining the Mechanical (true) Chain with Qualisys

The reference frames associated with the V -chain have to be transformed before being considered a true measure against which the electrogoniometer can be compared. The transformation process is illustrated in figure 8.3. The V -chain is ultimately transformed to the U_1 -chain through two calibration procedures. It is then the U_1 -chain that acts as the comparative measure for the electrogoniometer.

The global reference frame (defined by the Qualisys system) is labeled " G ". The reference frames of the other three chains (V , U and U_1) are numbered from the base of the chain starting with zero. The transformations indicated in black are known through measurements. The red transformations are calculated algorithmically. The transformations not only relates a reference frame within a chain, but also between chains (e.g. between chains V and U in figure 8.3). These transformations are referred to as inter-chain transformations. All the inter-chain transformations are constant (fixed) since the triads and mechanical chain are rigidly connected. The inter-chain transformations thus describe

an "offset" orientation and position between frames. Calibration methods are employed later to determined these transformations.

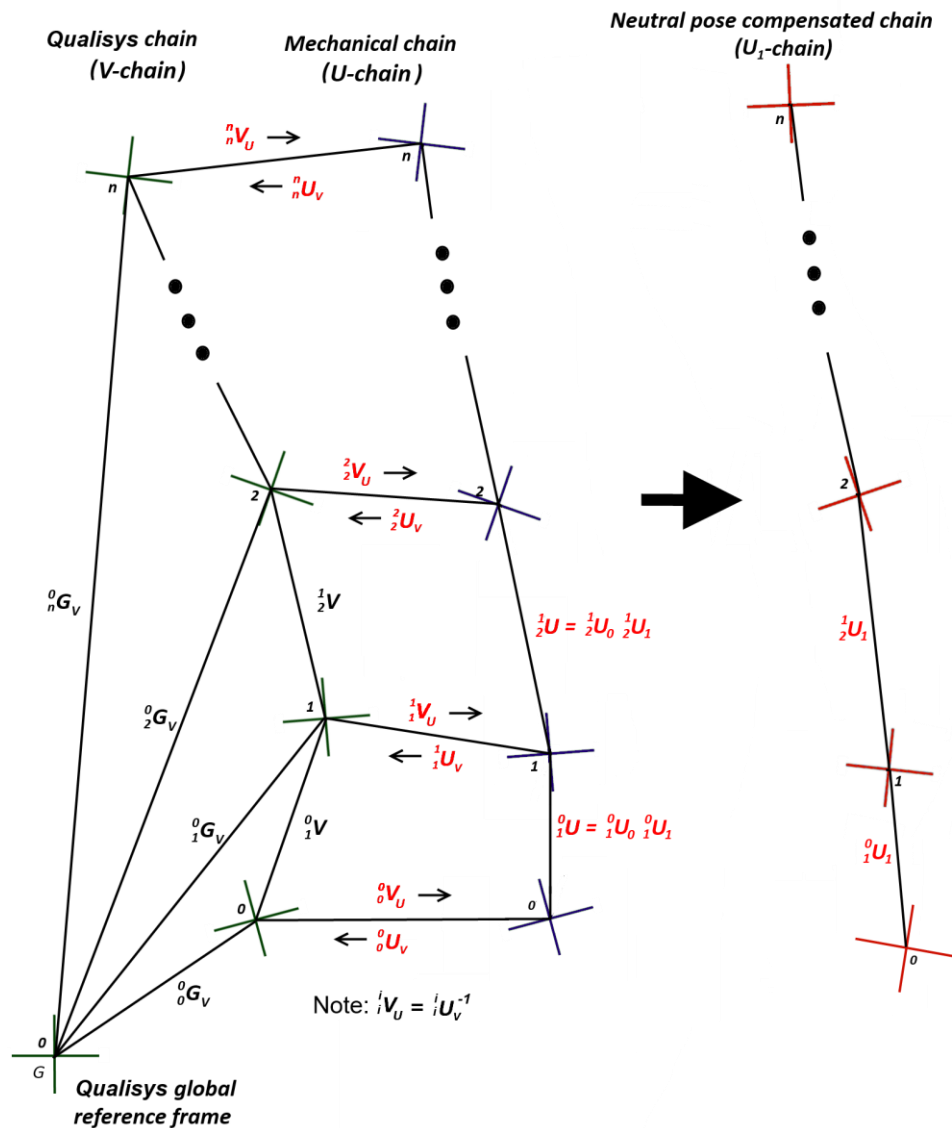


Figure 8.3: Reference frame representation of the kinematic chains. Black transformations are known through direct measurements and red transformations has to be determined algorithmically. The objective is to determine the U_1 -chain which then serves as benchmark to compare electrogoniometer measurements against.

8.2.1 Notations

Prior to this chapter, kinematics was associated with a single chain. The multiple-chain scheme in figure 8.3 requires additional notation to distinguish between the different

chains. Three "types" of transformations are identified and the notations necessary to describe the matrices are shown in figure 8.4. A transformation can be between joints within a chain; joints between two chains (inter-chain) and a decomposition (i.e. the product of two matrices). As in chapter four, the super and sub-scripts to the left of the matrix variable indicates the source and destination joints respectively. To distinguish between chains, the matrix variable indicates the source chain and an alphabet subscript to the right of the matrix variable the destination chain. If the subscript is however a number, then it indicates a decomposition. For example, the equation ${}^1_2U = {}^1_2U_0 {}^1_2U_1$ in figure 8.3 implies the transformation 1_2U is decomposed into two matrices 1_2U_0 and 1_2U_1 .

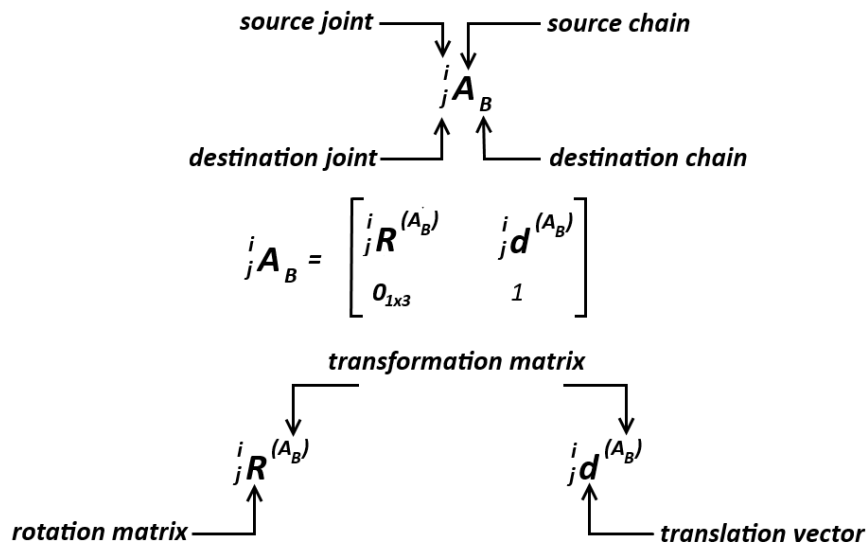


Figure 8.4: Notations used to describe matrices in terms of the joints and chains they are related to.

Further, when a transformation is expressed in terms of its rotation (R) and translation (d) components, the transformation matrix variable is indicated between brackets as a superscript on the right of the rotation matrix and translation vector (as illustrated in figure 8.4).

The notation is also useful to indicate the direction of the transformation. For example, in figure 8.3 the inter-chain transformation of $U-1$ (U -chain, joint 1) relative to $V-1$ (V -chain, joint 1) is expressed as 1_1V_U , whereas the transformation in the opposite direction is 1_1U_V . (Note, it is easy to show the two transformations are related, i.e.: ${}^1_1V_U = {}^1_1U_V^{-1}$.)

The final aspect the notation addresses, is the naming of reference frames. If the matrix notation is non-bold, then the symbol refers to a reference frame. The reference frame described by transformation 0_iU_1 is therefore 0U_1 . Here it is a global reference frame since the reference frame of join i is measured relative to frame 0 in chain U_1 .

8.2.2 Transforming the V -chain to the U -chain

The U -chain is determined by translating the V -chain reference frames to the corresponding joint location in the U -chain. These locations correspond to the centre-of-rotation (CoR) of the goniometer-nodes. The CoRs cannot be measured directly (with a caliper for example), since the joint are concealed within the device. An algorithmic method is consequently used to calculate the joint locations.

8.2.2.1 Finding the Centre-of-Rotation

The CoR of each joint is determined through a calibration procedure. The inter-chain transformations reposition the V -chain frames with a displacement ${}^i\mathbf{d}^{(V_U)}$ from outside the device to the corresponding joints (i.e. the CoR) inside the device as illustrated in figure 8.5. No rotation is applied at this point and the rotation component of the transformation matrix will therefore be the identity matrix. The inter-chain matrix can then be written as:

$${}^iV_U = \begin{bmatrix} I & {}^i\mathbf{d}^{(V_U)} \\ \mathbf{0}_{1 \times 3} & 1 \end{bmatrix} \quad \text{equ 8.1}$$

The translation vector, ${}^i\mathbf{d}^{(V_U)}$, is algorithmically determined through the SCoRE method (Ehrig et al., 2006). The method assumes two known reference frames (measured relative to the global reference G) that rotates purely relative to the joint (CoR).

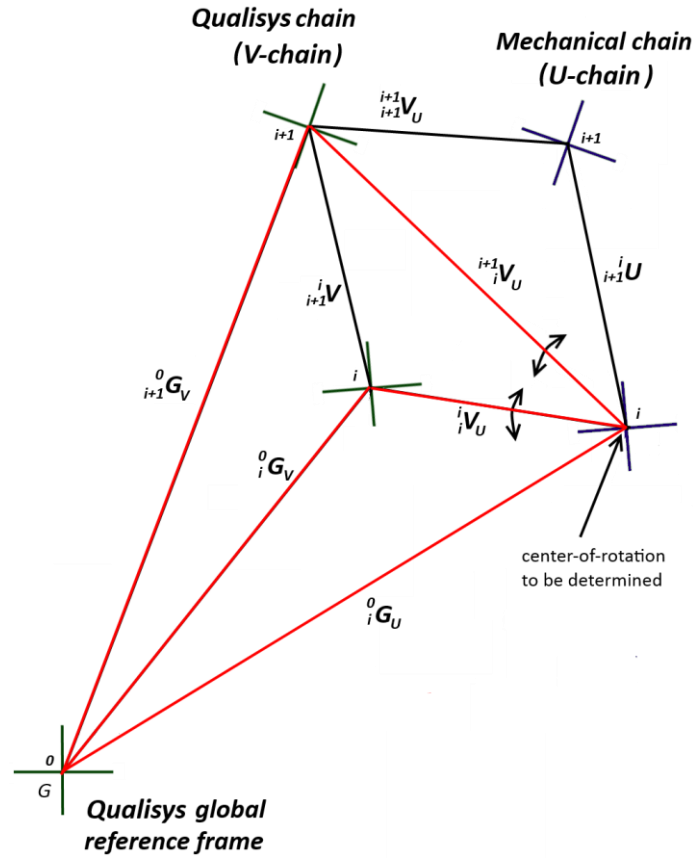


Figure 8.5: Determining the CoR of joint i using the SCoRE method.

The SCoRE method is now derived from first principles. The pose of reference frame 0G_U in figure 8.5 can be expressed in two ways:

$${}^0G_U = {}^0G_V {}^iV_U \tag{equ 8.2}$$

and

$${}^0G_U = {}^{i+1}G_V {}^{i+1}V_U \tag{equ 8.3}$$

When combined and expanded, the two equations are written as:

$$\begin{bmatrix} {}^0R^{(G_V)} & {}^0d^{(G_V)} \\ \mathbf{0}_{1 \times 3} & 1 \end{bmatrix} \begin{bmatrix} I & {}^i d^{(V_U)} \\ \mathbf{0}_{1 \times 3} & 1 \end{bmatrix} = \begin{bmatrix} {}^{i+1}R^{(G_V)} & {}^{i+1}d^{(G_V)} \\ \mathbf{0}_{1 \times 3} & 1 \end{bmatrix} \begin{bmatrix} I & {}^{i+1}d^{(V_U)} \\ \mathbf{0}_{1 \times 3} & 1 \end{bmatrix}$$

$$\begin{bmatrix} {}^0R^{(G_V)} & ({}^0R^{(G_V)} {}^i d^{(V_U)} + {}^0d^{(G_V)}) \\ \mathbf{0}_{1 \times 3} & 1 \end{bmatrix} = \begin{bmatrix} {}^{i+1}R^{(G_V)} & ({}^{i+1}R^{(G_V)} {}^{i+1}d^{(V_U)} + {}^{i+1}d^{(G_V)}) \\ \mathbf{0}_{1 \times 3} & 1 \end{bmatrix} \tag{equ 8.4}$$

The CoR is only dependent on the translation components and the rotation components can therefore be ignored. The left and right translation components are then:

$${}^0\mathbf{R}^{(G_V)} {}^i\mathbf{d}^{(V_U)} + {}^0\mathbf{d}^{(G_V)} = {}_{i+1}\mathbf{R}^{(G_V)} {}^{i+1}\mathbf{d}^{(V_U)} + {}_{i+1}\mathbf{d}^{(G_V)} \quad \text{equ 8.5}$$

and can conveniently be rewritten as:

$${}^0\mathbf{R}^{(G_V)} {}^i\mathbf{d}^{(V_U)} - {}_{i+1}\mathbf{R}^{(G_V)} {}^{i+1}\mathbf{d}^{(V_U)} = {}_{i+1}\mathbf{d}^{(G_V)} - {}^0\mathbf{d}^{(G_V)}$$

$$\begin{bmatrix} {}^0\mathbf{R}^{(G_V)} & {}_{i+1}\mathbf{R}^{(G_V)} \end{bmatrix} \begin{bmatrix} {}^i\mathbf{d}^{(V_U)} \\ -{}^{i+1}\mathbf{d}^{(V_U)} \end{bmatrix} = \begin{bmatrix} {}_{i+1}\mathbf{d}^{(G_V)} - {}^0\mathbf{d}^{(G_V)} \end{bmatrix} \quad \text{equ 8.6}$$

where vectors ${}^i\mathbf{d}^{(V_U)}$ and ${}^{i+1}\mathbf{d}^{(V_U)}$ are the only unknowns. The above equation is linear and can thus be written as a linear system of equations:

$$\mathbf{A}\mathbf{x} = \mathbf{y} \quad \text{equ 8.7}$$

where \mathbf{A} is a non-square matrix representing rotations measurements captured by the video motion capture system, \mathbf{y} the corresponding captured translation vectors and \mathbf{x} the unknown local CoR vectors (${}^i\mathbf{d}^{(V_U)}$ and ${}^{i+1}\mathbf{d}^{(V_U)}$). The problem can be solved iteratively (using for example the Levenberg-Marquardt method) or by calculating the pseudo inverse of \mathbf{A} . The latter is used here and the full solution is detailed in appendix A.3.

For joint i , ${}^0\mathbf{R}^{(G_V)}$, ${}_{i+1}\mathbf{R}^{(G_V)}$, ${}_{i+1}\mathbf{d}^{(G_V)}$ and ${}^0\mathbf{d}^{(G_V)}$ were determined from the captured data and ${}^i\mathbf{d}^{(V_U)}$ and ${}^{i+1}\mathbf{d}^{(V_U)}$ then calculated by solving the system of equations (equation 8.7). The vectors ${}^i\mathbf{d}^{(V_U)}$ and ${}^{i+1}\mathbf{d}^{(V_U)}$ expressed the CoR of joint i relative to the corresponding V-chain frames. The average of the global locations are taken to be the CoR of joint i , i.e.:

$${}^0\mathbf{d}^{(G_V)} = \frac{\left({}^0\mathbf{R}^{(G_V)} {}^i\mathbf{d}^{(V_U)} + {}^0\mathbf{d}^{(G_V)} \right) + \left({}_{i+1}\mathbf{R}^{(G_V)} {}^{i+1}\mathbf{d}^{(V_U)} + {}_{i+1}\mathbf{d}^{(G_V)} \right)}{2} \quad \text{equ 8.8}$$

In practice the calibration data to determine the CoRs requires special consideration. As stated above, the SCoRE method demands rotation-only movement. Care must therefore be taken not to stretch the device but only apply bending and twisting actions during calibration motion capture.

8.2.2.2 Finding the Minimum Link Length (${}_{i+1}\delta_0^{(U)}$)

The minimum link length (MLL), ${}_{i+1}\delta_0^{(U)}$, is a parameter specifying the minimum Euclidean distance between two adjacent joints, i.e. the distance between connecting links when the device is not stretched. In theory the distance should be the same for all goniometer-nodes, however in practice the parameter varies from node to node since the mechanical components are handmade. Variation of the node lengths are however not critical for evaluating the prototype device, since it does not affect the measurement method. The MLL is related to the link length, ${}_{i+1}\delta^{(U)}$, as follow:

$${}_{i+1}\delta^{(U)} = {}_{i+1}\delta_0^{(U)} + {}_{i+1}\delta_1^{(U)} \quad \text{equ 8.9}$$

where ${}_{i+1}\delta_1^{(U)}$ is the displacement of goniometer-node i when the device is stretched. The relationship is illustrated graphically in figure 8.6.

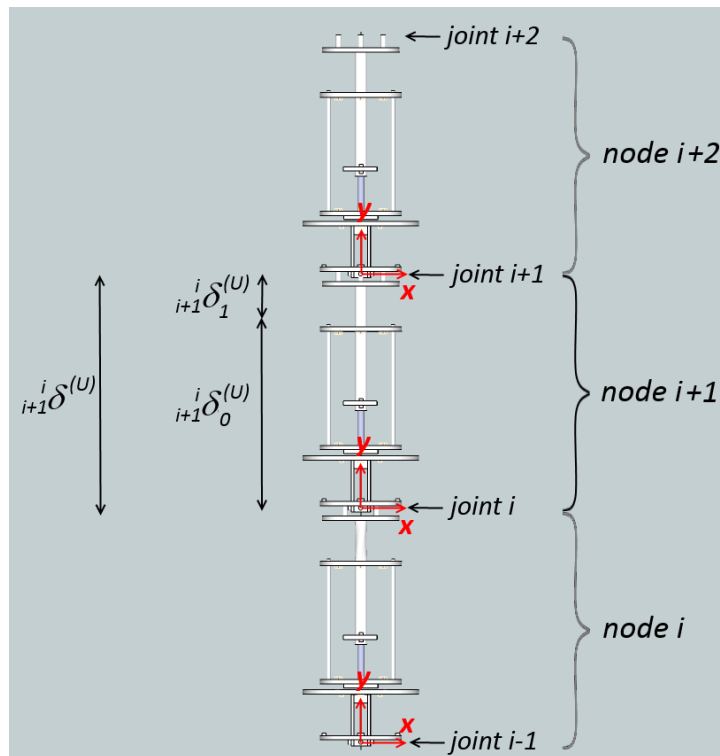


Figure 8.6: The link length in relation to the goniometer-nodes. The link length is decomposed into two components: the minimum link length (MLL) and measured displacement.

The MLL can be determined directly from the CoR calibration procedure derived in the previous section. The minimum length of link i is simply the length of the difference

between the corresponding (non-stretched) CoRs when expressed relative to the global reference frame, i.e.:

$${}_{i+1}^i\delta_0^{(U)} = \left\| {}_{i+1}^0\mathbf{d}^{(G_U)} - {}_i^0\mathbf{d}^{(G_U)} \right\| \quad \text{equ 8.10}$$

and where ${}_{i+1}^0\mathbf{d}^{(G_U)}$ and ${}_i^0\mathbf{d}^{(G_U)}$ are calculated by equation 8.8. The MLL is a system parameter and saved to non-volatile memory post the calibration procedure.

Note, the MLL of the last node in a chain of n goniometer-nodes cannot be determined algorithmically, since the device consists of only n joints and n links (i.e. the chain terminates with a link). The chain must however terminate with a joint for the last MLL to be determined (i.e. consists of $n + 1$ joints and n links).

8.2.2.3 Kinematics of the U-chain

The U -chain kinematics can now be determined from the calibration parameters and V -chain kinematics. According to figure 8.3, the local transformation of reference frame ${}_{i+1}^iU$ is given by the sequence of transformations:

$${}_{i+1}^iU = {}_i^iU_V {}_{i+1}^iV {}_{i+1}^{i+1}V_U \quad \text{equ 8.11}$$

The rotation matrices of the inter-chain transformations (${}_i^iU_V$ and ${}_{i+1}^{i+1}V_U$) have identity rotation matrices (see equation 8.1) and translation components determined by the SCoRE method. Thus equation 8.11 can be expanded as follow:

$$\begin{aligned} {}_{i+1}^iU &= \begin{bmatrix} I & {}_i^i\mathbf{d}^{(U_V)} \\ \mathbf{0}_{1 \times 3} & \mathbf{1} \end{bmatrix} \begin{bmatrix} {}_{i+1}^i\mathbf{R}^{(V)} & {}_{i+1}^i\mathbf{d}^{(V)} \\ \mathbf{0}_{1 \times 3} & \mathbf{1} \end{bmatrix} \begin{bmatrix} I & {}_{i+1}^{i+1}\mathbf{d}^{(V_U)} \\ \mathbf{0}_{1 \times 3} & \mathbf{1} \end{bmatrix} \\ &= \begin{bmatrix} {}_{i+1}^i\mathbf{R}^{(V)} & {}_{i+1}^i\mathbf{R}^{(V)} {}_{i+1}^i\mathbf{d}^{(V_U)} + {}_{i+1}^i\mathbf{d}^{(V)} + {}_i^i\mathbf{d}^{(U_V)} \\ \mathbf{0}_{1 \times 3} & \mathbf{1} \end{bmatrix} \quad \text{equ 8.12} \end{aligned}$$

All the matrices and vectors in equation 8.12 are known. The rotation matrix ${}_{i+1}^i\mathbf{R}^{(V)}$ is the orientation of triad $i + 1$ relative to triad i , as measure by the video system; ${}_{i+1}^i\mathbf{d}^{(V)}$ is the corresponding displacement between the origins of the two triads and ${}_i^i\mathbf{d}^{(U_V)}$ and ${}_{i+1}^i\mathbf{d}^{(V_U)}$ are calculated from the SCoRE method by solving equation 8.7.

8.2.2.4 Neutral-pose Calibration

The SCoRE method translated the triad (V) reference frames to the joints of the mechanical (U) chain. Yet, the U -chain cannot be compared to the electrogoniometer (T) since their frame orientations are not aligned. The problem is solved by defining a neutral pose (the term bind-pose is sometimes used by the 3D graphics animation community (Zink et al., 2011)). A neutral pose is a kinematic chain with a known shape and therefore known reference frame transformations. Any shape will do, e.g. the device can be affixed to a cylinder. The shape (a circle in this case) is known and the frame transformations can therefore be determined. A circle perhaps overcomplicates the matter, since the diameter of the device also has to be accounted for when calculating the frame transformations. A simpler neutral-pose can be obtained by holding the device in an elongated (non-curved) pose as illustrated in figure 8.7. The rotation matrices of the neutral-pose chain are then simply the identity matrix.

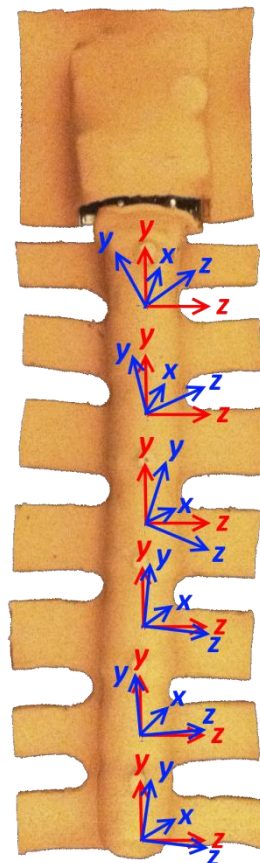


Figure 8.7: The neutral-curve calibration pose. Red is the neutral pose axes and blue the actual measured axes.

If the device is kept in a static straight (non-curved pose) manner, then the rotation of reference frame ${}_{i+1}^iU$ is the identity matrix. However, in reality the video motion capture system will measure a non-identity orientation since an arbitrary rotational offset exists which has to be removed through the calibration process. A neutral-pose rotation matrix, ${}_{i+1}^iR^{(U_0)}$, is subsequently introduced to transform the measured orientation (${}_{i+1}^iR^{(U)}$) into the identity matrix, i.e.:

$$\begin{aligned} {}_{i+1}^iR^{(U)} &= {}_{i+1}^iR^{(U_0)} {}_{i+1}^iR^{(U_1)} \\ {}_{i+1}^iR^{(U)} &= {}_{i+1}^iR^{(U_0)} I \\ \therefore {}_{i+1}^iR^{(U_0)} &= {}_{i+1}^iR^{(U)} \end{aligned} \quad \text{equ 8.13}$$

where ${}_{i+1}^iR^{(U_1)}$ is the desired orientation which is set to the identity matrix during the calibration process. The rotation matrix ${}_{i+1}^iR^{(U_0)}$ will from now on be referred to as the neutral-pose rotation matrix.

8.2.3 Transforming the U -chain to the U_1 -chain

The neutral-pose compensated (U_1) chain (figure 8.3) is a calibrated chain against which the electrogoniometer can be compared. During calibration ${}_{i+1}^iR^{(U)}$, ${}_{i+1}^iR^{(U_1)}$ and ${}_{i+1}^i\mathbf{d}^{(U)}$ are known and ${}_{i+1}^iR^{(U_0)}$ is unknown. Post calibration, the neutral-pose compensated chain (U_1) is the unknown. The rotation matrix, ${}_{i+1}^iR^{(U_1)}$, and translation vector, ${}_{i+1}^i\mathbf{d}^{(U_1)}$, are then determined by applying the calibration matrix ${}_{i+1}^iR^{(U_0)}$ to each reference frame. This amounts to the reverse multiplication of equation 8.13, i.e.:

$${}_{i+1}^iR^{(U_1)} = {}_{i+1}^iR^{(U_0)^{-1}} {}_{i+1}^iR^{(U)} \quad \text{equ 8.14}$$

The neutral-pose compensated transformation, ${}_{i+1}^iU_1$, modifies the rotation matrix of ${}_{i+1}^iU$ (note, the translation components are the same), i.e.:

$$\begin{aligned} {}_{i+1}^iU_1 &= \begin{bmatrix} {}_{i+1}^iR^{(U_1)} & {}_{i+1}^i\mathbf{d}^{(U_1)} \\ \mathbf{0}_{1 \times 3} & 1 \end{bmatrix} \\ &= \begin{bmatrix} {}_{i+1}^iR^{(U_0)^{-1}} {}_{i+1}^iR^{(U)} & {}_{i+1}^i\mathbf{d}^{(U)} \\ \mathbf{0}_{1 \times 3} & 1 \end{bmatrix} \end{aligned} \quad \text{equ 8.15}$$

And finally, the transformation of joint i relative to the base of the chain can then be determined by applying the forward kinematics sequence of transformations:

$${}^0U_1 = \prod_{j=1}^i {}^{j-1}U_j \quad i = 1, \dots, n \quad \text{equ 8.16}$$

8.3 Estimating the Mechanical Chain with the Electrogoniometer

8.3.1 Determining the Electrogoniometer Chain

Compared to the U -chain, the electrogoniometer (T) chain is much simpler to determine. Recalling from chapter four, the local transformation matrix (equation 4.5) for the linkage system was shown to be (when expressed in the new notation):

$${}_{i+1}{}^i T = \begin{bmatrix} {}_{i+1}{}^i R^{(T)} & {}_{i+1}{}^i R^{(T)} & {}_{i+1}{}^i d^{(T)} \\ \mathbf{0}_{1 \times 3} & 1 & 1 \end{bmatrix} \quad \text{equ 8.17}$$

and according to equation 4.3, the vector ${}_{i+1}{}^i d^{(T)}$ is:

$${}_{i+1}{}^i d^{(T)} = \begin{bmatrix} 0 \\ {}_{i+1}{}^i d \\ 0 \end{bmatrix} \quad \text{equ 8.18}$$

The scalar value ${}_{i+1}{}^i d$ is the length of the goniometer-node and can be expressed in terms of the minimum link length and the displacement measured by the goniometer-node, i.e.:

$${}_{i+1}{}^i d^{(T)} = {}_{i+1}{}^i \delta_0^{(U)} + {}_{i+1}{}^i \delta_1^{(T)} \quad \text{equ 8.19}$$

The local transformation matrix is thus:

$${}_{i+1}{}^i T = \begin{bmatrix} {}_{i+1}{}^i R^{(T)} & {}_{i+1}{}^i R^{(T)} \left[0 \quad {}_{i+1}{}^i \delta_0^{(U)} + {}_{i+1}{}^i \delta_1^{(T)} \quad 0 \right]^T \\ \mathbf{0}_{1 \times 3} & 1 \end{bmatrix} \quad \text{equ 8.20}$$

8.3.2 Determining the Neutral-pose Compensated Chain

The goniometer-nodes measure relative to the joints of the mechanical linkage system. There may however exist arbitrary orientation offsets similar to the V -chain offsets. The offsets are typically due to improper alignment during the chain assembly. A neutral-pose

calibration procedure similar to the one used to determine the U_I -chain, is subsequently applied.

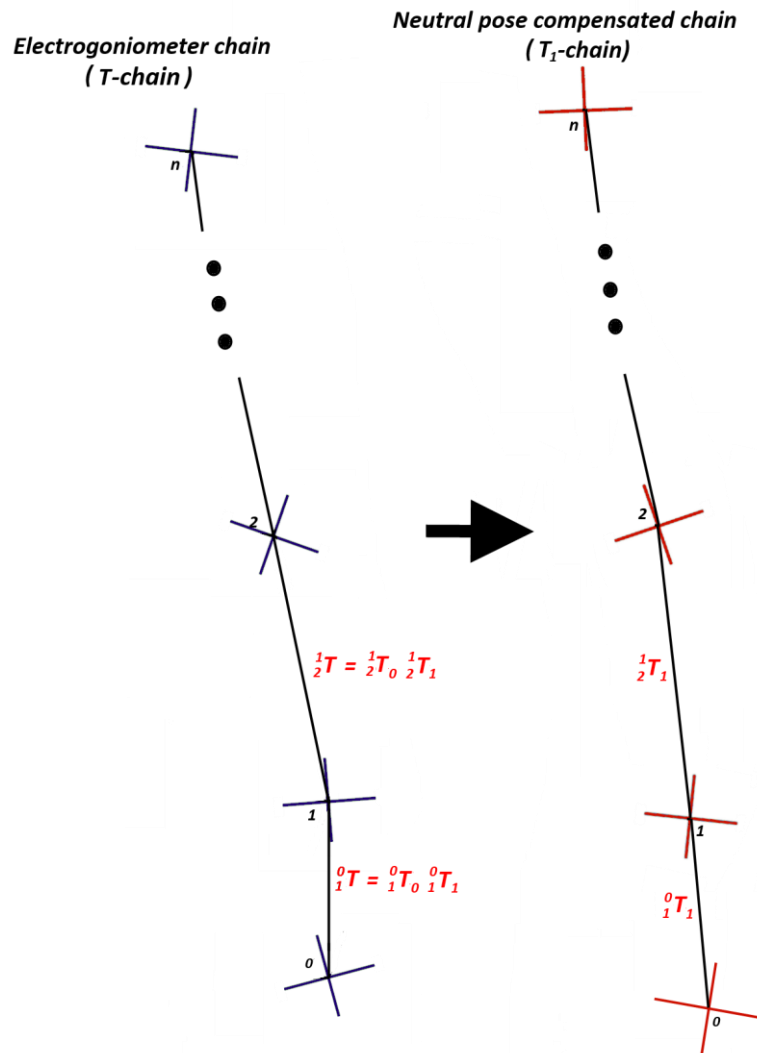


Figure 8.9: The neutral-pose compensated (T_1) chain which is derived from the T -chain. The T_1 chain is later compared against the U_I -chain to determine the accuracy of the electrogoniometer.

Figure 8.9 shows T -chain decomposition. The neutral-pose rotation matrix is obtained during calibration (similar to equation 8.13 for the U -chain) and is now applied to the T -chain, i.e.:

$${}_{i+1}^iR^{(T_0)} = {}_{i+1}^iR^{(T)} \tag{equ 8.21}$$

Neutral-pose compensation is purely a rotation operation and the transformation matrix is therefore:

$${}^{i+1}T_0 = \begin{bmatrix} {}^{i+1}R^{(T_0)} & \mathbf{0}_{3 \times 1} \\ \mathbf{0}_{1 \times 3} & 1 \end{bmatrix} \quad \text{equ 8.22}$$

As with U_i -chain, the local neutral-pose transformation is the product between the inverse of the neutral-pose compensated matrix and the local transformation as measured by the goniometer-node:

$${}^{i+1}T_1 = {}^{i+1}T_0^{-1} {}^{i+1}T \quad \text{equ 8.23}$$

And finally, the transformation of joint i relative to the base of the chain is determined by multiplying the sequence of transformations (i.e. apply the forward kinematics procedure):

$${}^0T_1 = \prod_{j=1}^i {}^{j-1}T_j \quad \text{equ 8.24}$$

8.4 Comparing Reference Frames

In order to compare ${}^{i+1}U_1$ and ${}^{i+1}T_1$, both local frames must be expressed relative to a common frame. This requirement has been achieved through the neutral-pose calibration discussed above. Comparison procedures are now devised to compare the reference frames in terms of translation and rotation differences.

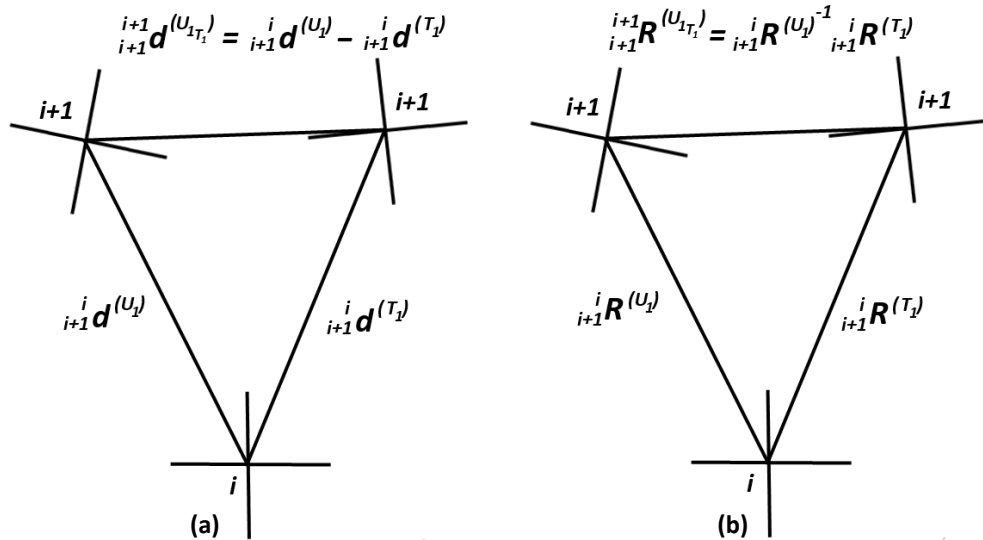


Figure 8.10: a) Difference in position of reference frames ${}^{i+1}U_1$ and ${}^{i+1}T_1$; b) Difference in rotation frames ${}^{i+1}U_1$ and ${}^{i+1}T_1$ (note, the chain rotations super- and subscripts are omitted in the text to reduce clutter).

8.4.1 Comparison of Translations

Consider the three frames in figure 8.10a. Transformations ${}_{i+1}^iU_1$ and ${}_{i+1}^iT_1$ are expressed relative to a common frame i . A straightforward method to compare the locations of frames ${}_{i+1}^iU_1$ and ${}_{i+1}^iT_1$ is to simply determine the Euclidean (error) distance between them:

$${}_{i+1}^i d^{(U_1 T_1)} = \left\| {}_{i+1}^i \mathbf{d}^{(U_1)} - {}_{i+1}^i \mathbf{d}^{(T_1)} \right\| \quad \text{equ 8.25}$$

8.4.2 Comparison of Rotations

Comparing rotations are more complicated. Firstly, a metric similar to the Euclidean distance defined in equation 8.25 is formulated, i.e. the orientation of frame ${}_{i+1}^iT_1$ relative to frame ${}_{i+1}^iU_1$ is:

$${}_{i+1}^i \mathbf{R}^{(U_1 T_1)} = {}_{i+1}^i \mathbf{R}^{(U_1)^{-1}} {}_{i+1}^i \mathbf{R}^{T_1} \quad \text{equ 8.26}$$

where ${}_{i+1}^i \mathbf{R}^{(U_1 T_1)}$ represents the "difference" in rotation of ${}_{i+1}^iT_1$ relative to ${}_{i+1}^iU_1$. The difference rotation is illustrated graphically in figure 8.10b. It is clear that if both frames have the same orientation, then the difference rotation is the identity matrix.

Rotation when expressed as a matrix, consists of three basis vectors and described by nine scalar values in total. The difference rotation is therefore difficult to interpret when expressed as a rotation matrix. A more sensible approach is to decompose the difference rotation into its Cardan angles.

8.4.1.1 Comparison of Cardan Angles

Let the rotations of reference frames ${}_{i+1}^iT_1$ and ${}_{i+1}^iU_1$ be decompose into their Cardan angles so that (the joint sub- and superscripts are temporary dropped to reduce clutter):

$$\mathbf{R}^{U_1}(\psi, \theta, \phi) = \mathbf{R}_{y,\psi}^{U_1}(\psi) \mathbf{R}_{z,\theta}^{U_1}(\theta) \mathbf{R}_{x,\phi}^{U_1}(\phi) \quad \text{equ 8.27}$$

and

$$\mathbf{R}^{T_1}(\psi + n_\psi, \theta + n_\theta, \phi + n_\phi) = \mathbf{R}_{y,\psi}^{T_1}(\psi + n_\psi) \mathbf{R}_{z,\theta}^{T_1}(\theta + n_\theta) \mathbf{R}_{x,\phi}^{T_1}(\phi + n_\phi) \quad \text{equ 8.28}$$

Both frames have the same Cardan angles rotations (i.e. ψ , θ and ϕ). In addition, it is assumed the goniometer-node frame has additive error components n_ψ , n_θ and n_ϕ which may be due to system noise and/or the inaccuracy of the node itself.

The idea is now to determine if the difference rotations are dependent on the noise components only. Thus the two frame rotations, expressed as Cardan rotations (equations 8.27 and 8.28), are substituted into the difference rotation (equation 8.26). However, due to the non-commutative nature of matrix multiplication, the following inequality holds:

$$\mathbf{R}^{(U_1T_1)} \neq \mathbf{R}_{y,\psi}^{(U_1T_1)}(n_\psi) \mathbf{R}_{z,\theta}^{(U_1T_1)}(n_\theta) \mathbf{R}_{x,\phi}^{(U_1T_1)}(n_\phi) \quad \text{equ 8.29}$$

The difference rotation can therefore not be expressed in terms of the three Cardan noise components (n_ψ , n_θ and n_ϕ). In conclusion, comparing the *individual* Cardan angles does not have merit since rotation is defined through a sequence of (non-commutative) Cardan angle multiplications.

8.4.1.2 SO(3) Rotation Metrics

Rotation metrics (also called rotation distance functions) express the relative orientation of two rotations as a single number (usually in degrees or radians but it can also be dimensionless) (Huynh, 2009).

A metric must fulfil three axioms (Huynh, 2009). The first states the rotation distance between frame ${}_{i+1}^i T_1$ relative to ${}_{i+1}^i U_1$ must be the same as ${}_{i+1}^i U_1$ relative to ${}_{i+1}^i T_1$ (i.e. the metric is symmetrical); the second axiom states distance is larger and equal to zero (if it is zero then the frames are the same); and thirdly the "Euclidean" rotation distance between the two frames is the shortest possible distance.

A metric, Φ_1 , which satisfies the above axioms, compares the relative orientation of two rotation matrices (\mathbf{R}^{U_1} and \mathbf{R}^{T_1}) based upon the trace (tr) of the relative orientation (Grankow, 2001):

$$\Phi_1(\mathbf{R}^{U_1}, \mathbf{R}^{T_1}) = \cos^{-1} \left(\frac{tr(\mathbf{R}^{U_1^{-1}} \mathbf{R}^{T_1}) - 1}{2} \right) \quad \text{equ 8.30}$$

Another metric is based upon the Cardan angles (equations 8.27 and 8.28) and defined by Huynh (2009):

$$\begin{aligned}\Phi_2(\mathbf{R}^{T_1}, \mathbf{R}^{U_1}) &= \sqrt{(\psi + n_\psi - \psi)^2 + (\theta + n_\theta - \theta)^2 + (\phi + n_\phi - \phi)^2} \\ &= \sqrt{n_\psi^2 + n_\theta^2 + n_\phi^2}\end{aligned}\quad \text{equ 8.31}$$

Metrics Φ_1 and Φ_2 produce very similar solutions for relative small differences in rotation. Metric Φ_2 is however more intuitive since it is based upon the Euclidean distance between the two Cardan angle sets. The Euclidean distance as a metric is however not very useful here. The aim is to define a metric based on the average axis distance which can serve as a direct indication of accuracy between the U_1 and T_1 -chain measurements. The average Manhattan (also known as the city-block or taxicab) metric fulfils this requirement:

$$\Phi_3(\mathbf{R}^{T_1}, \mathbf{R}^{U_1}) = \frac{|n_\psi| + |n_\theta| + |n_\phi|}{3}\quad \text{equ 8.32}$$

In conclusion, Φ_3 is proposed here to measure the difference in rotation between the video motion capture and electrogoniometer reference frame. The metric describes the rotation difference as a single value (in degrees). It is calculated as the average Manhattan difference between the Cardan angles of the U_1 and T_1 -chain reference frames.

8.5 Method Summary

The measurement method is summarised in table 8.1. It is divided into two categories: calibration and evaluation. During calibration the system parameters are determined from data specifically generated to calculate the parameters from. These parameters are saved and use during the evaluation process.

Evaluation (or testing) applies the system parameters. During evaluation the device is moved in all axes (i.e. stretched, bent and twisted). The two systems can then be directly compared in terms of accuracy and precision.

Description	Equation	Data description
Calibration and Parameter Estimation		
<i>Qualisys</i>		
• Calculate CoR of mechanical chain joints	8.7	Rotation (bend and twist motions)
• Calculate MLL of mechanical links	8.10	
• Neutral-pose calibration:		calibration pose (static)
○ Calculate neutral-pose transformation	8.13	
○ Calculate neutral-pose compensated chain	8.15	
<i>Electrogoniometer</i>		
• Neutral-pose calibration		calibration pose (static)
○ Calculate neutral-pose transformation	8.21	
○ Calculate neutral-pose compensated chain	8.23	
Evaluation		
• Compare Qualisys and electrogoniometer transformation:		rotation and translation (bend, twist and stretch motions)
○ Determine translation accuracy	8.25	
○ Determine rotation accuracy	8.32	

Table 8.1: Summary of the measurement method.

8.6 Conclusion

The electrogoniometer is to be evaluated against a Qualisys video motion capture system. Before a comparison can be made, a measurement method has to be devised. To do so, reflective triads were attached to each electrogoniometer node. A reference frame is calculated for each triad. However, the external location of the triad reference frames make a direct comparison between the video and electrogoniometer measurements difficult.

A method was subsequently developed to align the reference frames of the two sets of measurements. For the triad reference frames, this entailed transforming the external reference frames to the mechanical joint locations of the goniometer-nodes. The task was accomplished in two steps. First, the reference frames were translated to the joint locations through the SCoRE procedure. Secondly the reference frames were rotated to be aligned with a predefined neutral pose. Since the electrogoniometer reference frames were already located at the joints, only neutral pose calibration is required.

The next step was to define difference metrics to compare the two sets of measurements. As independent components, the translation and rotation differences can be determined separately. Difference in translation is simply the Euclidean distances between the nodes of the corresponding chains. Comparing rotations were not so straightforward however. A metric based upon the average Manhattan difference of the Cardan angles between the two chains was proposed. The implication was that rotation was not compared on an individual axis basis, but rather on the average of the differences in the Cardan angles.

In conclusion, this chapter described a custom measurement method specific to this research project. The method, as summarised in table 8.1, compares marker-based video motion measurements to that of the electrogoniometer measurements on a local and global reference frame basis. Much of the method relies on algorithm calculations. In contrast with many other biomechanical measurement methods which only compares measurements in a single plane (e.g. motion in the sagittal plane) (e.g. Williams et al., 2010; Wong and Wong, 2009), this method compares kinematics in all three planes.

9.0 Results

This chapter presents the results necessary to validate the accuracy and precision performance of the electrogoniometer, a subject that is central to the objectives set out in this thesis. Results are divided into three sections. The goniometer-node results are first reported. The practical transfer functions as measured by the calibrate and test (CaT) instrument, and predicted by the theoretical model, are presented. Based upon the measurements from the CaT instrument, the static accuracy and precision of the individual goniometer-nodes are then determined.

The second part investigates the validity of the Qualisys motion capture system as a measurement standard. The system is validated in terms of accuracy and precision. Also discussed is the measurement setup.

The final results consider the evaluation of the electrogoniometer against the Qualisys system and applies the measurement method developed in chapter eight. The method results are reported in two parts. Firstly, the calibration parameters are obtained from motion capture data. Secondly, the local and global accuracy and precision of the electrogoniometer are calculated based upon the metrics discussed in chapter eight.

9.1 Theoretical Model

A theoretical model, predicting the transfer functions of the detectors, was developed in chapter five. In order to determine the validity of the model, it has to be compared to practical measurements. The practical transfer functions of the universal and cylindrical joints are determined by the CaT instrument. The instrument systematically samples the detectors while adjusting the mechanical axes of the node under test. The subsequent scatter data is then approximated with a surface plot and represents the practical transfer functions. The theoretical model response is determined based upon the physical design parameters of the node.

The transfer functions for detectors 3, 4 and 5 (upper section) of the cylindrical joint are shown in figure 9.1a and b. Figure 9.1a (a repeat of figure 5.6d) is the response predicted by the model. Figure 9.1b is the transfer function as measured by the CaT instrument for the same set of detectors. (The responses for detectors 0, 1 and 2 (lower sections of the cylindrical joint) exhibit similar results and are therefore not shown here.)

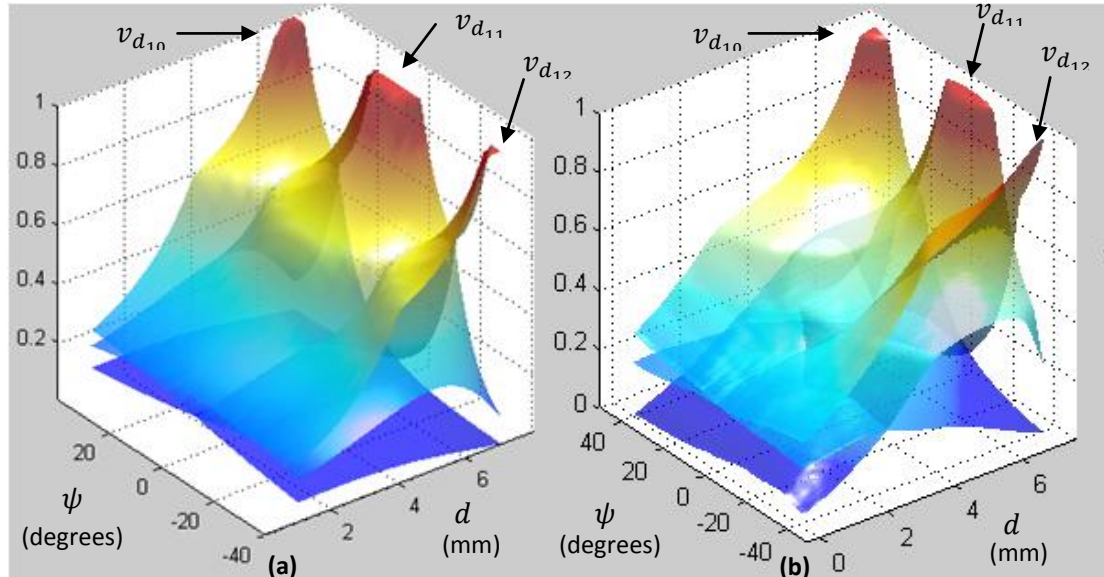


Figure 9.1: Comparison of the transfer functions of detectors 0, 1 and 2 as determined by the a) mathematical model; b) calibration and test instrument.

The same procedure is applied to determine the response of the universal joint. Figures 9.2a and b show the difference response between detectors 0 and 1 (i.e. $v_a = v_{d_{00}} - v_{d_{11}}$; equation 5.25), whereas figures 9.2c and d are the theoretical and actual difference responses for detectors 2 and 3 (i.e. $v_b = v_{d_{22}} - v_{d_{33}}$; equation 5.26). (Shadowing is used in the figures to help with the visual interpretation of the functions.) The irregular boundaries of the CaT results (figures 9.2b and d) are due to the mechanical stop (figure 6.3a) limiting the movement of the universal joint to be within circular bounds.

It is evident from the figures that the theoretical and actual transfer functions show a remarkable agreement for both the cylindrical and universal joints. (An quantitative comparison is not offered here since ultimately the kinematic data is not determined by a parametric model but by a non-parameter model. The model is however useful in chapter ten to identify the reasons for the poor precision of the ψ -axis.) The subtle differences between the theoretical and actual transfer functions may be due to the issues raised in

chapter five (multipath, non alignment of the mechanical and optical axes and non-accurate placement of components).

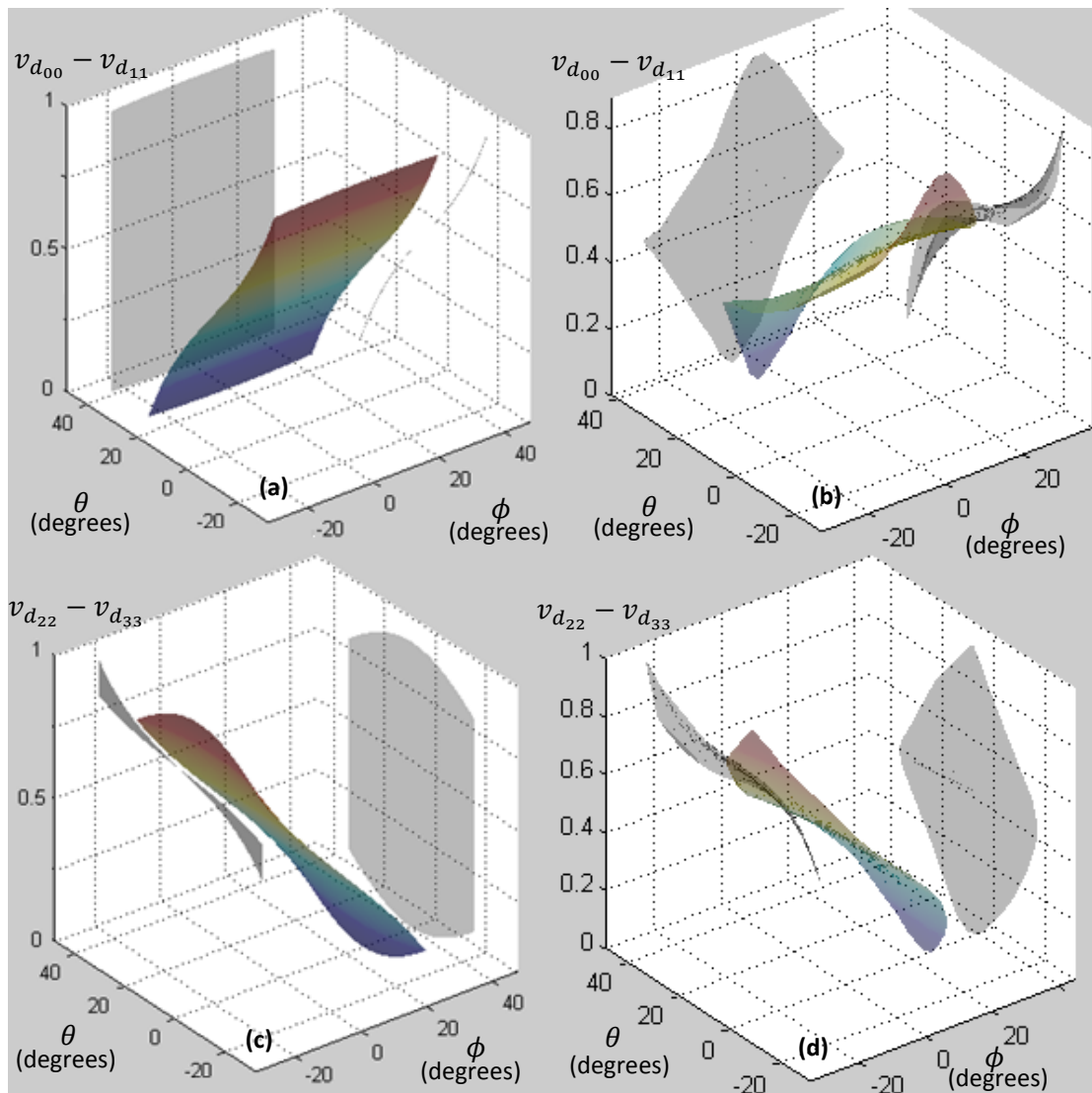


Figure 9.2: Transfer functions of detectors 0, 1 as determined by the a) theoretical model and; b) CaT instrument. Transfer functions of detectors 2, 4 as determined by the c) theoretical model and; d) CaT instrument.

9.2 Goniometer-Node Accuracy and Precision

The goniometer-nodes are the building blocks of the electrogoniometer. The accuracy and precision of the device is therefore directly related to that of the nodes. The CaT instrument generates a data set to which a polynomial fit is applied. Once calibrated, the nodes are

evaluated for accuracy and precision against a separate data set, using the same instrument.

The goniometer-nodes are calibrated by sampling detector outputs while systematically changing the kinematic (input) variables over the allowed range (the video clip [universal_joint_calibration](#) demonstrated how this is done for the universal joint). A polynomial function is fitted to the data and maps the detector voltages to the kinematic variables (equations 5.27 to 5.30). In the case of the cylindrical joint, six detector signals map to the d and ψ axes, and four detector signals to the ϕ and θ axes of the universal joints.

The approximation power of the polynomial functions is determined by the order of the functions. By increasing the order, the calibration data set can be approximated arbitrarily close (assuming the data conforms to the properties of a function). Care must be taken however to not over fit the data. Any practical data has noise embedded within. If the function order is too high, the function will fit the signal and the noise (a random process). To prevent this from happening, the polynomial function must be evaluated against a second data set. If the fit error is more or less the same in both data sets, the polynomial function captures the true underlying signal instead of the signal and noise. Empirical results suggested a fifteenth and sixth order fits are appropriate to approximate the cylindrical and universal joint transfer functions respectively.

The accuracy and precision of the five goniometer-nodes are presented in table 9.1. The average error (μ) (i.e. the difference between average measurement and the true value) is used as a metric for accuracy, and the standard deviation (σ) as a metric for precision. The blue highlighted column in the table is the average accuracy and precision across the nodes.

Joint	Kinematic variable	0_1T	1_2T	2_3T	3_4T	4_5T	Mean
Cylindrical	d ($\mu\pm\sigma$) mm	0.009 \pm 0.052	0.020 \pm 0.046	0.006 \pm 0.025	0.024 \pm 0.04	0.027 \pm 0.045	0.017 \pm 0.042
	ψ ($\mu\pm\sigma$) degrees	0.005 \pm 0.348	0.010 \pm 0.981	0.020 \pm 0.295	0.060 \pm 0.50	0.243 \pm 0.838	0.066 \pm 0.60
Universal	ϕ ($\mu\pm\sigma$) degrees	0.038 \pm 0.132	0.021 \pm 0.161	0.075 \pm 0.114	0.042 \pm 0.158	0.053 \pm 0.172	0.046 \pm 0.15
	θ ($\mu\pm\sigma$) degrees	0.027 \pm 0.151	0.015 \pm 0.134	0.015 \pm 0.234	0.011 \pm 0.187	0.013 \pm 0.156	0.016 \pm 0.17

Table 9.1: Accuracy (μ) and precision (σ) of the four kinematic variables as measured by the calibration and test instrument.

9.3 Measurement Setup and Qualisys Evaluation

9.3.1 Measurement Setup

A Qualisys video motion capture system (software: Qualysis track manager, version 2.9; cameras: Oqus 3), consisting of four cameras arranged in a half circle, was used to capture the kinematic data. The setup is shown in figure 9.3. The electrogoniometer was located at the desk, with the triads directed towards the cameras. The video motion capture system was calibrated before motion capture took place (residual error of 0.42 mm). The video motion capture sample rate was 60 Hz and 31.87 Hz for the electrogoniometer.



Figure 9.3: Qualisys video motion capture setup. The global reference frame (G) as defined by the Qualisys system is shown in red.

Triads, consisting of three 6.5 mm reflective markers, and spaced approximately 50 mm apart, were rigidly joined to the goniometer-nodes. A reference frame was calculated for each triad and attached to one of the markers as illustrated in figure 9.4.

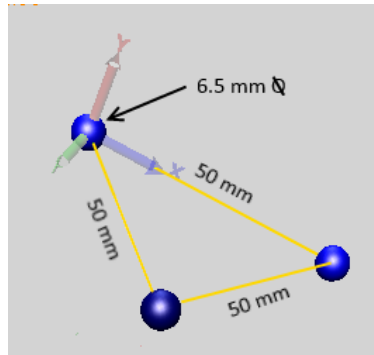


Figure 9.4: The triad with attached reference frame.

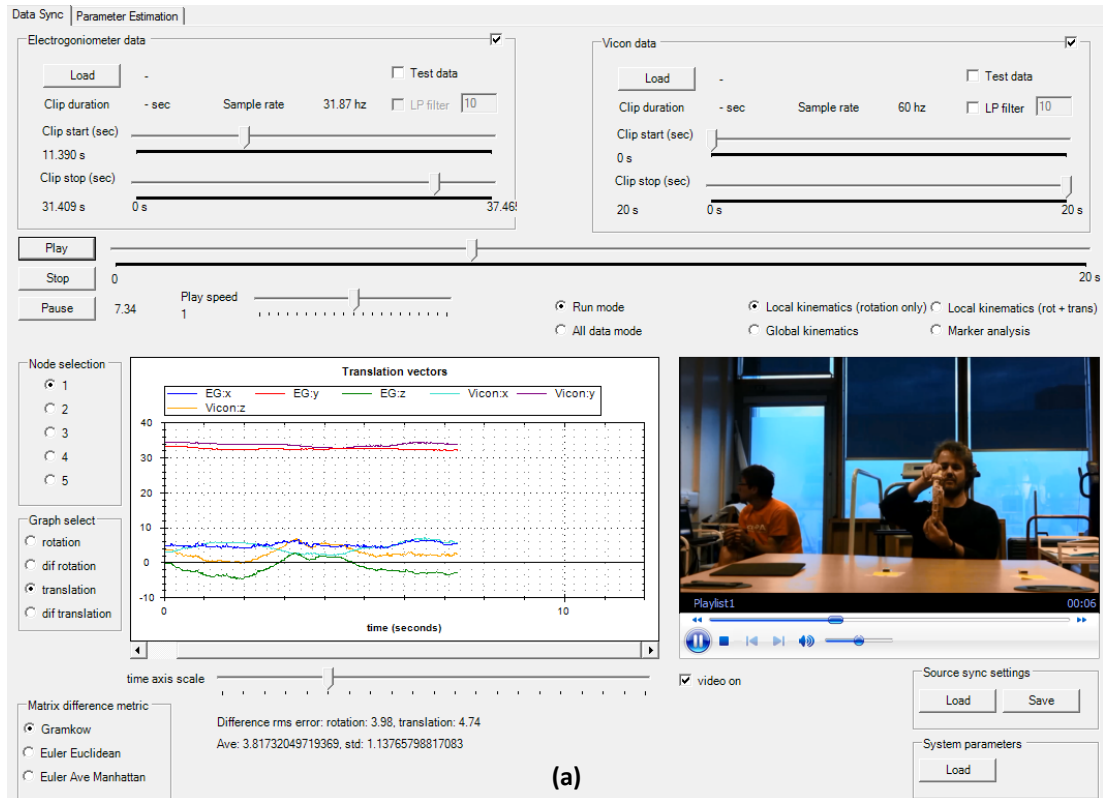
9.3.2 Data Acquisition and Analysis

An application was developed in XNA Game Studio using C# to process and analyse the data offline. XNA is widely used to develop 3D games. A major benefit of this development suite, is that most of the matrix functionality required to determine the kinematics have already been implemented. Secondly, the captured data can easily be displayed within a 3D virtual environment. The application performs the following tasks:

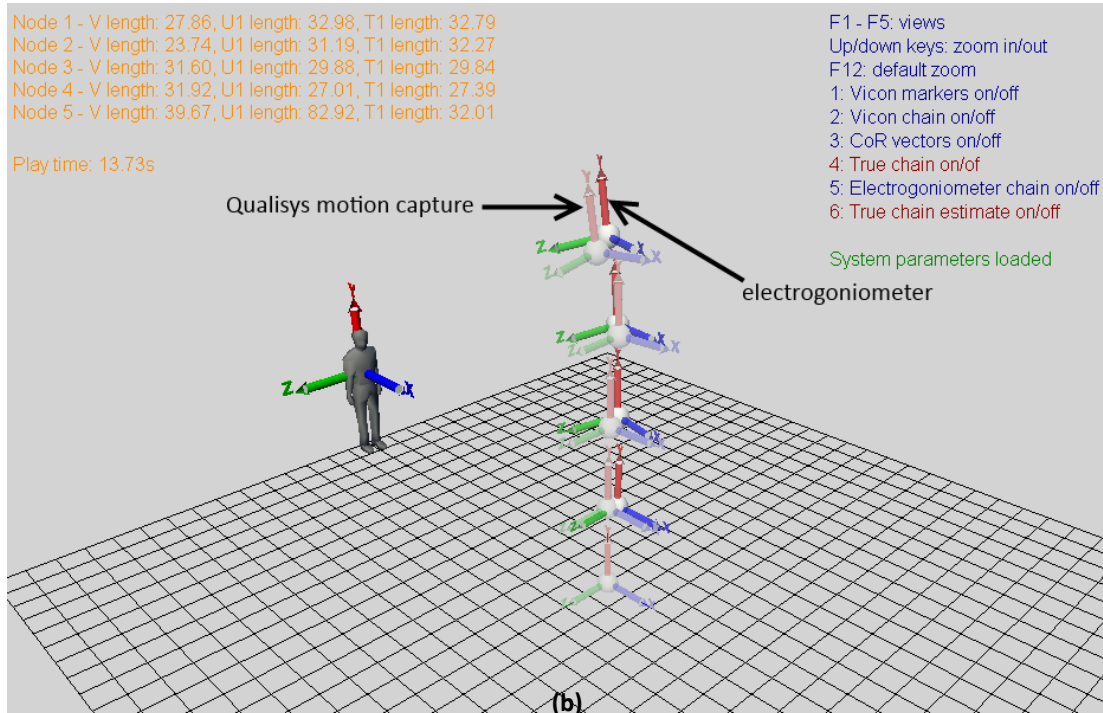
- Synchronise the captured Qualisys and electrogoniometer data;
- Implement the measurement method discussed in chapter eight (summarised in table 8.1);
- Compare and display the temporal Qualisys and electrogoniometer signals and
- Display the Qualisys and electrogoniometer results in a 3D environment in a comparative manner.

Screen captures of the application are shown in figures 9.5a and b. Figure 9.5a shows the graphical user interface. The temporal kinematic data shown in the graph of figure 9.5a is synchronised with the video (also in figure 9.5a) and the 3D representation of the serial kinematic chain (depicted in figure 9.5b).

Many of the results presented later in this chapter consist of temporal-spatial data which is difficult to display as static images. In such cases, references will be made to video clips included in the DVD accompanying this thesis.



(a)



(b)

Figure 9.5: a) The graphical user interface of the data analysis application; b) 3D rendering of the captured data by the same application. The Qualisys (U_i) chain is slightly transparent and the electrogoniometer (T_i) chain is solid in appearance.

9.3.3 Qualisys Evaluation

Marker based video motion capture systems are widely regarded as benchmark systems against which other systems and device can be compared (e.g. Wong and Wong (2009) and Williams et al. (2010)). The accuracy and precision of video motion capture systems were investigated in the literature review (section 2.2.2.1). Windolf et al. (2008) examined the accuracy and precision of a Vicon 460 system but the results were specific to their research study. It is outside the scope of this project to reproduce the Windolf study, but a simple experiment was however conducted to estimate precision. Accuracy was however omitted as it requires a more elaborate setup.

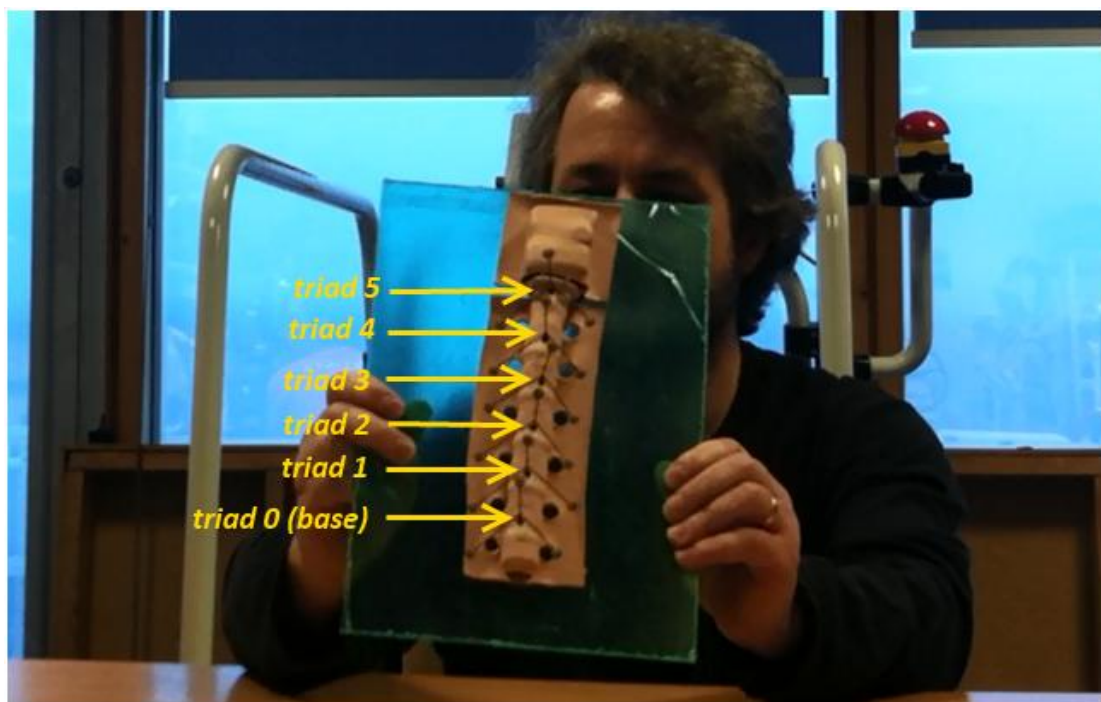


Figure 9.6: Static and dynamic testing of the Qualisys motion capture system. The device is attached to an acrylic sheet to ensure no inter-node movement occurs during testing.

The experiment investigated both the static and dynamic precision of the Qualisys motion capture system. The electrogoniometer was attached to an acrylic sheet, as shown in figure 9.6, to ensure no relative movement between triads. For the static test, the sheet was directed towards the cameras and kept motionless while being measured by the Qualisys system. The test was repeated but this time the acrylic sheet is moved about. The distance and orientation of a triad relative to the preceding triad was calculated and the precision determined for both the static and dynamic tests. As is the case of the CaT instrument results earlier, the standard deviation is used as a metric for precision. The precision

statistics for the V and U -chain reference frames are summarised in table 9.1 and 9.2 respectively.

The results show that the translation and rotation static precision is approximately a factor of four better than the dynamic precision for both the V and U -chains. It is further evident that the translation precision of the V -chain is significantly smaller than that of the U -chain. The phenomenon is a consequence of the manner in which the U -chain reference frames are calculated from the V -chain frames. The issue is discussed in chapter ten (section 10.3.3). The results show that rotation is however unaffected.

Precision (σ)		0_1V	1_2V	2_3V	3_4V	4_5V	Average
Translation	Static (mm)	0.020	0.010	0.014	0.027	0.016	0.017
	Dynamic (mm)	0.062	0.078	0.043	0.078	0.077	0.068
Rotation	Static (degrees)	0.090	0.087	0.016	0.056	0.022	0.054
	Dynamic (degrees)	0.181	0.236	0.154	0.216	0.234	0.20

Table 9.2: Qualisys static and dynamic precision as measured by the V -chain.

Precision (σ)		0_1U	1_2U	2_3U	3_4U	4_5U	Average
Translation	Static (mm)	0.052	0.028	0.067	0.023	-	0.043
	Dynamic (mm)	0.305	0.368	0.256	0.399	-	0.332
Rotation	Static (degrees)	0.090	0.087	0.016	0.056	0.022	0.054
	Dynamic (degrees)	0.181	0.236	0.154	0.216	0.234	0.20

Table 9.3: Qualisys static and dynamic precision as measured by the U -chain

9.4 Calibration

Before the electrogoniometer can be evaluated against the Qualisys motion capture system, a number of parameters have to be determined through calibration. These parameters (CoR, MLL and the neutral pose matrices) are specific to the measurement method discussed in chapter eight and can only be obtained through video motion capture.

9.4.1 Joint Centre-of-Rotation, Minimum Link Length and Pose Calibration

The joint CoR's of the electrogoniometer are determined by the SCoRE procedure outlined in section 8.2.2.1. The SCoRE method requires data based upon joint rotations only. A data set was subsequently acquired where the electrogoniometer was bent and twisted but, importantly, not stretched. Once the joint locations are known, the MLL is calculated as the distance between two adjacent joints.

The results summarised in table 9.4 shows the CoR fit error to be on average, less than 0.52 mm. The MLL determined from the CoR calculations are sensible results, and considering the manufacturing tolerances, agrees more or less with the original design requirements of 27 mm. Node four is however slightly shorter than the other nodes. This is due to a manufacturing mistake that could not be rectified afterwards.

Measurement	joint/node 0	joint/node 1	joint/node 2	joint/node 3	joint/node 4	joint/node 5	Mean±SD
Joint CoR fit error (mm)	0.47	0.44	0.62	0.49	0.56	0.56	0.52±0.068
Node MLL (mm)	n/a	32.11	31.80	29.80	25.60	n/a	29.83±3.00

Table 9.4: The CoR fit errors and MLL as calculated from the Qualisys motion capture data.

9.4.2 Neutral-Pose Calibration

Neutral-pose calibration determines the "correction" matrices needed to transform both the U and T -chains into a known pose. The pose presumes that the rotation of each reference frame is the identity matrix orientation, and the translation axis is aligned with the y axis. The neutral-pose calibration of the U and T -chains are completed simultaneously while the device is kept in pose position during motion capture. Based upon the captured data, ${}_{i+1}^i\mathbf{R}^{(U_0)}$ (equation 8.13) and ${}_{i+1}^i\mathbf{R}^{(T_0)}$ (equation 8.21) are calculated and saved as system parameters.

9.5 Electrogoniometer Evaluation

The electrogoniometer, with triads attached, was manipulated by hand for forty seconds while the accompanying data stream was recorded. The device, held at its proximal and

distal ends, was bent, twisted and stretched to ensure all joint axes experience motion. The Qualisys and electrogoniometer data were saved and then processed offline using the application described in section 9.3. The motion capture results, consisting of two video clips, are included in the *motion capture* folder of the accompanying DVD. Clips *local_kinematics* and *global_kinematics* show the local and global reference frame results respectively.

9.5.1 Local Accuracy and Precision

The local reference frames accuracy and precision results are reported in tables 9.5 and 9.6. Table 9.5 displays the error statistics of the Euclidean difference (equation 8.25) between the distal-ends as measured by the goniometer-node and Qualisys. Table 9.6 shows similar statistics but determined from the differences in rotations measured by the device and system (equation 8.32). The temporal error signals from which the statistics were calculated are shown in figure 9.8. The top figure shows the translation differences and the bottom figure the rotation differences for each of the four nodes.

The average location error across the four nodes is 3.5 ± 1.76 mm. The rotation error, based upon the average Manhattan difference between the Cardan angles, is $1.9 \pm 0.97^\circ$. The errors are larger than specified in the requirements (table 3.1). The causes of the larger than expected errors are discussed in the next chapter.

Local translation	$\ {}^0_1\mathbf{d}^{(U_1)} - {}^0_1\mathbf{d}^{(T_1)}\ $	$\ {}^1_2\mathbf{d}^{(U_1)} - {}^1_2\mathbf{d}^{(T_1)}\ $	$\ {}^2_3\mathbf{d}^{(U_1)} - {}^2_3\mathbf{d}^{(T_1)}\ $	$\ {}^3_4\mathbf{d}^{(U_1)} - {}^3_4\mathbf{d}^{(T_1)}\ $	Average
Accuracy (mm)	6.3	2.4	2.3	3.1	3.5
Precision (mm)	2.15	0.75	1.89	2.25	1.76

Table 9.5: Local accuracy and precision as calculated from the distance error metric (equation 8.25).

Local rotation	$\Phi_3({}^0_1\mathbf{R}^{T_1}, {}^0_1\mathbf{R}^{U_1})$	$\Phi_3({}^1_2\mathbf{R}^{T_1}, {}^1_2\mathbf{R}^{U_1})$	$\Phi_3({}^2_3\mathbf{R}^{T_1}, {}^2_3\mathbf{R}^{U_1})$	$\Phi_3({}^3_4\mathbf{R}^{T_1}, {}^3_4\mathbf{R}^{U_1})$	Average
Accuracy (degrees)	2.4	1.6	1.4	2.3	1.9
Precision (degrees)	0.90	0.99	0.92	0.99	0.97

Table 9.6: Local accuracy and precision as calculated from the rotation error metric (equation 8.32).

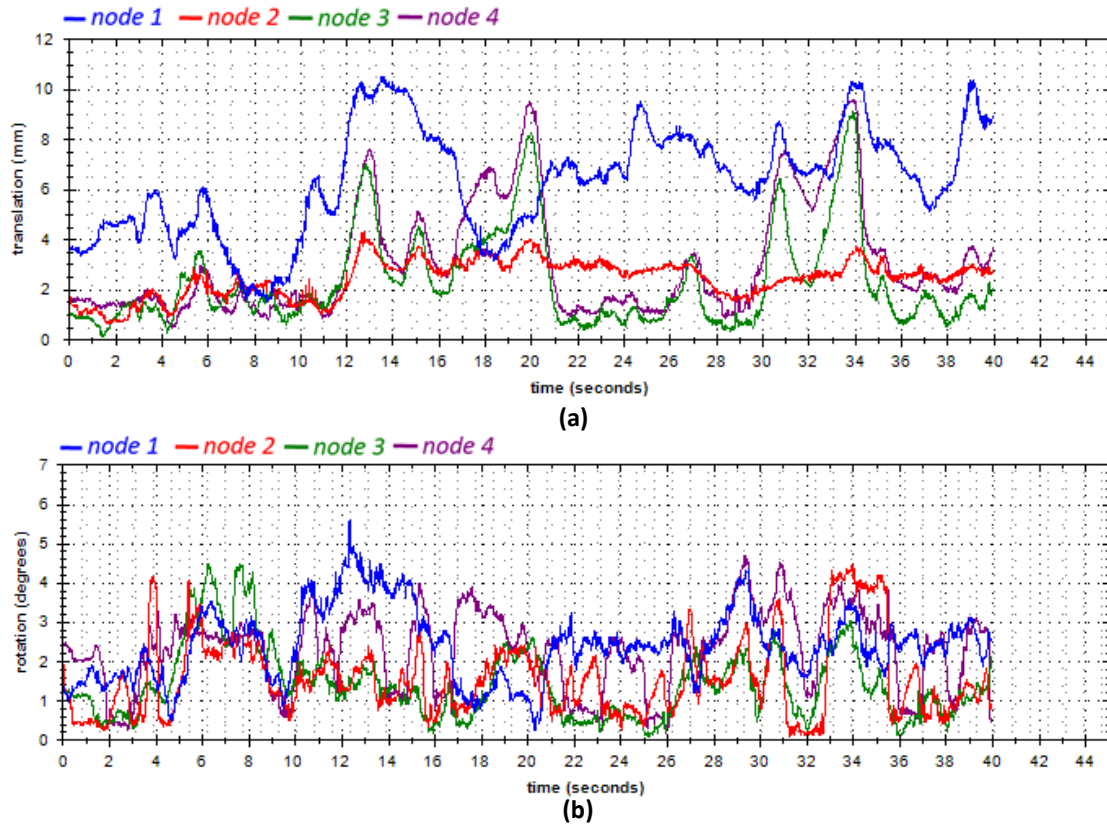


Figure 9.8: a) Local as calculated from the distance error metric (equation 8.25); b) Local as calculated from the rotation error metric (equation 8.32).

9.5.2 Global Accuracy and Precision

The global reference frame results are presented in a similar fashion to the local results. The global accuracy and precision are calculated relative to the base reference frame by applying the forward kinematics equation. The translation and rotation errors are then determined based upon the differences between the corresponding U_1 and T_1 -chain joints. Tables 9.8 and 9.9 summarise the difference translation and rotation statistics respectively as determined from error measurements obtained in figures 9.9ax and b. No average column is included since the global results are cumulative.

The global translation errors appear to accumulate through the chain. There is a 16.1 ± 6.0 mm difference between the location of the final node's distal-end as measured by the electrogoniometer and Qualisys systems. A similar accumulation phenomenon is apparent in the rotation errors. As a result, the two systems measure a rotation difference of almost $6.5 \pm 2.91^\circ$ at the final node. The mechanism of error propagation through the serial chain, is discussed in more detail in chapter ten (section 10.3.4).

Global translation	$\ {}^0_1\mathbf{d}^{(U_1)} - {}^0_1\mathbf{d}^{(T_1)} \ ^2$	$\ {}^0_2\mathbf{d}^{(U_1)} - {}^0_2\mathbf{d}^{(T_1)} \ ^2$	$\ {}^0_3\mathbf{d}^{(U_1)} - {}^0_3\mathbf{d}^{(T_1)} \ ^2$	$\ {}^0_4\mathbf{d}^{(U_1)} - {}^0_4\mathbf{d}^{(T_1)} \ ^2$
Accuracy (mm)	6.3	9.0	12.0	16.1
Precision (mm)	2.15	3.15	4.33	6.0

Table 9.8: Global error as calculated from the distance error metric.

Global rotation	$\Phi_3({}^0_1\mathbf{R}^{T_1}, {}^0_1\mathbf{R}^{U_1})$	$\Phi_3({}^0_2\mathbf{R}^{T_1}, {}^0_2\mathbf{R}^{U_1})$	$\Phi_3({}^0_3\mathbf{R}^{T_1}, {}^0_3\mathbf{R}^{U_1})$	$\Phi_3({}^0_4\mathbf{R}^{T_1}, {}^0_4\mathbf{R}^{U_1})$
Accuracy (degrees)	2.4	4.0	4.3	6.5
Precision (degrees)	0.90	1.64	2.25	2.91

Table 9.9: Global accuracy and precision as calculated from the rotation error metric.

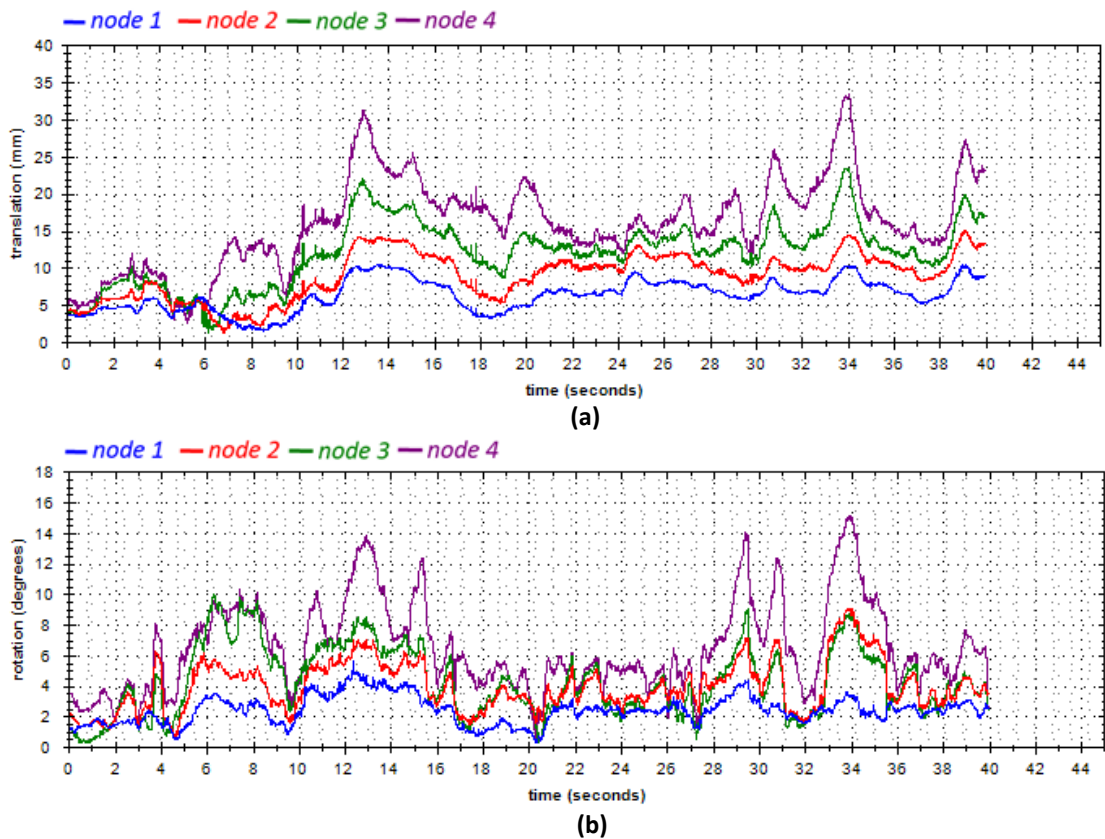


Figure 9.9: a) Global distance errors calculated from the distance metric; b) Global errors as calculated from the rotation error metric.

9.6 Conclusion

This chapter considered the results from comparing the CaT instrument and video motion capture against the electrogoniometer. The theoretical transfer functions of the universal and cylindrical joints were compared to actual measured transfer functions and showed good agreement. The accuracy and precision of the non-parametric fit were then determined by the CaT instrument for each goniometer-node. Average errors of 0.017 ± 0.042 mm for the d axis and $0.043 \pm 0.306^\circ$ for the rotation axes were measured. All the kinematic variables appear to have relatively small errors, except for the ψ axis precision error (0.60°), which was larger than expected. The cause of this error is discussed in chapter ten. According to the CaT instrument, all the errors are well within the ranges specified in chapter three.

The Qualisys motion capture system is assumed to be a valid benchmark against which the electrogoniometer can be compared. This claim was verified by measuring the static and dynamic precision of the six triads attached to the electrogoniometer. It was observed that the dynamic precision (0.068 mm and 0.204°) was approximately four times worse than the static precision (0.017 mm and 0.054°). This is however within the range of the precision to which the electrogoniometer will be measured. Furthermore, a difference in translation precision exists between the V and U -chains. As will be explained in chapter ten, the difference in translation precision (0.068 mm versus 0.33 mm for the V and U -chain respectively) is due to algorithmic calculations relating the U -chain to the V -chain. It will also be shown in chapter ten that this error contributes to the difference in measurements as reported by the CaT instrument and Qualisys system. Accuracy was not determined since a more involved experimental setup is required.

The calibration parameters essential to the measurement method presented in chapter eight were subsequently determined. These parameters were obtained from a video motion capture data set, which required the electrogoniometer to be bent and twisted but not stretched. The CoR and MLL parameters were obtained by applying the data to the SCoRE method. The CoR fit error was 0.52 ± 0.068 mm. The error is significant when compared to the dimensions of the goniometer-nodes and can therefore, as will be discussed in chapter ten, help to explain the differences between the electrogoniometer

and video system measurements. The neutral-pose calibration matrices were then calculated from a separate calibration procedure based upon a calibration-pose.

The final set of results reported on the accuracy and precision of the electrogoniometer as measured against a Qualisys video capture system. Average local accuracy and precision of 3.5 ± 1.76 mm for the translation and $1.9 \pm 0.97^\circ$ for rotation were measured. Global error results revealed that the local errors accumulated through the chain. The global translation and rotation errors of the last node in the chain, were reported to be 16.1 ± 6.0 mm for translation and $6.5 \pm 2.91^\circ$ for rotation measurements.

It is clear from the above that the local accuracy and precision measurements, when using the video motion capture system is poorer than expected. Yet when compared to the CaT instrument, the errors appears to be well within the bounds specified in chapter three. There is a number of reasons for this apparent discrepancy which is extensively discussed in chapter ten.

10. Discussion and Concluding Remarks

This chapter discusses the results presented in chapter nine and provides an overall commentary on the entire project. The calibration and test results are first considered. It is evident from the results that the ψ axis has poorer precision than the other three kinematic variables (θ , ϕ and d). The cause is traced to the sensitivity response, which in turn is attributed to the locations of the detectors within the mechanical structure. To improve precision, solutions are suggested to solve the poor sensitivity issue.

The Qualisys motion capture system as a benchmark is then scrutinised. Based upon the static and dynamic precision measurements and results reported in literature, it is concluded that the system is adequate to evaluate the electrogoniometer.

Following on from this, the results comparing the electrogoniometer against the Qualisys system are discussed. The two systems show good agreement but is worse than the comparative results obtained when the CaT instrument is used as benchmark. The reasons for the differences between the two sets of results are discussed. These include: the CaT instrument results were obtained under static conditions compared to the Qualisys results measured under dynamic conditions; the CaT instrument has unknown calibration and testing characteristics; and the measurement method introduced unavoidable errors in the measurement and local reference frame errors propagate through the serial kinematic chains. Collectively these issues add an uncertainty to the electrogoniometer results when benchmarked against the Qualisys system.

The thesis concludes with comments on the research project in general. These include the problems that manifested during the engineering of the device, whether the original goals set out in the introduction have been achieved and future work to refine and perhaps commercialise the device.

10.1 Discussion of Calibration and Test Instrument Results

According to table 9.1, the nodes exhibit excellent accuracy and precision when evaluated against the CaT instrument. The exception is the ψ axis with an average precision of 0.60° (highlighted in red in table 9.1). The precision is much larger than the 0.15° and 0.17° reported for the ϕ and θ axis respectively. (These values are well within the accuracy and resolution measurements stated for the CaT instrument in chapter seven and can therefore not be attributed to the instrument.) Considering that nodes measure relative to a local reference frame, good precision is critical to ensure the electrogoniometer's global measurements are precise as well. Understanding the cause of the poor precision is therefore essential, as it impacts the overall performance of the device.

Poor precision is related to poor sensitivity. Sensitivity is defined as the amount of change in the detector voltage in response to a change in ψ (i.e. the derivative of $v_{d_{ji}}$ relative to ψ) (Bentley, 2005), i.e.:

$$S_{ji} = \left| \frac{\partial v_{d_{ji}}(\psi, d)}{\partial \psi} \right| \quad \text{where } (j, i) \in \{(0,0), (0,1), (0,2), (1,0), (1,1), (1,2)\} \quad \text{equ 10.1}$$

Here, the absolute value of the sensitivity is used since any change (being it a negative or positive gradient) is an indication of sensitivity. Figures 10.1a to c show the sensitivities of detectors 0, 1 and 2 (see figure 5.3 for detector labeling) as determined by the responses of the theoretical model. The average sensitivity of the three detectors are shown in figure 10.1d. Values close to zero (shown as darker grey in figure 10.1d) represents poor sensitivity and lighter shades of grey represent good sensitivity.

The average sensitivity as depicted in figure 10.1d, shows regions with poor sensitivity. An inspection of figure 9.1 clarifies why this is the case. Due to the non-linear response of the detector outputs, the signal amplitude quickly diminish as δ increases. However, the complementary detectors (3, 4 and 5) (figure 5.4) help to reduce the decline in sensitivity. Thus as the sensitivity of detectors 0, 1 and 2 decrease, the sensitivity of the detectors 3, 4 and 5 increase.

Secondly, the sensitivity of the detectors at their ψ axis locations is zero. For example in figure 10.1b, the gradient (and therefore sensitivity) of detector 1 is zero at $\psi = 0^\circ$ and all

values of d . Adjacent emitter-detectors do compensate to some extent for this lack of sensitivity but have a limited range.

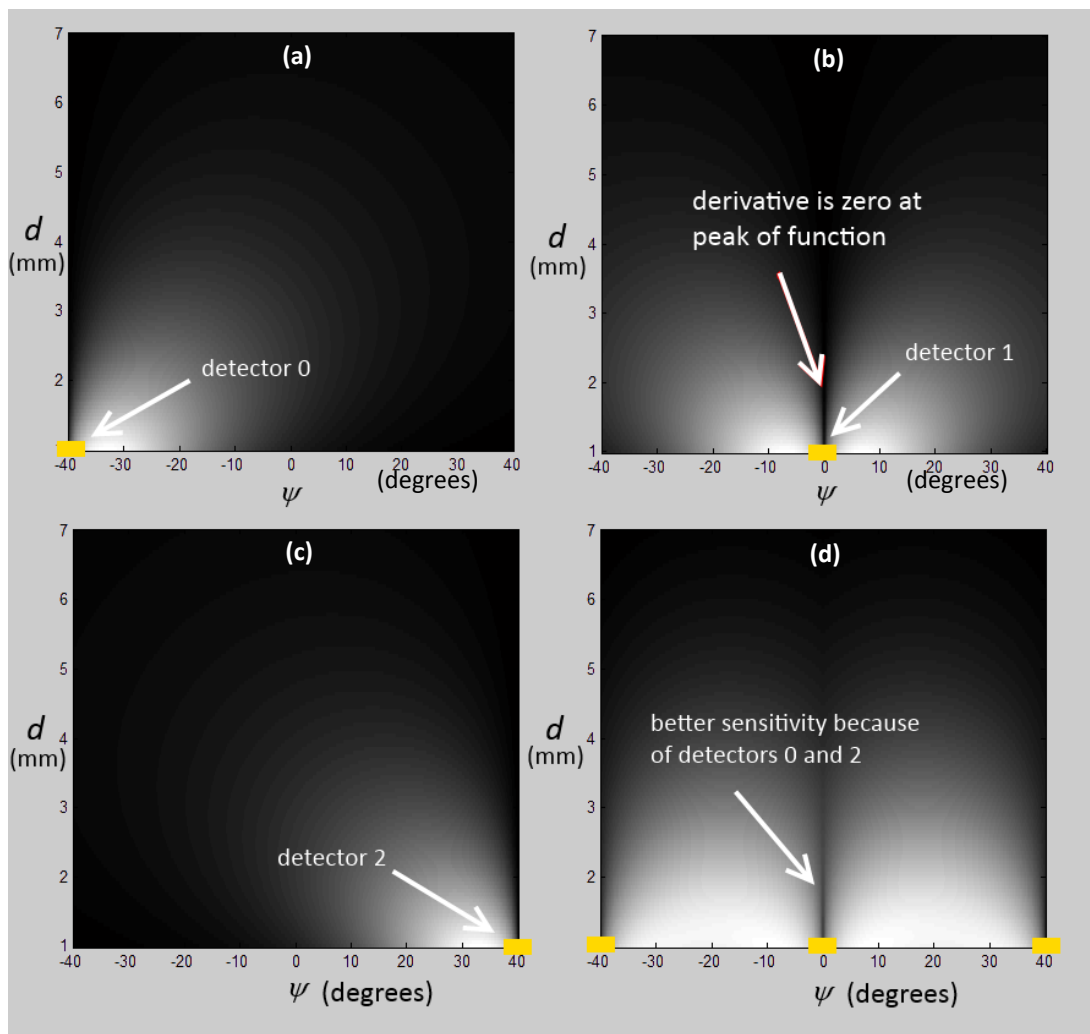


Figure 10.1: Sensitivity versus the precision of the ψ axis (lighter shades of grey represent good sensitivity): a) Sensitivity of detector 0; b) Sensitivity of detector 1; c) Sensitivity of detector 2; d) Average sensitivity of the three detectors.

The poor precision of the ψ axis is directly related to the sensitivity issue discussed above. The relationship between sensitivity and precision is illustrated in figure 10.2. The figure shows a cross-section of the transfer function of detector 0 and with $d = 1$ mm. Consider the derivatives at A and B in the figure. In the case of A, a change in ψ cause a significant change in $v_{d_{00}}$. In the case of B, the same change in ψ causes less change in $v_{d_{00}}$. A is therefore much more sensitive to changes in ψ than B. Now consider the inverse direction for B. A small change in $v_{d_{00}}$ will represent a large change in ψ . Stated differently, ψ is very sensitive to changes in $v_{d_{00}}$. Therefore, when a node determines ψ from the detector

measurements, any noise embedded in the measurement will cause significant changes in the value of ψ when calculated from the appropriate polynomial function. The variable ψ thus exhibits poor precision due to poor sensitivity. Fortunately the other axes do not suffer from this particular problem since their responses are more linear (see figure 9.2).

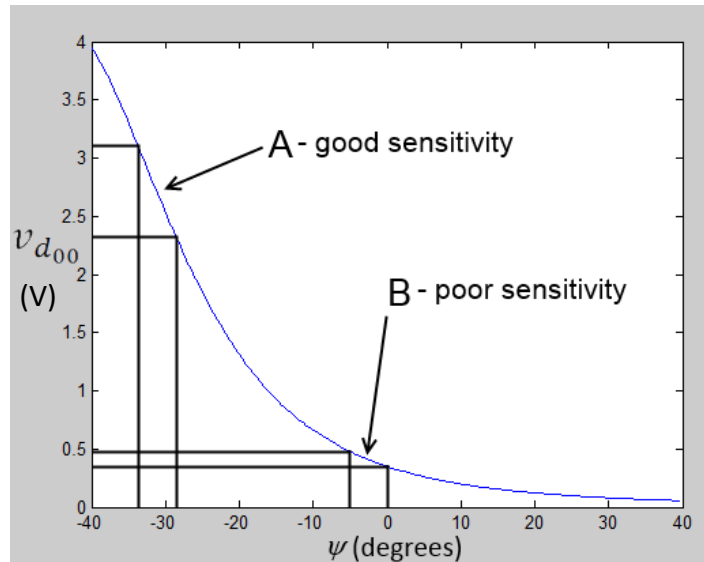


Figure 10.2: Different sensitivities of the transfer function detector 0 where $d = 1$ mm.

The sensitivity (and by implication the precision) can be improved in a number of ways. The first is to embed more detectors, which will consequently improve the average sensitivity response. Secondly, detectors and emitters with different spatial directivity patterns can be used. And thirdly, the detectors can be located closer to each other (but at the cost of the reducing the range of ψ). The easiest solution is however to simply adjust the gain. A gain factor, g (where $g > 1$), improves the sensitivity proportionally, i.e.:

$$S_{ji} = g \left| \frac{\partial v_{a_{ji}}(\psi, d)}{\partial \psi} \right| \quad \text{where } (j, i) \in \{(0,0), (0,1), (0,2), (1,0), (1,1), (1,2)\} \quad \text{equ 10.2}$$

Unfortunately because of practical reasons, none of the above solutions were implemented to the already constructed electrogoniometer. In a future development the solutions can be included as parameters within the theoretical model developed in chapter five. The model can then be solved as an optimisation problem to obtain a more even (constant) sensitivity.

10.2 The Qualisys System as a Benchmark

Up to now the Qualisys motion capture system was assumed to be an adequate measurement system against which the electrogoniometer can be compared. The CaT instrument can act as a similar benchmark but has two drawbacks. Firstly, it can only evaluate (after calibration) goniometer-nodes (thus local reference frame measurements), and secondly not all of its performance characteristics are known (despite that fact that off-the-shelf components were used for its construction). The specifications of the instrument as stated in table 7.1 are mostly based upon the characteristics of off-the-shelf components. However the instrument's performance characteristics also depends on being manufactured accurately. For example, whether the instrument's axes are accurately aligned with that of the goniometer-node's axes are difficult to determine. Consequently a measure of uncertainty is introduced.

10.2.1 Translation Errors

Section 9.2.3 reported on a simple experiment where the electrogoniometer was attached to a rigid acrylic sheet and then static and dynamic measurements were taken. The average static precision was obtained from the empirical results and is summarised in table 9.2 was $17.4 \mu\text{m}$. Windolf et al. (2008) reported similar static precision results of between 15 to 21 μm (dependent on the setup).

Unfortunately it was not possible to determine the experimental accuracy here. It requires a sophisticated setup similar to the one designed by Windolf and is therefore not part of the scope of this research project. However, since the measured and literature precision agree well, it is assumed the translation accuracy claimed by Windolf also has some validity here. Windolf reported a range of accuracies depending on the specific setup (i.e. marker size, camera position, lens filter and calibration). The Windolf setup with four cameras, marker size of 9.5 mm, lens filters used and full calibration is the closest to the setup described in chapter nine. Windolf reported the accuracy for their particular setup to be approximately $135 \mu\text{m}$ (figure 8, Windolf et al. (2008)). This value is consequently used as an estimate for the translation accuracy in the electrogoniometer setup.

10.2.2 Rotation Errors

Windolf's study did not include an analysis of the rotation errors, neither did the experiment in section 9.2.3. An elementary calculation is made here to estimate an upper

bound of the rotation accuracy about a single axis based upon the translation accuracy. The calculation, illustrated in figure 10.3, presumes the 135 μm translation accuracy reported earlier. Assuming the error is perpendicular to the rotated axis, a worst case scenario is established. The accuracy is then $a = \sin^{-1}\left(\frac{0.135}{25}\right) = 0.3^\circ$.

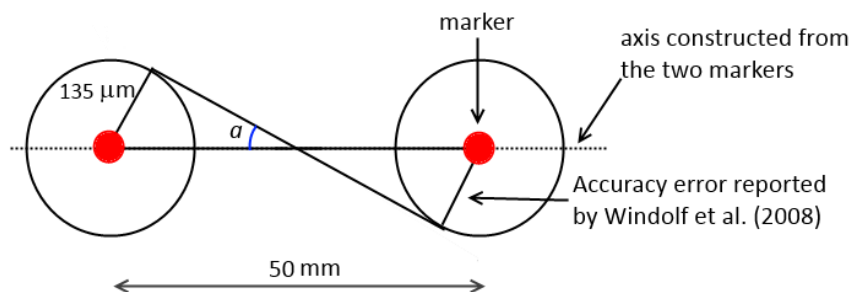


Figure 10.3: Upper bound estimation of the rotation error about a single angle based upon the accuracy reported by Windolf using a 9.5 mm marker.

A rotation error of 0.3° does not seem excessive. A study comparing different motion capture system done at Nippon Engineering College in Tokyo, more or less confirms this calculation. Their results were not peer-reviewed but are available to view at www.ne.jp/asahi/gait/analysis/comparison2002/Result/basic/basic_eng.html. In their study researchers mounted three markers (marker sizes and distances not stated) on triangle plates, and reported a rotation error of 0.14° for the Vicon system. An angle of 0.14° appears to be a good average for the 0.3° upper bound calculated above.

To summarise, under static conditions marker location can be measured to an accuracy and precision of approximately 135 μm and 17.4 μm respectively. Rotation errors of less than 0.3° can be expected under static conditions. It is consequently concluded that the Qualisys system has adequate accuracy and precision to measure location and rotation for the task at hand. The system offers better accuracy than the node accuracy requirements stated in chapter three (table 3.1).

10.3 Discussion of the Electrogoniometer Results

The electrogoniometer, when measured against the Qualisys system, showed average local accuracy and precision of approximately $2.0 \pm 1.0^\circ$ (table 9.6). However, according to table

9.1, the CaT instrument measured node errors of better than $0.066 \pm 0.60^\circ$. The results of the two systems therefore differ significantly.

The reasons for the difference in errors reported by the two systems are now investigated. It should be noted that the manner in which the two systems measure translation errors differs. The Qualisys system measures the difference as stated by equation 8.25 (i.e. the Euclidean distance between the two rotated and then translated frames). The CaT instrument however measures the difference between the translation components only. A direct comparison of the two sets of translation errors can therefore not be made.

10.3.1 Static versus Dynamic Measurements

The CaT instrument measures under static conditions. The goniometer-node is sampled while the mechanical axes are stationary and to reduce noise, measurements are calculated as the average of an ensemble of samples. The Qualisys system results however were acquired under dynamic conditions, i.e. the electrogoniometer with attached markers was bent and twisted as demonstrated by the video clip [global_kinematics](#).

An evaluation of the Qualisys system confirmed that the static and dynamic measurements differ significantly. The empirical results stated in table 9.2, indicate that the translation precision typically decreases from $17.4 \mu\text{m}$ under static conditions to $67.6 \mu\text{m}$ under dynamic conditions. Rotation precision exhibit a similar trend with a decrease from 0.054° under static to 0.20° under dynamic conditions. Thus, an almost four fold increase for both the translation and rotation precision were measured.

It is therefore expected that the dynamic nature under which the electrogoniometer was evaluated (against the Qualisys system), will cause a reduction in accuracy and precision. It is however not only the Qualisys system that is more prone to error, but also the electrogoniometer, as it measures under dynamic conditions as well. It is beyond the scope of this research to quantify how much the dynamic measurements affect the accuracy and precision. The effect can however be reduced by increasing the sample rate and/or reducing the movement (dynamic) speed.

10.3.2 Errors introduced by the CaT Instrument

The CaT instrument has unknown measurement characteristics. Off-the-shelf electronic and mechanical components were used with known performance characteristics. However, an

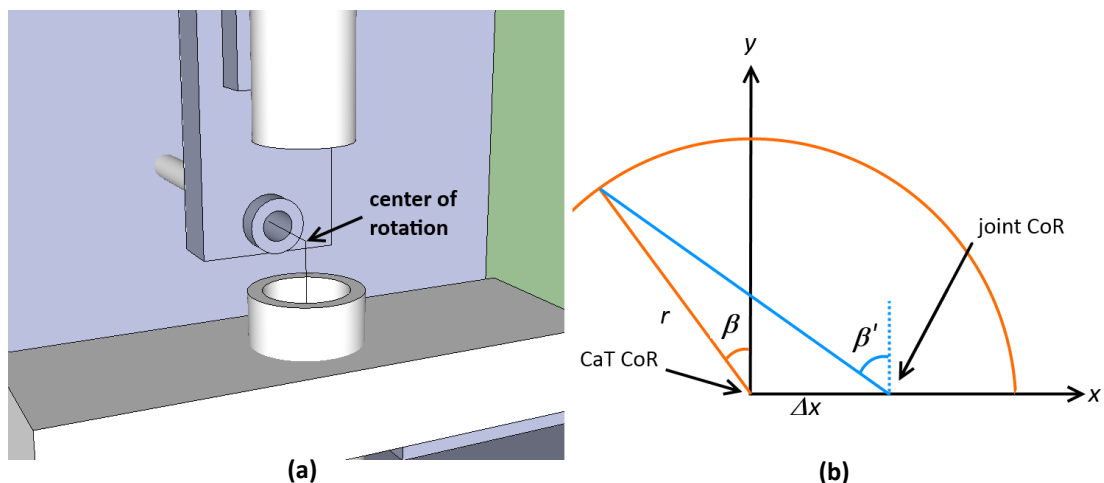
inaccurate assembly of the instrument will inadvertently introduce measurement errors. A specific concern with the instrument is the alignment of the instrument, and the universal joint centre-of-rotations (indicated in figure 10.4a). The alignment was done by hand and will therefore introduce an uncertainty into the setup. Given the millimeter dimensions of the goniometer-node, even tens of micrometers misalignment can have a significant impact on the accuracy of the instrument. Misalignment is graphically illustrated in figure 10.4b. Only rotation about the instrument's β axis is considered here since the α axis has a similar analysis. The misalignment angle, β' , to which the universal joint is subjected to, assuming a true angle of rotation β and rotation radius r , is:

$$\cos^2 \beta' = \frac{r^2 \cos^2 \beta}{r^2 + \Delta x^2 + 2r \Delta x \sin \beta} \quad \text{equ 10.3}$$

The angle error due to the misalignment is therefore:

$$\varepsilon = \beta - \beta' \quad \text{equ 10.4}$$

Figure 10.5c demonstrates the predicted error ($r = 4.6$ mm, misalignment $\Delta x = 250$ μm) over a 20° calibration range. Although the misalignment is relatively small, the resulting error is approximately 3° , with a change of about 0.25° . The measurement method (discussed in chapter eight) should however remove the 3° offset since it is a systematic error. The 0.25° variation can however not be removed since it is a random error.



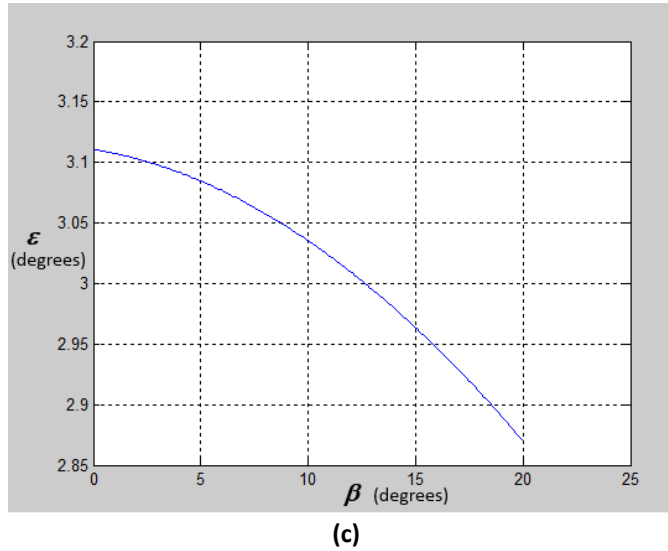


Figure 10.4: a) The CoR of the CaT instrument; b) Misalignment of the CaT instrument's CoR and the universal joint's CoR will cause the joint to be subjected to an angle of β' instead of β degrees; c) The angular error due to the misalignment where $r = 4.6$ mm and with a misalignment of $\Delta x = 250$ μm .

10.3.3 Errors introduced by the Measurement Method

The measurement method (summarised in table 8.1) is also a source of errors. It is evident from tables 9.5x and 9.6 that the translation errors are correlated with the rotation errors. This is expected since the translation component of reference frame ${}_{i+1}{}^i T_1$ is a function of the rotation (see equations 8.20 and 8.23). That is, any rotation errors within ${}_{i+1}{}^i R^{(T)}$ will also affect ${}_{i+1}{}^i d^{(T_1)}$ since:

$${}_{i+1}{}^i d^{(T_1)} = {}_{i+1}{}^i R_0^{-1} {}_{i+1}{}^i R^{(T)} \begin{bmatrix} 0 & {}_{i+1}{}^i \delta_0^{(U)} + {}_{i+1}{}^i \delta_1^{(T)} & 0 \end{bmatrix}^T \quad \text{equ 10.5}$$

A similar argument can be made for the translation errors associated with the ${}_{i+1}{}^i U$ reference frame. The transformation ${}_{i+1}{}^i U$ in terms of ${}_{i+1}{}^i V$ is (equation 8.11):

$${}_{i+1}{}^i U = {}_{i+1}{}^i U_V {}_{i+1}{}^i V {}_{i+1}{}^i V_U \quad \text{equ 10.6}$$

where the translation component of the above equation is (equation 8.12):

$${}_{i+1}{}^i d^{(U)} = {}_{i+1}{}^i R^{(V)} {}_{i+1}{}^i d^{(V_U)} + {}_{i+1}{}^i d^{(V)} + {}_{i+1}{}^i d^{(U_V)} \quad \text{equ 10.7}$$

The translation component ${}_{i+1}{}^i d^{(U)}$ (and by implication ${}_{i+1}{}^i d^{(U_1)}$) thus depends on the rotation matrices, and any errors in the rotation matrices will also therefore be present in corresponding translation components. Based upon the above analysis, it is clear that the

correlation between the translation and rotations components are unavoidable and this is a drawback of the measurement method.

A second cause of errors is introduced by the SCoRE method. The method relies on a system of equations, describing the joint rotation kinematics, to be solved. The CoR fit error, summarised in table 9.4, is approximately 0.5 mm. The error may have a significant effect on the global errors, given the local errors propagate through the kinematics chain, as will be discussed in the next section.

10.3.4 Propagation of Local Errors through a Kinematic Chain

In section 5.1.6 it was argued that local (as appose to global) reference frame measurements are one of the detractors of the optical sensing method employed here. Figure 9.9 clearly shows that the global errors (both translation and rotation) accumulate through the chain, i.e. errors of node i relative to node 0 are larger than that of the preceding node's global errors. Precision will always accumulate through the chains. However, it is not necessarily the case for accuracy. To help explain this concept, the propagation of local errors through the serial kinematic chain is illustrated graphically in figure 10.5. To keep the discussion simple, it is assumed that the device is held in the calibration pose. All the axis are therefore aligned so that the local rotation is the identity matrix. It is further assumed that there is only rotation errors about the z axis. Translations are not considered. The rotation errors of local frame i are assumed to be a random variable, ${}^{i-1}\theta$, with a normal distribution and parameters $N({}^{i-1}\mu, {}^{i-1}\sigma^2)$ as shown in figure 10.5a.

The global errors of frame i are also then a random variable and parameterised by ${}^0\theta = N({}^0\mu, {}^0\sigma^2)$. If it is assumed that the random variables of the local reference frames are uncorrelated, then the global accuracy is (Hayter, 2012):

$${}^0\mu = \sum_{j=1}^i {}^{j-1}\mu \quad \text{equ 10.8}$$

The accumulation of the global errors is depicted in figure 10.5b. According to the above equation, as long as the local accuracy are unbiased, the global accuracy will fluctuate about zero (i.e. not accumulate). Unfortunately the empirical results suggest this not to be the case. The global accuracy measurements reported in tables 9.8 and 9.9 show the accuracy decrease through the chain (for both rotations and translations). A correlation

therefore exist between the accuracy. The cause of the correlation is unclear, but may be due to the CaT instrument's unknown calibration accuracy.

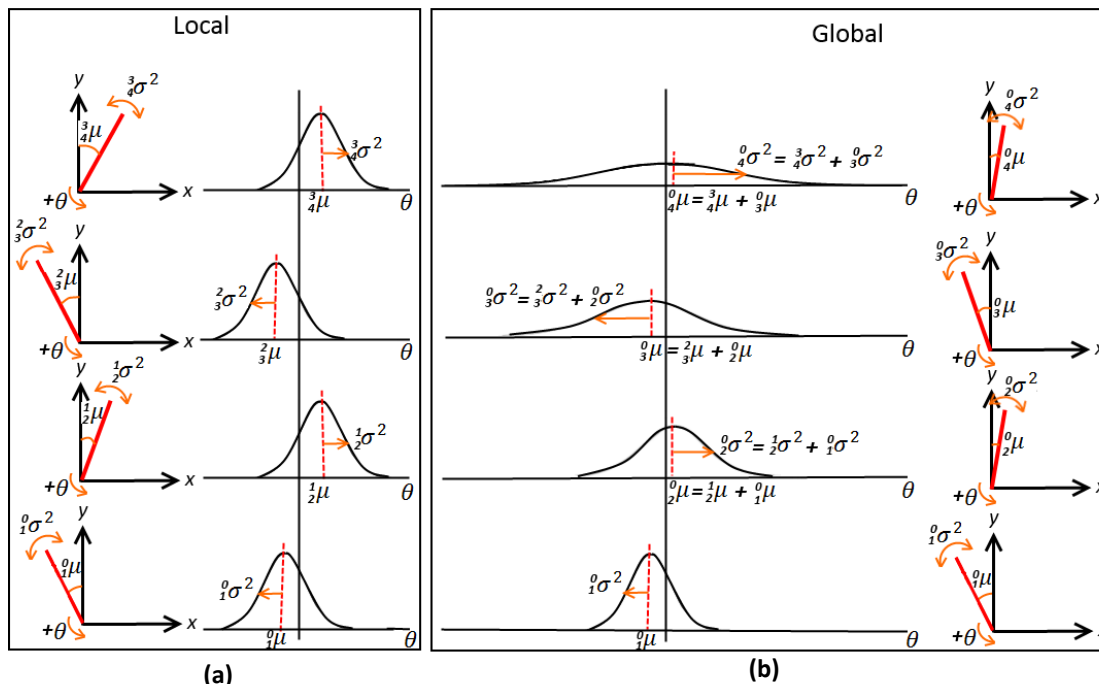


Figure 10.5: Statistical nature of the local and global accuracy and precision for the example stated in the text. The example assumes the local accuracy are unbiased. a) Local reference frame errors; b) Global reference frame errors.

Given the previously assigned random variables, the global precision is:

$$^0\sigma^2 = \sum_{j=1}^i {}^{j-1}\sigma^2 \tag{equ 10.9}$$

Unlike the global accuracy, the above equation implies the precision will always accumulate since $^{i-1}\sigma^2$ is positive. The outcome of this accumulation of errors causes a "smearing" of the distribution functions in figure 10.5b. This "smearing" is because mathematically, the global precision of a node is determined by convoluting its local distribution with the global precision of the preceding node.

10.4 Concluding Remarks

10.4.1 Engineering Issues

This research project proved to be an enormous undertaking. There were two versions of the CaT instrument built. Construction proved to be challenging. After completing the first

version, a number of design mistakes were identified. The second version solved most of the problems but further improvements can still be made. In particular, the accurate CoR alignment of the goniometer-nodes and instrument remains an issue.

A major source of difficulty was the manufacturing of the smaller mechanical parts. Tight tolerances were required, since any backlash/play will cause a hysteresis/deadband to be present in the measurements. This is particularly true in the case of the universal joint (figure 6.5a). About fifteen joints were manufactured by hand using off-the-shelf brass tubing. To complicate matters, solder wire with different temperature characteristics had to be used on different sections of the joints. Of those manufactured, only joints that moved freely without any noticeable backlash were used. Furthermore, wires connecting moving mechanical parts constantly failed due to metal fatigue (especially during the CaT calibration process), despite using high strand count wiring. The total cost of all the hardware (including the two CaT instruments) was approximately £3800.

10.4.2 Global versus Local Measuring Devices

In hindsight, the question may be asked whether it was sensible to design a device based upon local reference frame measurements instead of global measurements? Global measurements have a distinct advantage over local measurements. However, it must be remembered that the inertial-magnetic sensors, which is arguably the only feasible global measurement solution, also has its drawbacks. The author has had a fair amount of experience with these types of sensors, and given their disadvantages, is of the opinion that local optical sensing method is a promising alternative.

10.4.3 Research Aims

In chapter one the primary research aim was stated to be: "... to develop a non-invasive device that can accurately and precisely measure spinal movement down to the inter-vertebrae articulation. The device must be unobtrusive and suitable to monitor spinal kinematics in a non-clinical environment." A number of requirements called for in chapter three were not met and the prototype therefore did not quite attain the research aim.

The first is the accuracy and precision. The measurement procedure (consisting of the measurement method and calibration process) was identified in the first part of this chapter as the stumbling block. The procedure consisted of many different facets. A string

of small errors introduced along the way, will consequently affected its overall legitimacy. The electrogoniometer is therefore not necessarily entirely at fault, but errors can also be attributed to the measurement method and calibration process itself.

A valid question is: if these issues are solved, can the optical sensing method employed here, ever achieve the accuracy and precision necessary to construct an electrogoniometer with performance approaching that of video capture systems? The answer can be found in the CaT instrument results of table 9.1. With the exception of the ψ axis (and for reasons already explained), all the kinematic variables exhibit excellent accuracy and precision. The CaT instrument's performance is questionable, but this can be improved upon. The fact remains, when presented with the instrument's kinematic input, the optical sensing method was capable of accurately and precisely estimating these inputs down to a fraction of a degree.

10.4.4 Specifications

As discussed earlier, the ideal specifications stated in chapter three were not all met. The actual and original specifications are summarised in table 10.1. The original values are stated in brackets and the actual values are coloured-code (green if the specification was met and red if it was not met).

	Property	Value
Electrogoniometer	Diameter	20 mm (15 mm)
	Number of goniometer-nodes	5 (5)
	Mobility	20 DOF (20 DOF)
	Bend radius	90 mm (90 mm)
	Percentage stretching in long axis	22% (33%)
Goniometer-node	Communication method	Wireless (Bluetooth)
	Mobility	4 DOF (4 DOF)
	Rotation range (each axis)	-22° to 23° (-20° to 20°)
	Rotation accuracy	3.5° (2°)
	Rotation precision	1.76° (0.5°)
	Displacement range	0 to 7 mm (0 to 9 mm)
	Displacement accuracy	17µm (0.2 mm) (according to CaT instrument)
	Displacement precision	42µm (0.1 mm) (according to CaT instrument)
	Displacement range	30 to 37 mm (27 to 36 mm)
	Resolution	0.1° for rotation, 15µm for translation (0.2° for rotation, 20 µm for translation)
	Sample rate	32 Hz (30 Hz)

Table 10.1: Summary of the actual and original specifications of the electrogoniometer and goniometer-nodes (original specifications are in brackets; green: actual specification is better than original specification; red : actual specification is worse than original specification).

The reasons for not meeting the accuracy and precision specifications have been discussed extensively above. Other specifications not met are the node dimensions. The diameter is about 20 mm (including the skin), which is more than the recommended 15 mm, making it slightly more obtrusive. The nodes are also about 10% longer than the 27 mm specified. Furthermore, the maximum extension/translation of the goniometer-node was required to be 9 mm, but in reality it is about 7 mm. The dimensions have an impact on the obtrusiveness of the device. Despite not meeting all the specifications, the concepts has been validated and lays the foundation for a future developments.

10.4.5 Applications

The electrogoniometer evaluated here has somewhat limited spinal measurement applications since not all specifications were met. Lateral flexion and axial rotation can be measured given that the range of motion of the device ($22^\circ/\text{axis}$) is greater than that of the spine (up to $15^\circ/\text{axis}$). Sagittal flexing may however be difficult to measure since the electrogoniometer can only extend (stretch) approximately 22% (compared to the 33% specified for an "average" spine). Furthermore, since the electrogoniometer consists of only five nodes, it can only measure a partial spine (e.g. the lumbar spine). And finally, the accuracy and precision of the electrogoniometer limits the applications of the device to studies which do not require video motion capture accuracy.

The electrogoniometer offers similar accuracy to the fibre-optic goniometer discussed in chapter two (6.5° versus 5° for the electrogoniometer and fibre-optic goniometer respectively). The electrogoniometer however has a mobility of twenty DOF compared to the two DOF of the fibre-optic goniometer.

Despite the limitations of the prototype device, it does have applications in monitoring spinal activities in a free-living environment. A good example is assessing post-surgery spinal mobility as part of the rehabilitation process. Duc et al. (2013) measured the cervical activities (lateral bending, axial rotation or flexion–extension) in a free-living setting using two inertial sensors. Unlike the limited mobility of the inertial sensors, the electrogoniometer proposed here can measure spinal mobility over five motion segments, thus providing a much clearer picture of the mobility of the spinal segment under investigation.

Due to the large bend radius, the electrogoniometer has limited applications in measuring knee, elbow and shoulder movement. The hips are however another joint that can be monitored. During normal gait hip motion is on average 52° in the sagittal plane, 12° in the frontal plane, and 13° in the axial plane (Johnston and Smidt, 1969). Due to the high mobility of the electrogoniometer, a measuring system can be devised to monitor hip joint motion of post-surgery hip replacement patients. Measuring the joint movement in a free-living environment, in three planes and over an extended period of time, can help to determine the health of the joint. Any deviations in normal movement for the patient can be detected and serve as warning before the joint perhaps fails.

Only two applications are discussed above. Yet many other applications exist which require high mobility joint movement to be measured in a free-living environment. Once all the technical difficulties have been resolved, the electrogoniometer will have relevance in biomechanics, physical rehabilitation, the gaming industry, live performance motion capture and sport-science.

10.4.6 Future Work

The theoretical model is useful to predict the behaviour of the goniometer-nodes. It helped to explain the relatively poor precision of the ψ axis. In future, this can serve as a tool to develop goniometer-node configurations and predict performance without requiring the construction of the actual device. Once a design with adequate kinematic performance has been identified, the device can subsequently be built and tested. The model can perhaps be further refined by for example including multipath propagation. If a model with sufficient predictive capability can be devised, a parametric approach, instead of the non-parametric model currently used, can be applied. Such an approach will however require a computational intensive system of non-linear equations to be solved (as was done by Heo et al. (2011)). Heo used the same basic model derived here, but sacrificed accuracy and precision in favour of a simpler calibration method.

A statistical model to predict the accuracy and precision of the global measurements, which is composed of local measurements, will be another useful tool. A basic model has already been discussed in section 10.3.4 but only considered a single axis. The statistical model must include all axes and include phenomena like hysteresis and correlation between axes. The statistical model will be helpful to determine the goniometer-node accuracy and

precision based upon the desired electrogoniometer performance. Stated differently, if the global accuracy and precision of the distal node (i.e. the node with the worse global accuracy and precision) is specified (known), then the statistical model have to predict the worse case local accuracy and precision.

An issue not addressed here, is that of the practical biomechanical measurements. If the objective is to measure spinal kinematics, skin movement artifacts also has to be considered. The electrogoniometer measures the skin movement directly and the spinal motion indirectly. The device and skin thus acts as a parallel system with a collective stiffness constant determined by the sum of the individual stiffness constants. Some research has already been conducted in reducing skin movement artifacts. For example, Cerveri et al. (2005) used a Kalman filter to estimate the true movement of surface mount markers.

The device is currently being considered for commercialisation. A commercialisation effort will require a new more accurate and precise CaT instrument. The mechanical parts of the goniometer-node (especially the joints) will also have to be manufactured to tight tolerances. The dimensions, in particular the diameter, of the nodes will have to be scaled down.

Smaller nodes mean less space for the electronics. However, electronic components are becoming increasingly smaller. For example, the Kinetis KL03 by Freescale (Austin, Texas, USA), is a 32-bit microcontroller that measures only 1.6 x 2.0 mm. The microcontroller, shown in figure 10.6, has enough memory and processing power to perform algorithmic computation at the nodes.

Metal fatigue of the wiring is another important problem that has to be solved before the device can be successfully commercialised.



Figure 10.6: The 32-bit Kinetis KL03 microcontroller by Freescale measure only 1.6 x 2 mm.

10.4.7 Final Remarks

The proof-of-concept electrogoniometer presented here is a first attempt. It has been validated against a custom calibration instrument and a video motion capture system. Both the electrogoniometer and CaT instrument were significant development. However, not all the ideas have matured yet. It is therefore reasonable to expect that improvements can be made to subsequent developments and that the design specifications will be met with enough refinements. With sufficient resources available, a device is anticipated that is slightly thicker than a pencil and with accuracy and precision comparable to that of video capture systems. The device, perhaps costing a few thousand pounds, can then measure kinematics in environments where cutting-edge hundred thousand pound video motion capture systems can not.

Appendix A

A.1 Rotation Matrix of a Goniometer-Node

The local rotation matrices about the three axes are (Jazar, 2010):

$$\mathbf{R}_{x,\phi} = \begin{bmatrix} 1 & 0 & 0 \\ 0 & \cos\phi & \sin\phi \\ 0 & -\sin\phi & \cos\phi \end{bmatrix}, \mathbf{R}_{y,\psi} = \begin{bmatrix} \cos\psi & 0 & -\sin\psi \\ 0 & 1 & 0 \\ \sin\psi & 0 & \cos\psi \end{bmatrix}, \mathbf{R}_{z,\theta} = \begin{bmatrix} \cos\theta & \sin\theta & 0 \\ -\sin\theta & \cos\theta & 0 \\ 0 & 0 & 1 \end{bmatrix} \quad \text{equ A.1}$$

As discussed in chapter four (section 4.2), the sequence of rotations depends on the mechanical design. The rotation matrix of a goniometer-node is then:

$$\mathbf{R}_{y,\psi}\mathbf{R}_{z,\theta}\mathbf{R}_{x,\phi} = \begin{bmatrix} c\psi c\theta & s\phi s\psi + c\phi c\psi s\theta & c\psi s\phi s\theta - c\phi s\psi \\ -s\theta & c\phi c\theta & c\theta s\phi \\ c\theta s\psi & c\phi s\psi s\theta - c\psi s\phi & c\phi c\psi + s\phi s\psi s\theta \end{bmatrix} \quad \text{equ A.2}$$

where

$$c\phi = \cos\phi; \quad c\theta = \cos\theta; \quad c\psi = \cos\psi$$

and

$$s\phi = \sin\phi; \quad s\theta = \sin\theta; \quad s\psi = \sin\psi$$

A.2 CaT Instrument: $(\alpha, \beta) \mapsto (\phi, \theta)$ Transformation

The CaT instrument measures only three DOF (two rotation and one translation). The third rotation axes is determined through a simple calculation. An unit vector is rotated by the instrument as shown in figure A.1. The instrument manipulates axes α and β and thus indirectly axes ϕ and θ of the goniometer-node under calibration. The mapping between the two sets of kinematic variables are derived below.

The local rotations of the ϕ and θ axes are:

$$\mathbf{R}_{x,\phi} = \begin{bmatrix} 1 & 0 & 0 \\ 0 & \cos\phi & \sin\phi \\ 0 & -\sin\phi & \cos\phi \end{bmatrix}, \mathbf{R}_{z,\theta} = \begin{bmatrix} \cos\theta & \sin\theta & 0 \\ -\sin\theta & \cos\theta & 0 \\ 0 & 0 & 1 \end{bmatrix} \quad \text{equ A.3}$$

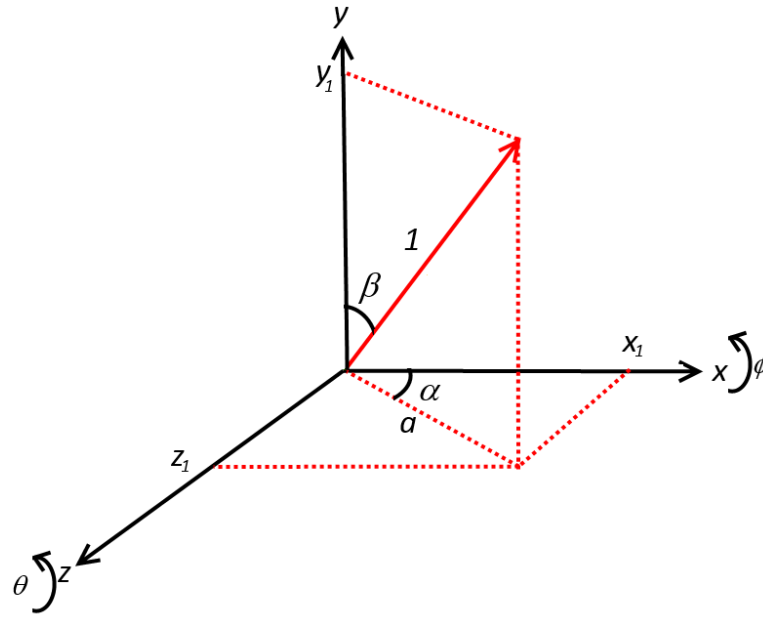


Figure A.1: Conversion between the CaT instrument and goniometer-node reference frames.

The order of the rotations enforced by the mechanical design while rotating the unit vector (originally aligned with the y axis) is then:

$$\begin{aligned} \mathbf{R}_{z,\theta}\mathbf{R}_{x,\phi} \begin{bmatrix} 0 \\ 1 \\ 0 \end{bmatrix} &= \begin{bmatrix} \cos\theta & \sin\theta \cos\phi & \sin\theta \sin\phi \\ -\sin\theta & \cos\theta \cos\phi & \cos\theta \sin\phi \\ 0 & -\sin\phi & \cos\phi \end{bmatrix} \begin{bmatrix} 0 \\ 1 \\ 0 \end{bmatrix} \\ &= \begin{bmatrix} \sin\theta \cos\phi \\ \cos\theta \cos\phi \\ -\sin\phi \end{bmatrix} \end{aligned} \quad \text{equ A.4}$$

However, it is evident from figure A.1 there exist the following trigonometric relationships:

$$a = \sin\beta \quad \text{equ A.5}$$

and

$$z_1 = \sin\alpha \sin\beta \quad \text{equ A.6}$$

but from equation A.4:

$$z_1 = -\sin\phi \quad \text{equ A.7}$$

Equation A.6 is substituted into A.7 and ϕ solved:

$$\therefore \sin\phi = -\sin\beta \sin\alpha \quad \text{equ A.8}$$

Next θ is solved. From figure A.1 the following trigonometric relationship exists:

$$y_1 = \cos \beta \quad \text{equ A.9}$$

but from equation A.4:

$$y_1 = \cos \theta \cos \phi \quad \text{equ A.10}$$

Replacing equation A.9 into equation A.10 gives:

$$\cos \beta = \cos \theta \cos \phi$$

$$\therefore \cos \theta = \frac{\cos \phi}{\cos \beta} \quad \text{equ A.11}$$

To conclude, equations A.8 and A.11 establish the relationships between (α, β) and (ϕ, θ) .

A.3 Solution to the SCoRE Problem

The SCoRE algorithm (Ehrig et al., 2006) requires the following matrix equation to be solved (see section 8.2.2.1 for a description of the method):

$$\begin{bmatrix} {}^0_i\mathbf{R}^{(G_V)} & {}^0_{i+1}\mathbf{R}^{(G_V)} \end{bmatrix} \begin{bmatrix} {}^i\mathbf{d}^{(V_U)} \\ -{}^{i+1}_i\mathbf{d}^{(V_U)} \end{bmatrix} = \begin{bmatrix} {}^{i+1}_0\mathbf{d}^{(G_V)} - {}^0_i\mathbf{d}^{(G_V)} \end{bmatrix} \quad \text{equ A.12}$$

or it can be written in a general form, i.e.:

$$\mathbf{A}\mathbf{x} = \mathbf{y} \quad \text{equ A.13}$$

where \mathbf{A} is a non-square matrix representing rotations measurements captured by the Qualisys system, \mathbf{y} the corresponding captured translation vectors and \mathbf{x} the unknown local CoR vectors (${}^i\mathbf{d}^{(V_U)}$ and ${}^{i+1}_i\mathbf{d}^{(V_U)}$).

To determine the CoR vectors, require a set of known calibration data captured by the Qualisys system. The dataset must only consist of joint rotations. Matrix \mathbf{A} can then be written as a $[3m \times 6]$ matrix and is constructed from the calibration data set (where m is the number of samples):

$$\mathbf{A} = \begin{bmatrix}
 {}^0R_{i11}^{(0)} & {}^0R_{i12}^{(0)} & {}^0R_{i13}^{(0)} & {}^0R_{i+111}^{(0)} & {}^0R_{i+112}^{(0)} & {}^0R_{i+113}^{(0)} \\
 {}^0R_{i21}^{(0)} & {}^0R_{i22}^{(0)} & {}^0R_{i23}^{(0)} & {}^0R_{i+121}^{(0)} & {}^0R_{i+122}^{(0)} & {}^0R_{i+123}^{(0)} \\
 {}^0R_{i31}^{(0)} & {}^0R_{i32}^{(0)} & {}^0R_{i33}^{(0)} & {}^0R_{i+131}^{(0)} & {}^0R_{i+132}^{(0)} & {}^0R_{i+133}^{(0)} \\
 {}^0R_{i11}^{(1)} & {}^0R_{i12}^{(1)} & {}^0R_{i13}^{(1)} & {}^0R_{i+111}^{(1)} & {}^0R_{i+112}^{(1)} & {}^0R_{i+113}^{(1)} \\
 {}^0R_{i21}^{(1)} & {}^0R_{i22}^{(1)} & {}^0R_{i23}^{(1)} & {}^0R_{i+121}^{(1)} & {}^0R_{i+122}^{(1)} & {}^0R_{i+123}^{(1)} \\
 {}^0R_{i31}^{(1)} & {}^0R_{i32}^{(1)} & {}^0R_{i33}^{(1)} & {}^0R_{i+131}^{(1)} & {}^0R_{i+132}^{(1)} & {}^0R_{i+133}^{(1)} \\
 \vdots & \vdots & \vdots & \vdots & \vdots & \vdots \\
 {}^0R_{i11}^{(m-1)} & {}^0R_{i12}^{(m-1)} & {}^0R_{i13}^{(m-1)} & {}^0R_{i+111}^{(m-1)} & {}^0R_{i+112}^{(m-1)} & {}^0R_{i+113}^{(m-1)} \\
 {}^0R_{i21}^{(m-1)} & {}^0R_{i22}^{(m-1)} & {}^0R_{i23}^{(m-1)} & {}^0R_{i+121}^{(m-1)} & {}^0R_{i+122}^{(m-1)} & {}^0R_{i+123}^{(m-1)} \\
 {}^0R_{i31}^{(m-1)} & {}^0R_{i32}^{(m-1)} & {}^0R_{i33}^{(m-1)} & {}^0R_{i+131}^{(m-1)} & {}^0R_{i+132}^{(m-1)} & {}^0R_{i+133}^{(m-1)}
 \end{bmatrix} \quad \text{equ A.14}$$

The superscripts \mathbf{G}_V has been dropped to reduce clutter and instead replaced with the sample number. A single sample is therefore a [3 x 6] matrix. Colour-coding is used to help distinguish between the samples.

The unknown matrix, \mathbf{x} , then a [6 x 1] matrix and is written as:

$$\mathbf{x} = \begin{bmatrix}
 {}_i d_x^{(V_U)} \\
 {}_i d_y^{(V_U)} \\
 {}_i d_z^{(V_U)} \\
 -{}_{i+1} d_x^{(V_U)} \\
 -{}_{i+1} d_y^{(V_U)} \\
 -{}_{i+1} d_z^{(V_U)}
 \end{bmatrix} \quad \text{equ A.15}$$

And finally, the known global position vectors is a [3*m* x 1] matrix:

$$\mathbf{y} = \begin{bmatrix}
 {}^0 d_x^{(0)} - {}^0 d_x^{(0)} \\
 {}^0 d_y^{(0)} - {}^0 d_y^{(0)} \\
 {}^0 d_z^{(0)} - {}^0 d_z^{(0)} \\
 {}^0 d_x^{(1)} - {}^0 d_x^{(1)} \\
 {}^0 d_y^{(1)} - {}^0 d_y^{(1)} \\
 {}^0 d_z^{(1)} - {}^0 d_z^{(1)} \\
 \vdots \\
 {}^0 d_x^{(m)} - {}^0 d_x^{(m-1)} \\
 {}^0 d_y^{(m)} - {}^0 d_y^{(m-1)} \\
 {}^0 d_z^{(m)} - {}^0 d_z^{(m-1)}
 \end{bmatrix} \quad \text{equ A.16}$$

The solution is then simply:

$$x = \mathbf{A}^+ \mathbf{y} \qquad \text{equ A.17}$$

where \mathbf{A}^+ is the pseudo inverse of \mathbf{A} . The Moore–Penrose method was employed here to determine the pseudo inverse (Penrose, 1955).

Appendix B

B.1 Detector Datasheet



TEMT7100X01
Vishay Semiconductors

Silicon Phototransistor in 0805 Package



DESCRIPTION

TEMT7100X01 is a silicon NPN epitaxial planar phototransistor with daylight blocking filter in a miniature, black 0805 package for surface mounting. Filter bandwidth is matched with 830 nm to 950 nm IR emitters.

FEATURES

- Package type: surface mount
- Package form: 0805
- Dimensions (L x W x H in mm): 2 x 1.25 x 0.85
- AEC-Q101 qualified
- High photo sensitivity
- Daylight blocking filter matches with 830 nm to 950 nm IR emitters
- Angle of half sensitivity: $\phi = \pm 60^\circ$
- Package matched with IR emitter series VSMB1940X01
- Floor life: 168 h, MSL 3, acc. J-STD-020
- Lead (Pb)-free reflow soldering
- Compliant to RoHS directive 2002/95/EC and in accordance to WEEE 2002/96/EC
- Find out more about Vishay's Automotive Grade Product requirements at: www.vishay.com/applications



APPLICATIONS

- Detector in automotive applications
- Photo interrupters
- Miniature switches
- Counters
- Encoders
- Position sensors

PRODUCT SUMMARY

COMPONENT	I _{caE} (μA)	φ (deg)	λ _{0.5} (nm)
TEMT7100X01	225 to 675	± 60	750 to 1010

Note

Test condition see table "Basic Characteristics"

ORDERING INFORMATION

ORDERING CODE	PACKAGING	REMARKS	PACKAGE FORM
TEMT7100X01	Tape and reel	MOQ: 3000 pcs, 3000 pcs/reel	0805

Note

MOQ: minimum order quantity

ABSOLUTE MAXIMUM RATINGS

PARAMETER	TEST CONDITION	SYMBOL	VALUE	UNIT
Collector emitter voltage		V _{CEO}	20	V
Emitter collector voltage		V _{ECO}	7	V
Collector current		I _C	20	mA
Power power dissipation	T _{amb} ≤ 55 °C	P _V	100	mW
Junction temperature		T _J	100	°C
Operating temperature range		T _{amb}	- 40 to + 100	°C
Storage temperature range		T _{stg}	- 40 to + 100	°C
Soldering temperature	Acc. reflow profile fig. 7	T _{sd}	260	°C
Thermal resistance junction/ambient	Acc. J-STD-051	R _{thJA}	270	K/W

Note

T_{amb} = 25 °C, unless otherwise specified

TEMT7100X01

Vishay Semiconductors Silicon Phototransistor in 0805 Package

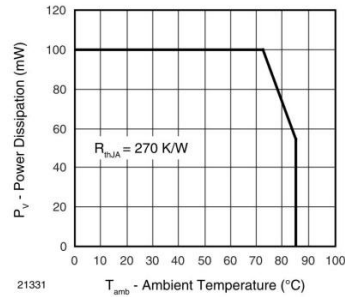


Fig. 1 - Power Dissipation Limit vs. Ambient Temperature

BASIC CHARACTERISTICS						
PARAMETER	TEST CONDITION	SYMBOL	MIN.	TYP.	MAX.	UNIT
Collector emitter breakdown voltage	$I_C = 0.1 \text{ mA}$	V_{CE0}	20			V
Collector dark current	$V_{CE} = 5 \text{ V}, E = 0$	I_{CE0}		1	100	nA
Collector emitter capacitance	$V_{CE} = 0 \text{ V}, f = 1 \text{ MHz}, E = 0$	C_{CEO}		25		pF
Collector light current	$E_e = 1 \text{ mW/cm}^2, \lambda = 950 \text{ nm}, V_{CE} = 5 \text{ V}$	I_{CA}	225	450	675	μA
Angle of half sensitivity		ϕ		± 60		deg
Wavelength of peak sensitivity		λ_p		870		nm
Range of spectral bandwidth		$\lambda_{0.5}$		750 to 1010		nm
Collector emitter saturation voltage	$I_C = 0.05 \text{ mA}$	V_{CEsat}			0.4	V

Note

$T_{amb} = 25 \text{ }^\circ\text{C}$, unless otherwise specified

BASIC CHARACTERISTICS

$T_{amb} = 25 \text{ }^\circ\text{C}$, unless otherwise specified

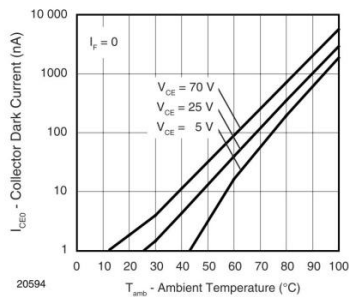


Fig. 2 - Collector Dark Current vs. Ambient Temperature

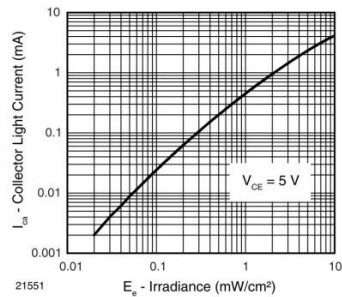


Fig. 3 - Collector Light Current vs. Irradiance



TEMT7100X01

Silicon Phototransistor in 0805 Package Vishay Semiconductors

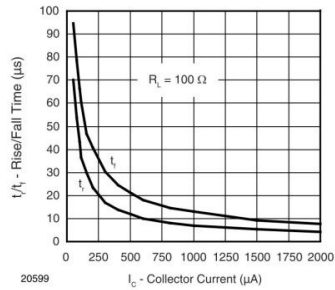


Fig. 4 - Rise/Fall Time vs. Collector Current

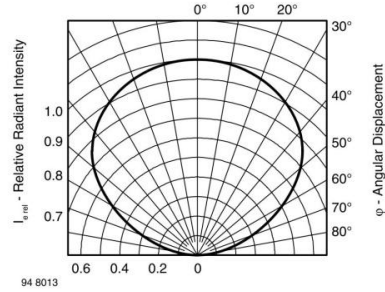


Fig. 6 - Relative Radiant Sensitivity vs. Angular Displacement

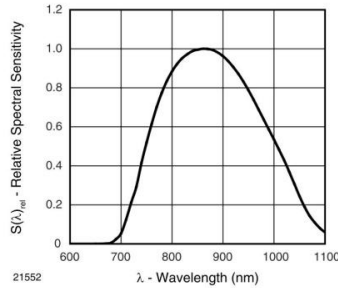


Fig. 5 - Relative Spectral Sensitivity vs. Wavelength

REFLOW SOLDER PROFILE

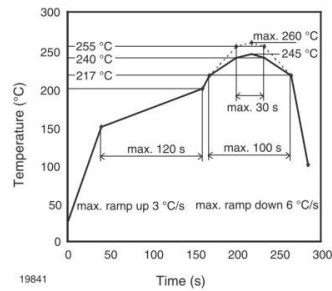


Fig. 7 - Lead (Pb)-free Reflow Solder Profile acc. J-STD-020D

DRYPACK

Devices are packed in moisture barrier bags (MBB) to prevent the products from moisture absorption during transportation and storage. Each bag contains a desiccant.

FLOOR LIFE

Floor life (time between soldering and removing from MBB) must not exceed the time indicated on MBB label:
 Floor life: 168 h
 Conditions: $T_{amb} < 30\text{ }^{\circ}\text{C}$, $RH < 60\%$
 Moisture sensitivity level 3, acc. to J-STD-020.

DRYING

In case of moisture absorption devices should be baked before soldering. Conditions see J-STD-020 or label. Devices taped on reel dry using recommended conditions 192 h at $40\text{ }^{\circ}\text{C}$ ($+5\text{ }^{\circ}\text{C}$), $RH < 5\%$.

B.2 Emitter Datasheet



VSMB1940X01

Vishay Semiconductors

High Speed Infrared Emitting Diode, 940 nm, GaAlAs Double Hetero



21531

DESCRIPTION

VSMB1940X01 is an infrared, 940 nm emitting diode in GaAlAs Double Hetero technology with high radiant power and high speed, molded in clear, untinted 0805 plastic package for surface mounting (SMD).

FEATURES

- Package type: surface mount
- Package form: 0805
- Dimensions (L x W x H in mm): 2 x 1.25 x 0.85
- AEC-Q101 qualified
- Peak wavelength: $\lambda_p = 940$ nm
- High reliability
- High radiant power
- High radiant intensity
- High speed
- Angle of half sensitivity: $\phi = \pm 60^\circ$
- Low forward voltage
- Suitable for high pulse current operation
- 0805 standard surface-mountable package
- Floor life: 168 h, MSL 3, acc. J-STD-020
- Lead (Pb)-free reflow soldering
- Compliant to RoHS directive 2002/95/EC and in accordance to WEEE 2002/96/EC



APPLICATIONS

- High speed IR data transmission
- High power emitter for low space applications
- High performance transmissive or reflective sensors

PRODUCT SUMMARY				
COMPONENT	I_e (mW/sr)	ϕ (deg)	λ_p (nm)	t_r (ns)
VSMB1940X01	6	± 60	940	15

Note

Test conditions see table "Basic Characteristics"

ORDERING INFORMATION			
ORDERING CODE	PACKAGING	REMARKS	PACKAGE FORM
VSMB1940X01	Tape and reel	MOQ: 3000 pcs, 3000 pcs/reel	0805

Note

MOQ: minimum order quantity

ABSOLUTE MAXIMUM RATINGS				
PARAMETER	TEST CONDITION	SYMBOL	VALUE	UNIT
Reverse voltage		V_R	5	V
Forward current		I_F	100	mA
Peak forward current	$t_p/T = 0.1, t_p = 100 \mu s$	I_{FM}	200	mA
Surge forward current	$t_p = 100 \mu s$	I_{FSM}	1	A
Power dissipation		P_V	160	mW
Junction temperature		T_J	100	$^\circ C$
Operating temperature range		T_{amb}	- 40 to + 85	$^\circ C$
Storage temperature range		T_{stg}	- 40 to + 100	$^\circ C$
Soldering temperature	$t \leq 5$ s, 2 mm from case	T_{sd}	260	$^\circ C$
Thermal resistance junction/ambient	J-STD-051, leads 7 mm, soldered on PCB	R_{thJA}	270	K/W

Note

$T_{amb} = 25 \text{ }^\circ C$, unless otherwise specified

VSMB1940X01

Vishay Semiconductors High Speed Infrared Emitting Diode,
940 nm, GaAlAs Double Hetero

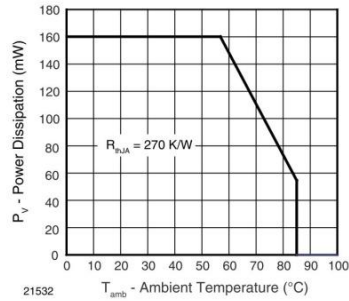


Fig. 1 - Power Dissipation Limit vs. Ambient Temperature

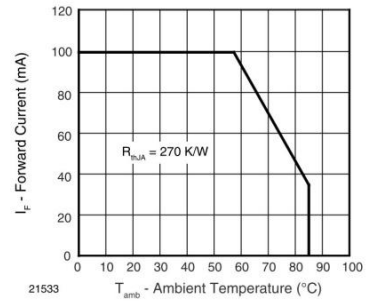


Fig. 2 - Forward Current Limit vs. Ambient Temperature

BASIC CHARACTERISTICS						
PARAMETER	TEST CONDITION	SYMBOL	MIN.	TYP.	MAX.	UNIT
Forward voltage	$I_F = 100 \text{ mA}, t_p = 20 \text{ ms}$	V_F	1.15	1.35	1.6	V
	$I_F = 1 \text{ A}, t_p = 100 \mu\text{s}$	V_F		2.2		V
Temperature coefficient of V_F	$I_F = 1 \text{ mA}$	TK_{VF}		- 1.5		mV/K
	$I_F = 100 \text{ mA}$	TK_{VF}		- 1.1		mV/K
Reverse current	$V_R = 5 \text{ V}$	I_R			10	μA
Junction capacitance	$V_R = 0 \text{ V}, f = 1 \text{ MHz}, E = 0 \text{ mW/cm}^2$	C_J		70		pF
Radiant intensity	$I_F = 100 \text{ mA}, t_p = 20 \text{ ms}$	I_e	3	6	12	mW/sr
	$I_F = 1 \text{ A}, t_p = 100 \mu\text{s}$	I_e		60		mW/sr
Radiant power	$I_F = 100 \text{ mA}, t_p = 20 \text{ ms}$	ϕ_e		40		mW
Temperature coefficient of radiant power	$I_F = 1 \text{ mA}$	TK_{ϕ_e}		- 1.1		%/K
	$I_F = 100 \text{ mA}$	TK_{ϕ_e}		- 0.51		%/K
Angle of half intensity		ϕ		± 60		deg
Peak wavelength	$I_F = 30 \text{ mA}$	λ_p		940		nm
Spectral bandwidth	$I_F = 30 \text{ mA}$	$\Delta\lambda$		25		nm
Temperature coefficient of λ_p	$I_F = 30 \text{ mA}$	TK_{λ_p}		0.25		nm
Rise time	$I_F = 100 \text{ mA}, 20 \% \text{ to } 80 \%$	t_r		15		ns
Fall time	$I_F = 100 \text{ mA}, 20 \% \text{ to } 80 \%$	t_f		15		ns
Virtual source diameter		d		0.5		mm

Note
 $T_{amb} = 25 \text{ }^\circ\text{C}$, unless otherwise specified



VSMB1940X01

High Speed Infrared Emitting Diode, Vishay Semiconductors
940 nm, GaAlAs Double Hetero

BASIC CHARACTERISTICS

$T_{amb} = 25\text{ }^{\circ}\text{C}$, unless otherwise specified

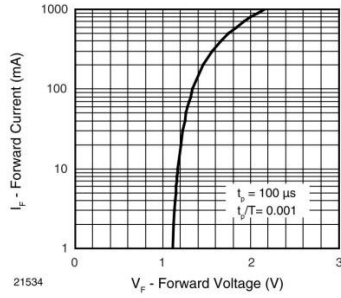


Fig. 3 - Forward Current vs. Forward Voltage

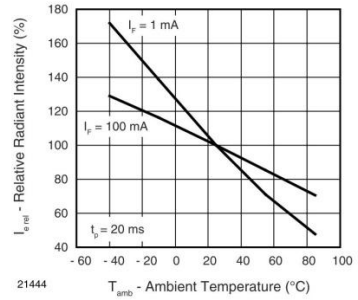


Fig. 6 - Relative Radiant Intensity vs. Ambient Temperature

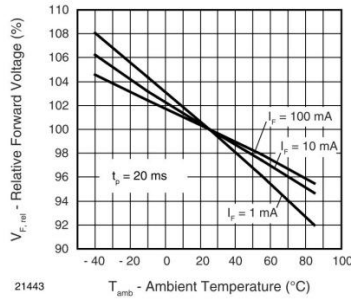


Fig. 4 - Relative Forward Voltage vs. Ambient Temperature

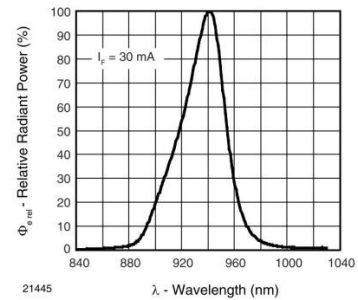


Fig. 7 - Relative Radiant Power vs. Wavelength

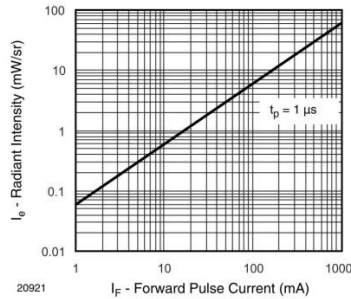


Fig. 5 - Radiant Intensity vs. Forward Current

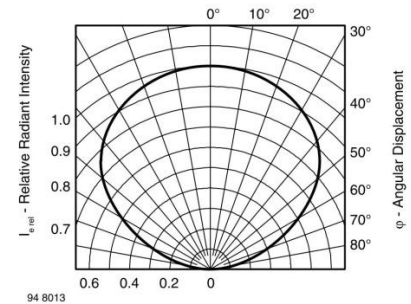


Fig. 8 - Relative Radiant Intensity vs. Angular Displacement

B.3 Goniometer-Node Schematics

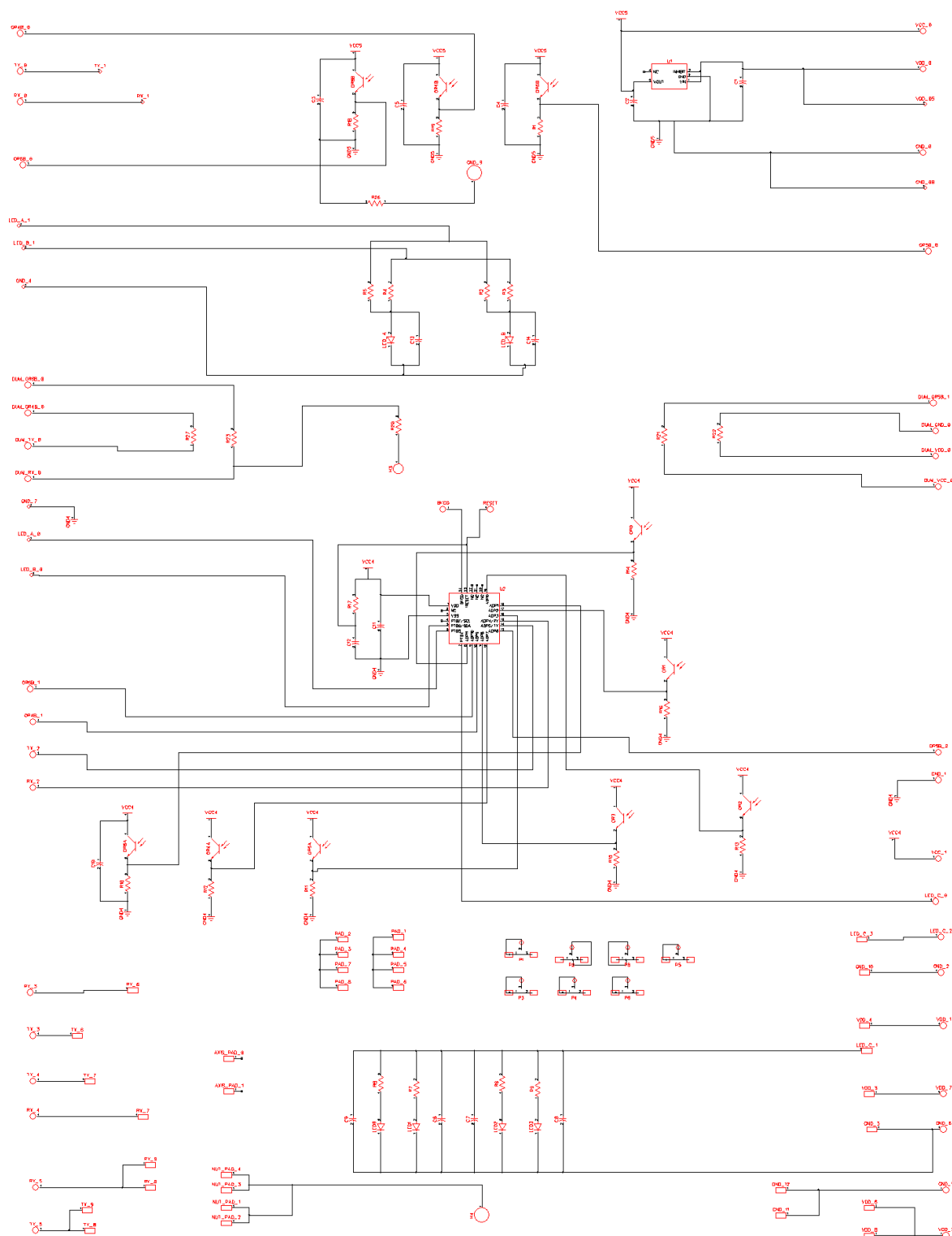


Figure B.1: Goniometer-node schematics.

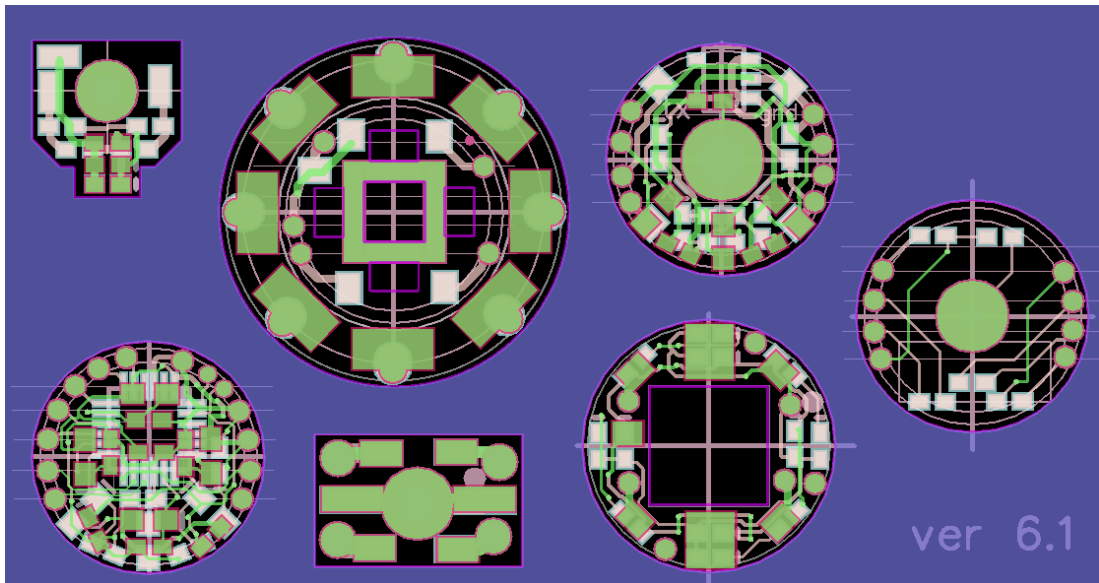


Figure B.2: Goniometer-node layout.

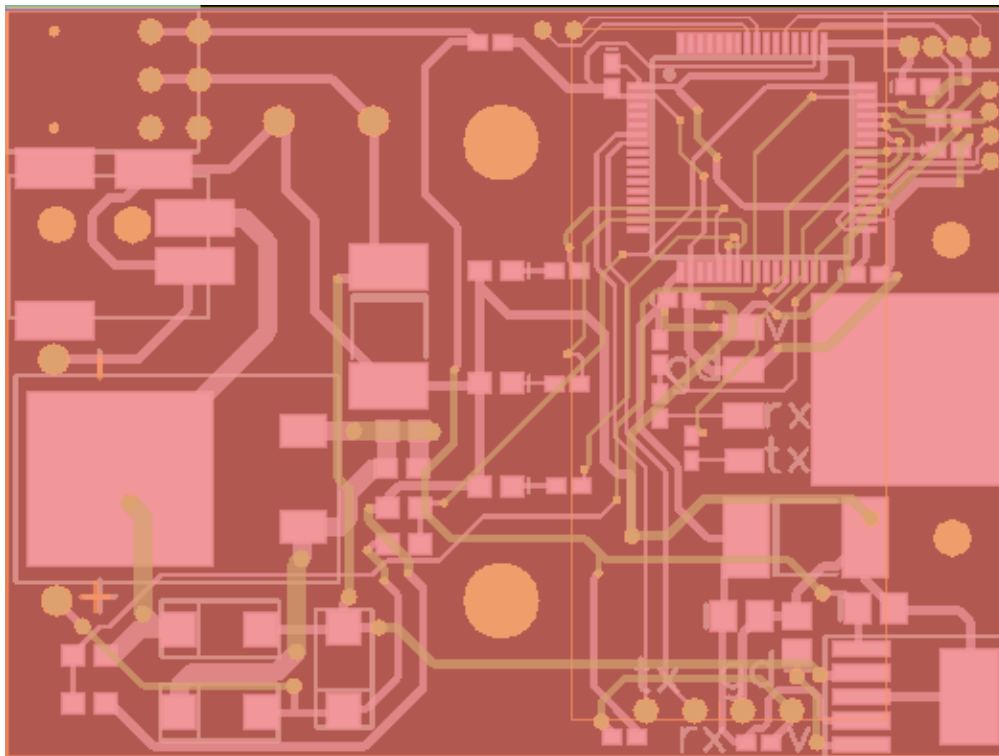


Figure B.4: Master-controller layout.

Reference	Value
C1	1uF
C2	1uF
C3	100nF
C4	100nF
C5	100nF
C6	100n
C7	100n
C8	100n
C9	100n
C10	2.2uF
C11	100nF
C12	100nF
C13	100n
C14	100n
LED_A	VSMB1940X01
LED_B	VSMB1940X01
LED_C_0	VSMB1940X01
LED_C_1	VSMB1940X01
LED_C_2	VSMB1940X01

APPENDIX B

LED_C_3	VSMB1940X01
OR0	TEMT7100X01
OR1	TEMT7100X01
OR2	TEMT7100X01
OR3	TEMT7100X01
OR4A	TEMT7100X01
OR4B	TEMT7100X01
OR5A	TEMT7100X01
OR5B	TEMT7100X01
OR6A	TEMT7100X01
OR6B	TEMT7100X01
R1	3k3
R2	1k
R3	1k5
R4	1k5
R5	1k
R6	1k
R7	1k
R8	1k
R9	1k
R10	3k3
R11	3k3
R12	3k3
R13	1k
R14	1k
R15	1k
R16	1k
R17	10k
R18	3k3
R19	3k3
R20	6k8
R21	6k8
R22	6k8
R23	6k8
R26	6k8
R27	6k8
U1	LD2980ABM30TR
U2	MC9S08SH8CFK

Table B.1: Goniometer-node bill of materials.

APPENDIX B

Reference	Value
B1	BATTERY HOLDER, AAA, 3WAY
C1	2.2uF
C7	2.2uF
C8	2.2uF
C13	2.2uF
C14	1u
C15	100nF
C17	1u
C18	150UF,16V
C19	1000UF,16V
C20	150UF,16V
C21	2.2uF
D4	GF1M-E3
D5	GF1M-E3
D6	GF1M-E3
K2	2Pole2Way
R24	6k8
R26	6k8
R27	6k8
R28	6k8
R29	6k8
R31	6k8
R32	3k3
R33	6k8
R34	6k8
R35	6k8
U2	MCF51CN128CLH
U3	TPS795xx
U6	LM317

Table B.2: Master-controller bill of materials.

BIBLIOGRAPHY

- Adams, M. A., Burton, A. K., Dolan, P., & Bogduk, N. (2007). *The biomechanics of back pain*. (2nd ed.). Churchill Livingstone.
- Akbarnia, B., Muharrem, Y., & H., T. G. (2010). *The Growing Spine: Management of Spinal Disorders in Young Children*. (1st ed.). Springer.
- Allread, W. G., Marras, W. S., & Burr, D. L. (2000). Measuring trunk motions in industry: variability due to task factors, individual differences, and the amount of data collected. *Ergonomics*, 43(6), 691-701.
- Bachmann, E. R., McGhee, R. B., Yun, X., & Zyda, M. J. (2001). Inertial and magnetic posture tracking for inserting humans into networked virtual environments. Paper presented at the Proceedings of the ACM symposium on Virtual reality software and technology, Banff, Canada.
- Balagué, F., Mannion, A. F., Pellisé, F., & Cedraschi, C. (2012). Non-specific low back pain. *The Lancet*, 379(9814), 482-491.
- Barker, S., Craik, R., Freedman, W., Herrmann, N., & Hillstrom, H. (2006). Accuracy, reliability, and validity of a spatiotemporal gait analysis system. *Medical engineering & physics*, 28(5), 460-467.
- Bebek, O., Suster, M. A., Rajgopal, S., Fu, M. J., Huang, X., Çavuşoğlu, M. C., ... & Mastrangelo, C. H. (2010). Personal navigation via high-resolution gait-corrected inertial measurement units. *Instrumentation and Measurement, IEEE Transactions on*, 59(11), 3018-3027.
- Bentley, J. P. (2004). *Principles of measurement systems*. (4th ed.). Pearson education.
- Bible, J. E., Biswas, D., Miller, C. P., Whang, P. G., & Grauer, J. N. (2010). Normal functional range of motion of the lumbar spine during 15 activities of daily living. *Journal of spinal disorders & techniques*, 23(2), 106-112.
- Bishop, C. M. (1995). *Neural networks for pattern recognition*. (1st ed.). Oxford

university press.

Braun, M. (2012). Eadweard Muybridge. (1st ed.). Reaktion Books.

Burdorf, A., & van Riel, M. (1996). Design of strategies to assess lumbar posture during work. *International Journal of Industrial Ergonomics*, 18(4), 239-249.

Cerveri, P., Pedotti, A., & Ferrigno, G. (2005). Kinematical models to reduce the effect of skin artifacts on marker-based human motion estimation. *Journal of Biomechanics*, 38(11), 2228-2236.

Ceseracciu, E., Sawacha, Z., Fantozzi, S., Cortesi, M., Gatta, G., Corazza, S., et al. (2011). Markerless analysis of front crawl swimming. *Journal of biomechanics*, 44(12), 2236-2242.

Cheng, L., Tan, H., Kuntze, G., Roskilly, K., Lowe, J., Bezodis, I. N., et al. (2010). Sensing for stride information of sprinters. In *Wireless Sensor Networks* (pp. 147-161). Springer.

Consmüller, T., Rohlmann, A., Weinland, D., Druschel, C., Duda, G. N., & Taylor, W. R. (2012). Comparative evaluation of a novel measurement tool to assess lumbar spine posture and range of motion. *European Spine Journal*, 21(11), 2170-2180.

Consmüller, T., Rohlmann, A., Weinland, D., Schmidt, H., Zippelius, T., Duda, G. N., et al. (2013). Automatic distinction of upper body motions in the main anatomical planes. *Medical engineering & physics*, 36(4), 516-521.

Corazza, S., Mündermann, L., & Andriacchi, T. (2007). A framework for the functional identification of joint centers using markerless motion capture, validation for the hip joint. *Journal of biomechanics*, 40(15), 3510-3515.

Danisch, L., Englehart, K., & Trivett, A. (1999). Spatially continuous six degree of freedom position and orientation sensor. *Sensor Review*, 19(2), 106-112.

Davis, S. W., Marras, W. S., Miller, R. J., & Mirka, G. A. (1991). Apparatus for monitoring the motion components of the spine. Patent number: US5012819A.

de Niet, M., Bussmann, J. B., Ribbers, G. M., & Stam, H. J. (2007). The stroke upper-limb activity monitor: its sensitivity to measure hemiplegic upper-limb

- activity during daily life. *Archives of physical medicine and rehabilitation*, 88(9), 1121-1126
- De Vries, W. H. K., Veeger, H. E. J., Baten, C. T. M., & Van Der Helm, F. C. T. (2009). Magnetic distortion in motion labs, implications for validating inertial magnetic sensors. *Gait & posture*, 29(4), 535-541.
- Donno, M., Palange, E., Di Nicola, F., Bucci, G., & Ciancetta, F. (2008). A new flexible optical fiber goniometer for dynamic angular measurements: application to human joint movement monitoring. *Instrumentation and Measurement, IEEE Transactions on*, 57(8), 1614-1620.
- Dopf, C. A., Mandel, S. S., Geiger, D. F., & Mayer, P. J. (1994). Analysis of spine motion variability using a computerized goniometer compared to physical examination a prospective clinical study. *Spine*, 19(5), 586-595.
- Duc, C., Salvia, P., Lubansu, A., Feipel, V., & Aminian, K. (2013). Objective evaluation of cervical spine mobility after surgery during free-living activity. *Clinical Biomechanics*, 28(4), 364-369.
- Ehrig, R. M., Taylor, W. R., Duda, G. N., & Heller, M. O. (2006). A survey of formal methods for determining the centre of rotation of ball joints. *Journal of biomechanics*, 39(15), 2798-2809.
- Ferguson, S., Gaudes-MacLaren, L., Marras, W., Waters, T., & Davis, K. (2002). Spinal loading when lifting from industrial storage bins. *Ergonomics*, 45(6), 399-414.
- Fox, W. P. (2012). *Mathematical modeling with maple*. Cengage Learning.
- Frost, N. E., Marsh, K. J., & Pook, L. P. (1999). *Metal fatigue*. Courier Dover Publications.
- Fuchs, S. (2010). Multipath interference compensation in time-of-flight camera images. Paper presented at the 20th International Conference on Pattern Recognition (ICPR), Istanbul.
- Ganapathi, V., Plagemann, C., Koller, D., & Thrun, S. (2010). Real time motion capture using a single time-of-flight camera. Paper presented at the IEEE Conference on Computer Vision and Pattern Recognition (CVPR), San

Fransisco.

Gentner, R., & Classen, J. (2009). Development and evaluation of a low-cost sensor glove for assessment of human finger movements in neurophysiological settings. *Journal of neuroscience methods*, 178(1), 138-147.

Gregory, J. (2009). *Game engine architecture*. (1st ed.). CRC Press.

Hayter, A. (2012). *Probability and statistics for engineers and scientists*. (4th ed.). Cengage Learning.

Heck, J. F., & Sparano, J. M. (2000). A classification system for the assessment of lumbar pain in athletes. *Journal of athletic training*, 35(2), 204.

Hendricks, G. (1975). *Eadweard Muybridge: The father of the motion picture*. Secker & Warburg.

Heo, S., Han, J., Choi, S., Lee, S., Lee, G., Lee, H.-E., et al. (2011). IrCube tracker: an optical 6-DOF tracker based on LED directivity. Paper presented at the Proceedings of the 24th annual ACM symposium on User interface software and technology, Santa Barbara.

Herda, L., Fua, P., Plänklers, R., Boulic, R., & Thalmann, D. (2001). Using skeleton-based tracking to increase the reliability of optical motion capture. *Human movement science*, 20(3), 313-341.

Irons, F. H., Riley, K. J., Hummels, D. M., & Friel, G. A. (2000). The noise power ratio-theory and ADC testing. *IEEE Transactions on Instrumentation and Measurement*, 49(3), 659-665.

Jazar, R. N. (2010). *Theory of applied robotics : Kinematics, Dynamics, and Control*. (2nd ed.). Springer.

Johnston, R. C., Smidt, G. L. (1969). Measurement of hip-joint motion during walking evaluation of an electrogoniometric method. *The Journal of Bone & Joint Surgery*, 51(6), 1083-1094.

Jonsson, P., Johnson, P. W., & Hagberg, M. (2007). Accuracy and feasibility of using an electrogoniometer for measuring simple thumb movements. *Ergonomics*, 50(5), 647-659.

Kellis, E., Adamou, G., Tziliou, G., & Emmanouilidou, M. (2008). Reliability of spinal

REFERENCES

- range of motion in healthy boys using a skin-surface device. *Journal of manipulative and physiological therapeutics*, 31(8), 570-576.
- Khandpur, R. S. (2005). *Printed Circuit Boards: Design, Fabrication, Assembly and Testing*. (1st ed.). McGraw-Hill.
- Konica Minolta. (2014). *Basic Properties of LEDs*. White paper: http://sensing.konicaminolta.us/learning-center/white-papers/basic-properties-of-leds/BasicProperties_LED.pdf.
- Krzyszowski, T., Kwolek, B., Michalczuk, A., Świtoński, A., & Josiński, H. (2012). View independent human gait recognition using markerless 3d human motion capture. In *Computer Vision and Graphics* (pp. 491-500). Springer.
- Kugler, P., Schlarb, H., Blinn, J., Picard, A., & Eskofier, B. (2012). A wireless trigger for synchronization of wearable sensors to external systems during recording of human gait. Paper presented at the Engineering in Medicine and Biology Society (EMBC), 2012 Annual International Conference of the IEEE, San Diego.
- Langer, M. S., & Zucker, S. W. (1997). What is a light source? Paper presented at the IEEE Computer Society Conference on Computer Vision and Pattern Recognition, San Juan.
- Lee, J. K., & Park, E. J. (2011). 3D spinal motion analysis during staircase walking using an ambulatory inertial and magnetic sensing system. *Medical & biological engineering & computing*, 49(7), 755-764.
- Leu, A., Ristic-Durrant, D., & Graser, A. (2011). A robust markerless vision-based human gait analysis system. Paper presented at the 6th IEEE International Symposium on Applied Computational Intelligence and Informatics (SACI), Timisoara.
- Li, G., Wang, S., Passias, P., Xia, Q., Li, G., & Wood, K. (2009). Segmental in vivo vertebral motion during functional human lumbar spine activities. *European Spine Journal*, 18(7), 1013-1021.
- Lindsay, D., & Horton, J. (2002). Comparison of spine motion in elite golfers with and without low back pain. *Journal of sports sciences*, 20(8), 599-605.

REFERENCES

- Malanga, G. A., & Nadler, S. (2006). *Musculoskeletal physical examination: an evidence-based approach*. (1st ed.). Elsevier Health Sciences.
- Maletsky, L. P., Sun, J., & Morton, N. A. (2007). Accuracy of an optical active-marker system to track the relative motion of rigid bodies. *Journal of biomechanics*, 40(3), 682-685.
- Mannion, A. F., Knecht, K., Balaban, G., Dvorak, J., & Grob, D. (2004). A new skin-surface device for measuring the curvature and global and segmental ranges of motion of the spine: reliability of measurements and comparison with data reviewed from the literature. *European Spine Journal*, 13(2), 122-136.
- Manolakis, D. E. (1996). Efficient solution and performance analysis of 3-D position estimation by trilateration. *IEEE Transactions on Aerospace and Electronic Systems*, 32(4), 1239-1248.
- Marras, W., Fathallah, F., Miller, R., Davis, S., & Mirka, G. (1992). Accuracy of a three-dimensional lumbar motion monitor for recording dynamic trunk motion characteristics. *International Journal of Industrial Ergonomics*, 9(1), 75-87.
- McCarthy, J. M., & Soh, G. S. (2010). *Geometric design of linkages* (Vol. 11). Springer.
- Mieritz, R. M., Bronfort, G., Jakobsen, M. D., Aagaard, P., & Hartvigsen, J. (2013). Reliability and measurement error of sagittal spinal motion parameters in 220 patients with chronic low back pain using a three-dimensional measurement device. *The Spine Journal*.
- Moeslund, T. B., & Granum, E. (2001). A survey of computer vision-based human motion capture. *Computer Vision and Image Understanding*, 81(3), 231-268.
- Morin, E., & Reid, S. (2002). The validation of measurand shapetape for measuring joint angles. Paper presented at the Proceedings of Canadian Medical and Biological Engineering Conference, Ottawa, Ontario.
- Muybridge, J. (1882). The horse in motion. *Nature*, 25, 605.
- Nevins, R. J., Durdle, N., & Raso, V. (2002). A posture monitoring system using accelerometers. Paper presented at the Canadian Conference on Electrical

REFERENCES

- and Computer Engineering, 2002. IEEE CCECE 2002.
- O'Sullivan, K., Galeotti, L., Dankaerts, W., O'Sullivan, L., & O'Sullivan, P. (2011). The between-day and inter-rater reliability of a novel wireless system to analyse lumbar spine posture. *Ergonomics*, 54(1), 82-90.
- Owens, P., Atkins, N., & O'Brien, E. (1999). Diagnosis of white coat hypertension by ambulatory blood pressure monitoring. *Hypertension*, 34(2), 267-272.
- Pearcy, M. J. (1985). Stereo radiography of lumbar spine motion. *Acta Orthopaedica*, 56(S212), 1-45.
- Penrose, R. (1955). A generalized inverse for matrices. Paper presented at the Proc. Cambridge Philos. Soc.
- Peters, A., Sangeux, M., Morris, M. E., & Baker, R. (2009). Determination of the optimal locations of surface-mounted markers on the tibial segment. *Gait & posture*, 29(1), 42-48.
- Polhemus. (2008). Fastrak - The Fast and Easy Digital Tracker. http://polhemus.com/_assets/img/FASTRAK_Brochure.pdf
- Pollintine, P., Dolan, P., Tobias, J. H., & Adams, M. A. (2004). Intervertebral disc degeneration can lead to "stress-shielding" of the anterior vertebral body: a cause of osteoporotic vertebral fracture? *Spine*, 29(7), 774-782.
- Roland, M., & Morris, R. (1983). A study of the natural history of back pain: part I: development of a reliable and sensitive measure of disability in low-back pain. *Spine*, 8(2), 141-144.
- Rosenthal, R. (1966). *Experimenter effects in behavioral research*. Appleton-Century-Crofts.
- Rowe, P., Myles, C., Hillmann, S., & Hazlewood, M. (2001). Validation of flexible electrogoniometry as a measure of joint kinematics. *Physiotherapy*, 87(9), 479-488.
- Sato, K., Smith, S. L., & Sands, W. A. (2009). Validation of an accelerometer for measuring sport performance. *The Journal of Strength & Conditioning Research*, 23(1), 341-347.
- Schuit, D., Petersen, C., Johnson, R., Levine, P., Knecht, H., & Goldberg, D. (1997).

- Validity and reliability of measures obtained from the OSI CA-6000 Spine Motion Analyzer for lumbar spinal motion. *Manual Therapy*, 2(4), 206-215.
- Schulte, E., & Schumacher, U. (2006). *Thieme Atlas of Anatomy: Latin Nomenclature: General Anatomy and Musculoskeletal System*. (1st ed.). Thieme.
- Schulze, M., Calliess, T., Gietzelt, M., Wolf, K., Liu, T., Seehaus, F., et al. (2012). Development and clinical validation of an unobtrusive ambulatory knee function monitoring system with inertial 9DoF sensors. Paper presented at the Engineering in Medicine and Biology Society (EMBC), 2012 Annual International Conference of the IEEE, San Diego.
- Siciliano, B., & Khatib, O. (Eds.). (2008). *Springer handbook of robotics*. Springer.
- Smit, P., Barrie, P., & Komninos, A. (2009). *Mirrored Motion: Pervasive Body Motion Capture using Wireless Sensors*. Paper presented at the Whole Body Interaction Workshop, ACM CHI2009, Boston MA.
- Smith, J. (2011). *Functional assessment to compare electromagnetic navigated and conventional total knee arthroplasty*. PhD thesis. University of Strathclyde.
- Stokes, I. A., Gardner-Morse, M., Churchill, D., & Laible, J. P. (2002). Measurement of a spinal motion segment stiffness matrix. *Journal of biomechanics*, 35(4), 517-521.
- Sun, S., Meng, X., Ji, L., Wu, J., & Wong, W.-C. (2010). Adaptive sensor data fusion in motion capture. Paper presented at the 13th Conference on Information Fusion (FUSION), Edinburgh.
- Świtoński, A., Mucha, R., Danowski, D., Mucha, M., Cieślak, G., Wojciechowski, K., et al. (2011). Human identification based on a kinematical data of a gait. *Electrical Review*(12b), 169-172.
- Szeto, G., Wong, K., Law, K., & Lee, E. (2013). A study of spinal kinematics in community nurses performing nursing tasks. *International Journal of Industrial Ergonomics*, 43(3), 203-209.
- Szulc, P., Boch-Kmieciak, J., Bartkowiak, P., & Lewandowski, J. (2011). The impact of rugby training on the spinal functional parameters. *New Medicine*, 15(2), 46-

51.

- Theobald, P. S., Jones, M. D., & Williams, J. M. (2012). Do inertial sensors represent a viable method to reliably measure cervical spine range of motion? *Manual therapy, 17*(1), 92-96.
- Thong, Y., Woolfson, M., Crowe, J., Hayes-Gill, B., & Jones, D. (2004). Numerical double integration of acceleration measurements in noise. *Measurement, 36*(1), 73-92.
- Tojima, M., Ogata, N., Yozu, A., Sumitani, M., & Haga, N. (2013). Novel 3-Dimensional Motion Analysis Method for Measuring the Lumbar Spine Range of Motion: Repeatability and Reliability Compared With an Electrogoniometer. *Spine, 38*(21), E1327-E1333.
- Unsöld, A., & Baschek, B. (2001). *The new cosmos: an introduction to astronomy and astrophysics*. (4th ed.). Springer.
- Wang, F., Skubic, M., Abbott, C., & Keller, J. M. (2010). Body sway measurement for fall risk assessment using inexpensive webcams. Paper presented at the Engineering in Medicine and Biology Society (EMBC), 2010 Annual International Conference of the IEEE, Buenos Aire.
- Welch, G., Bishop, G., Vicci, L., Brumback, S., & Keller, K. (1999). The HiBall tracker: High-performance wide-area tracking for virtual and augmented environments. Paper presented at the Proceedings of the ACM symposium on Virtual reality software and technology.
- White, A. A., & Panjabi, M. M. (1990). *Clinical biomechanics of the spine* (Vol. 2). Lippincott Philadelphia.
- White, G. C., & Garrott, R. A. (1990). *Analysis of wildlife radio-tracking data*. (1st ed.). Elsevier.
- Williams, J. M., Haq, I., & Lee, R. Y. (2010). Dynamic measurement of lumbar curvature using fibre-optic sensors. *Medical engineering & physics, 32*(9), 1043-1049.
- Windolf, M., Götzen, N., & Morlock, M. (2008). Systematic accuracy and precision analysis of video motion capturing systems—exemplified on the Vicon-460

REFERENCES

- system. *Journal of biomechanics*, 41(12), 2776-2780.
- Wong, W. Y., & Wong, M. S. (2009). Measurement of Postural Change in Trunk Movements Using Three Sensor Modules. *Instrumentation and Measurement, IEEE Transactions on*, 58(8), 2737-2742.
- Wong, W. Y., & Wong, M. S. (2008a). Detecting spinal posture change in sitting positions with tri-axial accelerometers. *Gait & posture*, 27(1), 168-171.
- Wong, W. Y., & Wong, M. S. (2008b). Trunk posture monitoring with inertial sensors. *European Spine Journal*, 17(5), 743-753.
- Woodman, O. J. (2007). An introduction to inertial navigation. University of Cambridge, Computer Laboratory, Tech. Rep. UCAMCL-TR-696, 14, 15.
- Wu, G., & Cavanagh, P. R. (1995). ISB recommendations for standardization in the reporting of kinematic data. *Journal of Biomechanics*, 28(10), 1257-1261.
- Wu, G., Siegler, S., Allard, P., Kirtley, C., Leardini, A., Rosenbaum, D., et al. (2002). ISB recommendation on definitions of joint coordinate system of various joints for the reporting of human joint motion—part I: ankle, hip, and spine. *Journal of biomechanics*, 35(4), 543-548.
- Yang, Y., Pu, F., Li, Y., Li, S., Fan, Y., & Li, D. (2014). Reliability and Validity of Kinect RGB-D Sensor for Assessing Standing Balance. *IEEE Sensors Journal*, 14(5), 1633-1638.
- Youssef, J., Denis, B., Godin, C., & Leseq, S. (2012). Pedestrian tracking solution combining an impulse radio handset transmitter with an ankle-mounted inertial measurement unit. *International Journal of Navigation and Observation*, 2012.
- Yun, X., & Bachmann, E. R. (2006). Design, implementation, and experimental results of a quaternion-based Kalman filter for human body motion tracking. *Robotics, IEEE Transactions on*, 22(6), 1216-1227.
- Xsens 3D motion tracking, (2013). MVN BIOMECH Awinda - Products - Xsens 3D motion tracking. [online] Available at: <http://www.xsens.com/products/mvn-biomech-awinda/> [Accessed 25 Sep. 2014].

REFERENCES

- Zatsiorsky, V. M. (1998). Kinematics of human motion. Human Kinetics.
- Zhang, Z. Q., Pansiot, J., Lo, B., & Yang, G. Z. (2011). Human back movement analysis using bsn. Paper presented at the International Conference on Body Sensor Networks (BSN).
- Zink, J., Pettineo, M., & Hoxley, J. (2011). Practical Rendering and Computation with Direct3D 11. (1st ed.). CRC Press.